Kinetics and mechanism of model reactions in thermoresponsive nanoreactors

D I S S E R T A T I O N

zur Erlangung des akademischen Grades
d o c t o r r e r u m n a t u r a l i u m
(Dr. rer. nat.)
im Fach: Chemie

eingereicht an der
Mathematisch-Naturwissenschaftlichen Fakultät
der Humboldt-Universität zu Berlin

von
M. Sc. Daniel Besold

Präsident der Humboldt-Universität zu Berlin
Prof. Dr.-Ing. Dr. Sabine Kunst

Dekan der Mathematisch-Naturwissenschaftlichen Fakultät
Prof. Dr. Elmar Kulke

Gutachter/in: 1. Prof. Dr. Matthias Ballauff

2. Prof. Dr. Nicola Pinna

3. Prof. Dr. Helmut Schlaad

Eingereicht am: 15.05.2020

Tag der mündlichen Prüfung: 11.12.2020

If I have seen further, it is by standing on the shoulders of giants.

Isaac Newton

to my Parents, Family and Friends

Abstract

Two model reactions are investigated with thermoresponsive core-shell nanoreactors. The widely used reduction of 4-nitrophenol (Nip) and the reduction of potassium hexacyanoferrate(III) (HCF), both reduced with sodium borohydride. The nanoreactors comprise of a polystyrene (PS) core surrounded by a thermoresponsive hydrogel shell of poly-*N*-isopropylacrylamide (PNIPAM) crosslinked with *N,N'*-methylenebisacrylamide. Metal nanoparticles are immobilised inside the hydrogel shell on the surface of which the model reactions are catalysed.

Prior to the kinetic analysis, mechanistic studies of the nitroarene reduction mechanism and kinetic studies of the 4-nitrophenol reduction with the focus on gold and silver catalysts are reviewed in a comprehensive literature survey. For the reaction to be suitable as a model reaction, the reaction path is required to follow the so-called *direct route* from the nitroarene reactant to the aminoarene product (via nitroso- and hydroxyalamine intermediates). This was found to be the case for gold, silver, platinum and palladium catalysts. Here, the precise mechanism appears to be highly sensitive to combinations of catalyst metal, nitroarene substituents, solvent, and reaction conditions. For the aqueous reduction of Nip, indications for a difference in the rate-determining step between gold and silver are found. On gold, the last step from 4-hydroxylaminophenol to 4-aminophenol is rate-determining while on silver it could be the first reaction step. The review of kinetic studies shows that isosbestic points in the UV-Vis spectra are found with a higher probability with silver- than with gold catalysts, supporting the hypothesis of a difference in the rate-determining step between gold and silver.

The kinetics of the aqueous reduction of 4-nitrophenol is investigated with silver nanoparticles immobilised in PS-PNIPAM core-shell nanoreactors. The deconvolution of the UV-Vis spectra discloses that 4-nitrophenol is directly converted to 4-aminophenol without accumulation of intermediates, additionally supporting the hypothesis of a rate-determining first reaction step on silver. Based on a kinetic model derived previously for gold catalysts, a modified kinetic model is derived. The model accounts for the conversion of reactants to products in a two-step reaction without accumulation of intermediates. The kinetic data are fitted accurately at low conversions, but the fit begins to deviate towards higher conversions. An analysis of the relative deviation between experimental data and fit indicates that the adsorption of the product 4-aminophenol, not accounted for in the model, could be the reason.

Investigations of the influence of the temperature reveal the typical non-Arrhenius dependency of the reaction rate, which was found previously for thermoresponsive PNIPAM based catalysts. The temperature dependence of the adsorption constant of borohydride provides evidence that the partition ratios (i.e. the concentration ratio between bulk/hydrogel) of the reactants are relevant parameters for the kinetics of catalysts embedded in hydrogels.

The reduction of potassium hexacyanoferrate(III) is investigated with gold nanoparticles embedded in PS-PNIPAM core-shell nanoreactors. The kinetic measurements reveal a strong influence of the ionic strength on the reaction rate and an inhibiting effect, increasing with increasing HCF concentration. Based on these observations, a new kinetic model is described, which accounts for the relevant influence factors of the hydrogel, the catalyst geometry, diffusional-, and electrostatic effects. Due to the diffusion-controlled reaction kinetics, the reaction product accumulates inside the hydrogel shell and repels the reactant HCF. As a consequence, the diffusion rate of HCF to the catalyst and thus, the reaction rate itself decrease.

The results show that the reaction rate is increasing with increasing ionic strength as the charges of the accumulated products are screened better. With increasing HCF concentration, the rate is decreasing because more products accumulate and increase the repulsion of the reactant. Furthermore, the model shows the influence of ion partitioning inside the hydrogel. Even at constant bulk ionic strength the ionic strength inside the hydrogel is changing upon replacement of one ion species by another with a different partition coefficient. Investigating the influence of the reaction temperature discloses that the activation energy for the diffusion of reaction products is in the regime of thermal activation. The permeability of the hydrogel for HCF shows a minimum around the lower critical solution temperature (LCST) of PNIPAM while it is generally increasing with increasing temperature, pointing to a strong affinity to the hydrogel at elevated temperatures. The model demonstrates the importance of electrostatic effects in diffusion-controlled reactions in hydrogels with only a few relevant and physically meaningful fit parameters.

Keywords: 4-nitrophenol, hexacyanoferrate(III), kinetics, nanoparticles, PNIPAM, smart catalysis, thermoresponsive nanoreactors.

Zusammenfassung

Zwei Modellreaktionen wurden mit thermoresponsiven Kern-Schale Nanoreaktoren untersucht. Die weit verbreitete Reduktion von 4-Nitrophenol (Nip) und die Reduktion von Kaliumhexacyanidoferrat(III) (HCF) mit Natriumborhydrid. Die Nanoreaktoren bestehen aus einem Polystyrol Kern, umgeben von einer Hydrogel Schale aus mit *N,N'*-Methylenbis-acrylamid vernetztem Poly-(*N*-Isopropylacrylamid) (PNIPAM). Die Reaktionen werden von Metall Nanopartikeln katalysiert, die in der Hydrogel Schale synthetisiert und fixiert wurden.

Vor der kinetischen Analyse wurden mechanistische Studien der Reduktion von Nitroarenen und kinetische Studien der Reduktion von Nip mit, dem Fokus auf Gold- und Silber Katalysatoren, in einer umfassenden Literaturstudie zusammengefasst. Um als Modellreaktion geeignet zu sein, muss der Reaktionsweg der sogenannten *direkten Route* vom Nitroaren Reaktand zum Aminoaren Produkt (über Nitroso- und Hydroxylamin Zwischenstufen) folgen. Dies ist für Gold-, Silber-, Platin- und Palladiumkatalysatoren der Fall. Hierbei scheint der genaue Mechanismus hochsensibel auf die Kombination aus Katalysatormetall, Nitroaren Substituenten, Lösungsmittel und Reaktionsbedingungen zu sein. Für die wässrige Reduktion von Nip wurden Anzeichen für einen Unterschied im geschwindigkeitsbestimmenden Schritt zwischen Gold und Silber gefunden. Auf Gold ist es der letzte Reaktionsschritt von 4-Hydroxylaminophenol zu 4-Aminophenol während es auf Silber der erste Reaktionsschritt sein könnte. Die Durchsicht von kinetischen Studien zeigte, dass isosbestische Punkte in den UV-Vis Spektren mit höherer Wahrscheinlichkeit mit Silber als mit Gold Katalysatoren zu finden sind. Dies unterstützt die Hypothese eines Unterschieds im geschwindigkeits-bestimmenden Schritt zwischen Gold und Silber Katalysatoren.

Die Kinetik der wässrigen Reduktion von 4-Nitrophenol wurde mit Silber Nanopartikeln untersucht. Die Dekonvolution der UV-Vis Spektren hat gezeigt, dass Nip ohne Anreicherung von Zwischenprodukten zu 4-Aminophenol umgesetzt wird. Dies erhärtet die Hypothese eines geschwindigkeitsbestimmenden ersten Reaktionsschrittes auf Silber weiter. Basierend auf einem zuvor für Gold Katalysatoren entwickelten Modell wurde ein neues kinetisches Modell abgeleitet. Das Modell beschreibt die Reaktion in zwei Schritten ohne Anreicherung von Zwischenprodukten. Die kinetischen Daten konnten bei niedrigen Umsätzen gut gefittet werden, bei höheren Umsätzen beginnt der Fit jedoch abzuweichen. Die Analyse der relativen Abweichung zwischen experimentellen Daten und Fit deutet darauf hin, dass die Adsorption

des Produktes, die im Modell nicht berücksichtig wurde, der Grund dafür sein könnte. Untersuchungen des Einflusses der Temperatur ergaben die typische, von Arrhennius abweichende Abhängigkeit der Reaktionsrate, die bereits zuvor für auf PNIPAM basierende Katalysatoren gefunden wurde. Die Temperaturabhängigkeit der Adsorptionskonstante von Borhydrid liefert Hinweise, dass die Partitionierungsverhältnisse (d.h. das Konzentrations-verhältnis zwischen außer- und innerhalb des Hydrogels) der Reaktanden relevante Parameter für die Kinetik von in Hydrogelen eingebetteten Katalysatoren sind.

Die Reduktion von Kaliumhexacyanidoferrat(III) wurde mit Gold Nanopartikeln untersucht. Die kinetischen Messungen zeigen einen starken Einfluss der Ionenstärke auf die Reaktionsate, sowie einen mit der HCF Konzentration ansteigenden inhibierenden Effekt. Basierend auf diesen Beobachtungen wird ein neues kinetisches Modell beschrieben, dass die relevanten Einflussfaktoren durch das Hydrogel, die Katalysatorgeometrie, Diffusions- sowie elektrostatische Effekte berücksichtigt. Weil die Reaktion diffusionskontrolliert ist, reichert sich das Produkt in der Hydrogel Schale an und stößt den Reaktand HCF ab. Als Folge sinken die Diffusionsrate und dadurch die eigentliche Reaktionsrate.

Die Ergebnisse zeigen, dass die Reaktionsrate mit steigender Ionenstärke ansteigt, da die Ladungen des angereicherten Produkts besser abgeschirmt sind. Mit steigender HCF Konzentration sinkt die Reaktionsrate weil sich mehr Produkt anreichert und dadurch die Abstoßung des Reaktanden verstärkt wird. Darüber hinaus zeigt das Modell den Einfluss der Partitionierungsverhältnisse. Selbst bei im Volumen konstanter Ionenstärke ändert sich die Ionenstärke im Hydrogel, wenn eine Ionenspezies durch eine Andere mit verschiedenem Partitionierungsverhältnis ersetzt wird. Der Einfluss der Temperatur zeigt, dass die Aktivierungsenergie der Diffusion des Produktes im Bereich der thermischen Aktivierung liegt. Die Permeabilität des Hydrogels für HCF zeigt ein Minimum im Bereich der unteren kritischen Lösungstemperatur von PNIPAM, steigt aber insgesamt mit der Temperatur, was auf eine starke Affinität von HCF zum Hydrogel bei erhöhter Temperatur hinweist. Insgesamt zeigt das Modell die Wichtigkeit von elektrostatischen Effekten in diffusionskontrollierten Reaktionen in Hydrogelen mit nur wenigen physikalisch interpretierbaren Parametern.

Schlüsselwörter: 4-Nitrophenol, Hexacyanidoferrat(III), Kinetik, Nanopartikel, PNIPAM, intelligente Katalyse, thermoresponsive Nanoreaktoren.

Table of Contents

1. Introduction

Catalysis has been a crucial concept in the chemical industry for more than a century and is of enormous technical significance for the economy.[1, 2] Nowadays, around 90% of all chemical processes and 60 to 80% of all chemicals produced globally are based on catalytic processes.[3, 4, 5] Heterogeneous catalysis has here a pivotal role due to its practicability in large scale industrial processes. The simple separation of reactants/products from the catalyst allows converting raw materials in an economically efficient way.[6, 7, 8, 9] Since the first large-scale industrial processes have revolutionised the fertilizer production and thus the global food production, heterogeneous catalytic processes have been developed for many other large scale productions and dominate the petro-/bulk chemical industry today.[7] With the increasing challenges of becoming economically/energetically more efficient and the trend to "greener" (and more selective) chemical processes to protect the environment, novel approaches are emerging for rational catalyst design.[3, 4, 9]

In this context, metallic nanoparticles have become subject of intense research during the last two decades.[8, 10, 11] Industrially, metal catalysts are for example used in hydrogenation reactions, reduction of NOx compounds and (partial) oxidations.[12] While silver is for example applied in the oxidation of ethene,[13] gold was thought to be catalytically inactive for a long time.[14] In the 1970s the first evidence was found that gold nanoparticles are catalytically active in the hydrogenation of olefins.[15, 16] However, the finding of Haruta et al. in 1987 that gold can catalyse the oxidation of carbon monoxide far below room temperature is often seen as the seminal work regarding the catalytic activity of gold nanoparticles.[17, 18, 19] Since then gold has been demonstrated to be catalytically active in various other reactions such as the oxidation of methane,[20] the oxidation of propane to acetone[21] or the hydrochlorination of acetylene to vinyl chloride.[22] Today both gold[17, 23] and silver[4, 24] as well as other transition metal (catalytic) nanomaterials receive great attention and are among the most active fields in nano-science.[8, 10, 25, 26]

1.1 Preparation of metal nanoparticle based catalysts

Metal nanoparticles can be synthesised by two general approaches.[27] In the top-down approach, nanoparticles are generated by disintegrating the bulk metal, e.g. by pulsed laser ablation in liquid.[28, 29] In bottom-up approaches, a metal precursor, usually a metal salt like

tetrachloroauric acid, gold(III) chloride or silver nitrate, is reduced either by chemical reducing agents like sodium borohydride or the reduction is physically triggered by pulsed laser photolysis,[30] electromagnetic irradiation (microwave up to gamma),[31, 32, 33, 34, 35, 36] ultrasonication[37, 38] or thermolysis.[39]

The main challenge with metal nanoparticles is that they tend to coalesce and aggregate.[3, 8, 10] As a consequence, the catalytically active surface area is reduced, and the particles may precipitate and lose their catalytic activity (partially or entirely). Therefore, metal nanoparticles always require a suitable stabilisation to sustain their colloidal stability and morphology (size and shape) over long periods.[27, 40] For that purpose, the metal precursors are commonly reduced in the presence of soluble or colloidal stabilising/capping agents or (porous) support materials.[8, 26, 27] The stabilisation can be of electrostatic or steric nature.[27] Pivotal is that the metal surface is still accessible for the reactants in catalysis, i.e. the surface must not be irreversibly and entirely covered by the stabiliser.[10]

For a long time, a standard method for the production of gold nanoparticles was the reduction of tetrachloroauric acid with citrate developed by Turkevich et al. in 1951.[23, 41] Here citrate acts as reducing- and capping agent at the same time. Since then many other systems have been developed where the nanoparticles are stabilised by various small molecules like surfactants,[42] alkylamines[43, 44] or alcohols,[45] or by larger molecules like dendrimers[46, 47, 48] or polymers.[49, 50, 51] The advantage of using polymers is their versatility. They can be combined to (block-)copolymers to form micellar structures,[52, 53, 54, 55] star- or branched polymers,[56, 57, 58, 59] spherical polyelectrolyte brushes[60, 61, 62, 63] or hydrogels[64, 65, 66, 67] and thus offer an almost unlimited number of possible support architectures.[40, 50] Furthermore, if so-called responsive polymers are applied, the support can provide an environment which not only stabilises the metal nanoparticles but provides additional functionality.

1.2 Stabilisation with responsive polymers

Responsive polymers are polymers which are sensitive to stimuli such as pH,[68, 69] light,[64, 70] concentration of cosolutes,[71] temperature[66, 72, 73, 74] or even multiple triggers.[60, 75, 76] Hence the catalytic activity of nanoparticles stabilised by such polymers can be modulated externally. Therefore, such systems are termed *active carriers* or nanoreactors.[10] Recently systems comprising the thermoresponsive polymer poly-*N*-isopropylacrylamide (PNIPAM) are under

intense research due to their potential use in biomedical applications[77, 78, 79] such as drug delivery[80, 81] or biosensing[82, 83] and catalysis.[2, 10, 84] PNIPAM exhibits a so-called lower critical solution temperature (LCST). It is hydrophilic at low temperatures and becomes hydrophobic above its LCST of 32 °C.[84, 85, 86] As a consequence, hydrogel networks of PNIPAM undergo a volume transition upon heating where they expel water, and the hydrogel collapses.

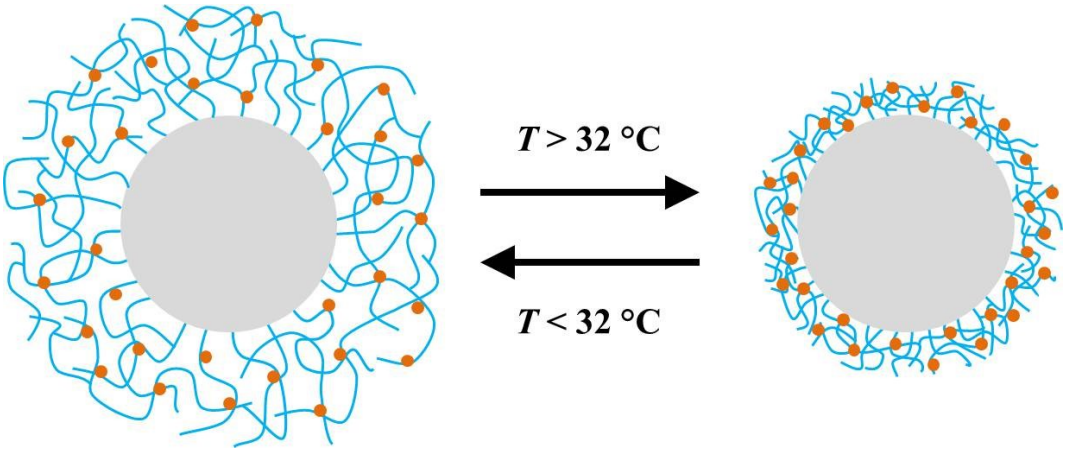

Figure 1: Core-shell nanoreactors comprising of a PS core (grey), a thermoresponsive PNIPAM shell (blue) and gold or silver nanoparticles immobilised in the shell (orange). Upon heating above (cooling below) 32 °C the network changes its volume and shrinks (swells).

In this work, core-shell hydrogels comprising of a polystyrene (PS) core surrounded by a PNIPAM hydrogel network are applied as carriers for silver and gold nanoparticles. The latter are synthesised by adsorbing the metal precursor in the PNIPAM hydrogel and subsequent reduction by sodium borohydride. The as-obtained nanoreactors and their thermoresponsive behaviour are shown schematically in Figure 1.

1.3 Heterogeneous catalysis with metal nanoparticles

The fast development in nanoscience and the development of new synthetic protocols has enabled the synthesis of metal nanoparticles with well-controlled morphology.[2, 9, 25, 26, 87, 88, 89] This enables catalytic studies of the coherences between catalytic activity and the size, shape and composition of nanoparticles. For that purpose model reactions are applied which offer the possibility to test, assess and compare the catalytic activity of different nanomaterials. For that, model reactions need to fulfil some criteria in order to allow quantitative comparison between different catalysts.[10, 11]

- It should be a well-established reaction from reactant to product without the occurrence of side reactions or by-product formation.

- The reaction should not occur without the catalyst.

- The reaction rate is easily accessible and can be measured with high precision in order to allow for a detailed kinetic analysis.

- The reaction can be measured under mild conditions, i.e. at moderate (room) temperature and in mild solvents.

Subjects of this work are two model reactions which are used in noble metal catalysis and introduced hereafter.

1.3.1 Model reactions – reduction of 4-nitrophenol

The catalytic reduction of 4-nitrophenol (Nip) with borohydride in aqueous solution by noble metal nanoparticles has been first investigated by the groups of Pal et al. and Esumi et al.[46, 90] It was shown that the reaction can be catalysed by gold, silver and copper nanoparticles. In contrast, Nip and borohydride alone showed no reaction.[46, 90, 91] Since then the reaction became the probably most widely applied benchmark reaction to assess the catalytic activity of metal nanoparticle catalysts of diverse architectures and compositions.[11, 40, 92]

The general reaction scheme for the reduction of nitroarenes, shown in Figure 2, was first established by Haber in 1898 based on the electrochemical reduction of nitrobenzene on a platinum cathode.[93] Two reaction routes were identified. In the so-called *direct route* nitroarenes (1) yield the respective arylamine (4) in three reaction steps via nitroso (2) and hydroxylamine (3) intermediates. In the *condensation route*, the latter two intermediates undergo a condensation reaction in solution to yield an azoxy intermediate (5) which is subsequently reduced to the respective arylamine via azo (6) and hydrazo (7) intermediates. Since then all intermediates have been verified, and the reaction scheme was extended by a *disproportionation mechanism* where two arylhydroxylamine molecules are transformed into an arylamine and a nitrosoaryl molecule.[94] The disproportionation was only shown to occur on Raney nickel catalyst together with additional promoting agents such as vanadium salts and therefore plays no role for the reduction on noble metal catalysts discussed here.[95, 96] However, the *condensation route* mechanism could occur as undesired parallel reaction to the

desired *direct route* if the intermediates desorb from the catalyst surface. Therefore, care should be taken during the kinetic evaluation.

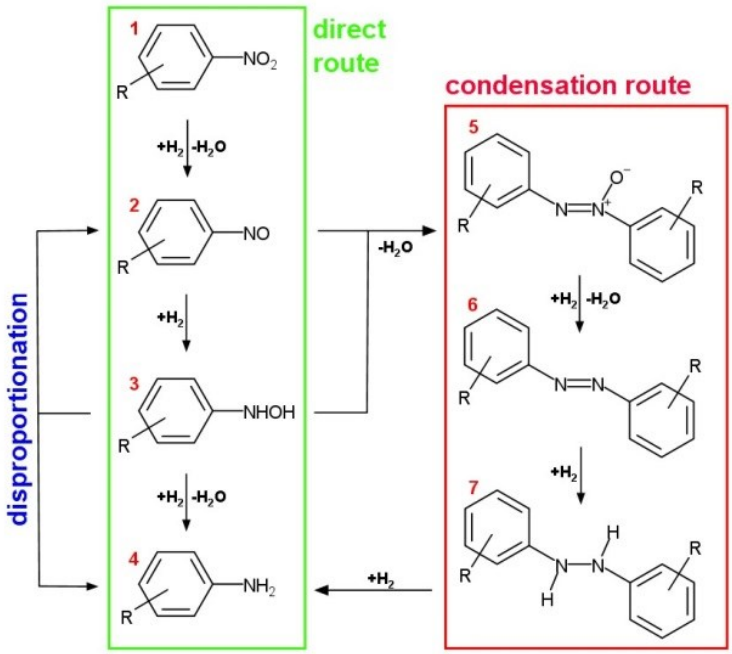

Figure 2: Reaction scheme for the reduction of nitroarenes. *Direct route* (green), *condensation route* (red) and *disproportionation mechanism* (blue).

The advantage of the reduction of Nip is the cost-efficient and straightforward implementation of catalytic tests with standard lab equipment available in many laboratories. Mixed with an aqueous solution of borohydride, 4-nitrophenol is deprotonated to 4-nitrophenolate (due to the basic pH caused by borohydride) which shows a strong absorption peak at $\lambda = 400$ nm. Therefore, the reaction can be monitored in situ by UV-Vis spectroscopy, as shown in Figure 3 (a).

During the reaction, the absorption peak of Nip disappears and a new peak caused by 4-aminophenol (Amp) appears at $\lambda = 300$ nm. The presence of isosbestic points (where all spectra intersect) shows that only two species with varying concentration are present in solution (i.e. the reactant and product) and therefore indicate a clean reaction along the *direct route*. However, the presence of isosbestic points is, by far, not the norm and often overlooked in the literature.[44, 52, 97, 98, 99, 100, 101, 102, 103] Even for catalysts based on the same metal examples with and without isosbestic points can be found abundantly.[44, 47, 48, 49, 53, 73, 104, 105, 106, 107, 108]

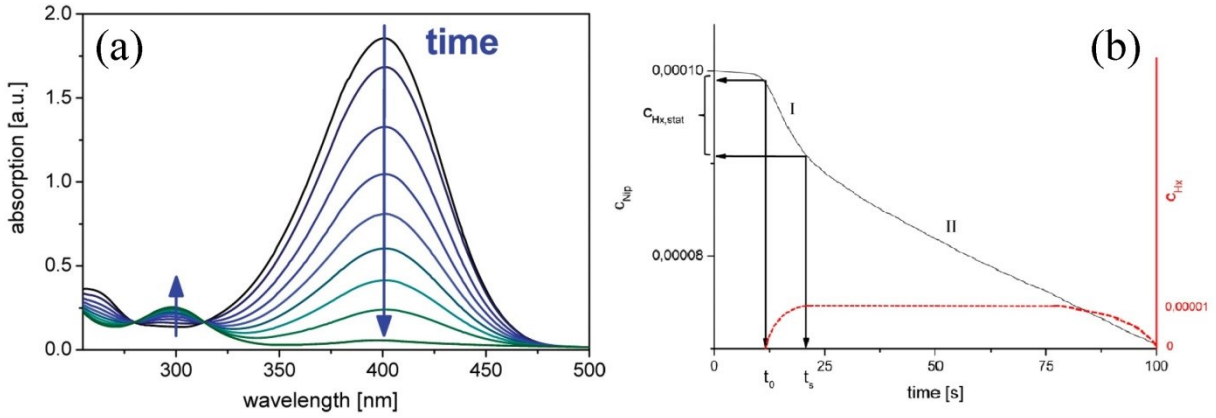

Figure 3: Reduction of *Nip* with borohydride. Optical absorption spectra (a) recorded subsequently during the reduction by platinum nanoparticles and idealised time dependency of the concentration of *Nip* and 4-hydroxylaminophenol (b) during the intermediate- (I) and the stationary state (II) regime. Reprinted with permission; (a) © 2010[107] and (b) © 2014,[109] American Chemical Society.

For the kinetic evaluation, the time dependence of the reactant concentration, shown in Figure 3 (b), can be obtained from the absorption maximum of *Nip* at $\lambda = 400$ nm according to

$$\frac{Abs(t)-Abs(t=\infty)}{Abs(t=0)-Abs(t=\infty)} = \frac{c_r(t)}{c_r(t=0)}, \tag{1.1}$$

where $Abs(t)$ is the absorbance at $\lambda = 400$ nm and $c_r(t)$ is the reactant (Nip) concentration at time t. If the reaction is conducted under excess concentration of borohydride relative to *Nip* (i.e. $c_{BH4} \gg c_{Nip}$) the reaction can be evaluated with pseudo first order kinetics according to

$$-\frac{dc_{Nip}}{dt} = k_{app}c_{Nip} = k_1 S c_{Nip}, \tag{1.2}$$

where the apparent reaction rate constant k_{app} can be obtained from the slope of the linear regime (II) in Figure 3 (b). In the early catalytic studies k_{app} was used to compare the catalytic activity of different catalysts and is still widely used today.[46, 90, 91, 92, 108, 110] However, with this evaluation strategy, the catalytic activity of different catalysts can only be compared if equal amounts of metal nanoparticles with equal size are applied. To our best knowledge, Mei et al. were the first who showed that k_{app} is proportional to the catalytically active metal surface area.[63] For a quantitative comparison/evaluation k_{app} needs to be normalised to the catalytically active metal surface area per unit volume of the reaction mixture S to obtain the surface-normalised reaction rate constant k_1.

Figure 3 (b) schematically shows the typical features of the course of the Nip concentration upon reduction, which can be distinguished in three time regimes. The first regime is the induction time t_0 where no reaction takes place, and the reactant concentration remains constant. The induction time was ascribed to various reasons by different groups and is still under debate today.[111, 112] After that, the concentration decreases rapidly in an intermediate regime (I) before a stationary state (II) is achieved.

Based on the pseudo first order kinetic analysis of the stationary state regime (II), Wunder et al. conducted a study with gold and platinum nanoparticles stabilised in spherical polyelectrolyte brushes (SPB).[107] As the reaction is heterogeneously catalysed on the metal surface, a Langmuir-Hinshelwood model has been applied. The reactants (Nip and borohydride) adsorb at the catalyst surface where the reduction to Amp takes place before the latter desorbs quickly. The adsorption of the reactants was modelled with Langmuir-Freundlich adsorption isotherms, and the rate law was obtained as

$$-\frac{dc_{Nip}}{dt} = k_{app}c_{Nip} = k_{L-H}S\theta_{Nip}\theta_{BH4} = \frac{k_{L-H}\,S\,(K_{ad,Nip}c_{Nip})^{n}(K_{ad,BH4}c_{BH4})^{m}}{(1+(K_{ad,Nip}c_{Nip})^{n}+(K_{ad,BH4}c_{BH4})^{m})^{2}} \qquad (1.3)$$

where k_{L-H} is the Langmuir-Hinshelwood reaction rate constant, n and m are the Freundlich exponents and θ_{Nip}, θ_{BH4} and $K_{ad,Nip}$, $K_{ad,BH4}$ are the surface coverages and the adsorption constants of the reactants, respectively. Prerequisite to apply this model is the assumption of fast diffusion compared to the surface reaction (i.e. the latter determines the kinetics) which was confirmed by calculation of the second Damköhler number $DaII$ in a subsequent study.[113] With equation (1.3) the apparent reaction rates measured against both reactant concentrations could be fitted successfully. As a result, the adsorption of Nip to the catalyst surface was found to be much stronger than for borohydride.

Despite the success of the model, it does not provide a complete picture of the kinetics as it describes only the stationary state regime (II). The model was further advanced by Gu et al. to directly fit the entire time dependency of the concentration of Nip to account for that.[109] The approach is based on the results of Corma et al. They found that the reduction of nitrobenzene with hydrogen proceeds only via the direct route on gold catalysts where the reduction from nitrobenzene to hydroxylamine can be regarded as one (fast) step followed by the slower reduction to aniline (i.e. the rate-determining step).[114] Based on this assumption, the intermediate regime in Figure 3 (b) could be explained. At the beginning of the reaction, Nip

is first reduced to 4-hydroxylaminophenol (Hx) during the intermediate regime (I). The latter accumulates and slows down the reaction to the lower reaction rate in the stationary state regime (II); subsequently, the concentration of 4-hydroxylaminophenol remains approximately constant up to the end of the reaction. A two-step Langmuir-Hinshelwood model was developed, and the kinetic data were fitted by numerically solving the coupled differential equations

$$-\frac{dc_{Nip}}{dt} = \frac{k_a\, S\, (K_{ad,Nip}c_{Nip})^n K_{ad,BH4}c_{BH4}}{(1+(K_{ad,Nip}c_{Nip})^n + K_{ad,Hx}c_{Hx} + K_{ad,BH4}c_{BH4})^2} \tag{1.4}$$

and

$$\frac{dc_{Hx}}{dt} = -\frac{dc_{Nip}}{dt} - \frac{dc_{Amp}}{dt} = \frac{SK_{ad,BH4}c_{BH4}\left(k_a(K_{ad,Nip}c_{Nip})^n - k_b K_{ad,Hx}c_{Hx}\right)}{(1+(K_{ad,Nip}c_{Nip})^n + K_{ad,Hx}c_{Hx} + K_{ad,BH4}c_{BH4})^2}, \tag{1.5}$$

where c_{Hx} and $K_{ad,Hx}$ are the concentration and adsorption constant of the hydroxylamine intermediate, c_{Amp} is the concentration of Amp and k_a and k_b are the reaction rate constants of the first and the second reaction step, respectively.

The kinetic model described above could successfully explain the features of the reaction as observed on gold and platinum nanoparticles. However, an intermediate regime is not always present.[73, 107, 113, 115, 116, 117, 118, 119] The different results found in the literature even for similar catalysts show that the coherences regarding kinetics and mechanism of this reaction appear to be more complicated than it seems at first. Open questions to be answered are whether the kinetic and mechanistic findings described above can be transferred to other catalyst metals as well. Associated with this is the question of why isosbestic points are observed in some cases only. Therefore, additional kinetic studies with other catalyst metals are desirable. Together with the already existing studies and reviewed in a broader literature context, the picture of the reduction as a model reaction for noble metal catalysts may be further supplemented.

1.3.2 Model reactions – reduction of hexacyanoferrate(III)

The reduction of hexacyanoferrate(III) (HCF) with borohydride has been first investigated by Freund et al. and Bhattacharjee et al. as uncatalysed reaction.[120, 121] Later it was found that the reduction of HCF with thiosulfate can be catalysed by gold and platinum nanoparticles.[122, 123] Based on these findings, Carregal-Romero et al. were the first to investigate the catalysed reduction with borohydride by citrate stabilised gold nanoparticles.[124] The reaction can be

monitored by UV-Vis spectroscopy, as shown in Figure 4 (a).[124] The reactant HCF has a distinct absorption maximum at $\lambda = 420$ nm, which decreases and leaves a weak absorption baseline of the product hexacyanoferrate(II) after completion of the reaction. Therefore, the time dependence of the reactant concentration can be derived according to equation (1.1) shown previously. Here $Abs(t)$ is the absorbance at $\lambda = 420$ nm and $c_r(t)$ is the HCF concentration at time t. The isosbestic point at $\lambda \sim 280$ nm indicates that only the reactant and product are present and thus no undesired side reactions take place.[119]

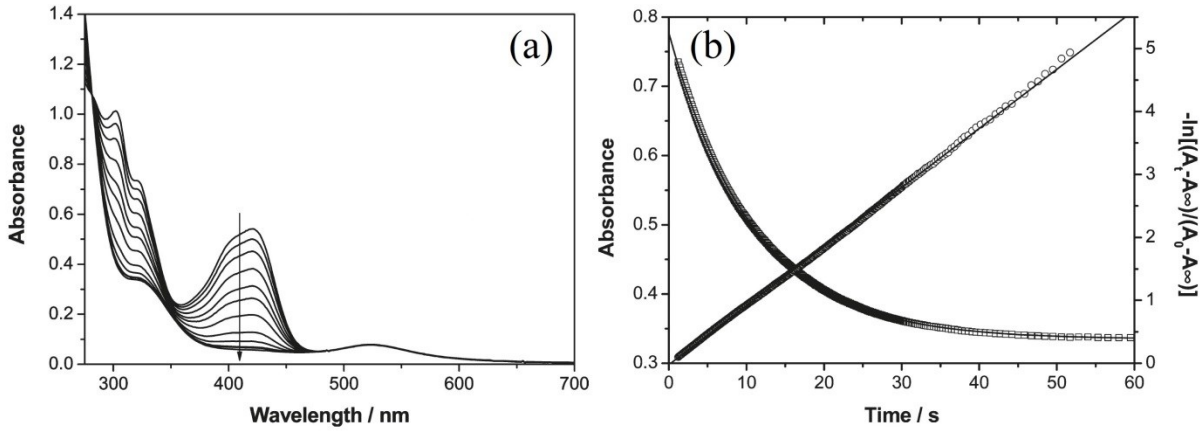

Figure 4: Reduction of HCF with borohydride. Optical absorption spectra (a) recorded subsequently during the reaction and decay of the absorption maximum (b) at $\lambda = 420$ nm throughout the course of the reaction. Reprinted with permission; © 2010, American Chemical Society.[124]

As the catalysed reaction was found to be about four orders of magnitude faster than the uncatalysed one, the latter can be disregarded for the kinetic evaluation shown in Figure 4 (b).[120, 121, 124] The reaction was found to follow pseudo first order kinetics with respect to HCF at excess borohydride concentration according to[124, 125]

$$-\frac{dc_{HCF}}{dt} = k_{app} c_{HCF} = k_1 S c_{HCF}. \tag{1.6}$$

This shows that the reaction proceeds indeed via surface catalysis as k_1 is independent of the applied amount of nanoparticles. With gold nanoparticles (formed by boiling $H[Au(Cl)_4]$ in an aqueous citrate solution) it was found that the redox reaction with the net equation

$$BH_4^- + 8[Fe(CN)_6^{3-}] + 3H_2O \rightarrow H_2BO_3^- + 8[Fe(CN)_6^{4-}] + 8H^+ \tag{1.7}$$

proceeds very fast and reaches the diffusion limit of HCF at higher borohydride concentrations.[124, 126] The scheme in Figure 5 shows that the reaction proceeds in two steps

where the gold nanoparticles separate the reduction and the oxidation steps of the redox process and thus accelerate the reaction. First, borohydride is oxidised, the gold nanoparticles serve as a reservoir for electrons and become negatively charged. In a second step one electron is transferred to hexacyanoferrate and reduces it.[124]

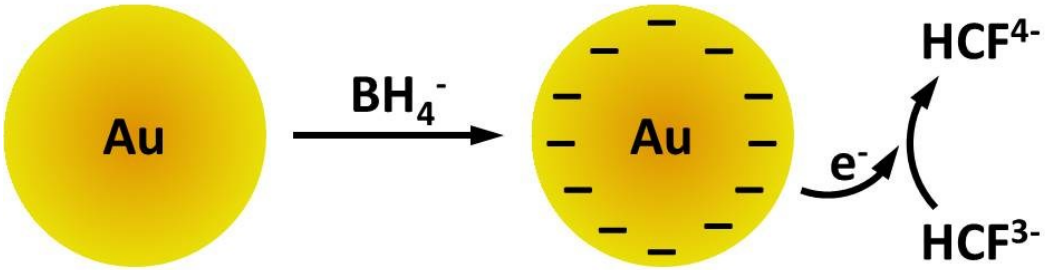

Figure 5: Scheme of the reduction reaction of hexacyanoferrate(III) to hexacyanoferrate(II) at the surface of gold nanoparticles by borohydride. The sphere represents a gold nanoparticle which is negatively charged by borohydride in a first step, followed by the transfer of one electron to hexacyanoferrate in a second step.

An analysis of the catalytic activity of gold nanoparticles centred inside a spherical polymer network of thermoresponsive PNIPAM showed the importance of diffusional processes on the catalytic rate.[125] Figure 6 (a) shows that with increasing temperature the observed rate exhibits similar non-Arrhenius behaviour as observed in the reduction of 4-nitrophenol with thermoresponsive catalysts.[72, 73] Additionally, it shows that dependent on the density of crosslinking of the PNIPAM hydrogel with *N,N'*-methylenebisacrylamide (Bis) the catalytic activity can be modified. With increasing crosslinking density, the rate is decreasing, and the thermoresponsive effect is diminished. The reason for that can be seen in Figure 6 (b) which shows that with increasing crosslinking density the swelling ratio of the PNIPAM hydrogel decreases because the network becomes more rigid.[125]

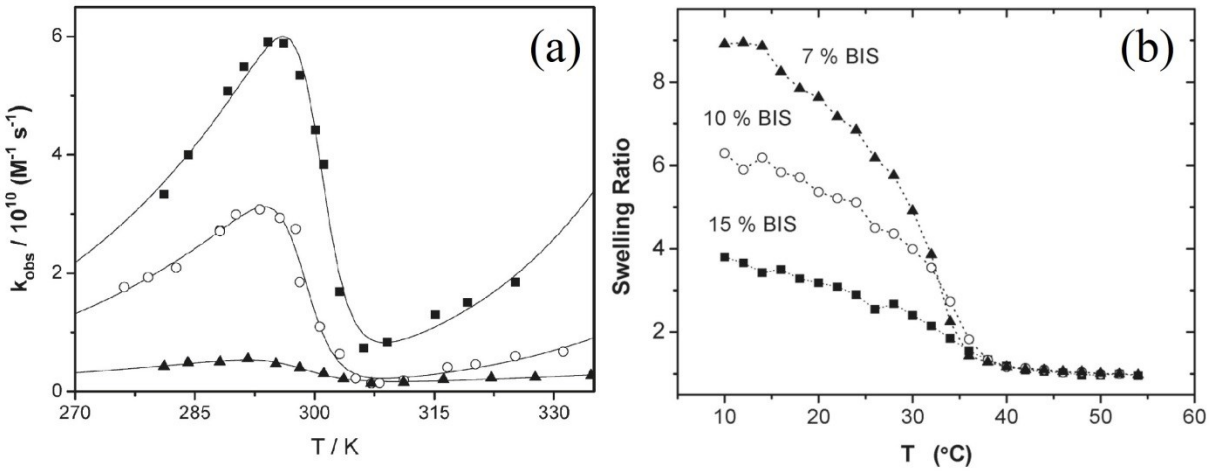

Figure 6: Influence of temperature on the apparent reaction rates ($\triangleq k_{obs}$) (a) and the swelling ratio (b) of Au@PNIPAM nanoreactors with 7 % (squares), 10 % (circles) and 15 % (triangles) crosslinking density. Reprinted with permission; © 2010, American Chemical Society.[125]

The temperature dependence in Figure 6 (a) was fitted by a two-state model applying a temperature-dependent equilibrium constant $K_{collapse}(T)$, accounting for the transition between the swollen ($T <$ LCST) and the collapsed ($T >$ LCST) state of the PNIPAM hydrogel with a Van 't Hoff relation. The reaction rates for each state were then modelled by two rate constants $k_{app,T}(T)$ following Arrhenius dependencies, and the apparent reaction rate constant k_{app} was fitted by[125]

$$k_{app} = \frac{1}{1+K_{collapse}(T)} k_{app,T<LCST}(T) + \frac{K_{collapse}(T)}{1+K_{collapse}(T)} k_{app,T>LCST}(T). \quad (1.8)$$

In the catalytic studies described above the ionic strength was kept constant.[124, 125] However, a significant effect of the ionic strength on the reaction rate was found in the uncatalysed reduction of HCF with citrate.[127] Investigations of the reaction on gold nanoparticles, stabilised with differently charged thiol ligands, have further shown that the surface potential of the catalyst strongly influences the reaction rate.[128] For gold nanoparticles with a positive surface potential (i.e. attractive interactions between HCF and the catalyst), the reaction rate was substantially higher than for nanoparticles with a negative surface potential. This shows that electrostatic effects play a significant role in the catalysed reaction as well. Here, a full kinetic model accounting for electrostatic effects and diffusional processes would provide more in-depth insight in the coherences of this reaction and contribute to a more profound understanding of diffusion-controlled reactions in hydrogels.

2. Objective

In this thesis, two heterogeneously catalysed model reactions are addressed. First, the frequently used surface controlled reduction of 4-nitrophenol and second, the fast diffusion-controlled reduction of hexacyanoferrate(III). The decisive factors in the kinetic analysis of diffusion and reaction-controlled reactions are compiled and subsequently exemplified in the respective kinetic model/analysis. Both reactions are investigated with thermoresponsive PNIPAM based nanoreactor catalysts to gain detailed insights into the kinetics and the influence of temperature.

The reaction scheme for 4-nitrophenol shows that more than one reaction route exists. For the successful application as a model reaction, the reaction must follow the direct route only. A literature review concerning mechanistic investigations shall clarify whether the reaction always follows the direct route under different reaction conditions and with different catalyst metals. Isosbestic points in the UV-Vis spectra, obtained during the reduction, are not always found. An investigation of their prevalence with a focus on gold and silver catalysts shall clarify when isosbestic points are present or not and why. The influence of the catalyst metal and support constituents shall be investigated to draw possible conclusions for the reaction kinetics and the comparability of kinetic data obtained with different catalysts.

Previous kinetic studies showed that an intermediate regime in the reaction kinetics is found on gold but not on silver. With a kinetic analysis of the 4-nitrophenol reduction on silver, the existing picture of the reaction kinetics shall be further supplemented. A model is needed to describe the kinetics at constant temperature and to investigate the temperature dependence.

A detailed kinetic analysis of the hexacyanoferrate(III) reduction on gold shall be conducted to identify the critical factors of the kinetics in diffusion-controlled reactions in thermoresponsive hydrogel nanoreactors with particular attention on the influence of ionic strength and temperature. Based on the results of the kinetic experiments, a new kinetic model shall be described, accounting for the relevant influence factors of the hydrogel, the nanoreactor geometry as well as diffusion and electrostatics. The experimental data shall be described by physically meaningful parameters to allow for an evaluation of their values.

3. Theory

3.1 Thermoresponsive hydrogels as host for metal nanoparticles

Hydrogels are water containing networks of polymers which provide the possibility to immobilise metal nanoparticles and prevent their coagulation and precipitation while maintaining their catalytic activity over long periods.[129, 130] Other than capping agents such as small ligand molecules, they provide an environment with properties which can differ significantly from the bulk properties (outside the hydrogel) and thus influence the catalytic activity of nanoparticles.[131] The relevant factors are the permeability of the hydrogel to solutes[126] and the influence of the temperature on the network properties elucidated subsequently.[10, 125, 132]

3.1.1 Permeability

The permeability P of a hydrogel describes the ability of a solute to permeate and diffuse inside the hydrogel network.[133] It is defined as the product of the solute diffusion coefficient D_g inside the hydrogel and the dimensionless partition coefficient K_{part}. The latter is defined as the ratio of the solute concentration inside the hydrogel c_i^g and the bulk concentration c_i according to[126, 134]

$$P = K_{part} D_g = \frac{c_i^g}{c_i} D_g = e^{-\beta \Delta G} D_g \tag{3.1}$$

where ΔG is the transfer free energy describing the interaction between solute and hydrogel and $\beta^{-1} = k_B T$. K_{part} is a pure thermodynamic property and D_g is a kinetic transport property.[131] Both quantities are determined by several physical and chemical interactions which are a result of the specific combination of polymer and solute as well as the hydrogel structure.[131, 135] The diffusion coefficient inside the gel is usually never higher than the bulk diffusion coefficient. Physicochemical and frictional influences can be distinguished. Physicochemical interactions include electrostatic, hydrophobic and specific binding interactions.[136] Frictional influences comprise the increase in the hydrodynamic resistance and in the solvent viscosity due to solvent structuring around polymer chains as well as the increased path length due to obstruction by polymer chains.[137] The partition ratio is determined by size exclusion, electrostatic and hydrophobic interactions.[134, 135, 138] While size

exclusion can only lead to a decrease of c_i^g relative to c_i, the other interactions can lead to a significant increase in c_i^g above the bulk concentration. As a consequence, the permeability can be higher than the bulk diffusion coefficient in case of a high polymer-solute affinity.

3.1.2 Thermoresponsivity

Thermoresponsive polymers undergo a solubility change upon temperature increase. The majority of such polymers exhibits an LCST (change from hydrophilic to hydrophobic); polymers with an upper critical solution temperature (UCST, change from hydrophobic to hydrophilic) are less abundant.[85]

For PNIPAM the reason for the solubility change is the presence of hydrophilic amide groups together with hydrophobic isopropyl groups. The amide groups can form hydrogen bonds with water, leading to an enthalpy gain while the hydrophobicity of the isopropyl groups leads to an entropy loss, known as hydrophobic effect. At low temperatures, the enthalpy gain due to H-bonding exceeds the hydrophobic entropy loss, and the polymer remains solubilised (the hydrogel is swollen with water). Upon heating above the LCST, the H-bonds are cleaved, and the adverse entropic situation around the isopropyl groups becomes dominant, causing a phase separation between polymer and water (the hydrogel collapses and expels water).[139, 140]

As a consequence, both the partition ratio and the diffusion coefficient inside the hydrogel change, which influences the catalytic activity of embedded nanoparticles, leading to non-Arrhenius-like temperature dependence.[72, 73, 84]

3.2 Aspects of kinetic modelling in surface reactions

In order to investigate the kinetics of a reaction, a suitable model is required to describe the kinetic data. Generally, there are many types of kinetic models with different levels of complexity, ranging from very simple (macroscopic) models to detailed (microscopic) models describing the full reaction dynamics. The probably most straightforward approach is to use the in principle purely empiric power laws which do not require further mechanistic information and can be applied both in homogeneously and heterogeneously catalysed reactions, respectively.[6]

If a more detailed kinetic model is applied in heterogeneous catalysis, a general aspect must be minded. Heterogeneously catalysed reactions are generally a sequence of at least two processes, the diffusion of the reactant to the catalyst surface followed by the surface reaction (including adsorption/desorption processes).[10] The simplest possible case would be a catalysed unimolecular reaction where one reactant diffuses from bulk to the catalyst surface first and then reacts at the surface. In this general case no further details regarding the shape of the catalyst particle to which diffusion occurs, and the surface reaction mechanism shall be defined. If we consider the diffusion and the surface reaction as two consecutive reaction steps (of which the diffusion is reversible) the reaction scheme can be written as[141, 142]

$$A_B \underset{k_{D'}}{\overset{k_D}{\rightleftharpoons}} A_S \overset{k_{surf}}{\rightarrow} P. \tag{3.2}$$

Here A_B is the reactant in bulk solution, A_S is the reactant at the catalyst surface, k_D and $k_{D'}$ are the rate constants for the diffusion (to and from the catalyst surface), and k_{surf} is the rate constant for the surface reaction. The rate equations are then derived as

$$-\frac{dc_{A_B}}{dt} = \left(k_D c_{A_B} - k_{D'} c_{A_S}\right) c_{NR} \tag{3.3}$$

and

$$\frac{dc_{A_S}}{dt} = \left(k_D c_{A_B} - k_{D'} c_{A_S} - k_{surf} c_{A_S}\right) c_{NR} = \left(k_D c_{A_B} - \left(k_{D'} + k_{surf}\right) c_{A_S}\right) c_{NR}. \tag{3.4}$$

Here, the rate expressions need to be multiplied by the catalyst concentration c_{NR} as the rate constants would otherwise depend on its concentration. Macroscopically usually only the reactant bulk concentration can be measured while the reactant concentration at the catalyst surface cannot be obtained. If a stationary state is assumed, i.e. a constant concentration c_{A_S} (which can be considered as intermediate of the two reaction steps), according to

$$\frac{dc_{A_S}}{dt} = 0, \tag{3.5}$$

it follows that

$$c_{A_S} = \frac{k_D\, c_{A_B}}{k_{D'} + k_{surf}}. \tag{3.6}$$

Therefore, c_{A_S} can be substituted in equation (3.3) according to

$$-\frac{dc_{A_B}}{dt} = \left(k_D c_{A_B} - k_{D'} \frac{k_D c_{A_B}}{k_{D'}+k_{surf}}\right) c_{NR}$$

$$= k_D \left(1 - \frac{k_{D'}}{k_{D'}+k_{surf}}\right) c_{A_B} c_{NR} = k_D \left(\frac{k_{surf}}{k_{D'}+k_{surf}}\right) c_{A_B} c_{NR}. \quad (3.7)$$

and the overall reaction rate constant k_{tot} can be expressed as

$$k_{tot} = \frac{k_D\, k_{surf}}{k_{D'}+k_{surf}}. \quad (3.8)$$

This corresponds to the rate constant as derived for a classic two-step reaction where a stationary state is assumed for the intermediate.[141] As in the present case the first reaction step describes diffusion, it is clear that $k_D = k_{D'}$ (diffusion will always equilibrate concentration gradients by time if undisturbed) and equation (3.8) can be written as

$$k_{tot}^{-1} = k_D^{-1} + k_{surf}^{-1}. \quad (3.9)$$

This is the classic expression for the total reaction rate in catalysed unimolecular reactions.[10, 126, 143] Equation (3.9) shows that if one of the two processes is much faster than the other, the reaction kinetics will be determined by the slower process.

This can be estimated with the second Damköhler number $DaII$, which states the ratio between the mass transfer rate (diffusion through a stagnant film over a catalyst particle) and the chemical reaction rate.[11, 144] The latter means the real surface reaction rate without any mass transfer limitations. The second Damköhler number is given as[144]

$$DaII = \frac{k_{\#} c_{i,0}^{n^{\#}}}{\frac{D_i S}{\delta} c_{i,0}} = \frac{surface\ reaction\ rate}{diffusion\ rate} = \frac{k_{\#} c_{i,0}^{n^{\#}-1} \delta}{D_i S}, \quad (3.10)$$

where $n^{\#}$ is the order of the reaction, $k_{\#}$ is the nth order (apparent) reaction rate constant, $c_{i,0}$ is the initial reactant concentration, D_i is the diffusion coefficient of the reactant, S is the surface area of the catalyst per unit volume and δ is the thickness of the stagnant film over which film diffusion occurs. If $DaII \ll 1$, the reaction kinetics is governed by the surface reaction mechanism, and if $DaII \gg 1$, the slower diffusion determines the kinetics. The knowledge about the relative rates of diffusion and surface reaction is the prerequisite to

know how a kinetic model is to be set up to describe the kinetics of a heterogeneous reaction in more detail. The essential aspects for both cases are elucidated in the following.

3.2.1 Reaction-controlled kinetics

If the diffusion is much faster than the surface reaction, the kinetics are determined by the latter. A surface reaction is described by three consecutive steps.[1] Adsorption of the reactants, reaction on the catalyst surface and desorption of the reaction product. Usually, sorption processes are assumed to be much faster than the surface reaction and are therefore in equilibrium.[6, 144] However, as every substance has an individual adsorption-desorption equilibrium, the relative concentrations of the reactants on the surface are not necessarily the same as in solution. Therefore, both, the sorption processes as well as the surface reaction are relevant for the reaction kinetics.

3.2.1.1 Adsorption isotherms

The sorption equilibrium on an ideal surface can be described by the Langmuir adsorption isotherm.[1] Here, each surface site can adsorb only one molecule; the adsorption energy is equal for all adsorption sites and independent of the surface coverage. The rates r_{ad} and r_{de} for adsorption and desorption are given as

$$r_{ad} = k_{ad} c_i (1 - \theta_i) \quad \text{and} \quad r_{de} = k_{de} \theta_i, \tag{3.11}$$

where k_{ad} and k_{de} are the rate constants for ad- and desorption, c_i is the concentration in solution and θ_i is the normalised surface coverage. In equilibrium the rates of both processes are equal, hence

$$k_{ad} c_i (1 - \theta_i) = k_{de} \theta_i. \tag{3.12}$$

Therefore, the coverage can be expressed as

$$\theta_i = \frac{k_{ad} c_i}{k_{ad} c_i + k_{de}} = \frac{K_{ad} c_i}{1 + K_{ad} c_i}, \tag{3.13}$$

giving the classical Langmuir isotherm where the adsorption constant is defined as $K_{ad} = k_{ad}/k_{de}$. To account for a distribution of adsorption energies due to the heterogeneity of the catalyst surface, a Langmuir-Freundlich adsorption isotherm[145]

$$\theta_i = \frac{(K_{ad}c_i)^n}{1+(K_{ad}c_i)^n} \tag{3.14}$$

can be applied instead.[107, 146] The Freundlich exponent $0 < n < 1$ accounts for a distribution of adsorption energies similar to a Gaussian distribution where smaller values of n represent a wider energy distribution.[147, 148] For $n = 1$ all adsorption energies are equal, and the classic Langmuir isotherm is restored.

3.2.1.2 Langmuir-Hinshelwood mechanism

Surface catalysed bimolecular reactions where both reactants adsorb on the catalyst surface are described by the Langmuir-Hinshelwood mechanism.[144, 149] The elementary steps for a bimolecular reaction on the surface are[1]

$$A + B + 2\,* \rightleftharpoons A* + B* \overset{k_{L-H}}{\rightarrow} P*_2 + * \rightleftharpoons P + 2\,*, \tag{3.15}$$

where A and B are the reactants in solution, $A*$ and $B*$ are the adsorbed reactants, $P*_2$ is the adsorbed product, P is the product in solution, and $*$ denotes free adsorption sites. The first step is the adsorption equilibrium for the reactants, the second step is the surface reaction, and the third step is the desorption equilibrium of the product. In the classic Langmuir-Hinshelwood kinetics, a weak product adsorption is assumed and therefore disregarded in the adsorption equilibria of the reactants.[150] As all sorption processes are assumed to be in equilibrium, the surface concentration of the product is approximately zero (due to its weak adsorption), and the reverse reaction can be disregarded.[1, 144] With these prerequisites, and assuming Langmuir adsorption isotherms for both reactants, the reaction rate can be expressed as[150]

$$-\frac{dc_A}{dt} = Sk_{L-H}\theta_A\theta_B = Sk_{L-H}\frac{K_{ad,A}c_A K_{ad,B}c_B}{\left(1+K_{ad,A}c_A+K_{ad,B}c_B\right)^2}, \tag{3.16}$$

where θ_A, θ_B and $K_{ad,A}$, $K_{ad,B}$ are the surface coverages and adsorption constants of the reactants, respectively. If the adsorption energies are not equal for all adsorption sites, Freundlich adsorption isotherms can be used instead, and equation (3.16) is obtained as[107, 113]

$$-\frac{dc_A}{dt} = Sk_{L-H}\theta_A\theta_B = Sk_{L-H}\frac{\left(K_{ad,A}c_A\right)^n\left(K_{ad,B}c_B\right)^m}{\left(1+\left(K_{ad,A}c_A\right)^n+\left(K_{ad,B}c_B\right)^m\right)^2}. \tag{3.17}$$

3.2.2 Diffusion-controlled kinetics

If the surface reaction of a heterogeneous reaction is faster than the diffusion of reactants to the catalyst, the reaction kinetics will be determined by diffusion. The diffusion rate to a spherical catalyst particle can be described by the classic Smoluchowski equation[151]

$$r_{SM} = k_{SM} N_A c_{NR} c_i = 4\pi D_0 r_{NP} N_A c_{NR} c_i, \tag{3.18}$$

where $k_{SM} = 4\pi D_0 r_{NP}$ is the Smoluchowski diffusion rate constant, D_0 is the bulk diffusion coefficient of the reactant, c_{NR} is the concentration of the catalyst, and c_i is the concentration of the reactant (i.e. the diffusing solute). Equation (3.18) describes the simplest case of a single spherical particle of radius r_{NP} and undisturbed reactant diffusion (i.e. no hydrogel shell). However, in hydrogel supported catalyst systems, the situation is more complicated. As shown in chapter 3.1.1, the permeability of hydrogels to solutes usually differs from the bulk diffusion coefficient, and often many catalyst particles are supported in one carrier particle.

3.2.2.1 Geometric aspects of nanoreactors

The diffusion rate for supported catalyst particles is generally determined by the geometry of the system. For hydrogel supported metal nanoparticles, two typical configurations are found regularly.[10] Figure 7 (a) depicts systems where one catalytically active nanoparticle is centred inside a spherical hydrogel, and Figure 7 (b) shows systems where multiple nanoparticles are randomly distributed within the hydrogel.

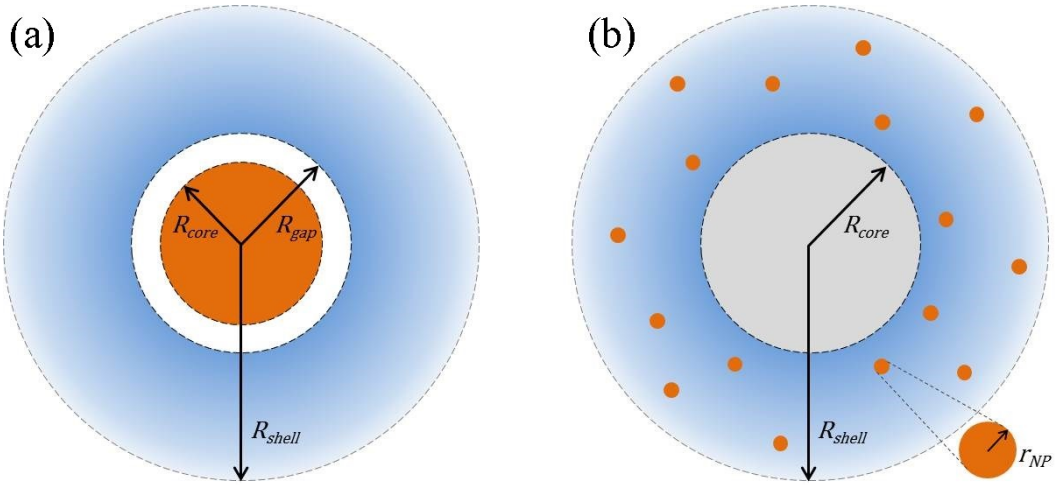

Figure 7: Typical configurations of nanoreactors comprising of catalytically active metal nanoparticle(s) (orange) and a (thermoresponsive) hydrogel shell (blue). One metal nanoparticle embedded in a spherical hydrogel (a) and multiple nanoparticles distributed randomly inside a hydrogel (b) which optionally comprises an inert core (grey). The presence of a gap between core and shell in (a) is optional as well ($R_{core} \leq R_{gap}$).

For both configurations expressions for the diffusion rate were derived, accounting for the geometry of the system as well as the diffusive properties of the hydrogel.[126, 152] For the configuration shown in Figure 7 (a), the diffusion rate constant is derived as[126]

$$k_{D,(a)} = 4\pi D_0 R_{core} N_A \left[1 + \left(\frac{D_0}{P} - 1\right)\left(\frac{R_{core}}{R_{gap}} - \frac{R_{core}}{R_{shell}}\right)\right]^{-1}. \tag{3.19}$$

Equation (3.19) is applicable for yolk-shell nanoreactors with ($R_{core} < R_{gap}$) as well as core-shell nanoreactors without ($R_{core} = R_{gap}$) a gap between core and shell.

For the setup shown in Figure 7 (b) the diffusion rate constant is derived as[152]

$$k_{D,(b)} = 4\pi P r_{NP} N_{NP} N_A \left[1 + \left(\frac{r_{NP} N_{NP} P}{D_0 R_{shell}}\right)\right]^{-1}, \tag{3.20}$$

where N_{NP} is the number of metal nanoparticles in the hydrogel. It should be noted that equation (3.20) does not contain the size of the inert core. It was shown that for small to moderate core sizes ($R_{core} \lesssim 0.35\ R_{shell}$) and small metal nanoparticles ($r_{NP} \ll R_{shell}$), the size of the inert core has only negligible influence on the diffusion rate.

3.2.2.2 Influence of electrostatic effects

In many chemical reactions, reactants and products are charged, causing a significant effect on the diffusion of both.[11, 153] In simulations it could be shown that if both, reactant and product are equally charged and repel each other, the concentration of the reactant in the vicinity of the catalyst surface is decreased, leading to a lower reaction rate at the catalyst surface.[153] The decisive factor for the strength of electrostatic effects is the ionic strength $I(r)$ of the reaction medium, which determines the range of electrostatic forces before they are screened. This screening length, known as the Debye length $\lambda_D(r)$ is given as[154]

$$\lambda_D(r) = \kappa^{-1}(r) = \sqrt{\frac{\varepsilon_0 \varepsilon_r k_B T}{2 N_A e^2 I(r)}}, \tag{3.21}$$

where $\kappa(r)$ is the inverse screening length. An increase in the ionic strength reduces the screening length, and therefore the range of electrostatic repulsion. This can, in turn, reduce the electrostatic repulsion and lead to a significant increase in the diffusion and thus the reaction rate.[155]

4. Results and Discussion

4.1 Synthesis and characterisation of nanoreactors

For all catalytic measurements nanoreactors with a polystyrene (PS) core and a thermoresponsive poly-*N*-isopropylacrylamide (PNIPAM) hydrogel shell, containing either gold or silver nanoparticles, were used. Two batches of nanoreactors were synthesised, one batch with silver nanoparticles inside the PNIPAM shell was used in the kinetic study of the 4-nitrophenol reduction (henceforth termed as Ag@PS-PNIPAM catalyst), and another batch with gold nanoparticles was used in the kinetic study of the hexacyanoferrate(III) reduction (termed as Au@PS-PNIPAM catalyst).

The nanoreactors were prepared in 3 (4) steps as described previously.[132, 156] The steps include preparation of the PS core, growth of the PS core (where necessary), preparation of the PNIPAM shell and the formation of metal nanoparticles by reduction of either $AgNO_3$ or $H[AuCl_4]$ by $NaBH_4$ inside the hydrogel shell. Silver nanoparticles were prepared inside core-shell nanoreactors, containing a PS core with a negative zeta potential ζ_{core}. Here, sodium dodecylsulfate (SDS) was applied as surfactant, and the PS core could be prepared in a single step. Gold nanoparticles were prepared inside nanoreactors, containing a PS core with a positive zeta potential. Here, hexadecyltrimethylammonium bromide (CTAB) was applied as surfactant during the preparation of the PS core, which required an additional growth step. The hydrogel shell was crosslinked with a molar fraction of 2.5% *N,N'*-methylenebisacrylamide (Bis) with respect to NIPAM for both catalysts. After each step, the particles were cleaned, either by dialysis (core synthesis) or ultrafiltration, the solid content was determined, and the size was measured via dynamic light scattering (DLS). The details of the nanoreactor syntheses are described in chapters 6.2.2.2 to 6.2.2.5. The metal fraction f_m of the readily prepared nanoreactors was measured via thermogravimetric analysis (TGA) and the size of the metal nanoparticles was determined graphically with cryogenic transmission electron microscopy (cryo-TEM) images. About 400 particles were measured and averaged to obtain the mean metal nanoparticle radius r_{NP}. The molar mass was calculated as described in chapter 6.3.6. The hydrodynamic radii $r_{H,core}$ and the zeta potentials ζ_{core} of the PS core particles, the metal fractions f_m, the mean metal nanoparticle radii r_{NP}, and the molar masses of the readily prepared nanoreactors (including metal nanoparticles) MW_{m+} for both nanoreactor batches are given in Table 1.

Table 1: Results of the characterisation of the nanoreactors with silver and gold, respectively.

parameter		Ag@PS-PNIPAM	Au@PS-PNIPAM
$r_{H,core}$	/ nm	53	30 (after first synth. step) 71 (after growth process)
ζ_{core}	/ mV	- 52.3	+ 60.7 (after growth process)
f_m	/ [1]	0.099	0.034
r_{NP}	/ nm	2.8 ± 1.2	1.6 ± 0.5
MW_{m+}	/ g mol^{-1}	5.11*10^8	1.69*10^9

Figure 8 (a) and (b) show the cryo-TEM images, obtained with the two batches of catalysts. The images show the PS core as big dark spheres, surrounded by the silver (a) and gold (b) nanoparticles, which are predominantly located close to the PS core. For both catalyst batches, the PNIPAM shell is only weakly visible around the PS core because the hydrogel shell swollen with water gives only a very weak contrast in the images, which is difficult to be distinguished by our cryo-TEM instrument without energy filter. However, the existence of a thermoresponsive shell is undoubted, as disclosed by the measurements of the hydrodynamic radii against temperature in Figure 8 (c) and (d). Here, a clear trend can be observed, both, with and without the metal nanoparticles inside the shell. Both particle batches show the expected trend where the hydrodynamic radius shrinks from its size at low temperatures to about 50 to 60% of that size at high temperatures. The steepest change in size occurs around the LCST of $T = 32$ °C for PNIPAM where the polymer changes from hydrophilic to hydrophobic, expels water and collapses. The observed trends are in accordance with previous results.[72, 119, 132] Figure 8 (e) and (f) show the obtained size distributions for the metal nanoparticles.

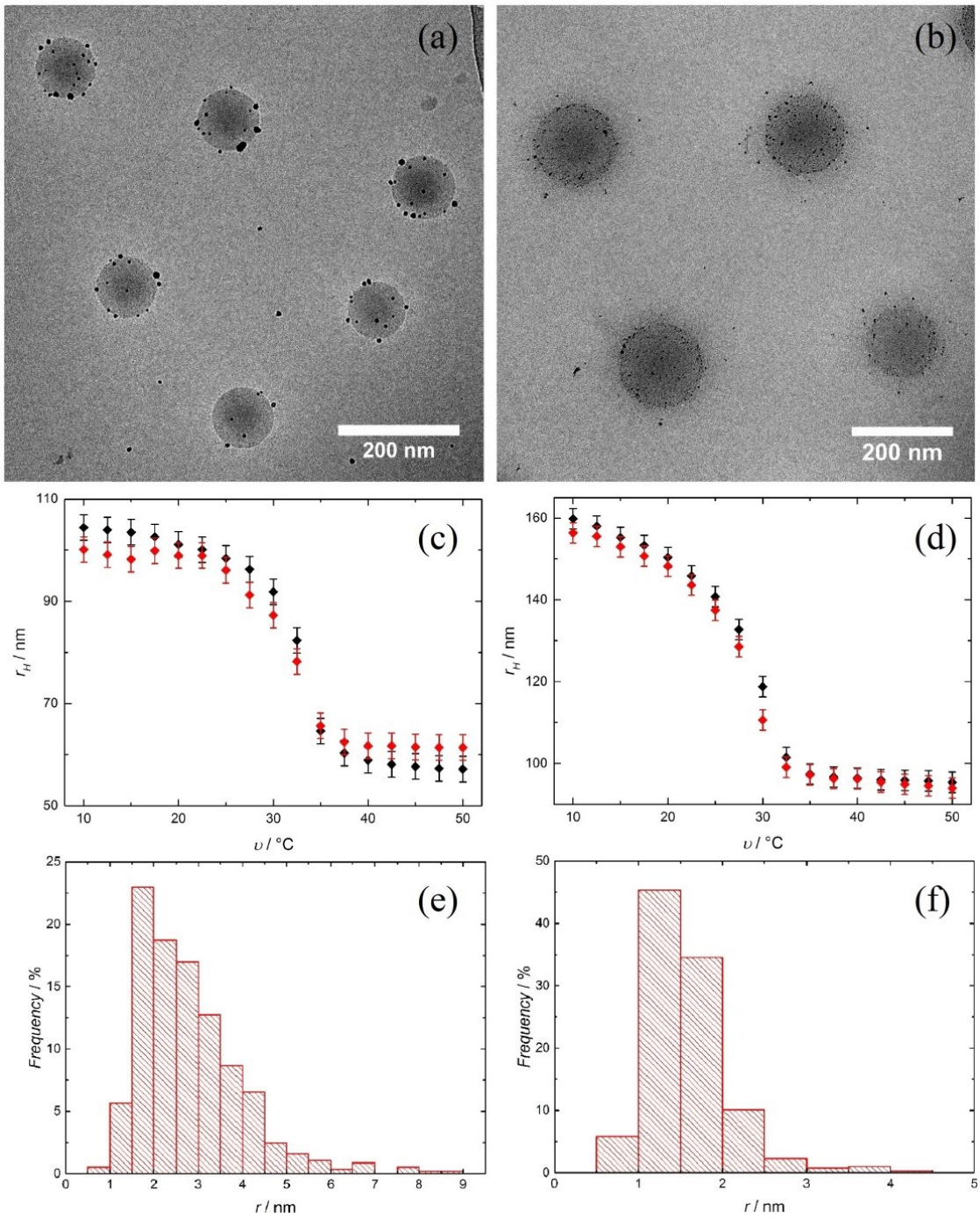

Figure 8: Characterisation of nanoreactors used for kinetic studies. Cryo-TEM images (a) and (b) of the core-shell nanoreactors with metal nanoparticles in the shell, hydrodynamic radii r_H (c) and (d) of the core-shell nanoreactors before (black) and after (red) the immobilisation of metal nanoparticles measured between 10 and 50 °C and histograms (e) and (f) of the metal nanoparticles determined from cryo-TEM images. Shown are the results for Ag@PS-PNIPAM nanoreactors (a), (c) and (e) and for Au@PS-PNIPAM nanoreactors (b), (d) and (f).

4.2 Reduction of nitroarenes – literature survey

Herein an overview of mechanistic and kinetic studies on the reduction of nitroarenes shall be given. Particular attention is given to the existence of isosbestic points in the UV-Vis spectra recorded during the reduction on gold and silver catalysts. Together with mechanistic investigations, a possible explanation for the differences between catalytic studies is elaborated. Additionally, the results of different groups concerning catalytic performance are compared, and kinetic studies with thermoresponsive catalysts are highlighted.

4.2.1 Reaction mechanism

Among the vast amount of metal-based catalysts that have been developed and applied for the reduction of nitroarenes throughout the last decades, literature concerning the mechanistic aspects of this reaction is less abundant. An overview of all mechanistic investigations addressed in the following is shown in Table 2. This summary addresses the work of approximately the last three decades, a summary of earlier work back to 1941 can be found in the work of Wisniak et al.[157]

Table 2: Overview of mechanistic investigations; applied catalyst, solvent and reducing agent.

solvent / red. agent	water	ethanol	methanol	other
H_2		Pd/C[158, 159] Ni[160]	Pd/C[161] Raney-Ni[96] Pt[162]	Au[114] (toluene-xylene) Raney-Ni[157] (without solvent)
$NaBH_4$	Au[163] Ag[164]			
NH_4OOCH		Au[165]		
H_3NBH_3		Au[166]		
N_2H_4		Au[167]		
Fe	Fe[168]			

Gold catalysts

Corma et al. published the probably most acknowledged mechanistic study with gold-based catalysts in 2007.[114] The reduction of nitrobenzene and nitrostyrene with hydrogen (9 bar) in a toluene-xylene mixture at $T = 110$ °C was investigated with a TiO_2 supported gold catalyst. Through in situ infrared spectroscopy (FTIR) analysis of batch reaction experiments nitrosobenzene, phenylhydroxylamine (as surface species) and aniline were detected but no

intermediates of the condensation route. Through experiments applying the intermediates as substrate, it could be concluded that the reaction takes place only via the direct route of the Haber mechanism. When nitrosobenzene was used as a reactant, the rate of phenylhydroxylamine formation was lower than with nitrobenzene. This lead to the conclusion that phenylhydroxylamine is produced via nitrosobenzene and in a parallel *fast step* reaction directly from nitrobenzene. From the accumulation of phenylhydroxylamine on the catalyst surface, it was concluded that the reduction of the latter to aniline is the rate-determining step.

In 2011, Lou et al. investigated the reduction of various nitroarenes, partly with other reducible substituents, under ambient conditions in ethanol and acetonitrile, respectively.[165] As catalyst, gold nanoparticles on TiO_2 were used, and ammonium formate was applied as reducing agent. For mechanistic insight, the intermediates nitrosobenzene, azobenzene and hydrazobenzene, were applied as substrate while conversion and product selectivity were monitored by gas chromatography (GC). Because the yield of aniline was in all three cases below 15%, it was concluded that the reaction occurs mainly via the *fast step* route proposed by Corma et al.[114]

In 2012, Layek et al. conducted similar investigations in water, applying a MgO supported gold catalyst and $NaBH_4$ as reducing agent.[163] Nitrosobenzene and azobenzene were reduced separately. For azobenzene, thin layer chromatography (TLC) revealed no product formation within 45 minutes while for nitrosobenzene, about 70% of aniline was formed within the same time. After that, no nitrosobenzene was detected anymore; instead, a decreasing amount of phenylhydroxylamine was present, yielding more aniline. It was concluded that the reaction follows the direct route of the Haber mechanism with the reduction from hydroxylamine to aniline being the rate-determining step. To our best knowledge, this is to date the only mechanistic investigation of an aqueous, gold catalysed system applying borohydride as reducing agent.

In 2013 groups conducted mechanistic investigations in cooperation. Both groups applied TiO_2 supported gold catalysts in ethanol and monitored the reaction via TLC.

Vasilikogiannaki et al. used ammonia borane as reducing agent to investigate the reduction of various nitroarenes, partly containing other reducible substituents.[166] At $T = 25\,°C$ all derivatives could be reduced to the respective amino compound within 15 to 90 minutes with

yields over 80%. For mechanistic insight, nitrosobenzene and azoxybenzene were applied as substrate, yielding hydrazobenzene almost quantitatively without the subsequent formation of aniline. Hence it was concluded that nitrosobenzene cannot be an intermediate and the mechanism follows the *fast step* proposed by Corma et al.[114]

Gkizis et al. used hydrazine as reducing agent.[167] With a minimum amount of four equivalents necessary to provide quantitative reaction, the amine derivatives were obtained in yields over 80% within one to 48 hours at $T = 60$ °C. Investigating the reactions of the different derivatives revealed that the only detectable intermediates were arylhydroxylamines. These intermediates were not detected for nitroarenes with electron-donating groups at the para-position. Further, it was noticed that nitrosobenzene is rapidly reduced to aniline without any catalyst. A condensation route mechanism was excluded as azo- and azoxybenzene were reduced to aniline very slowly. It was concluded that the reaction follows one of two possible pathways. If electron donating-groups are present at the para-position, the nitroso intermediate may be formed and rapidly reduced to the amine by hydrazine. Without electron-donating groups, the reaction follows the *fast step* route proposed by Corma et al.[114]

Pd-C catalysts

Makaryan et al. conducted the earliest mechanistic investigation on Pd-C. in 1993.[158] By GC, polarography, and monitoring of the hydrogen consumption rate, it was found that the reduction rate of nitroarenes was proportional to the hydrogen pressure while the rate of arylhydroxylamine reduction was independent. Thus, the reaction is suggested to follow the disproportionation mechanism in Figure 2.

In 2004, Gelder et al. investigated the reduction of nitrobenzene and nitrosobenzene in methanol, respectively.[161] To investigate the kinetic isotope effect, they applied hydrogen and deuterium (3 bar) as reductant at $T = 50$ °C, respectively. The reaction mixture was investigated via gas chromatography-mass spectrometry (GC-MS) and by monitoring the hydrogen and deuterium uptake. For the hydrogenation of nitrobenzene a much faster reaction with hydrogen than with deuterium was found. When applying nitrosobenzene as reactant there was no isotope effect for the first 20 minutes and an inverse effect for longer reaction times. The reaction profile of nitrosobenzene shows that its initial product is azoxybenzene which is subsequently converted to aniline at a much lower rate than the aniline formation from nitrobenzene. After a detailed analysis, a new mechanism was proposed in which an

adsorbed surface intermediate phenyl-NOH(ads) is proposed. Nitrobenzene yields aniline via this surface intermediate and phenylhydroxylamine on a direct route. In contrast, nitrosobenzene yields aniline through a condensation-type route where two surface intermediates form azoxybenzene. Similar results were obtained using Raney nickel as catalyst.

In 2006 Visentin et al. investigated the reduction in ethanol with hydrogen (13 bar) between $T = 35$ and 60 °C.[159] The reaction order was found to be approximately zero with respect to nitrobenzene while no accumulation of phenylhydroxylamine was found. For ethyl-4-nitrobenzoate accumulation of the hydroxylamine intermediate to more than 50% of the initial concentration was observed. It is concluded that the arylhydroxylamine accumulation is amplified by electron-withdrawing substituents which stabilise it.

Nickel catalysts

In 1984 Wisniak et al. investigated the reduction of pure nitrobenzene with hydrogen (5 to 50 bar) on Raney nickel.[157] Experiments were carried out at $T = 100$ to 210 °C, and samples were taken time-dependent. With GC and nuclear magnetic resonance spectroscopy (NMR), azobenzene and azoxybenzene were detected. Interestingly, a completely different pressure dependency was found for $T = 150$ and 170 °C, respectively. In order to find a kinetic model, eight different models (based on the reaction scheme proposed by Debus and Jungers in 1959[169]), applying different combinations of possible reaction routes, were tested without success.

In 2010 Wang et al. investigated the reduction of nitrobenzene with hydrogen (5 to 30 bar) in ethanol at $T = 70$ to 90 °C with nickel on nanosized silica gel.[160] The batch reactions were analysed by GC at different stages of the reaction. As intermediates, nitrosobenzene and azoxybenzene, but no phenylhydroxylamine was detected. The concentration-time dependencies disclosed that after 90% nitrobenzene is consumed, the rate of aniline formation increased. This was addressed to an inhibition of the reduction of azoxybenzene to aniline by the stronger adsorbed nitrobenzene.

In 2000 Studer et al. investigated the effect of vanadium-based promoters on the arylhydroxylamine accumulation during the reduction of electron-deficient nitroarene derivatives on Raney nickel.[96] Experiments were carried out in methanol at $T = 35$ °C, using

hydrogen as reductant (1.1 bar) and monitored via GC, HPLC and NMR. With unmodified Raney nickel, arylhydroxylamines accumulated up to 80% of the initial substrate concentration. Vanadium promoters usually decreased the arylhydroxylamine accumulation, accompanied by a decrease in the reaction rate. In a previous study, the effect of different metal salts on the decomposition of arylhydroxylamine derivatives was investigated.[95] Based on this study, it was assumed that the vanadium promoters catalyse the disproportionation of arylhydroxylamines. With the pure nickel catalyst, an acceleration of the amine production similar to the observations of Wang et al. was observed at high conversions of the reactant.

Platinum catalyst

In 1987 Karwa et al. investigated the reduction of nitrobenzene in methanol and other solvents with and without DMSO in order to investigate the accumulation of arylhydroxylamine.[162] Reactions were carried out at $T = 40$ to 60 °C with a Pt-C catalyst, applying hydrogen as reductant (7 to 21 bar), and analysed by HPLC. A significant effect of the nature of the solvent on the accumulation of the only intermediate, phenylhydroxylamine, was found upon investigating different solvents. Investigations in methanol/DMSO confirmed the results of Rylander et al. who found that the addition of DMSO enhances the accumulation of phenylhydroxylamine.[170] An increase in the rate of aniline formation after nitrobenzene is consumed was observed only with DMSO. Contrary to the findings of Makaryan et al., an increase in hydrogen pressure lead to a general increase in the reaction rate. Applying derivatives with electron-donating moieties lead to both, an increase in the reaction rate and of the maximum accumulation of hydroxylamine. Changing the initial nitrobenzene concentration (while retaining the initial nitrobenzene to catalyst ratio) showed no effect on the hydroxylamine formation rate before nitrobenzene is used up. Subsequently, a higher initial nitrobenzene concentration resulted in a higher phenylhydroxylamine reduction rate to aniline. Based on this finding, a new reaction mechanism is proposed. First, nitrobenzene yields phenylhydroxylamine and aniline in two parallel reactions until the reactant is used up. Subsequently, phenylhydroxylamine is converted to aniline, which is inhibited by nitrobenzene.

Silver catalyst

In 2015 Li et al. investigated the reduction of nitrobenzene with $NaBH_4$ in aqueous solution under ambient conditions.[164] The applied nanoporous silver catalyst was obtained by

dealloying Al_3Ag with NaOH (10%). By GC-MS nitrosobenzene was found as the only intermediate and the reaction was concluded to follow the direct route with the reduction of nitrobenzene to nitrosobenzene being the rate-determining step.

Combined catalyst/reducing agent iron

In 1996 Agrawal et al. investigated the reduction of nitrobenzene by iron in aqueous bicarbonate buffer solution.[168] Here iron was applied as the catalyst and reductant at the same time. Monitoring the reaction via HPLC and UV-Vis, nitrosobenzene was found as the only detectable intermediate besides the reactant and product. A dip in the overall mass balance of these three compounds was found, which was ascribed to another intermediate, corresponding to an unidentified HPLC peak which could be phenylhydroxylamine. Investigations of the influence of the pH revealed no aniline production at $pH < 5$.

Summary

Despite the differences between the respective systems which are compared, all groups agree that the reaction proceeds via a Langmuir-Hinshelwood reaction mechanism. Though not always directly mentioned, no inconsistencies were found.

With gold and silver catalysts, the only detectable intermediates were nitrosoarenes and arylhydroxylamines while on nickel, azo- and azoxyarenes were detected as well. On palladium and platinum catalysts arylhydroxylamines were detected as the only intermediates. The investigation of iron provides evidence for a direct route mechanism as well; nitrosobenzene was detected, and evidence for phenylhydroxylamine was found.

All studies which investigated the intermediates could either find proof for nitrosoarene- or arylhydroxylamine intermediates in solution. Especially the works of Gkizis et al., Visentin et al. and Studer et al. provide evidence that arylhydroxylamine derivatives are more likely to occur for electron-deficient derivatives. In contrast, the presence of electron-donating groups seems to stabilise the nitroso intermediate through mesomeric dislocation. Contrary to that, Karwa et al. found arylhydroxylamines as the only intermediates for the reduction of nitroarene derivatives with electron-donating groups on platinum. Corma et al. were the only group to detect both intermediates of the *direct route*.

Overall, the precise mechanism seems to be highly dependent on the substrate substituent(s), the catalyst metal, the reducing agent, temperature, pressure, pH, and the solvent. Evidence for direct route type mechanisms prevails in most works but especially for the metals of the nickel group additional evidence for a condensation type mechanism, decreasing with increasing period of the catalyst metal, was found. Consequently, the validity of any given mechanism is presumably confined to a distinct system and range of reaction conditions.

4.2.2 Isosbestic points

Regarding kinetic studies of the reduction of 4-nitrophenol (Nip) literature is abundant and can hardly be overlooked. Table 17 to Table 19 in chapter 7.1 give an overview of kinetic studies of the aqueous reduction with borohydride on gold and silver catalysts as well as on other metals, mixed metal and alloy catalysts, respectively. Listed are catalysts with highly diverse architectures stabilised by dendrimers, micelles, microgels, yolk-shell structures, solid, hollow or porous microspheres or -cubes, spherical polyelectrolyte brush particles, nanofibers, -tubes and -sheets, particles stabilised by small molecule or polymer ligands, on inorganic supports as well as support free catalysts. The tables indicate the particular reference, the support constituents and a brief description of the architecture, size and shape of the active metal catalyst particles, the reaction temperature and the derived kinetic constant. The latter is given in several different forms such as k_{app}, k_1 or k_{mol}; an explanation of the respective meaning can be found in chapter 7.1.

Furthermore, the existence of isosbestic points in the UV-Vis spectra recorded during the reduction is listed. Therefore, the tables include only catalysts where the UV-Vis spectra are graphically depicted in the reference, and allow for verification. As explained in chapter 1.3.1, when isosbestic points are present the reactant Nip and the final product 4-aminophenol (Amp) should be the only species present in solution at varying concentrations and all criteria for a model reaction are fulfilled. An evaluation of the prevalence at which isosbestic points are present shall be given in the following. Here, particular emphasis is placed on the comparison of gold- and silver-based catalysts and possible reasons for the presence or absence of isosbestic points.

Before addressing the different catalyst metals in more detail, the different characteristic appearances found repeatedly for the UV-Vis spectra recorded during the reduction with gold and silver catalysts are elucidated.

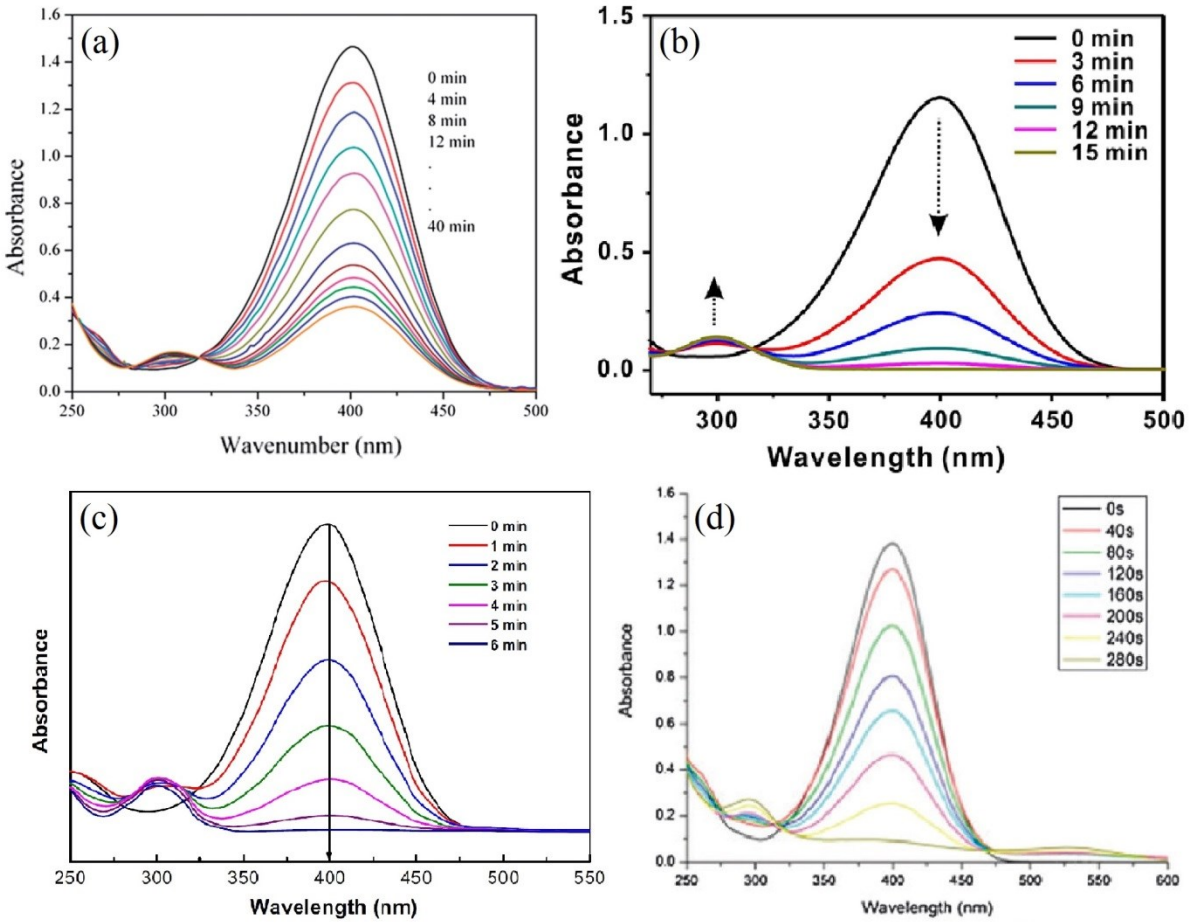

Figure 9: Typical UV-Vis spectra obtained with gold catalysts with two isosbestic points around the aminophenol peak ((a) and (b)), an increase in the aminophenol peak followed by a decrease (c) and absorption at $\lambda > 500$ nm (d). Reprinted with permission; (a) © 2014 The Royal Society of Chemistry,[171] (b) © 2013 American Chemical Society,[53] (c) © 2015 Springer Nature[97] and (d) © The Royal Society of Chemistry.[100]

Figure 9 (a) shows the spectra obtained during the reduction with gold nanoparticles stabilised by magnetic Fe_2O_3 nanoparticles covered with carboxylated cellulose. Two clear isosbestic points are discernible left and right to the *Amp* peak at $\lambda = 300$ nm, and the increase of the latter corresponds to the decrease in the *Nip* peak at $\lambda = 400$ nm. Figure 9 (b) shows the spectra obtained with gold nanoparticles stabilised inside double hydrophilic block copolymer (DHBC) micelles of poly(ethyleneglycol)-*b*-poly(acrylic acid) (PEG-*b*-PAA). Again two isosbestic points are discernible around the *Amp* peak. However, the increase of the latter does not correspond to the decrease of the *Nip* peak. After the first spectrum, the *Amp* peak already reaches approximately its maximum and subsequently does not change significantly while the *Nip* peak is still decreasing. Figure 9 (c) shows the spectra obtained with gold nanoparticles immobilised in spherical polymer brushes of poly-2-(dimethylamino) ethyl

methacrylate (PDMAEMA) grafted to hollow spheres of poly-2-(1-methylimidazolium-3-yl) ethyl methacrylate chloride (PMIMC). Here the *Amp* peak increases first and then decreases again. Figure 9 (d) shows the spectra obtained with gold nanoparticles stabilised by 1,2,3-triazole-polyethyleneglycol monomethyl ether ligands. The spectra are fluctuating at the wavelengths around the aminophenol peak where isosbestic points are typically expected. At the same time, the spectra show a slight absorbance at $\lambda > 500$ nm, visible after the first spectrum. Absorbance in this wavelength region is typically caused by larger aromatic systems than those of *Nip*. This indicates that the reaction is at least partially following a *condensation route* mechanism (the intermediates of which would explain such absorption).

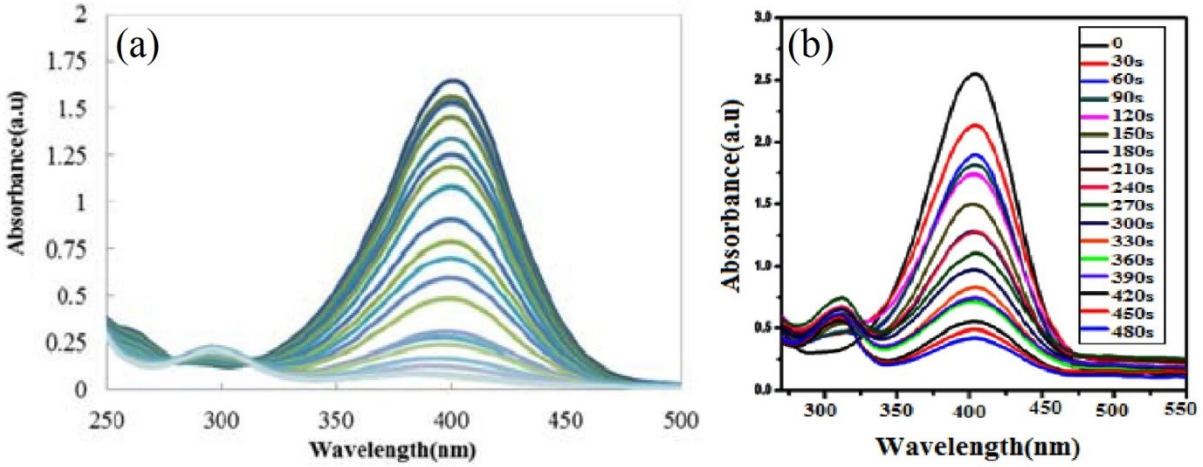

Figure 10: Typical UV-Vis spectra obtained with silver catalysts with two isosbestic points around the aminophenol peak (a) and an increase in the aminophenol peak followed by a decrease (b). Reprinted with permission; (a) © 2017 The Research Center for Eco-Environmental Sciences, Chinese Academy of Sciences. Published by Elsevier B.V.[172] and (b) © 2017 Elsevier B.V.[44]

Figure 10 (a) shows the spectra recorded during the reduction with silver nanoparticles embedded in a copolymer hydrogel comprising of poly-*N*-isopropylacrylamide, 2-hydroxyethyl methacrylate and acrylic acid (P(NIPAM-HEMA-AAc)). Figure 10 (b) shows the spectra obtained with silver nanoparticles stabilised by nitrolotriacetic acid. Here, the spectra in Figure 10 (a) and (b) display the same features as those obtained with gold catalysts shown in Figure 9 (a) and (c), respectively. The characteristic appearances showed above cover over 70% of all kinetic studies listed in chapter 7.1 and show that despite the diverse catalyst architectures, most systems display a limited number of features in the UV-Vis spectra upon *Nip* reduction.

Gold catalysts

In total, 70 independent catalysts were reviewed and listed in Table 17. 31 catalysts were found to display isosbestic points in the UV-Vis spectra, 32 did not show such points, and for seven catalysts it was not clear. Thus, 49% of the catalysts where a clear decision was possible, display isosbestic points. Considering the support type, a conspicuous amount of 67% of the catalysts where inorganic materials (predominantly metal oxides or metal ions) are part of the support or involved in the preparation show isosbestic points. Contrary to that only 35% of the catalysts which are stabilised by pure organic (predominantly polymeric supports) show isosbestic points. Considering only those catalysts on organic support which show isosbestic points, in 55% of the cases carboxylic groups are involved. This shows a tendency that isosbestic points are more likely to be found with inorganic supports or more general in the presence of oxygen species; however, more precise indications were not found.

Silver catalysts

For silver, 57 independent catalysts were reviewed and listed in Table 18. Here, 41 catalysts showed isosbestic points while only for ten catalysts, no isosbestic points were discernible, and in six cases it was unclear. This yields isosbestic points in 80% of the cases and shows that on silver catalysts it is far more likely for the reduction to run cleanly than on gold. However, as only ten catalysts of diverse architectures did not show isosbestic points, no common indication could be found.

Other metal catalysts

Another 28 catalysts which apply other metals, mixed metals or alloys were reviewed and listed in Table 19. In 14 cases isosbestic points were present, in 12 cases no isosbestic points were discernible, and for two catalysts it was unclear. Here no indications concerning isosbestic points can be found as only 28 examples, comprising catalysts based on five different single metals and six different bimetallic catalysts, were reviewed. However, it can be said that on average 54% of the catalysts show isosbestic points, which lies between the results for gold and silver catalysts.

In accordance with chapter 4.2.1, the results show that the kinetics seem to be highly sensitive to the reaction conditions and catalyst metal as well. As shown by the following examples, the statement here needs to be extended, including the support. Ciganda et al. prepared two gold

catalysts, bot stabilised by thiolated PEG ligands of different molar weight.[49] With SH-PEG_{550} no isosbestic points are visible, contrary to nanoparticles stabilised with SH-PEG_{2000}. Fedorczyk et al. synthesised gold nanoparticles embedded in a macroscopic film of poly-1,8-diaminocarbazole and applied it for *Nip* reduction in successive experiments.[173] Isosbestic points were not present during the first catalytic run but appeared when the catalyst was reused. Biondi et al. investigated the *Nip* reduction with gold nanoparticles stabilised by a polyelectrolyte containing imidazolium groups at different concentration ratios of the catalyst particles to *Nip*.[174] While the UV-Vis spectra obtained at a ratio of 1:70 did not show isosbestic points, they were present if the reaction was recorded at a ratio of 1:140. Xiong et al. prepared catalysts stabilised on magnetic Fe_3O_4 nanoparticles coated with a shell of carboxylated cellulose loaded with different amounts of gold.[171] The obtained catalysts had gold nanoparticle sizes of 14.3, 24.1 and 38.3 nm, respectively. Only the UV-Vis spectra obtained with the particle batch of the largest gold nanoparticles showed isosbestic points. Similar behaviour was observed by Das et al. who synthesised silver nanoparticles stabilised on polydopamine coated hydroxylapatite particles with a rod-like geometry.[175] Five batches were synthesised with 1, 2, 3, 4 and 5% of $AgNO_3$, respectively. Here all batches of catalyst showed isosbestic points except the batch prepared with the lowest amount of $AgNO_3$. These examples demonstrate that even minor changes in the synthesis, the stabiliser architecture, or even the experimental conditions of the kinetic measurements can influence the reaction enough to cause visible differences in the appearance of UV-Vis spectra obtained during the reaction.

It needs to be mentioned that the results above cannot give unambiguous indications of when isosbestic points exist. The investigated systems are very diverse, and it is problematic to find enough examples of a similar catalyst type for a meaningful basis of argumentation. Besides that, experimental details are stated only briefly and incomplete in many cases, leaving doubts about the quality of the works. For less than half of the 155 investigated catalysts, oxygen is removed from the reaction mixture prior to catalytic measurements, and for 25% of the catalysts, the temperature at which kinetic measurements were conducted is not given. For only 19% of the catalysts, a surface-normalised rate constant is given. In 12% of the cases, a rate constant normalised to mass or molar amount of catalyst is given, and another 8% state no rate constant at all. The majority of 61% states only the apparent reaction rate constant k_{app}. Therefore, a more condensed overview of only the works which state the surface-normalised reaction rate constant k_1 is given in the next chapter.

4.2.3 Surface-normalised reaction rate constant

For obvious reasons it is impossible to compare catalytic activities given in different variables, but also the comparison of variables of the same type remains problematic for kinetic constants which are not normalised to the catalytically active metal surface area. Therefore, this chapter summarises only catalysts where k_1 is given directly or can be recalculated with the values given in the respective reference. Besides the works where the existence of isosbestic points is graphically depicted, additional works are listed where k_1 is given. Rate constants which were obtained after removal of oxygen from the reaction mixture prior to the kinetic measurements are indicated* in Table 3 to Table 5.

Table 3: List of references of the nitrophenol reduction on gold catalysts with surface-normalised reaction rates k_1.

reference	support; structure	kinetic constant	isosbest. points	size / nm; shape	*T* / °C
Fu et al., 2016[176]	Si waver macroscopic support	$k_1 = 6.0*10^{-2}$	Yes	10 polyhedral	20
Cao et al., 2015[116]	gibbsite@PDA hexagonal platelets	$k_1 = 8.0*10^{-2}$*	Yes	11.7 spherical	RT
Wu et al., 2012[72]	Au@PNIPAM yolk-shell structure	$k_1 = 2.2*10^{-1}$*	Yes	15 ± 3 spherical	20
Ciganda et al., 2014[49]	1,2,3-triazole-PEG-2000 ligand molecules	$k_1 = 1.7*10^{-2}$	No	3 spherical	13
	PEG-2000-1,2,3-triazole-CH_2-O-CH_2-TTEGb ligand molecules	$k_1 = 1.4*10^{-2}$	No	3 spherical	13
	1,2,3-triazole-PEG-2000 ligand molecules	$k_1 = 4.3*10^{-2}$	No	6 spherical	20
	polymeric 1,2,3-triazole-PEG polymeric ligands	$k_1 = 1.9*10^{-2}$	Yes	3.6 spherical	20
	HS-PEG-550 ligand molecules	$k_1 = 1.0*10^{-3}$	No	3.5 spherical	20
	HS-PEG-2000 ligand molecules	$k_1 = 3.0*10^{-3}$	Yes	13.5 spherical	20
	citrate small ligand molecules	$k_1 = 4.0*10^{-4}$	Yes	13.5 spherical	20
Jia et al., 2015[177]	α-CD-PVCL microgel	$k_1 = 2.5*10^{-2}$*	(No)	- spherical	RT

reference	support; structure	kinetic constant	isosbest. points	size / nm; shape	*T* / °C
Kuroda et al., 2009[12]	PMMA commercial microspheres	$k_1 = 5.1*10^{-1}$	Yes	6.9 ± 5.5 spherical	22
Wu et al., 2011[178]	Au@SiO_2 yolk shell structure	$k_1 = 4.8*10^{-3}$	Yes	3.3 ± 0.6 spherical	25
Muruga-doss et al., 2008[179]	citrate + acetanilide small ligand molecules	$k_1 = 6.5*10^{-1}$	-	5.0 ± 1.7 spherical	RT
Schrinner et al., 2007[180]	PS@PAEMH SPB particles	$k_1 = 5.1*10^{-1}$	-	2.3 ± 1 spherical	20
Yuan et al., 2012[181]	PS@PEVIB SPB particles	$k_1 = 4.1*10^{-1}$	-	2.1 ± 0.2 spherical	20
Lu et al., 2010[42]	PS@PNIPAM-Au NR core-shell microgel	$k_1 = 1.4*10^{-1}$	-	6.6 ± 0.3 (d) 34.5 ± 5.2 (L)	25

Among gold catalysts, Murugadoss et al. reported the highest rate constant with $k_1 = 6.5*10^{-1}$ L m^{-2} s^{-1}, obtained on citrate stabilised nanoparticles at a low concentration of acetanilide.[179] Increasing the concentration of the latter results in a chain-like arrangement of the nanoparticles and lowering of the reaction rate due to the less accessible metal surface in those structures. Contrary to that, Ciganda et al. reported the lowest rate constant of $k_1 = 4.0*10^{-4}$ L m^{-2} s^{-1}, which was also obtained with citrate stabilised nanoparticles.[49] For gold nanoparticles stabilised inside SPB particles, rate constants of $k_1 = 5.1*10^{-1}$ and $4.1*10^{-1}$ L m^{-2} s^{-1} were reported.[180, 181] For microgel supported catalysts Jia et al. reported a rate constant of $k_1 = 2.5*10^{-2}$ L m^{-2} s^{-1} obtained with spherical gold nanoparticles[177] whereas Lu et al. obtained a rate constant of $k_1 = 1.4*10^{-1}$ L m^{-2} s^{-1} with gold nanorods.[42]

Table 4: List of references of the nitrophenol reduction on silver catalysts with surface-normalised reaction rates k_1.

reference	support; structure	kinetic constant	isosbest. points	size / nm; shape	*T* / °C
Lu et al., 2006[73]	PS@PNIPAM core-shell microgel	$k_1 = 5.2*10^{-2}$	Yes	7.3 ± 1.5 spherical	20
Lu et al., 2006[61]	PS@PEGMA spherical branched polymer brushes	$k_1 = 7.3*10^{-2}$	Yes	7.5 ± 2.0 spherical	20
Yuan et al., 2013[182]	Ag@PANI core-shell structure	$k_1 = 3.6*10^{-2}$* $k_1 = 4.5*10^{-2}$* $k_1 = 6.6*10^{-2}$*	No	63.5 ± 6.0 64.6 ± 8.0 65.2 ± 8.0	RT

reference	support; structure	kinetic constant	isosbest. points	size / nm; shape	*T* / °C
				spherical	
Eising et al., 2011[183]	Dextran T500 commercial polysaccharide	$k_1 = 1.4*10^{-1}$*	No	6.1 ± 1.3 spherical	25
Signori et al., 2010[184]	octane- + EtOH-functionalised branced PEI polymer ligand	$k_1 = 5.7*10^{-1}$*	Yes	24.5 ± 4.1 spherical	25
This work	PS@PNIPAM core-shell microgel	$k_1 = 1.5*10^{-2}$*	Yes	5.6 ± 2.4 spherical	20
Lu et al., 2007[185]	PS@PAA SPB particles	$k_1 = 7.8*10^{-2}$	-	3.0 ± 1.2 spherical	20
Lu et al., 2007[186]	(PS@PEGMA)@PVA spherical branched polymer brushes embedded in macrogel	$k_1 = 7.8*10^{-5}$*	-	35.0 ± 5.0 spherical	20
	PVA macrogel	$k_1 = 7.3*10^{-5}$*	-	45.0 ± 5.0 spherical	20
Zhang et al., 2009[187]	TiO_2 nanocomposite	$k_1 = 7.8*10^{-1}$	-	3.0 spherical	21
Zhang et al., 2010[188]	P(NIPAM-MCC) copolymer microgel	$k_1 = 2.0*10^{-1}$	-	3.5 ± 0.7 spherical	-

For catalysis with silver nanoparticles, Lu et al. prepared two types of spherical brush particles.[61, 185] For polyacrylic acid based SPB and for spherical branched polymer brushes similar rate constants of $k_1 = 7.8*10^{-2}$ and $7.3*10^{-2}$ L m^{-2} s^{-1} were obtained, respectively. In a subsequent work the latter particles were incorporated in a polyvinyl alcohol (PVA) macrogel which yielded a rate constant of $k_1 = 7.8*10^{-5}$ L m^{-2} s^{-1}.[186] For silver nanoparticles inside a pure PVA macrogel a rate constant of $k_1 = 7.3*10^{-5}$ L m^{-2} s^{-1} was obtained. These are the lowest rate constants reported on silver catalysts. Comparing the latter to the highest rate constant of $k_1 = 7.8*10^{-1}$ L m^{-2} s^{-1}, obtained with silver nanoparticles supported on TiO_2, the importance of the diffusion of the reactants to the catalytically active metal surface for the reaction rate becomes apparent.[187] Inside the macrogel the reactants have to diffuse macroscopic distances through the gel to reach the silver nanoparticles deep inside the gel whereas the TiO_2 supported silver nanoparticles are at the surface of the catalyst particles, yielding a rate constant four orders of magnitude higher.

For platinum nanoparticles stabilised with magnetic SPB particles Wu et al. obtained a rate constant of $k_1 = 3.9*10^{-1}$ L m^{-2} s^{-1}.[189] With SPB particles comprising of a polystyrene core and the same brush polymer, poly(2-(methylacryloyloxy)ethyltrimethylammonium chloride) (PMTAC), Mei et al. obtained a slightly higher rate constant.[63] In a subsequent work to the latter, the same support was used for palladium nanoparticles, yielding a reaction rate of $k_1 = 1.1$ L m^{-2} s^{-1}.[119] For SPB particles applying poly(1-ethyl-3-vinylimidazolium bromide) (PEVIB) as brush polymer to stabilise palladium nanoparticles, a rate constant of $k_1 = 2.1*10^{-1}$ L m^{-2} s^{-1} was obtained.[181] Antonels et al. investigated ruthenium nanoparticles stabilised by hydroxyl-terminated polyamidoamine dendrimers.[190] The ruthenium nanoparticle size increased slightly with the dendrimer generation and the obtained rate constants were $k_1 = 8.7*10^{-4}$, $1.5*10^{-3}$ and $3.6*10^{-4}$ L m^{-2} s^{-1} for generations 4, 5 and 6, respectively.

Table 5: List of references of the nitrophenol reduction on other metal, mixed metal and alloy catalysts with surface-normalised reaction rates k_1. The used metals are indicated in the "support" column.

reference	support; structure	kinetic constant	isosbest. points	size / nm; shape	*T* / °C
Mei et al., 2005[63]	PS@PMTAC-**Pt** SPB particles	$k_1 = 5.6*10^{-1}$ $k_1 = 1.1$	No	2.1 ± 0.4 spherical	15 30
Wu et al., 2012[189]	Fe_3O_4@P(S-DVB) @PMTAC-**Pt** SPB particles	$k_1 = 3.9*10^{-1}$	Yes	3.5 ± 0.5 spherical	20
Yuan et al., 2010[191]	**Pt**@P-2-(P($APTS_{72}$-b-$METAI_{95}$)-IEM_{2300} organosilica hybrid nanowires	$k_1 = 3.1*10^{-1}$	No	3.0 ± 0.5 spherical	-
Lu et al., 2010[42]	PS@PNIPAM-**Pt** core-shell microgel	$k_1 = 8.6*10^{-2}$	-	3.7 ± 1.2 spherical	25
Mei et al., 2007[119]	PS@PMTAC-**Pd** SPB particles	$k_1 = 1.1$*	Yes	2.4 ± 0.5 spherical	15
	PS@PNIPAM-**Pd** microgel	$k_1 = 1.0*10^{-1}$*	-	3.87 ± 0.6 spherical	15
Halder et al., 2011[192]	oleylamine capped **Pd** nanoporous structure	$k_1 = 1.3*10^{-4}$	No	-	RT
Yuan et al., 2012[181]	PS@PEVIB-**Pd** SPB particles	$k_1 = 5.8*10^{-1}$	-	2.5 ± 0.3 spherical	20
Lu et al., 2010[42]	PS@PNIPAM-**Au-Pt** NR microgel	$k_1 = 2.1*10^{-1}$	(No)	7.4 ± 0.8 (d) 39.5 ± 6.5 (L)	25

reference	support; structure	kinetic constant	isosbest. points	size / nm; shape	*T* / °C
Antonels et al., 2013[190]	**Ru**@PAMAM-G4-OH dendrimer stabilised	$k_1 = 8.7*10^{-4}$*	(No)	1.2 ± 0.1 spherical	25
	Ru@PAMAM-G5-OH dendrimer stabilised	$k_1 = 1.5*10^{-3}$*	(No)	1.4 ± 0.1 spherical	25
	Ru@PAMAM-G6-OH dendrimer stabilised	$k_1 = 3.6*10^{-4}$*	(No)	2.2 ± 0.3 spherical	25

Considering the statement of the surface-normalised rate constant k_1 as a criterion, the works listed in this chapter can be regarded as a group of more sophisticated works. This is also discernible as only two of the 27 works listed above state no temperature (7% compared to 25% in the previous chapter). With only the catalysts listed in this chapter, the prevalence of isosbestic points is now 67% for gold (8 of 12), 67% for silver (4 of 6), and 40% for other catalyst metals (2 of 5). The numbers in parentheses show that due to the low number of works left, it is difficult to make a statistical statement here. However, the numbers show that even for works of a supposedly better quality, still cases with and without isosbestic points are found. If the removal of oxygen is added as criterion, only 37% of the works within this chapter (10 of 27) would be left, making a statistical evaluation impossible.

4.2.4 Thermoresponsive catalysts

As elucidated in chapter 3.1.2, thermoresponsive catalysts change their catalytic activity in a non-Arrhenius-like mode with temperature. Table 6 lists only such catalysts, independent of the applied catalyst metals or the type of rate constant stated. Thus, this chapter refrains from a comparison of reaction rate constants. Most commonly PNIPAM is applied as the thermoresponsive polymer; references on catalysts based on other polymers are scarce.

Wu et al. prepared a catalyst where gold nanoparticles are located freely movable inside a shell of PNIPAM.[72] By adjusting the temperature, the selectivity could be switched between 4-nitrophenol and nitrobenzene. Liu et al. prepared a magnetically recoverable catalyst with a Fe_3O_4 core and a copolymer shell comprising of PNIPAM and a second thermoresponsive polymer PDMAEMA.[66] As active catalyst, readily prepared citrate stabilised gold nanoparticles were loaded into the polymer shell. Zhang et al. prepared spherical polymer brush particles comprising of a polystyrene core and a PDMAEMA brush layer comprising gold nanoparticles.[60] Additionally to the thermoresponsivity, the brush layer is sensitive to the pH, and the concentration of NaCl. By using SiO_2 nanoparticles as a template and final

etching, He et al. were able to prepare hollow nanosphere brush particles, comprising of a poly(2-(1-methylimidazolium-3-yl)-ethyl methacrylate chloride) (PMIMC) hollow sphere grafted with PDMAEMA.[97] After precipitating gold nanoparticles into the PDMAEMA brush, the catalytic activity showed a minimum at 55 °C, and the catalyst could be reused for five cycles without significant loss of activity. Liu et al. prepared a copolymer macrogel comprising of poly(2-acrylamido-2-methyl-1-propane sulfonic acid) (PAMPS) and PNIPAM loaded with nickel nanoparticles by in situ reduction with $NaBH_4$.[193] With a minimum of the reaction rate at a temperature of 37 °C, this system is potentially interesting for biomedical applications. By incorporating a central gold nanorod inside a PNIPAM microgel and subsequent precipitation of silver nanoparticles inside the polymer shell, Li et al. prepared a thermoresponsive catalyst which shows a strong photothermal effect.[64] The catalyst particles could be heated from within by infrared irradiation, to induce the volume transition and modulation of the catalytic activity by light.

Table 6: List of references of the nitrophenol reduction on thermoresponsive catalysts. The used metals are indicated in the "support" column.

reference	support; structure	kinetic constant	isosbest. points	size / nm; shape	*T* / °C
Wu et al., 2012[72]	**Au**@PNIPAM yolk-shell structure	$k_1 = 2.2*10^{-1}$	Yes	15 ± 3 spherical	20
Lu et al., 2010[42]	PS@PNIPAM-**Au** NR core-shell microgel	$k_1 = 1.4*10^{-1}$	-	6.6 ± 0.3 (d) 34.5 ± 5.2 (L)	25
He et al., 2015[97]	PMIMC@ PDMAEMA-**Au** hairy hollow spheres	$k_{app} = 1.8*10^{-3}$ $k_{app} = 3.0*10^{-3}$	No	1.5 ± 0.2 spherical	25 55
Zhang et al., 2007[60]	PS@PDMAEMA-**Au** spherical polymer brush	$k_{app} = 3.2*10^{-3}$	No	4.1 spherical	-
Wang et al., 2007[52]	P4VP-*b*-PNIPAM-**Au** micelles	$k_{app} = 1.5*10^{-3}$	No	3.3 ± 0.2 spherical	25
Pich et al., 2006[65]	**Au**@P(AAEM-VCL) copolymer microgel	$k_{app} = 1.2*10^{-3}$	Yes	- spherical	20
Liu et al., 2015[66]	Fe_3O_4@P(NIPAM-DMAEMA)-**Au** core-shell microgel	$k_{app} = 2.4*10^{-3}$	Yes	10 spherical	20
Shi et al., 2014[75]	**Au**@SH-P(NIPAM-MAA) copolymer microgel	$k_{app} = 1.4*10^{-3}$	Yes	3.9 ± 0.6 spherical	30
Wu et al., 2015[71]	**Au**@P(NIPAM-VPBA-AAm)	$k_{app} = 2.0*10^{-3}$	No	7.0 ± 3.0 spherical	30

reference	support; structure	kinetic constant	isosbest. points	size / nm; shape	*T* / °C
	copolymer microgel				
Lu et al., 2006[73]	PS@PNIPAM-**Ag** core-shell microgel	$k_1 = 5.2*10^{-2}$	Yes	7.3 ± 1.5 spherical	20
This work	PS@PNIPAM-Ag core-shell microgel	$k_1 = 1.5*10^{-2}$	Yes	5.6 ± 2.4 spherical	20
Zhang et al., 2010[188]	**Ag**@P(NIPAM-MCC) copolymer microgel	$k_1 = 2.0*10^{-1}$	-	3.5 ± 0.7 spherical	-
Lu et al., 2006[132]	PS@PNIPAM-**Ag** core-shell microgel	$k_{app} = 2.2*10^{-3}$	Yes	8.5 ± 1.5 spherical	20
Shah et al., 2017[74]	**Ag**@P(NIPAM-MAA) copolymer microgel	$k_{app} = 3.4*10^{-3}$	(Yes)	6.5 ± 0.5 spherical	-
Lu et al., 2010[42]	PS@PNIPAM-**Pt** core-shell microgel	$k_1 = 8.6*10^{-2}$	-	3.7 ± 1.2 spherical	25
Mei et al., 2007[119]	PS@PNIPAM-**Pd** core-shell microgel	$k_1 = 1.0*10^{-1}$	-	3.87 ± 0.6 spherical	15
Liu et al., 2015[193]	**Ni**@P(NIPAM-AMPS) copolymer macrogel	$k_{app} = 3.8*10^{-3}$	Yes	26.2 spherical	21
Li et al., 2016[64]	**Au** NR@PNIPAM-**Ag** core-shell microgel	$k_{app} = 2.2*10^{-3}$	Yes	Ag: 8.0 ± 2.0 spherical	25
Lu et al., 2010[42]	PS@PNIPAM-**Au-Pt** NR core-shell microgel	$k_1 = 2.1*10^{-1}$	(No)	7.4 ± 0.8 (d) 39.5 ± 6.5 (L)	25

4.2.5 Summary of the reduction on gold and silver catalysts

Both, chapter 4.2.1, addressing mechanistic studies, as well as the statistics on the prevalence of isosbestic points in the following chapters show that the kinetics and mechanism are very sensitive to the precise reaction conditions. However, for the aqueous reduction of *Nip* with gold and silver, the following picture can be drawn:

The work of Layek et al. indicates that the last reaction step from phenylhydroxylamine to aniline is the slowest step (i.e. rate-determining) on gold catalysts.[163] In contrast to that, Li et al. concluded in their work that the first reaction step from nitrobenzene to nitrosobenzene could be the rate-determining step on silver catalysts.[164]

If the first step of the reaction is rate-determining, and the subsequent reaction steps are faster, the accumulation of intermediates on the catalyst surface remains low as they react faster than

they are formed. If instead, the last step of the reaction is rate-determining, intermediates are formed faster than they react and therefore accumulate on the catalyst surface.

As a consequence, it is far more likely that intermediates desorb into solution to a notable degree if the last step is rate-determining. In both cases, it depends on the adsorption strength of the intermediates on the particular catalyst (i.e. the combination of metal and support) if enough intermediates desorb into solution so that no isosbestic points are seen in the UV-Vis spectra. Chen et al. demonstrated nicely how modifications of the electronic structure of platinum nanowires by adsorbed ethylenediamine ligands can alter the adsorption strength of phenylhydroxylamine to that extent that the reaction even stops at this intermediate.[194] It is therefore realistic to find various examples with and without isosbestic points for the same catalyst metal, considering the diversity of catalyst architectures and ligands/supports.

Chapter 4.2.2 has shown that isosbestic points are found in most cases on silver catalysts while on gold it is less likely. This supports the hypothesis that the rate-determining step differs between gold and silver. In addition, it is conceivable that the influence of ligands on the electronic structure of the catalyst not only influences the adsorption strength but the reaction rates of each reaction step as well and therefore may even alter the rate-determining step.

In conclusion, the nitroarene reduction remains a highly complex topic where combinations of catalyst metal, support and reaction conditions can influence and alter the kinetics of the reaction significantly. Utmost care is therefore necessary upon applying the reaction as a model reaction, especially when different catalyst metals are to be compared. It should be considered whether other reactions, preferably with only one reaction step (i.e. avoiding the possibility of desorbing intermediates and changing rate-determining step), can be applied as a model reaction more reliably than the reduction of Nip.

4.3 Reduction of 4-nitrophenol by Ag@PS-PNIPAM nanoreactors

The previous chapter has shown that the kinetics of the reduction of 4-nitrophenol (Nip) is sensitive to the precise combination of reaction conditions and catalyst. For the reaction catalysed by gold nanoparticles, a model has been developed which could successfully describe the full kinetics including the intermediate regime.[109, 115, 195] However, as mentioned in chapter 1.3.1, an intermediate regime is not always observed. Previous studies showed that no such regime was found with silver catalysts.[73, 132] Therefore, the kinetics of the Nip reduction catalysed by thermoresponsive Ag@PS-PNIPAM nanoparticles is investigated in the following to expand the existing picture of the reaction kinetics to silver. Additionally, the effect of the thermoresponsive PNIPAM hydrogel on the kinetics is investigated.

4.3.1 Spectral deconvolution

Prior to the kinetic analysis, the spectra recorded during the reduction of Nip with borohydride are analysed. Previous kinetic studies were always based on the concentration-time dependency of Nip derived from its optical absorption maximum at $\lambda = 400$ nm. However, with this approach, only the reactant concentration can be monitored. In order to obtain the product concentration as well and additionally verify the absence of intermediates, the full spectra recorded during the reduction from $\lambda = 250$ to 500 nm, shown in Figure 11 (a), are deconvoluted with the Levenberg-Marquardt algorithm. Prerequisite for the deconvolution are reference spectra of all species to be detected. Figure 11 (b) shows the molar extinction spectra of the reactant Nip, the product 4-aminophenol (Amp), one intermediate of the *direct route* (4-nitrosophenol; NSP) and one intermediate of the *condensation route* (4,4'dihydroxy-azobenzene; $DHAB$). The resulting concentration-time curves are shown in Figure 11 (c). Only the reactant and the final product were detected, NSP and $DHAB$ were not present. The residual spectra in Figure 11 (d) exhibit an overall low intensity compared to the absorbance of the original spectra, as shown in the inset. The sum concentration of Nip and Amp in Figure 11 (c) is constant to $\Delta c < 1\%$ of the initial Nip concentration. This shows that Nip is directly transferred to Amp via the *direct route* while intermediates remain adsorbed. Additionally, the first derivatives of Nip and Amp, shown in Figure 11 (c), coincide, emphasising further that Nip is directly transferred to Amp without accumulation of intermediates. This is in accordance with the absence of an intermediate regime in the logarithmic concentration-time dependencies.

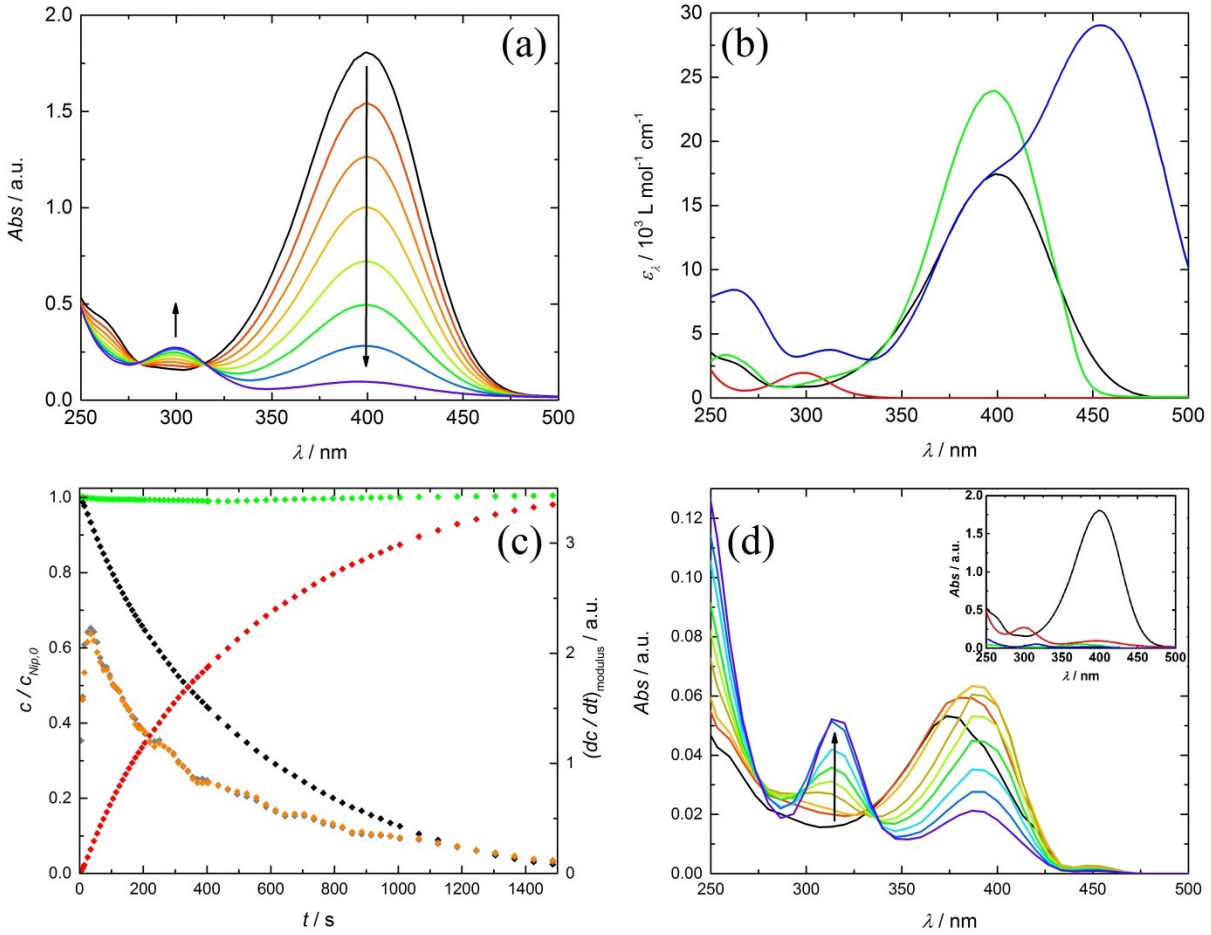

Figure 11: Absorption spectra (a) recorded during *Nip* reduction; molar extinction spectra (b) for *Nip* (black), *Amp* (red), *NSP* (green) and *DHAB* (blue) recorded at $pH = 10$; obtained concentration-time curves (c) for *Nip* (black), *Amp* (red), sum concentration of both (green) relative to the initial concentration of *Nip* $c_{Nip,0} = 1*10^{-4}$ mol L^{-1} and modulus of the first derivatives for *Nip* (grey) and *Amp* (orange) and obtained residual spectra (d). The inset shows the first (black) and last (red) spectrum recorded during the reduction compared to the corresponding first (green) and last (blue) residual spectrum. Arrows indicate the course of reaction.

4.3.2 Kinetic model

The model for the analysis of the reduction catalysed by Ag@PS-PNIPAM nanoreactors is based on the two-step model applied for the analysis of the reaction on gold and gold-palladium alloy catalysts as described in chapter 1.3.1.[109, 115, 195] The differential rate equations for *Nip* and 4-hydroxylaminophenol (*Hx*) are given in equations (1.4) and (1.5). The spectral deconvolution in the previous chapter showed that the decrease in the reactant concentration directly corresponds to the increase in the concentration of the final product *Amp* with high

precision. Hence, a stationary state for the concentration of the intermediate c_{Hx} is present from the very beginning of the reaction onwards and therefore

$$-\frac{dc_{Nip}}{dt} = \frac{dc_{Amp}}{dt}. \tag{4.1}$$

With equation (1.4) and (1.5) it follows that

$$K_{ad,Hx}c_{Hx} = \frac{k_a}{k_b}\left(K_{ad,Nip}c_{Nip}\right)^n, \tag{4.2}$$

$K_{Hx}c_{Hx}$ can be substituted in equation (1.4), and the rate equation for the reactant is derived as

$$-\frac{dc_{Nip}}{dt} = k_a S \frac{\left(K_{ad,Nip}c_{Nip}\right)^n K_{ad\prime,BH4}c_{BH4}}{\left(1+\left(1+\frac{k_a}{k_b}\right)\left(K_{ad,Nip}c_{Nip}\right)^n + K_{ad',BH4}c_{BH4}\right)^2}. \tag{4.3}$$

Equation (4.3) was described previously for the stationary state of the reduction by gold nanoparticles, but as a stationary state was not present from the beginning of the reaction, it could not describe the entire kinetics.[109] Here it provides a full description of the kinetics of the reaction with the five fitting parameters k_a, k_b, $K_{ad,Nip}$, $K_{ad',BH4}$ and n. A closer look reveals that equation (4.3) is underdetermined. Substituting the fit parameters with

$$K_1 = k_a\left(K_{ad,Nip}\right)^n \quad \text{and} \quad K_2 = \left(1+\frac{k_a}{k_b}\right)\left(K_{ad,Nip}\right)^n \tag{4.4}$$

reduces their number to four and equation (4.3) is obtained as

$$-\frac{dc_{Nip}}{dt} = K_1 S \frac{\left(c_{Nip}\right)^n K_{ad\prime,BH4}c_{BH4}}{\left(1+K_2\left(c_{Nip}\right)^n + K_{ad',BH4}c_{BH4}\right)^2}. \tag{4.5}$$

The substitution of fit parameters shows that for the present model, it is impossible to obtain the two reaction rate constants k_a and k_b separately. However, a reduced reaction rate constant k_{red} can be obtained from the two substituted parameters K_1 and K_2 as

$$\frac{K_1}{K_2} = k_{red} = \frac{k_a k_b}{k_a + k_b}. \tag{4.6}$$

This is reasonable considering that Nip is directly reduced to Amp without accumulation of intermediates in solution. Similar to the case of a consecutive diffusion-reaction sequence described in chapter 3.2, both reaction steps are coupled, and the ratio K_1/K_2 can be regarded

as the overall reaction rate. In chapter 3.2 it is the concentration of reactants at the catalyst surface which determines the concentration gradient and thus the diffusion rate (i.e. the first reaction step) while here it is the coverage of the catalyst surface with intermediates, determining the rate of the first reaction step.

Two limiting cases can be distinguished:

If a) $k_a \gg k_b$, $K_1/K_2 \rightarrow k_b$ follows, the intermediates will accumulate on the catalyst surface, and slow down the overall reaction to k_b. The spectral deconvolution revealed that the sum concentration of Nip and Amp remains constant throughout the whole reaction. This means that in this case, the adsorption of the intermediate must be sufficiently high to suppress its desorption.

If b) $k_b \gg k_a$, $K_1/K_2 \rightarrow k_a$ follows, and the intermediates are immediately reduced to products without accumulating on the catalyst surface. Furthermore, equation (4.5) reduces to the classic one-step Langmuir-Hinshelwood kinetics in equation (3.16) as K_2 reduces to $K_2 = \left(K_{ad,Nip}\right)^n$. This shows that the present two-step Langmuir-Hinshelwood model is mathematically indistinguishable from the classical one-step model and only the interpretation of the obtained fit parameters K_1 and K_2 differs. As k_b disappears if $k_b \gg k_a$, the number of fit parameters is reduced to four, equation (4.5) is not underdetermined, and the adsorption constant $K_{ad,Nip}$ can be derived as well.

4.3.3 Fit algorithm

The differential equation (4.5) was used to fit the kinetic data by a genetic approach.[196] The data were fitted with Mathematica and with the help of Dr Sebastian Risse. Figure 12 shows the flow chart of the fit algorithm. After importing the discrete experimental data and transferring them into continuous data with a spline fit, a conversion limit was set up to which the data are fitted. For each parameter p_i, a range was defined, and test parameters were derived in N_i logarithmic equidistant intervals to generate parameter sets which are tested with the target function

$$\varepsilon_j(t_l, s_j) = \frac{1}{2N_{exp}}\left(\sum_1^{N_{exp}}\left(\sum_{t=0}^{t=t_l}\frac{\left|c_{exp}(t)-c_{fit}(t,s_j)\right|}{c_{exp}(t)}\right)+\sum_1^{N_{exp}}\left(\sum_{t=0}^{t=t_l}\frac{\left|c'_{exp}(t)-c'_{fit}(t,s_j)\right|}{c'_{exp}(t)}\right)\right) \quad (4.7)$$

to derive a reasonable starting parameter set s_j^* for the mutation step. Here, N_{exp} is the number of experimental curves which were fitted simultaneously, t_l is the limiting time of each experimental curve at which the conversion limit is reached, $c_{exp}(t)$, $c_{fit}(t)$, $c'_{exp}(t)$ and $c'_{fit}(t)$ are the experimental and the fitted concentration-time curves and their first derivatives (i.e. the curvature), respectively. In the subsequent mutation step, each fit parameter of s_j^* was randomly varied within the margins of $\Delta p_i \leq \pm$ 1%, and the new parameter set s_j^{**} was tested with the target function $\varepsilon_j(t_l, s_j^{**})$. If its value decreased, compared to the value for $\varepsilon_j(t_l, s_j^*)$, the new parameter set was used in the next mutation cycle (otherwise the previous set is maintained). This is repeated until no improved set of fit parameters is obtained in $c_n = 200$ consecutive mutation cycles. The code for the fit algorithm can be found in chapter 6.5.1.

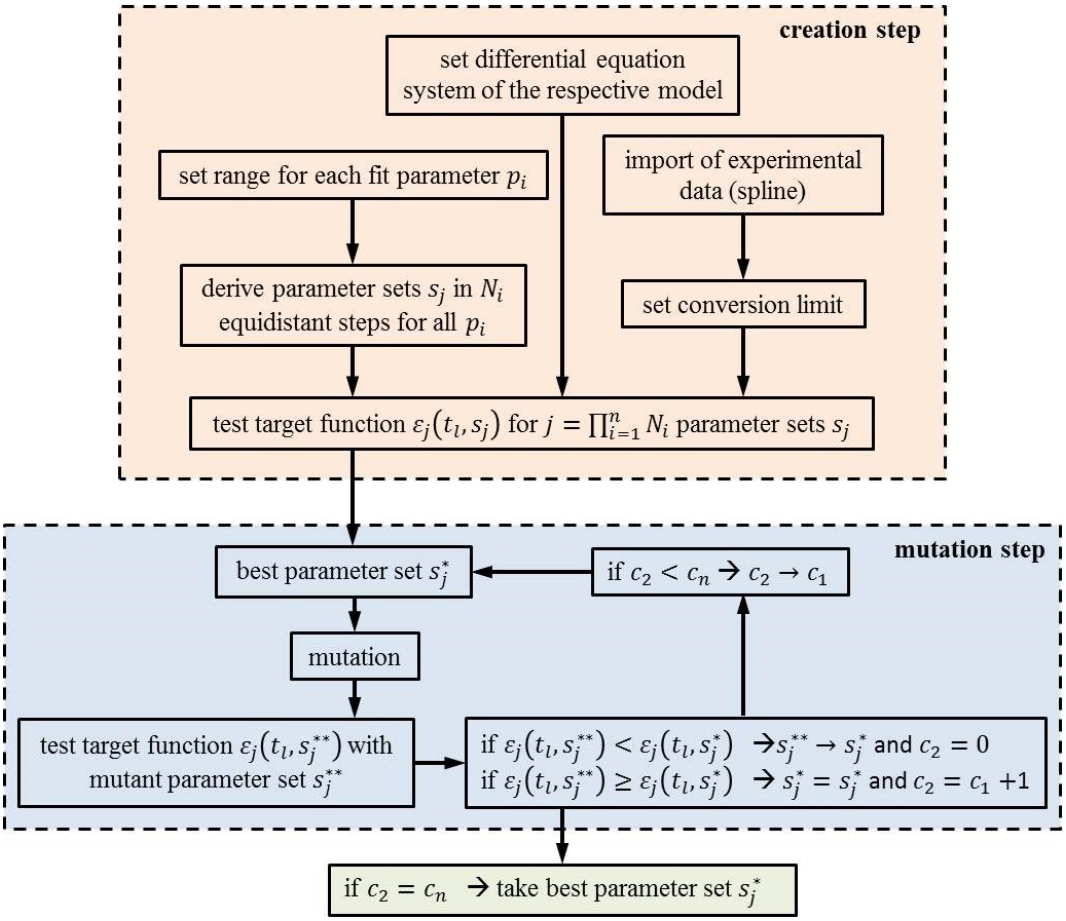

Figure 12: Flow chart of the genetic fit algorithm. In the creation step a spline fit is used to transfer the discrete experimental data into continuous datasets. The final fit is obtained after no further improvement is achieved in c_n consecutive mutation loops.

4.3.4 Kinetic analysis at constant temperature

For the kinetic analysis at $T = 20$ °C, measurements at three Nip and three borohydride concentrations were conducted, yielding a grid of nine combinations. All measurements were conducted at a ratio of borohydride to Nip concentration of $c_{BH4}/c_{Nip} \geq 50$. Therefore, the borohydride concentration can be regarded as constant throughout all experiments. All experiments were conducted three times and averaged. The catalyst surface area per unit volume was $S = 0.0625$ m^2 L^{-1}.

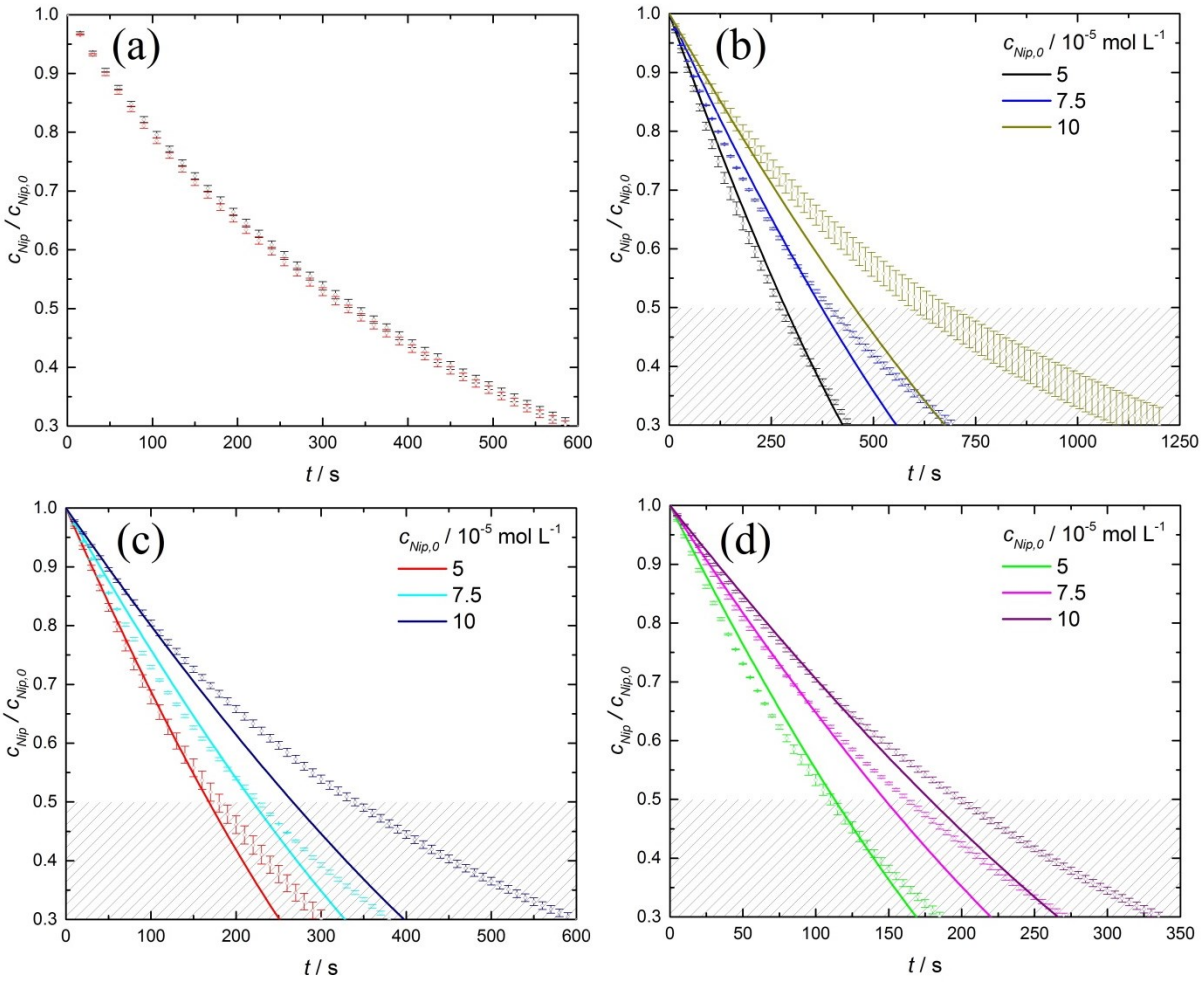

Figure 13: Comparison of the Nip concentration (a) obtained via spectral deconvolution (black) and obtained from the optical absorption at $\lambda = 400$ nm (red) and time dependencies of the experimental Nip concentration (symbols) and fit results (lines) for the reduction at $c_{BH4} = 5*10^{-3}$ (b), $1*10^{-2}$ (c) and $2*10^{-2}$ mol L^{-1} (d). The data were fitted up to 50% conversion; the shaded areas indicate extrapolations of the fits up to 70% conversion.

Figure 13 (a) shows that the curves of the concentration of Nip, obtained via spectral deconvolution, and obtained from the absorption maximum of Nip at $\lambda = 400$ nm, are virtually identical. Therefore, the following kinetic analysis is based on the latter. Consistent with previous results on gold and platinum catalysts, the reaction rate is increasing with increasing borohydride concentration, and decreasing with increasing Nip concentration.[107, 109, 115]

All data were fitted globally up to a conversion limit of 50%. A second fit to a conversion limit of 30% revealed no marked difference in the fit quality and parameters. Therefore, the results for the fits with the conversion limit of 50% are discussed in the following. Figure 13 (b) to (d) show the obtained time dependencies of the Nip concentration and the fit results. The data and fits in Figure 13 (b) to (d) are plotted up to 70% conversion to visualise the deviation between experimental data and fit at higher conversion discussed in chapter 4.3.6. The shaded area in the graphs indicates extrapolations of the obtained fits and data which were not part of the fitting.

The fit results in Figure 13 show that the model fits the data successfully at low conversions, but the fits begin to deviate towards lower concentrations subsequently. The deviation is lower at higher borohydride concentrations while it increases with increasing Nip concentration. Two potential reasons for the deviation are conceivable: A decrease in the borohydride concentration due to its decomposition over the reaction time, and the adsorption of the reaction product Amp to the catalyst surface. Both effects are not captured by the model. A detailed analysis of the deviation is discussed in chapter 4.3.6. The obtained fit parameters for the two limiting cases of a faster first and second reaction step, respectively, are given in Table 7.

Table 7: Obtained fit- and recalculated parameters for both limiting cases described in chapter 4.3.2.

parameter		$k_a \gg k_b$	$k_b \gg k_a$
n	/ [1]	0.397	0.397
$K_{ad',BH4}$	/ L mol^{-1}	20.8	20.8
K_1	/ L^n mol^{1-n} m^{-2} s^{-1}	1.12*10^{-3}	1.12*10^{-3}
K_2	/ L^n mol^{-n}	5.36	5.36
k_{red}	/ mol m^{-2} s^{-1}	2.10*10^{-4}	2.10*10^{-4}
$K_{ad,Nip}$	/ L mol^{-1}	-	68.62

The fit parameters n and $K_{ad',BH4}$ are identical for both cases and similar to the values obtained previously on gold ($n = 0.5$ and $K_{ad,BH4} = 50 \pm 4$).[109] If $k_a \gg k_b$, the reduced reaction rate constant represents the rate constant k_a of the first reaction step, and the adsorption constant on Nip can be derived. The obtained rate constant is slightly lower than the value obtained on gold ($k_a = 9.3*10^{-4} \pm 2.5*10^{-4}$) while the adsorption constant of Nip obtained on gold is over 50 times higher.[109]

4.3.5 Influence of temperature

Measurements were conducted in intervals of $\Delta T = 5$ °C between $T = 10$ and 50 °C, and at concentrations of $c_{Nip} = 1*10^{-4}$ and $c_{BH4} = 1*10^{-2}$ mol L^{-1} to investigate the influence of the reaction temperature. All experiments were conducted three times and averaged. The data were fitted individually for each temperature up to a conversion limit of 50%.

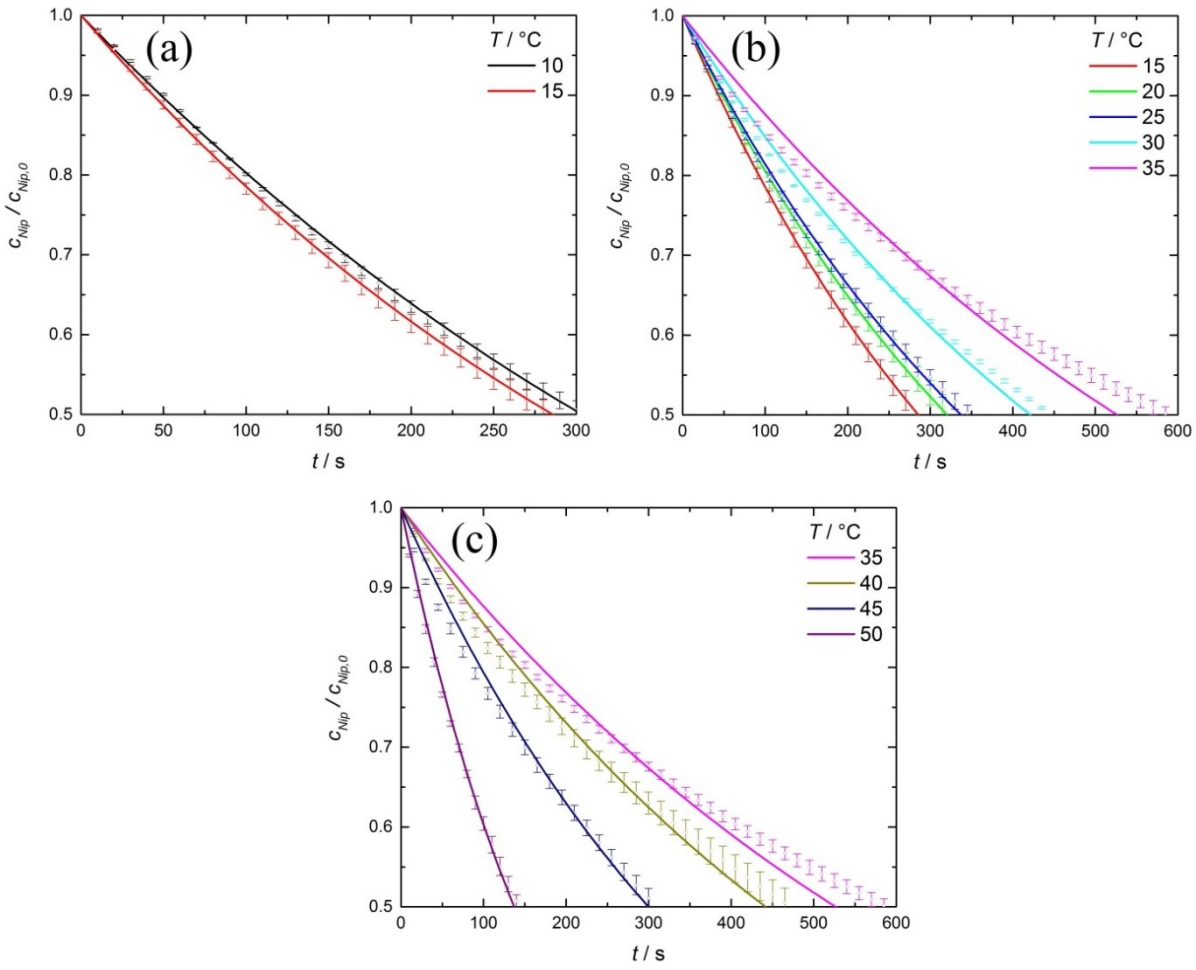

Figure 14: Time dependencies of the experimental Nip concentration (symbols) and fit results (lines) for the reduction at $T = 10$ to 50 °C and $S = 0.0625$ m^2 L^{-1}. The data were fitted up to 50% conversion.

Figure 14 (a) to (c) show the experimental *Nip* concentrations and the fit results as a function of time. With increasing temperature, the reaction rate increases first between $T = 10$ and 15 °C, followed by a decrease up to $T = 35$ °C before it decreases again. This coincides with previous results obtained with PNIPAM-based silver and palladium catalysts.[73, 119, 132] The fit results in Figure 14 show that the model fits the data satisfactorily for all temperatures; however, slight deviations occur for long reaction times. Overall, the temperature-dependent measurements are better fitted than the data obtained at $T = 20$ °C shown in the previous chapter because only one experimental concentration-time curve is fitted at once (compared to nine curves fitted globally at $T = 20$ °C).

The results for the obtained parameters k_{red}, n and $K_{ad',BH4}$ are shown in Figure 15. A separate interpretation of the temperature dependencies of the fit parameters K_1 and K_2 is not possible as they comprise three and four (temperature-dependent) parameters, respectively. The obtained fit parameters (at $T = 20$ °C) differ significantly from the parameters obtained in the previous chapter. This is a consequence of the different number of experimental datasets which are simultaneously fitted (nine compared to one).

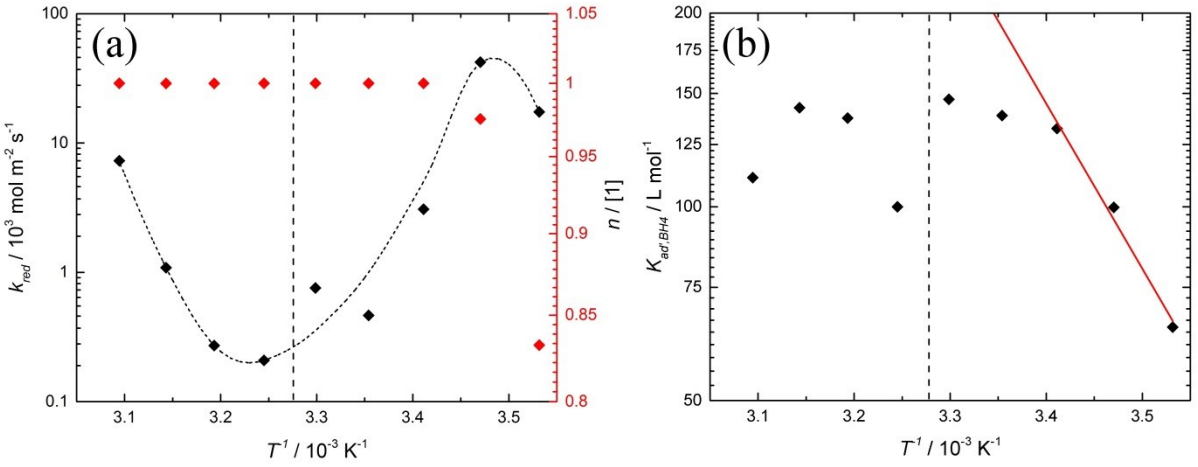

Figure 15: Arrhenius plots of the obtained fit parameters n and $k_{red} = k_1/k_2$ (a) and Van't Hoff plot of $k_{ad',BH4}$ (b). The horizontal lines indicate the LCST of $T = 32$ °C. The dashed line in (a) is a guide to the eye. The red line in (b) shows the linear fit to $K_{ad',BH4}$ between $T = 10$ and 20 °C according to equation (4.8).

Figure 15 (a) shows that n is increasing at low temperatures but reaches a constant value of $n = 1$ for $T \geq 20$ °C. As n is a measure for the heterogeneity of the catalyst surface, the parameter is expected to be approximately constant at moderate temperatures, in accordance

with the obtained result. For k_{red}, a typical non-Arrhenius dependency is obtained which was found repeatedly for the reaction rate of PNIPAM-based thermoresponsive catalysts.[42, 60, 66, 73, 75, 119, 132, 188, 193] The reduced reaction rate increases first at low temperatures, decreases then and reaches a minimum around the LCST before it increases again.

Figure 15 (b) shows the Van't Hoff plot of $K_{ad',BH4}$, supposedly the adsorption constant of borohydride $K_{ad,BH4}$ alone. For the latter, a linear dependency would be expected in Figure 15 (b) according to the linearised Van't Hoff equation[1]

$$\ln\left(K_{ad,BH4}\right) = \frac{1}{T}\left(-\frac{\Delta H}{R}\right) + \left(\frac{\Delta S}{R}\right), \tag{4.8}$$

where ΔH and ΔS are the enthalpy and the entropy of adsorption, respectively.

However, the kinetic model applies the bulk concentrations for borohydride and Nip. As shown in chapter 3.1.1, the actual concentration inside a hydrogel network differs from the bulk concentration. The true concentration inside the hydrogel can be expressed by the product of the bulk concentration and the partitioning coefficient K_{part}. As the latter is not explicitly included in the present model, the derived constant $K_{ad',BH4}$ is expected to contain both, the adsorption constant $K_{ad,BH4}$ as well as the partitioning coefficient $K_{Part,BH4}$ according to

$$K_{ad',BH4} = K_{ad,BH4} K_{Part,BH4}. \tag{4.9}$$

The Van't Hoff plot in Figure 15 (b) shows that $K_{ad',BH4}$ follows a linear trend between $T = 10$ and 20 °C. If a constant value of $K_{Part,BH4} = 1$ is assumed in this temperature regime (i.e. $K_{ad',BH4} = K_{ad,BH4}$), the temperature dependence of the adsorption of borohydride can be derived with equation (4.8). The obtained values for the enthalpy and entropy of adsorption, $\Delta H = 49.1$ kJ mol^{-1} and $\Delta S = 208.3$ J mol^{-1} K^{-1}, are of the same order of magnitude as the values obtained previously by Gu et al. for gold ($\Delta H = 37$ kJ mol^{-1} and $\Delta S = 158$ J mol^{-1} K^{-1}, respectively).[109]

If $K_{ad',BH4}$ is divided by the as-derived temperature-dependent adsorption constant $K_{ad,BH4}$ (red line in Figure 15 (b)) the temperature-dependent partitioning constant of borohydride $K_{Part,BH4}$ is obtained according to equation (4.9). Figure 16 shows that the values qualitatively follow the partitioning coefficient of sodium chloride $K_{part,NaCl}$ in a PNIPAM

hydrogel, experimentally determined by Kawasaki et al.[197] This is in accordance with the findings of Kanduc et al., that the partitioning coefficients for small ions are similar, independently of the very type of ion (as the strongly bound hydration shell shields their specific character).[143] Obviously borohydride is not a simple ion such as chloride but it is still a monovalent ion with a symmetric charge distribution, and Figure 16 indicates that the findings of Kanduc et al. are valid for borohydride as well.

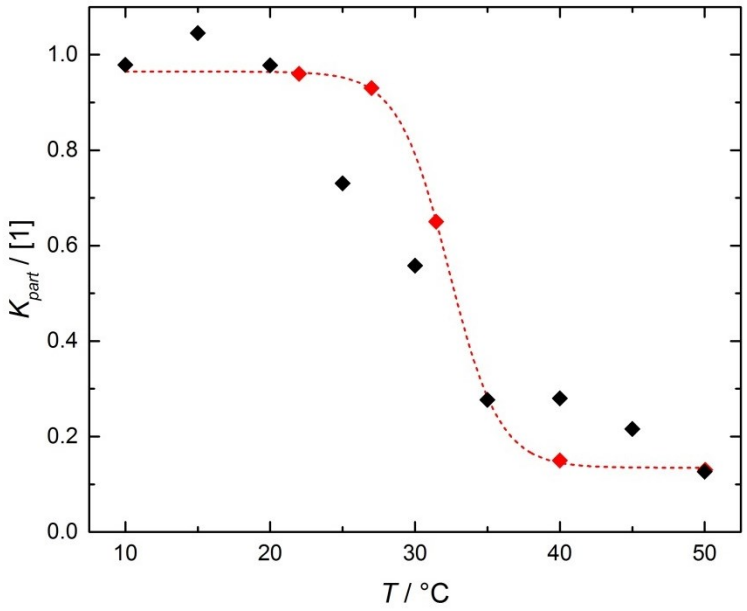

Figure 16: Comparison of the partition coefficient of borohydride $K_{Part,BH4}$ derived from the kinetic analysis (black) and the experimental partition coefficient of sodium chloride $K_{Part,NaCl}$ in a PNIPAM hydrogel (red).[197] The dashed line is a sigmoidal interpolation of the experimental values.

Overall the model shows the expected trends against temperature, though some information cannot be derived due to mathematical limitations (e.g. the temperature dependence of the adsorption constant for Nip). For an improved analysis, the partitioning constants for Nip and borohydride should be included additionally. However, an inclusion as additional fit parameters is impossible as one fit parameter would be replaced by two, and the model would become underdetermined. An alternative could be experimentally determined partitioning constants; however, to our best knowledge no studies thereof exist yet.

In conclusion, the kinetic analysis shows that the model for the reduction on gold can be simplified in the present case. The presence of a stationary state from the beginning of the

reaction onwards further supports the hypothesis drawn in the literature review that the first reaction step may indeed be rate-determining on silver.

4.3.6 Deviation of the fit from experimental data

To evaluate the difference between fitted and experimental curves of the Nip concentration at $T = 20$ °C, the relative residue is calculated according to

$$\Delta\left(c_{exp} - c_{fit}\right)_{rel} = \frac{c_{exp}(t) - c_{fit}(t)}{c_{exp}(t)} = 1 - \frac{c_{fit}(t)}{c_{exp}(t)}. \quad (4.10)$$

With equation (4.10), the deviation between fit and experiment can be evaluated relative to the absolute Nip concentration at the respective time and independently of the initial concentration. This way, a comparison of the deviation between the different experiments at $T = 20$ °C is possible. Furthermore, the deviation is plotted against conversion instead of reaction time as the data are always fitted up to 50% conversion (which is reached at different times for each experiment).

To evaluate whether the deviation may be caused by a decrease in the borohydride concentration (due to hydrolysis) or by adsorption of Amp, the deviation graphs are plotted in two ways. Figure 17 (a), (c) and (e) each show the three measurements at equal Nip- and varying borohydride concentration while Figure 17 (b), (d) and (f) compare measurements at equal borohydride- and varying Nip concentration.

The hydrolysis of borohydride is catalysed by protons, i.e. pH-dependent. Upon decomposition, the pH increases, and the rate of hydrolysis is therefore fast at the beginning and becomes exponentially slower with time as the pH increases.[198] However, as the reaction volume is the same for all experiments, the same amount of borohydride will be hydrolysed in all experiments before the pH increase retards the rate of hydrolysis. If this is the reason, the deviation should be more pronounced at lower initial borohydride concentrations where a larger fraction of the borohydride concentration is hydrolysed. Figure 17 (a), (c) and (e) show that no clear trend of the deviations with respect to borohydride concentration is discernible.

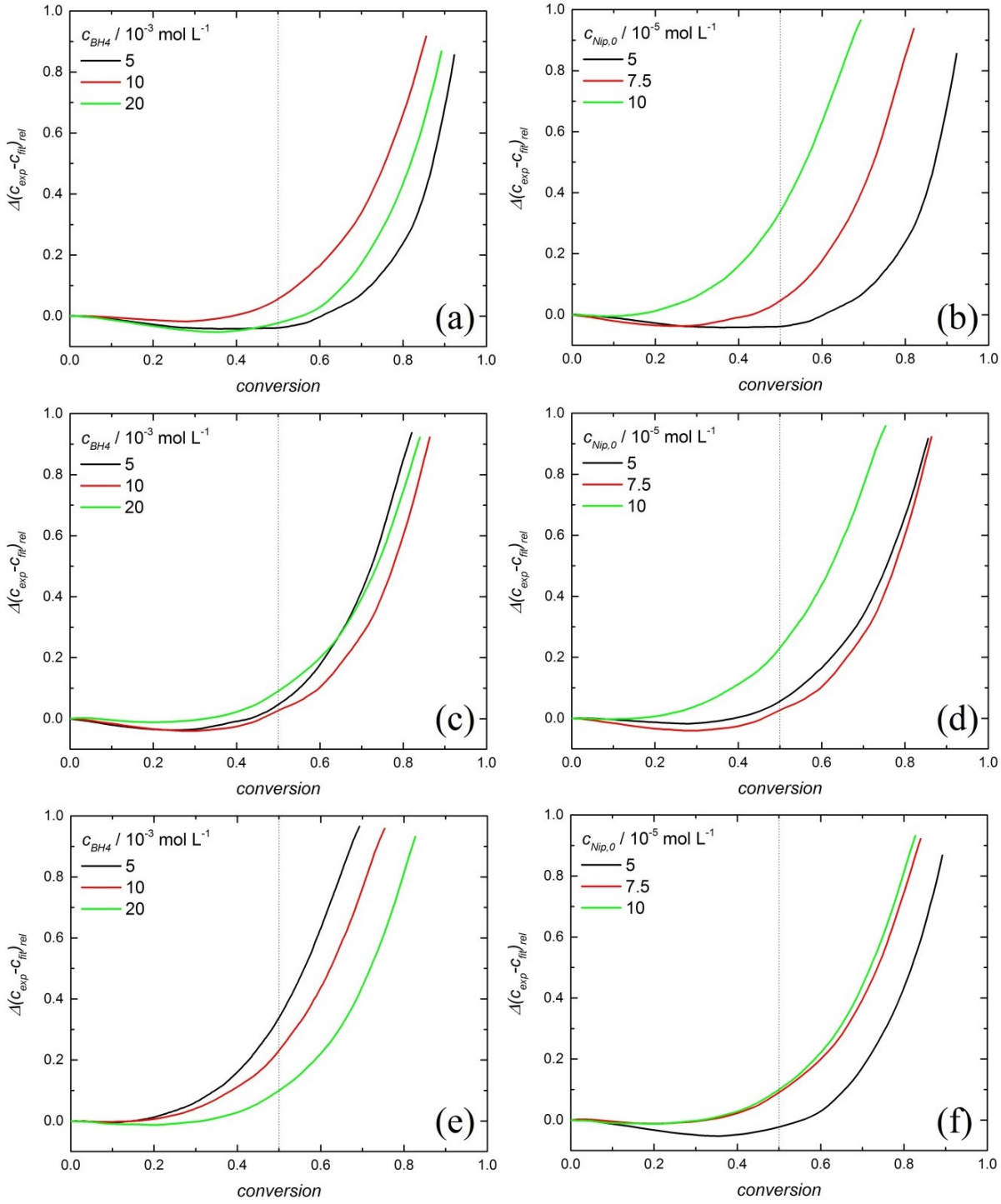

Figure 17: Relative deviation of fitted and experimental *Nip* concentration as function of conversion. Effect of increasing borohydride concentration at $c_{Nip} = 5*10^{-5}$ (a), $7.5*10^{-5}$ (c) and $1*10^{-4}$ mol L^{-1} (e) and effect of increasing *Nip* concentration at $c_{BH4} = 5*10^{-3}$ (b), $1*10^{-2}$ (d) and $2*10^{-2}$ mol L^{-1} (f). The dotted lines indicate the transition between the fitted regime and extrapolation of the fit results to higher conversions.

If the deviation is caused by the adsorption of Amp, the deviation should, at similar conversions, be higher at higher initial Nip concentration as the conversion correlates with the concentration of Amp (relative to the initial Nip concentration). Figure 17 (b), (d), and (f) show that this is the case with only one exception.

The analysis of the deviation between fit and experiment indicates that the deviation is caused by the adsorption of Amp. Unfortunately, no direct proof for notable adsorption of Amp compared to Nip was found in the literature. To our best knowledge, no studies comparing the adsorption energies of Nip and Amp exist for silver. However, some findings on the other coinage metals copper and gold support the possibility. In a DFT study, Simpson et al. investigated the adsorption of trisubstituted benzene derivatives on copper(111). Here, the binding energies of 1,3,5-trinitrobenzene and 1,3,5-triaminobenzene were found to be ΔE_{bond} = -141.0 and -219.3 kJ mol^{-1}, respectively. In a mechanistic investigation of the reduction of nitrobenzene on gold, Corma et al. found aniline as an adsorbed species on the catalyst surface during the reaction via infrared spectrometry.[114] The kinetic investigations by Gu et al. found an adsorption constant for 4-hydroxylaminophenol much higher than the one of Nip.[109, 115] As the molecules are similar, it is not unrealistic that the adsorption constant of Amp on silver is large enough to cause significant adsorption as well.

It needs to be mentioned that the analysis of the deviation between fit and experiment must not be understood as proof or disproof of one or another reason. All data were fitted in one global fit with a kinetic model which does mathematically account for neither of the two potential reasons. The fit algorithm, however, will still try to obtain the best fit and therefore compensate missing effects by adjusting the available fit parameters. Therefore, the found deviation may be distorted to some extent which makes an evaluation problematic. Another set of experiments at higher pH, to suppress the hydrolysis of borohydride, could yield more unambiguous results concerning the decomposition of borohydride as a potential reason. A fit with an extended model, including an additional term for the adsorption of Amp, could reveal if fits of better quality would be obtained. However, including another term would increase the number of fit parameters and it is therefore likely that the fit quality improves, irrespective if significant adsorption of Amp occurs or not. At this point, further experiments and analysis exceed the scope of this work.

4.4 Hexacyanoferrate(III) reduction

The reduction of hexacyanoferrate(III) (HCF) with borohydride can be used as a model reaction to investigate diffusional effects on the surface catalysed reaction. It was previously demonstrated that the reaction rate reaches the diffusion limit of HCF at high concentrations of borohydride and the effect of crosslinking density on the reaction rate with gold nanoparticles located inside a PNIPAM network was investigated.[124, 125] As elucidated in chapter 1.3.2, electrostatic effects are believed to play a significant role in the reaction and a comprehensive model accounting for such effects will provide a more profound understanding of the kinetics of the reaction.

4.4.1 Kinetic measurements and working hypothesis

The kinetics of the reaction was investigated with Au@PS-PNIPAM core-shell nanoreactors. All measurements were conducted at a ratio of borohydride to HCF concentration $c_{BH4}/c_{HCF} \geq 25$ where pseudo-unimolecularity can be assumed safely, and the diffusion of borohydride does not limit the reaction rate.[126] Measurements were conducted at different ionic strength, temperature and varying concentrations of HCF, borohydride and the catalyst.

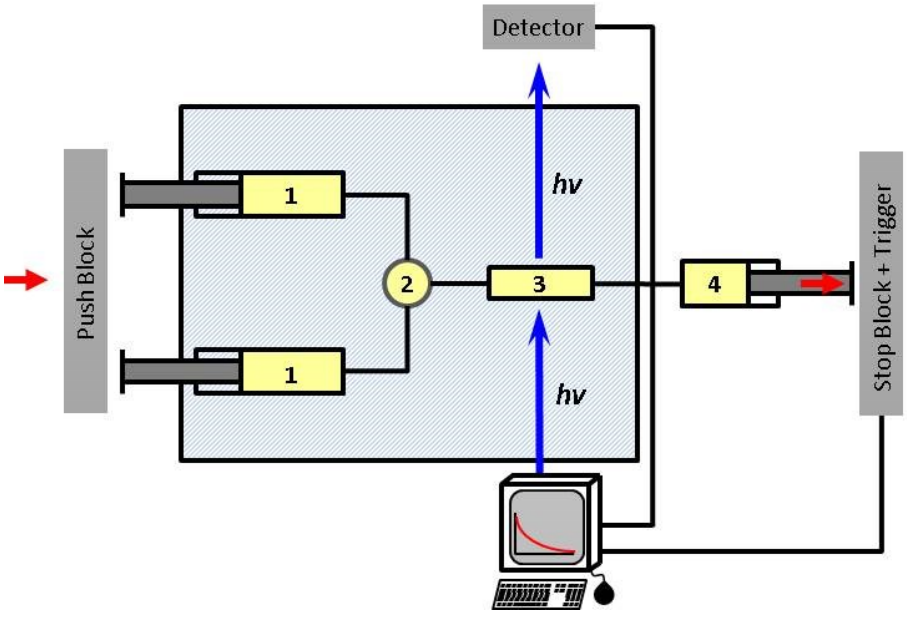

Figure 18: Schematic of the stopped-flow apparatus with drive syringes (1), mixing chamber (2), measurement cell (3) and stop syringe (4).

As the reaction is too fast to be recorded manually with UV-Vis spectroscopy, the measurements were conducted with stopped-flow. Figure 18 shows a schematic of the stopped-flow measurement principle. The blue shaded area indicates the thermostatted section of the apparatus. The reactants are filled into the drive syringes via Luer-lock loading ports at each drive syringe (not shown in Figure 18). The push block is pushed, and both reactant solutions are injected into the mixing chamber in a 1:1 ratio to trigger a measurement. From there, the mixture moves through the measurement cell and to the stopping syringe. The liquid flow continues until the stopping syringe is stopped at the stop block, where it triggers a digital signal that initiates the measurement. The ongoing liquid flow from the mixing chamber through the measurement cell up to the very moment the measurement is triggered ensures that the measurement can be recorded from the beginning (in intervals of $\Delta t = 0.5$ s).

Figure 19 shows the key features of the obtained data for the reduction, which lead to the conclusions on which the kinetic model described in the following is based. Firstly, if the same experiment is conducted at increasing ionic strength I_0, a significant increase in the reaction rate is observed in the concentration-time dependencies of HCF, as shown in Figure 19 (a). Secondly, if the same dependencies are plotted logarithmically as part of the data evaluation with pseudo first order kinetics, shown in Figure 19 (b), it is evident that the slope (which corresponds to the pseudo first order rate constant) is higher at the beginning of the measurement and decreases with time until a stationary state is achieved.

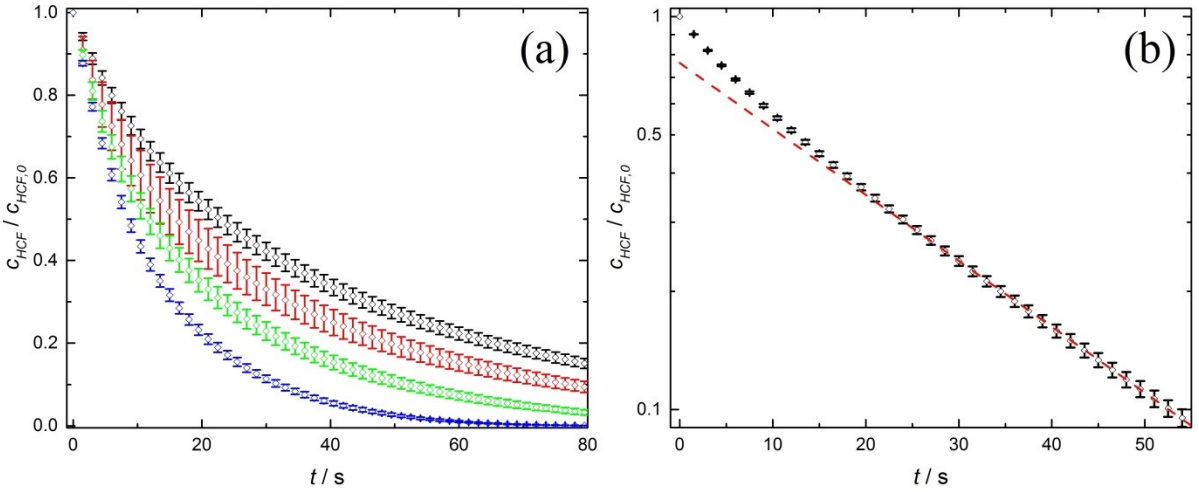

Figure 19: Concentration of HCF as a function of time (a) at $I_0 = 0.065$ (black), 0.075 (red), 0.1 (green) and 0.2 mol L^{-1} (blue) and logarithmic plot (b) of the concentration-time dependency for an exemplary measurement; the dashed red line illustrates as guide to the eye how the slope of the measurement data decreases with time.

From the first observation, it can be concluded that electrostatics plays a significant role in this reaction. At higher ionic strength where the high charges of hexacyanoferrate (-3e and -4e for the reactant and product, respectively) are screened better, the reaction is notably faster. The second observation points to a type of inhibition. This observation is found to be more pronounced at low ionic strength and high HCF concentrations. Based on this, the following working hypothesis as the basis for a kinetic model is derived.

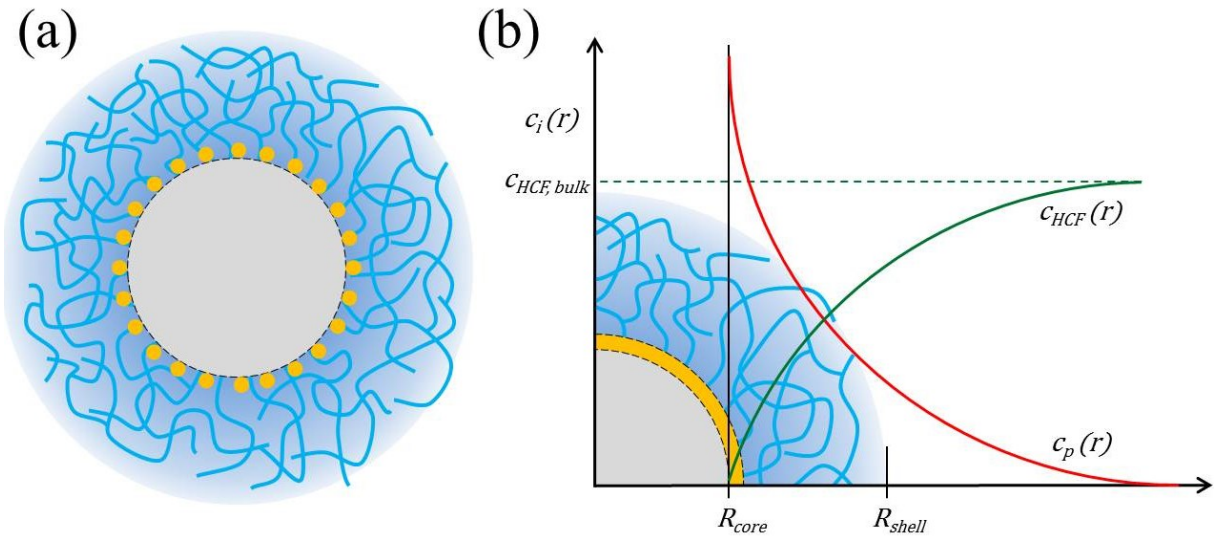

Figure 20: Simplified representation (a) of the nanoreactor architecture and continuous model representation (b) for the radial concentration profiles of the reactant $c_{HCF}(r)$ and the product $c_p(r)$. The gold nanoparticles (yellow) are predominantly located deep inside the PNIPAM hydrogel (blue) and close to the PS core (grey).

Most of the gold nanoparticles are located close to the PS core of the nanoreactor, as shown in Figure 8 (b) and illustrated in Figure 20 (a). The reactant hexacyanoferrate(III) diffuses to the gold nanoparticle surface where it is transformed into the product, hexacyanoferrate(II). The fast conversion at the gold nanoparticle surface leads to the accumulation of products in a layer around the PS core surface. For a spherical catalyst particle, it was shown previously that repulsive interactions between the reaction products can result in a product concentration at the catalyst surface higher than the reactant bulk concentration.[153] Besides that the diffusion coefficient for the reaction product was shown to be lower than for the reactant.[199] Because the reaction is in or close to the diffusion limit of HCF, this leads to product concentrations at the PS core above the reactant bulk concentration, as illustrated in Figure 20 (b).[124, 126] Additionally, hexacyanoferrate ions are known to have significant adsorption to gold nanoparticles.[200, 201] As a consequence of the accumulation of products, a negative charge

builds up around the PS core, which electrostatically repels the reactants diffusing towards the gold nanoparticles. Thus, the diffusion rate decreases, which is macroscopically observed as a decrease in the rate, as shown in Figure 19 (b). In the following, a rate theory, including electrostatic product inhibition and the screening of the latter by ionic solutes is described, as derived elsewhere.[202] The kinetic model was developed in the group of Professor Dr Joachim Dzubiella based on the results of the kinetic measurements.

4.4.2 Full kinetic analysis

4.4.2.1 Kinetic model

A few assumptions are made to arrive at an analytical theory and describe the observed effects by only a few physically meaningful parameters. As the majority of the gold nanoparticles inside the nanoreactors are located close to the PS core surface, the theory is formulated based on the assumption of a single reactive catalytic sphere with radius R_{core}, centred inside a hydrogel shell with radius R_{shell}. The size of the gold nanoparticles is small compared to the PS core, and therefore negligible. The rate of a diffusion-controlled unimolecular reaction for such a system can be derived from the Debye-Smoluchowski equation as[72, 126, 151, 203, 204]

$$k_D^{-1} = \int_{R_{core}}^{\infty} \frac{e^{\beta G(r)}}{4\pi N_A D(r) r^2} dr, \tag{4.11}$$

where $\beta^{-1} = k_B T$. The effective interaction potential $G(r)$ between the reactant and the hydrogel shell and the reactant diffusivity $D(r)$ are defined as[204]

$$G(r) = \begin{cases} \Delta G & R_{core} < r < R_{shell} \\ 0 & R_{shell} < r \end{cases} \tag{4.12}$$

and

$$D(r) = \begin{cases} D_g & R_{core} < r < R_{shell} \\ D_0 & R_{shell} < r \end{cases}. \tag{4.13}$$

As shown in chapter 3.2, the rates of the diffusion k_D and the surface reaction k_{surf} cannot be separated if the reactant concentration at the catalyst surface is unknown. Therefore, both terms are expressed by the intrinsic reaction rate constant k_{NR} according to[126]

$$k_{NR}^{-1} = k_{surf}^{-1} + k_D^{-1}. \tag{4.14}$$

The term "intrinsic" here emphasises that these rates are not influenced by electrostatic effects. To describe the electrostatic repulsion which reactants experience from accumulated products the electrostatic interaction $V_{DH}(r,t)$ is, on a Debye-Hückel level, defined as[205]

$$V_{DH}(r,t) = Q_r\psi(r,t) = \frac{p(t)Q_pQ_r}{4\pi\varepsilon_0\varepsilon_r r}\frac{e^{-\kappa(r)(r-R_{core})}}{(1+\kappa(r)R_{core})}, \tag{4.15}$$

where $p(t)$ is the time-dependent number of accumulated products, and Q_r and Q_p are the charges of the reactant and the product, respectively. $V_{DH}(r,t)$ accounts for the screening of the electrostatic potential due to ionic solutes with a screened coulomb potential. The ionic strength $I(r)$ (to derive the inverse screening length $\kappa(r)$ with equation (3.21)) is defined as

$$I(r) = \begin{cases} I_g = \sum_i \frac{1}{2} c_i^g {z_i}^2 & R_{core} < r < R_{shell} \\ I_0 = \sum_i \frac{1}{2} c_i {z_i}^2 & R_{shell} < r \end{cases} \tag{4.16}$$

where c_i^g and c_i are the concentrations of ionic species i inside and outside the hydrogel, respectively. The electrostatic interaction is added to the effective interaction potential in the expression for the intrinsic diffusion to include it, and the overall reaction rate constant k_{on} is thus obtained as

$$k_{on}^{-1} = k_{surf}^{-1} + \int_{R_{core}}^{\infty} \frac{e^{\beta(V_{DH}(r,t)+G(r))}}{4\pi N_A D(r) r^2}\, dr. \tag{4.17}$$

The electrostatic interaction is now regarded as perturbation of the intrinsic diffusion to separate the intrinsic diffusion from the inhibiting electrostatic effect. Assuming a weak electrostatic potential and applying first order perturbation theory, the term can be linearised and is obtained as

$$\int_{R_{core}}^{\infty} \frac{e^{\beta V_{DH}(r,t)+\beta G(r)}}{4\pi N_A D(r) r^2}\, dr \cong \int_{R_{core}}^{\infty} \frac{e^{\beta G(r)}}{4\pi N_A D(r) r^2}\, dr + \int_{R_{core}}^{\infty} \frac{\beta V_{DH}(r,t) e^{\beta G(r)}}{4\pi N_A D(r) r^2}\, dr. \tag{4.18}$$

Here, the electrostatic perturbation $E\left(P, \kappa_g\right)$ is defined as

$$E\left(P, \kappa_g\right) = \int_{R_{core}}^{\infty} \frac{\beta V_{DH}(r,t) e^{\beta G(r)}}{4\pi N_A p(t) D(r) r^2}\, dr$$

$$= \frac{Q_rQ_p}{16\pi^2 N_A k_B T \varepsilon_0 \varepsilon_r P}\left[\frac{e^{\kappa_g R_{core}}}{(1+\kappa_g R_{core})}\int_{R_{core}}^{R_{shell}} \frac{e^{-\kappa_g r}}{r^3}\, dr + \frac{P}{D_0}\frac{e^{\kappa_0 R_{core}}}{(1+\kappa_0 R_{core})}\int_{R_{shell}}^{\infty} \frac{e^{-\kappa_0 r}}{r^3}\, dr\right], \tag{4.19}$$

where P is the permeability of the hydrogel network for HCF as defined in equation (3.1). Due to the fast drop of the integral function with r, it is safe to assume

$$\frac{P}{D_0}\frac{e^{\kappa_0 R_{core}}}{(1+\kappa_0 R_{core})}\int_{R_{shell}}^{\infty}\frac{e^{-\kappa_0 r}}{r^3}dr \ll \frac{e^{\kappa_g R_{core}}}{(1+\kappa_g R_{core})}\int_{R_{core}}^{R_{shell}}\frac{e^{-\kappa_g r}}{r^3}dr, \tag{4.20}$$

and therefore the electrostatic perturbation $E(P,\kappa_g)$ simplifies to

$$\begin{aligned} E(P,\kappa_g) &\cong \frac{z_r z_p e^2}{16\pi^2 N_A k_B T \varepsilon_0 \varepsilon_r P}\frac{e^{\kappa_g R_{core}}}{(1+\kappa_g R_{core})}\int_{R_{core}}^{\infty}\frac{e^{-\kappa_g r}}{r^3}dr \\ &= \frac{z_r z_p \lambda_B}{4\pi N_A P}\frac{e^{\kappa_g R_{core}}}{(1+\kappa_g R_{core})}\int_{R_{core}}^{\infty}\frac{e^{-\kappa_g r}}{r^3}dr, \end{aligned} \tag{4.21}$$

with the Bjerrum length λ_B given as[206]

$$\lambda_B = \frac{e^2}{4\pi k_B T \varepsilon_0 \varepsilon_r}. \tag{4.22}$$

Now the overall reaction rate constant k_{on} can be written as

$$k_{on}^{-1} = k_{surf}^{-1} + k_D^{-1} + p(t)\,E(P,\kappa_g) = k_{NR}^{-1} + p(t)\,E(P,\kappa_g). \tag{4.23}$$

Obviously, k_{on} is not a constant as it comprises the electrostatic perturbation dependent on the number of accumulated products inside the nanoreactor, which is not constant throughout the temporal progress of the kinetic experiments. For a better understanding, the inverse of a reaction rate constant can be understood as the time required for the respective reaction step. Thus, k_{on}^{-1} is the sum of the reaction times for the diffusion and the surface reaction. The term $p(t)E(P,\kappa_g)$ adds the additionally required time to the intrinsic diffusion time k_D^{-1} (without electrostatic repulsion of reactants) to account for the slower diffusion due to the electrostatic repulsion between reactants and accumulated products.

To finally arrive at a macroscopic reaction rate, k_{on} needs to be multiplied by the concentration of nanoreactors c_{NR} and the reactant concentration c_{HCF}, and the corresponding rate law is derived as

$$-\frac{dc_{HCF}}{dt} = k_{on}\,c_{NR}\,c_{HCF} = \frac{k_{NR}\,c_{NR}\,c_{HCF}}{1+\,k_{NR}p(t)E(P,\kappa_g)}. \tag{4.24}$$

For a full description, a second rate equation describing the time-dependent number of accumulated product molecules $p(t)$ is required. Therefore, the overall reaction is regarded as

two consecutive steps. In the first step, the reactants diffuse to the gold surface and are transformed into products which contribute to the electrostatic repulsion from reactants. This step is already described by equation (4.24). After that, the accumulated products diffuse in the reverse direction and out into bulk solution (where they do not contribute to the electrostatic repulsion of approaching reactants anymore) with the diffusion rate k_{off}. Therefore, $p(t)$ can be regarded as intermediate of the above processes and is described by a rate equation including the formation (source) and the subsequent off-diffusion (drain) of accumulated products according to

$$\frac{dp(t)}{dt} = -\frac{dc_{HCF}}{dt}\frac{1}{c_{NR}} - p(t)\, k_{off}. \tag{4.25}$$

For the calculation of the electrostatic repulsion of reactants from accumulated products, it is necessary to consider the number of accumulated products $p(t)$ inside a single nanoreactor. Therefore, the bulk rate of product formation upon reaction defined in equation (4.24) needs to be divided by the nanoreactor concentration c_{NR} to arrive at an absolute number of accumulated products in equation (4.25).

4.4.2.2 Fit algorithm

Equations (4.24) and (4.25) provide a set of coupled differential equations which were used to fit the kinetic data as shown in the following. The data were fitted with Mathematica and with the help of Dr Sebastian Risse. The Fit parameters are the intrinsic reaction rate k_{NR}, the electrostatic perturbation $E(P, \kappa_g)$ and the rate k_{off} at which accumulated products leave the nanoreactor. The fit algorithm is described in chapter 4.3.3. Other than for the 4-nitrophenol reduction, not all fit parameters are fitted globally here. This means that the parameter sets s_j comprise of one value p_i for each global parameter (valid for all experimental curves in the respective fit) and a set of individual values $p_{i,s}$ for (one for each experimental curve s).

4.4.2.3 Fit results

Six series of measurements were performed against five variable parameters under otherwise constant conditions to test the kinetic model. The variable parameters were the reactant concentrations c_{HCF} and c_{BH4}, the catalyst concentration c_{NR}, ionic strength I, and temperature T. For each series of measurement, the data were fitted separately.

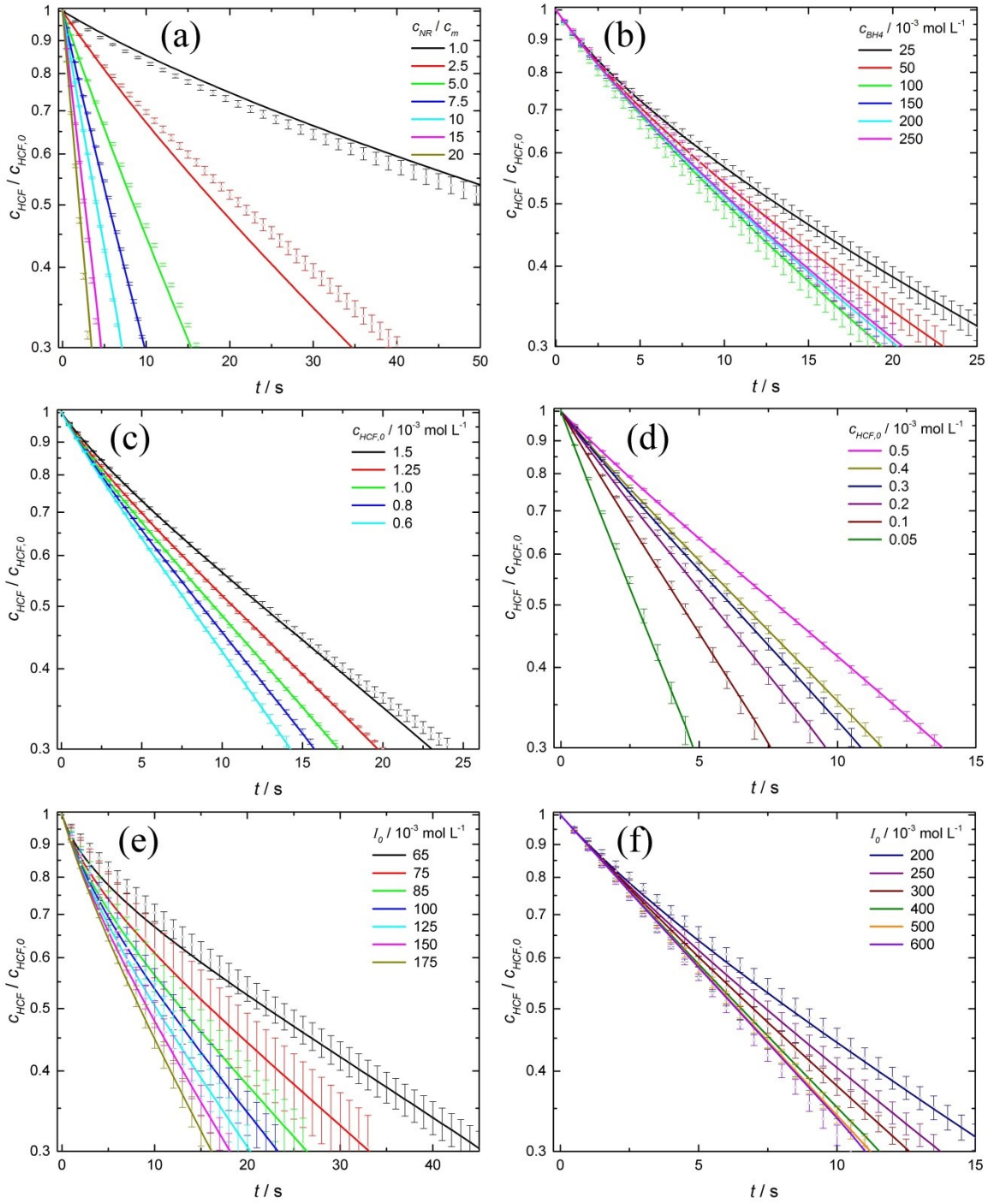

Figure 21: Measurements (symbols) and fit results (lines) of the HCF concentration as function of time recorded at $T = 20$ °C. Measurements at different catalyst concentrations c_{NR} (a), measured at $c_{BH4} = 0.25$ mol L^{-1}, $c_{HCF,0} = 5*10^{-4}$ mol L^{-1} and $I_0 = 0.269$ mol L^{-1} (c_{NR} is stated in multiples of the minimal nanoreactor concentration $c_m = 1.45*10^{-12}$ mol L^{-1}); at different borohydride concentrations (b), measured at $c_{HCF,0} = 1*10^{-3}$ mol L^{-1}, $I_0 = 0.272$ mol L^{-1} and $c_{NR} = 5\ c_m$; at different HCF concentrations (c) and (d), measured at $c_{BH4} = 0.25$ mol L^{-1}, $I_0 = 0.296$ mol L^{-1} and $\boldsymbol{c_{NR} = 5\ c_m}$; and at different ionic strength (e) and (f), measured at $\boldsymbol{c_{BH4}} = 0.05$ mol L^{-1}, $\boldsymbol{c_{HCF,0}} = 5*10^{-4}$ mol L^{-1} and $\boldsymbol{c_{NR} = 5\ c_m}$.

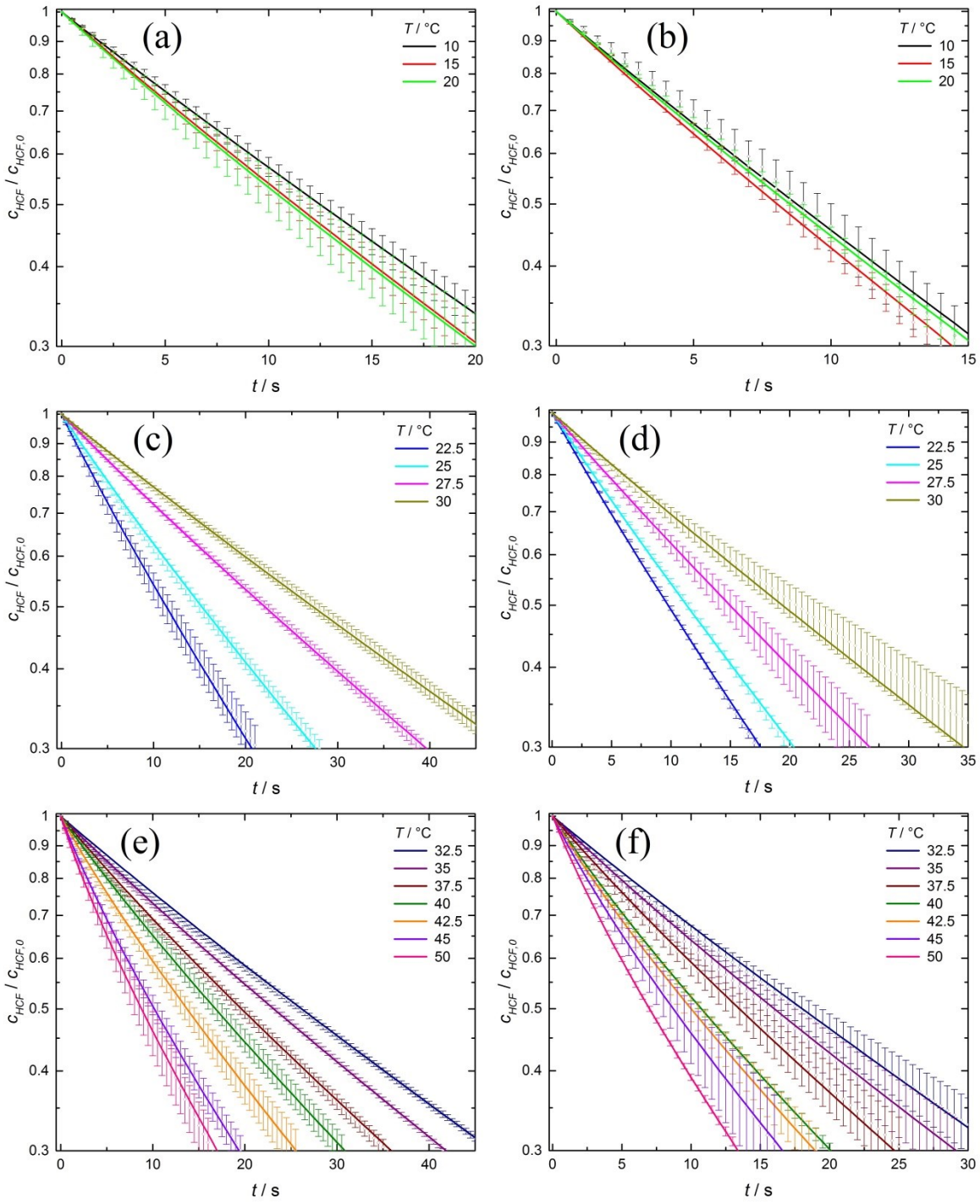

Figure 22: Measurements (symbols) and fit results (lines) of the HCF concentration as function of time for two series of measurements recorded at varying temperature. Measurements were recorded at ionic strength $I_0 = 0.065$ mol L^{-1} (a), (c) and (e) and $I_0 = 0.100$ mol L^{-1} (b), (d) and (f) and $c_{BH4} = 0.25$ mol L^{-1}, $c_{HCF} = 5*10^{-4}$ mol L^{-1} and $c_{NR} = 1.45*10^{-11}$ mol L^{-1}.

In the fit procedure for the respective series of measurements, the fit parameters were either variable (for each single measurement) or fitted as a global constant for the whole series where physically rational and possible to obtain a still satisfactory fit. As the diffusion rate is

believed to be the dominant factor in the intrinsic rate k_{NR} while k_{off} describes the off-diffusion of the product, both fitting parameters are treated equally and either both are variable or both constant for a measurement series. Two attempts in which the data were fitted to 50% and 70% conversion revealed no marked difference in the fit quality and results. Thus the results for the fits to the higher conversion of 70% are discussed here. Figure 21 and Figure 22 show the experimental data (symbols) and the obtained fits (lines) for all series of measurement. The error bars represent the standard deviation of three identical measurements of each experiment.

For the measurement series at varying nanoreactor concentration c_{NR}, all fit parameters were held constant and fitted globally. As c_{NR} is included in equation (4.24) and the reaction is catalysed on the surface of the gold nanoparticles, the fit parameters should be independent of the nanoreactor concentration. The fit results in Figure 23 (a) show that this is the case in good approximation. The obtained global fit parameters for all measurement series are given in Table 8.

Table 8: Overview of measurement and fit parameters for all series of measurement; variable parameters are depicted in Figure 23 and Figure 24.

measurement parameters					fit parameters		
c_{NR} / 10^{-12} mol L^{-1}	$c_{HCF,0}$ / mol L^{-1}	c_{BH4} / mol L^{-1}	I_0 / mol L^{-1}	T / °C	k_{NR} / 10^{10} L mol^{-1} s^{-1}	$E(P,\kappa_g)$ / 10^{-18} mol s L^{-1}	k_{off} / s^{-1}
variable	$5*10^{-4}$	0.25	0.267	20	1.24	0.402	$8.69*10^{-5}$
7.23	variable	0.25	0.296	20	variable	1.01	variable
7.23	$1*10^{-3}$	variable	0.272	20	1.19	variable	$1.25*10^{-4}$
7.23	$5*10^{-4}$	0.05	variable	20	1.52	variable	$2.22*10^{-2}$
14.5	$5*10^{-4}$	0.05	0.065	variable	variable	variable	variable
14.5	$5*10^{-4}$	0.05	0.1	variable	variable	variable	variable

For the measurement series at varying HCF concentration, the electrostatic perturbation $E(P,\kappa_g)$ was fitted globally as it should be constant at constant ionic strength and temperature. As no substantial effect of variations of the HCF concentration on the diffusion of reactants and products would be expected, the parameters k_{NR} and k_{off} were also attempted to be fitted globally. However, no good fit results were obtained, and the parameters were thus fitted individually. Figure 23 (a) and (b) reveal a clear decreasing trend with increasing HCF concentration for both fit parameters. While the increase of the off-diffusion

k_{off} could be a direct consequence of the increasing intrinsic reaction rate k_{NR}, it is not clear why the latter shows such a strong dependency on the HCF concentration. One possibility would be that the reaction is less diffusion-controlled than previously assumed. In case of a visible influence of the surface reaction rate on k_{NR}, a Langmuir effect could be observed. Strong adsorption of HCF to the gold surface could cause a substrate inhibition, visible as a decrease of k_{NR} with increasing HCF concentration. This possibility is discussed in chapter 4.4.2.4.

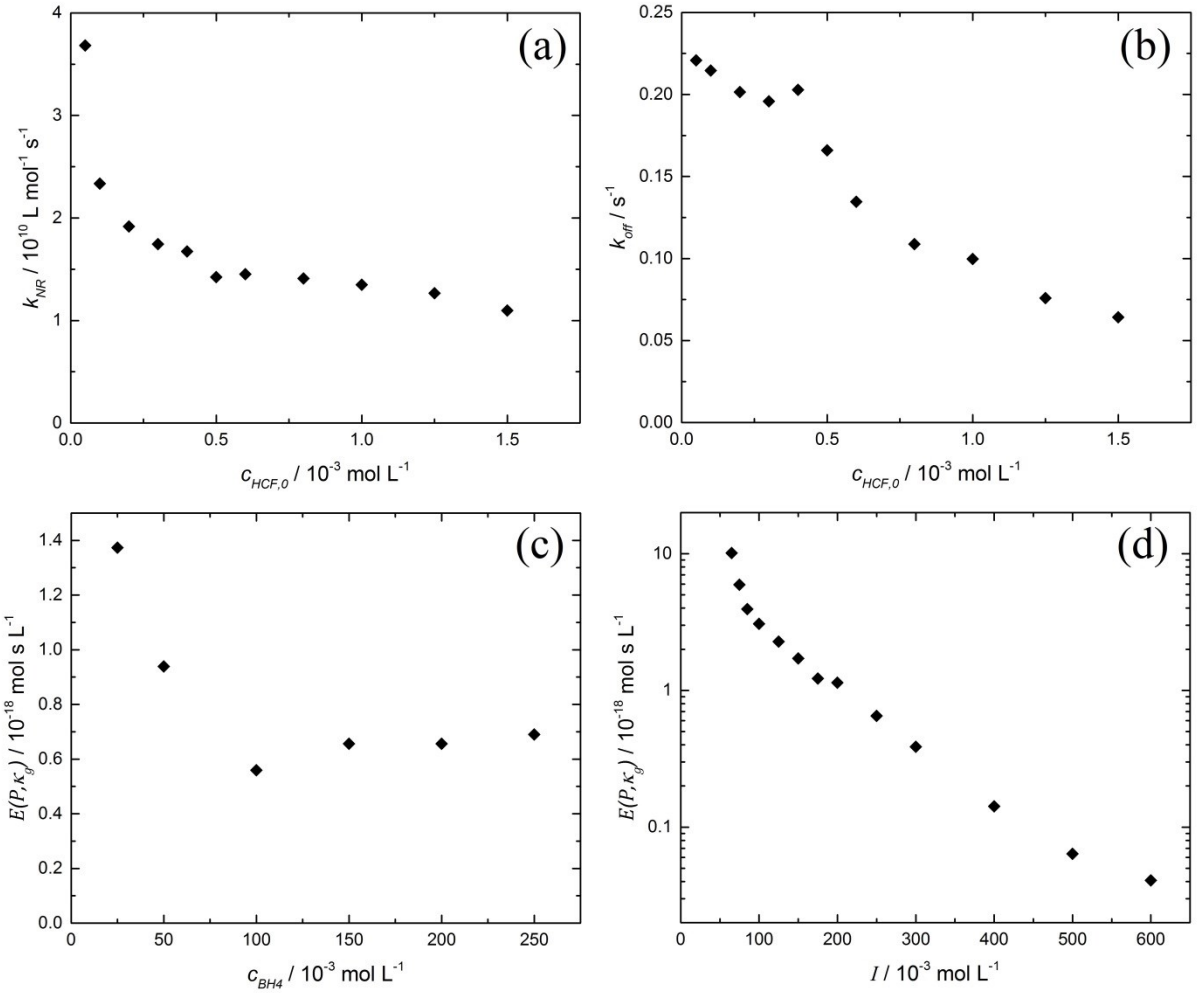

Figure 23: Results for the variable fit parameters of the measurement series at 20 °C. Intrinsic reaction rate k_{NR} (a) and off-diffusion k_{off} (b) at varying HCF concentration and electrostatic perturbation $E(P, \kappa_g)$ at varying borohydride concentration (c) and at varying ionic strength (d).

For the measurement series at varying borohydride concentration the parameters k_{NR} and k_{off} were fitted globally as all measurements were conducted at borohydride concentrations

where it is believed that the reaction is only limited by the diffusion of HCF. Thus the borohydride concentration should have no significant influence on the intrinsic reaction rate. The fit results in Figure 21 (b) confirm this assumption. However, the electrostatic perturbation had to be fitted individually, as shown in Figure 23 (c). Though the effect of the borohydride concentration on $E(P, \kappa_g)$ is moderate, it indicates that the ionic strength in the hydrogel changes with the borohydride concentration. This effect can be explained considering that the ionic strength was held constant in this series of measurement by compensating the varying borohydride concentration with NaCl. It is known that generally different ionic solutes can have different partitioning between bulk solution and a hydrogel network.[134, 207, 208] Even though the bulk ionic strength is held constant, the difference in the partition coefficients of two ionic solutes can lead to a change in the ionic strength inside the hydrogel and thus change $E(P, \kappa_g)$. This is elucidated in detail in chapter 4.4.2.5.

For the measurements at varying ionic strength, k_{NR} and k_{off} were fitted globally while $E(P, \kappa_g)$ was fitted individually. The fit results in Figure 21 (e) and (f) show that good fit results were obtained for all measurements. The dependency of $E(P, \kappa_g)$ on the ionic strength is shown in Figure 23 (d). As expected, a substantial decrease of $E(P, \kappa_g)$ is observed with increasing ionic strength. The charge of the accumulated products is screened better, and thus, the electrostatic perturbation decreases. However, the obtained values are lower than expected. Calculation of the electrostatic perturbation at bulk conditions ($P = D_{0,HCF} = 6.7*10^{-10}$m^2 s^{-1} and bulk ionic strength applied in the calculation of the inverse screening length κ_g^{-1} inside the hydrogel)[209] yields values of $E(P, \kappa_g) = 8.9*10^{-17}$ and $1.0*10^{-17}$ mol s L^{-1} for the lowest and the highest applied ionic strength of $I_0 = 0.065$ and 0.6 mol L^{-1}, respectively. The corresponding values of the fit results are $E(P, \kappa_g) = 1.0*10^{-17}$ and $4.1*10^{-20}$ mol s L^{-1} for $I_0 = 0.065$ and 0.6 mol L^{-1}, respectively. As explained in chapter 3.1.1, the permeability P inside the hydrogel usually differs from the bulk diffusivity. Due to the partitioning of ionic solutes, the ionic strength inside the hydrogel can differ from the bulk value as well. Therefore, a deviation between the fit results and the calculated bulk values was expected. However, both effects should not vary at constant temperature and can thus not explain the larger spread in $E(P, \kappa_g)$ of a factor of more than two orders of magnitude between the lowest and the highest ionic strength compared to one order of magnitude for the calculated bulk values. The reason for this could be the decreasing curvature of the measurement data with increasing ionic strength, as shown in Figure 21 (e)

and (f). The curvature is described by the denominator of equation (4.24). While at high curvature, it is no problem for the fit algorithm to find a significant value for $E(P, \kappa_g)$, this becomes problematic without a pronounced curvature, especially regarding the experimental error. This issue is addressed in more detail in chapter 4.4.2.6.

The results for the fit parameters of the two measurement series against temperature are shown in Figure 24. The intrinsic rate k_{NR} shows the expected dependency comparable to results obtained previously with thermoresponsive PNIPAM based catalysts for different model reactions catalysed by different metals.[72, 119, 125, 132] Starting from low temperatures the rate increases first up to about 20 °C, then decreases until the volume transition of the hydrogel is completed at about 35 °C, and then increases again.

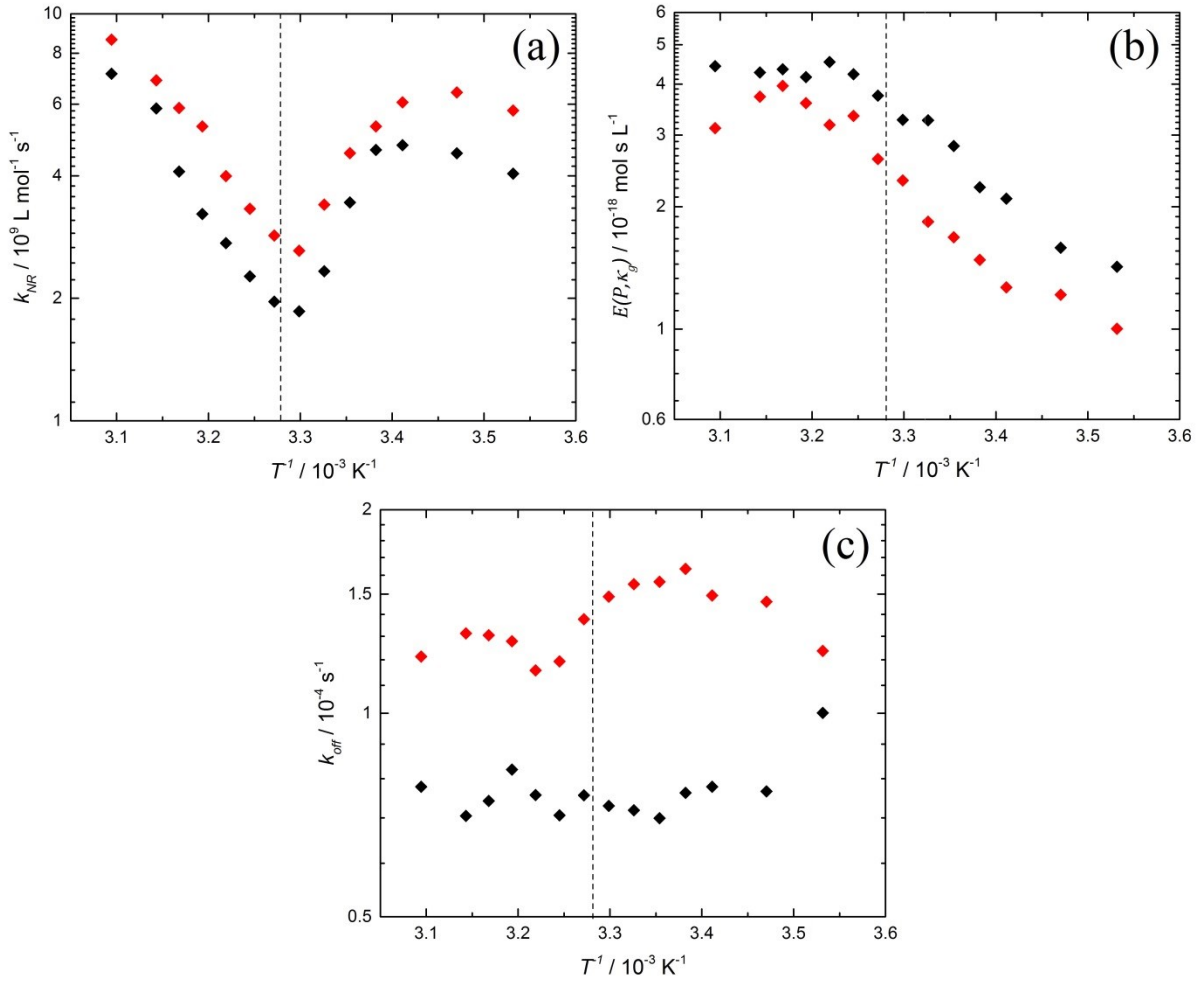

Figure 24: Results of the intrinsic reaction rate k_{NR} (a), electrostatic perturbation $E(P, \kappa_g)$ (b) and off-diffusion k_{off} (c) for the measurement series against temperature at ionic strength $I_0 = 0.065$ mol L^{-1} (black) and at $I_0 = 0.1$ mol L^{-1} (red). The dashed lines indicate the LCST of $T = 32$ °C for PNIPAM.

As expected, the intrinsic rate for the measurement series at higher ionic strength is higher. For the electrostatic perturbation $E(P, \kappa_g)$, an increasing trend with increasing temperature is found for both measurement series. This fits with the assumptions as well, considering that the hydrogel becomes more hydrophobic with increasing temperature. As a consequence, ionic solutes will be more and more excluded, and the ionic strength inside the hydrogel decreases, leading to an increase in $E(P, \kappa_g)$. Here, the measurement series at higher ionic strength yields lower values for $E(P, \kappa_g)$ throughout the whole temperature range. The obtained values for k_{off} show only slight variations where the values for the measurement series at higher ionic strength are higher, consistent with the results for k_{NR}.

The time-dependent number of accumulated product molecules $p(t)$ is calculated with equation (4.25) to fit the data with equation (4.24). Figure 25 shows the results of the obtained curves for $p(t)$ as a function of the reactant conversion exemplary for the measurement series at different HCF concentrations. The results show that the number of accumulated products increases with the available amount of HCF as expected. However, the absolute numbers are above a physically realistic regime.

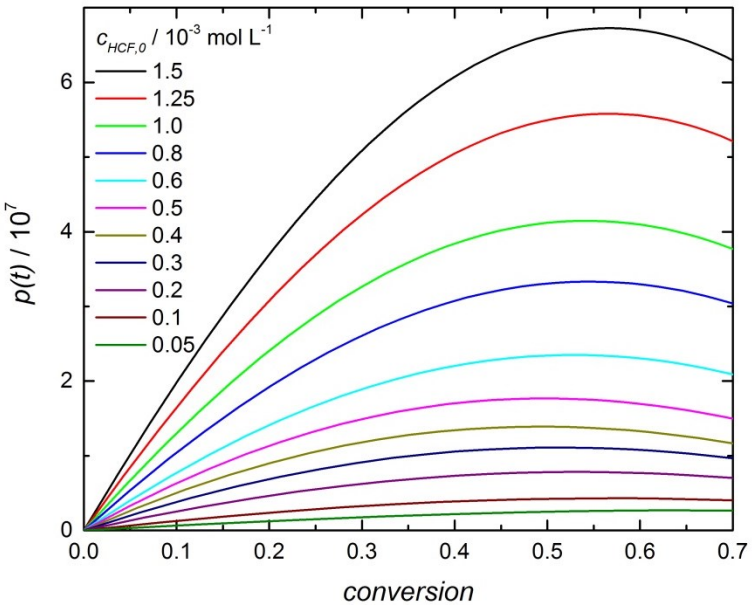

Figure 25: Curves for the number of accumulated products $p(t)$ per nanoreactor as a function of the reactant conversion for the measurement series at different HCF concentration obtained as a result of the fit procedure.

In conclusion, it can be said that the present model yields satisfactory fits and the obtained trends of the fit parameter qualitatively follow the physical expectations. However,

quantitatively the obtained values exceed physically realistic ranges in some cases. Therefore, different aspects of the present model are discussed in the following.

4.4.2.4 Calculation of the second Damköhler number

The fit results in the previous chapter revealed a substantial decrease of the intrinsic reaction rate with increasing reactant concentration. In order to verify the possibility of a Langmuir substrate inhibition effect (i.e. a decrease in the surface reaction rate due to strong adsorption of HCF) as the origin of this observation, the influence of the surface reaction rate k_{surf} on the intrinsic reaction rate k_{NR} is estimated with the second Damköhler number $DaII$. As described in chapter 3.2, $DaII$ gives the ratio of the surface reaction rate to the diffusion rate.

The difficulty upon estimating $DaII$ for the present core-shell system is that it is impossible to determine a real surface reaction rate constant k_{surf} as the reaction is either diffusion influenced or in total diffusion control. The reaction rate constant obtained by Carregal-Romero et al. with citrate stabilised gold nanoparticles is applied to circumvent this problem (which is the rate constant closest to a real surface reaction rate constant available).[124] A realistic diffusion rate valid for the present core-shell system is calculated by applying the gold surface area per unit volume S obtained with the properties of the Au@PS-PNIPAM nanoreactors and the catalyst concentration applied by Carregal-Romero et al. to obtain the abovementioned reaction rate constant. As the stagnant film thickness δ, the thickness of the hydrogel shell of the Au@PS-PNIPAM nanoreactors is applied. The values were $k_{\#} = 24.1\ \mathrm{s^{-1}}$, $n^{\#} = 1$, $S = 791.3\ \mathrm{m^{-1}}$, $\delta = 79.5{*}10^{-9}\ \mathrm{m}$ and the referenced value of $D_{HCF} = 6.7{*}10^{-10}\ \mathrm{m^2\ s^{-1}}$.[209] As a result, a value of $DaII = 3.61$ is obtained, which shows that the surface reaction rate is considerably faster than the estimated diffusion, and the reaction is in or close to diffusion control. Therefore, the reason for the dependency of k_{NR} in Figure 23 (a) is likely to be found elsewhere than in the intrinsic surface reaction rate constant k_{surf}.

4.4.2.5 The role of ion partitioning in hydrogels

The results, shown in Figure 23 (c), revealed a dependency of the electrostatic perturbation $E(P, \kappa_g)$ on the borohydride concentration at constant bulk ionic strength. In the following, it is elucidated how the difference in the partition coefficients of two ionic solutes can lead to a change in the ionic strength I_g inside the hydrogel and thus change $E(P, \kappa_g)$ while the bulk

ionic strength is constant. The model of non-ideal ion partitioning described in the following was derived in the group of Professor Dr Joachim Dzubiella as described elsewhere.[202]

In the present case, the bulk ionic strength was held constant by compensating the varying concentration of $NaBH_4$ with NaCl. As the concentration of HCF is much lower than those of $NaBH_4$ and NaCl, it is disregarded in the following. Generally, different solute species i can have different partitioning coefficients $K_{part,i}$ between bulk solution and hydrogel network.[134, 207, 208] According to equation (4.16), the ionic strength inside the hydrogel expressed by the concentrations c_i^g of the ionic solutes i inside the hydrogel is

$$I_g = \sum_i \frac{1}{2} c_i^g z_i{}^2 = \frac{1}{2}(c_+^g + c_A^g + c_B^g) \tag{4.26}$$

where the ionic species Na^+, Cl^- and BH_4^- are denoted with $i = +$, A, and B and the ion valencies are $z_+ = +1$ and $z_A = z_B = -1$, respectively. To express I_g through the bulk ion concentrations c_i, the electroneutrality condition

$$0 = \sum_i z_i c_i^g = \sum_i z_i c_i K_{part,i} e^{-z_i e\beta\phi} \tag{4.27}$$

is applied to obtain the Donnan potential ϕ as

$$e\beta\phi = -\ln \sqrt{\frac{c_A K_{part,A} + c_B K_{part,B}}{c_+ K_{part,+}}}. \tag{4.28}$$

Equation (4.28) shows that a potential between the hydrogel and bulk solution appears only if the partition coefficients of the ionic species differ. This is similar to the classic case where the impermeability of a membrane for certain species causes an unequal charge distribution and thus a Donnan potential. In the present case, an unequal charge distribution at the hydrogel-bulk interface is caused by the different partition coefficients of the particular ion species instead of a semipermeable membrane. With the expression

$$c_i^g = c_i K_{part,i} e^{-z_i e\beta\phi} \tag{4.29}$$

for the solute concentrations inside the hydrogel and equation (4.28), the ionic strength inside the hydrogel is derived as

$$I_g = \sqrt{c_+ K_{part,+}\left(c_A K_{part,A} + c_B K_{part,B}\right)}. \tag{4.30}$$

The expressions for bulk electroneutrality ($c_+ = c_A + c_B$) and -ionic strength

$$I_0 = \frac{1}{2}(c_+ + c_A + c_B) \tag{4.31}$$

are applied to express the ionic strength inside the hydrogel through the bulk ionic strength I_0 and -borohydride concentration c_B to arrive at

$$I_g = \sqrt{I_0 K_{part,+}\left[I_0 K_{part,A} + \left(K_{part,B} - K_{part,A}\right)c_B\right]}. \tag{4.32}$$

This shows that at constant bulk ionic strength the ionic strength inside the hydrogel still varies with varying bulk borohydride concentration c_B if the partition coefficients for borohydride and chloride differ. In the present case, a decrease in $E\left(P, \kappa_g\right)$ is observed with increasing borohydride concentration which means that the ionic strength is increasing. Therefore, $K_{part,B} > K_{part,A}$, i.e. borohydride is expected to have a higher affinity to the hydrogel than chloride at $T = 20$ °C.

4.4.2.6 Critical view on the kinetic model and fit results

The results for the electrostatic perturbation $E\left(P, \kappa_g\right)$ in Figure 23 (d) revealed a decrease over two orders of magnitude with increasing ionic strength which is much larger than expected. As mentioned in chapter 4.4.2.3, the reason for this could originate in the fit algorithm itself and the underlying equations (4.24) and (4.25). The following consideration shall help to get a better understanding of how the coupled differential equations intertwine to fit the data and where difficulties with the fit procedure/results arise.

The numerator of equation (4.24) describes the concentration-time dependency of a first order reaction (i.e. a linear dependency in the logarithmic concentration-time plots shown in Figure 21 and Figure 22). If we now consider the beginning of each reaction, it is clear that at $t = 0$ the number of accumulated products is still zero and equation (4.22) simplifies to

$$\left(\frac{dc_{HCF}}{dt}\right)_{t=0} = -k_{NR}\, c_{NR}\, c_{HCF}. \tag{4.33}$$

This means that $k_{NR}c_{NR}$ corresponds to the initial slope of the logarithmic concentration-time plots. The denominator comprises the term $p(t)E\left(P, \kappa_g\right)$ to account for the decrease in the slope (i.e. a decreasing reaction rate due to electrostatic product inhibition). The value of $p(t)$

is described by the second differential equation (4.25) where the fitting parameter k_{off} modulates $p(t)$. If k_{off} is increased, $p(t)$ will decrease (more precisely: the maximum of the curve will be lower and shift to earlier times). However, this can be compensated by an increase in the fit parameter $E(P, \kappa_g)$. Of course, this scenario is limited as the shape of the $p(t)$ curve will also change if k_{off} is varied but it makes the set of equations vulnerable to minor changes in the shape of experimental data which may lead to the mathematically best, but not necessarily to physically meaningful fit parameters.

This scenario becomes increasingly problematic for curves which are approaching linearity in the logarithmic concentration-time plots, e.g. with increasing ionic strength. Here it is virtually impossible for the algorithm to arrive at meaningful values for $E(P, \kappa_g)$ and k_{off}. Considering that all data additionally have a particular experimental error, it becomes clear that the present model may over-interpret the data basis and therefore yield distorted trends for the resulting fit parameters.

Another potential source of error with the present model could be seen in the assumption of an entirely reactive nanoreactor core. Though most of the gold nanoparticles are located close to the core surface, the total gold surface area is much smaller than the total core surface. A stationary state model is derived in the following to circumvent these issues and still preserve the underlying model of electrostatic product inhibition and assertions thereof.

4.4.3 Kinetic analysis of the stationary state

To circumvent the issues of the time-dependent analysis in chapter 4.4.2, a time-independent stationary-state model is derived which only evaluates the reaction rate constant after the stationary state is reached. This way the electrostatic effects can be evaluated while circumventing the curvature problem of the previous model. The first order reaction rate constant k_1 of the stationary state is derived as the slope of the stationary state regime in the logarithmic concentration-time curves as shown by the dashed red line in Figure 19 (b) according to equation (1.6).

4.4.3.1 Kinetic model

The number of accumulated products of the previous time-dependent model is now regarded as constant (i.e. $dp_{ss}/dt = 0$) to arrive at a time-independent stationary state model for the reaction rate. The total reaction rate constant of the stationary state $k_{on,ss}$ can be expressed as

$$k_{on,ss}^{-1} = k_{NR,ss}^{-1} + p_{ss}\, E\big(P, \kappa_g\big). \tag{4.34}$$

The time-independent number of accumulated products of the stationary state p_{ss} can be expressed (without the necessity of a second differential equation) as the ratio of the rates of product formation $k_{on,ss}$ (multiplied by the reactant concentration $c_{HCF,0}$) and off-diffusion $k_{off,ss}$ according to

$$p_{ss} = \frac{k_{on,ss}}{k_{off,ss}}\, c_{HCF,0}. \tag{4.35}$$

If the electrostatic perturbation $E\big(P, \kappa_g\big)$ is assumed to be weak, $k_{on,ss}$ can be approximated by

$$k_{on,ss} \cong k_{NR,ss}, \tag{4.36}$$

and the number of accumulated products is obtained as

$$p_{ss} \cong \frac{k_{NR,ss}}{k_{off,ss}}\, c_{HCF,0}. \tag{4.37}$$

Therefore, equation (4.24) of the previous model is now obtained as

$$\frac{dc_{HCF}}{dt} = -k_{on,ss}\, c_{NR}\, c_{HCF} = -\frac{k_{NR,ss}\, c_{NR}}{1+\frac{(k_{NR,ss})^2}{k_{off,ss}}\, c_{HCF,0}\, E(P,\kappa_g)}\, c_{HCF} = -k_{th} c_{HCF}. \tag{4.38}$$

Equation (4.38) is based on the assumption of an entirely reactive nanoreactor core. However, not the full nanoreactor core surface is reactive but only the surface of the gold nanoparticles which are partially covering it.

Therefore, the real rate constant is by an efficiency factor f_{eff} (see next chapter) lower than predicted by the theoretical reaction rate constant k_{th}. The latter is scaled by f_{eff} to connect it to the experimentally determined rate constant k_1 according to

$$f_{eff} k_{th} = k_1 S, \tag{4.39}$$

which yields the full theoretical expression

$$k_1 = \frac{f_{eff}}{S} \left(\frac{k_{NR,ss}\, c_{NR}}{1 + \frac{(k_{NR,ss})^2}{k_{off,ss}} c_{HCF,0} E(P, \kappa_g)} \right). \tag{4.40}$$

The efficiency factor f_{eff} is calculated based on a model describing the diffusion rate to a spherical particle with radius R covered with N circular receptors with radius a on its surface.[210, 211] Here, the term receptor is to be understood generally as a drain of any kind (e.g. particles disappearing upon reaction at a catalyst surface). The model accounts for the geometric aspects of diffusion in such system, and the effective rate constant is obtained as

$$k_E = k_{SM} \frac{Na}{Na + \pi R \left(1 - \frac{N\pi a^2}{4\pi R^2}\right)} \tag{4.41}$$

Equation (4.41) was shown to agree well with Brownian dynamics simulations of the system taking account for the competition between receptors.[212] Obviously, the geometry of flat discs on a spherical surface differs from the present system of spherical gold nanoparticles surrounding the nanoreactor core. However, the reaction was shown to be in or close to the diffusion limit of HCF. Therefore, applying the above geometry is reasonable. The reactants diffuse to the gold nanoparticle surface from outside the nanoreactor and are transformed to products quickly. From the perspective of a reactant in bulk, the gold nanoparticles at the nanoparticle core surface appear as discs, acting as drains for the reactants. Additionally, the gold nanoparticles are much smaller than the nanoreactor core and mostly located close to the core surface. Therefore, the diffusional flux will predominantly arrive at the gold nanoparticles coming from the solid angle hemisphere pointing away from the nanoreactor core surface as it would be the case for flat discs on a sphere. As the kinetic model is based on the Debye-Smoluchowski diffusion rate to a spherical particle, the efficiency factor is included according to

$$f_{eff} = \frac{Na}{Na + \pi R \left(1 - \frac{N\pi a^2}{4\pi R^2}\right)}. \tag{4.42}$$

Applying the gold nanoparticle radius r_{Au} for a, the nanoreactor core radius R_{core} for R, and the number of gold nanoparticles in one nanoreactor N_{NP} for N yields a value of f_{eff} = 0.576.

Corresponding to the full kinetic model shown previously, k_{th} comprises the three fit parameters $k_{NR,ss}$, $E(P,\kappa_g)$, and $k_{off,ss}$. Based on the findings of the full kinetic model and equation (3.19), $E(P,\kappa_g)$ and $k_{NR,ss}$ are replaced by the physically more essential parameters P, $K_{part,B}$, and k_{surf}, yielding a total number of four fit parameters (together with $k_{off,ss}$).

According to equation (4.21), the electrostatic perturbation $E(P,\kappa_g)$ is a function of the permeability P of the hydrogel network for HCF and the inverse screening length κ_g inside the hydrogel. The latter is, according to equation (3.21), a function of the ionic strength I_g inside the hydrogel. The results in chapter 4.4.2.5 show that I_g can be expressed as a function of the bulk ionic strength I_0, the borohydride concentration c_{BH4}, and the partitioning coefficients $K_{part,+}$, $K_{part,A}$, and $K_{part,B}$ according to equation (4.32). Kawasaki et al. measured the temperature-dependent partition coefficient for NaCl in a PNIPAM hydrogel.[197] The obtained values are in accordance with simulations of Milster et al. and Kanduč et al., both, for the swollen as well as the collapsed state of PNIPAM.[143, 213, 214] Therefore, the experimental values are applied for $K_{part,A} = K_{part,+}$. Together with the bulk ionic strength and borohydride concentration from the experiments, the only undetermined parameters in $E(P,\kappa_g)$ are now P and $K_{part,B}$.

The diffusion rate constant to a single sphere inside a hydrogel is given in chapter 3.2.2.1. As the time-independent model accounts for the partial coverage of the PS core with gold nanoparticles through the efficiency factor f_{eff}, equation (3.19) can be applied. With the experimentally determined radii R_{core}, R_{shell}, and the bulk diffusion coefficient of HCF $D_0(20\,°C) = 7.15*10^{-10}$ m^2 s^{-1}, only P and k_{surf} are left as undetermined parameters in the intrinsic reaction rate constant $k_{NR,ss}$.

4.4.3.2 Fit algorithm

The data are fitted with equation (4.40), applying the fit parameters P, K_B, k_{surf}, and $k_{off,ss}$. The data were fitted with Anaconda suite and with the help of Arne Ronneburg. The genetic fit algorithm is described in chapter 4.3.3.[215] Other than for the time-dependent analysis, no spline interpolation of the experimental data is necessary, and no conversion limit needs to be defined for the fit algorithm shown in Figure 12. For the fit with a combination of global and individual fit parameters (fit against temperature), the description in chapter 4.4.2.2 applies.

For the time-independent fits, the mutation cycle applies an additional recombination step. Therefore, the 200 best parameter sets s_j^* are submitted to the mutation cycle. Prior to the mutation step, the fit parameter values of the parameter sets are randomly recombined. The target function is given as

$$\varepsilon_k(s_j) = \frac{1}{N_{exp}} \sum_1^{N_{exp}} \left(\frac{|k_{1,exp} - k_{1,fit}(s_j)|}{k_{1,exp}} \right) \tag{4.43}$$

where N_{exp} is the number of experimental data points which were fitted simultaneously, and $k_{1,exp}$ and $k_{1,fit}$ are the experimental and fitted values of the surface-normalised rate constant, respectively. The mutation cycle is repeated until the relative deviation between the target functions is below 10^{-9}.

4.4.3.3 Fit results

As equation (4.40) accounts for the experimental concentrations of HCF, borohydride, as well as ionic strength, the experimental dependencies of k_1 on all three parameters are fitted in one global fit. Figure 26 shows the experimentally obtained dependencies of the first order rate constants (symbols). Against HCF concentration, a substantial decrease is observed between $c_{HCF,0} = 5*10^{-5}$ and $1.5*10^{-3}$ mol L^{-1} while k_1 increases with increasing borohydride concentration and ionic strength. This coincides with the time-dependent data shown previously. The fit results in Figure 26 (lines) show that a satisfactory fit quality is obtained against HCF and borohydride concentration, however, the fit against ionic strength can only qualitatively describe the experimental data.

The obtained fit parameters are $P = 6.41*10^{-11}$ m^2 s^{-1}, $K_B = 2.82$, $k_{surf} = 6.59*10^{14}$ L mol^{-1} s^{-1}, and $k_{off,ss} = 4.4*10^4$ s^{-1}. This means that the permeability of the PNIPAM hydrogel for HCF is ~ 9% of its bulk diffusion coefficient. The partitioning of borohydride is larger than for NaCl as predicted in chapter 4.4.2.5 based on the results of the time-dependent analysis. This means that the ionic strength inside the hydrogel is indeed increasing with increasing borohydride concentration (at constant bulk ionic strength). Thus, the decreasing screening length of the electrostatic repulsion is the reason for the increasing reaction rate constant, both, against borohydride concentration and bulk ionic strength.

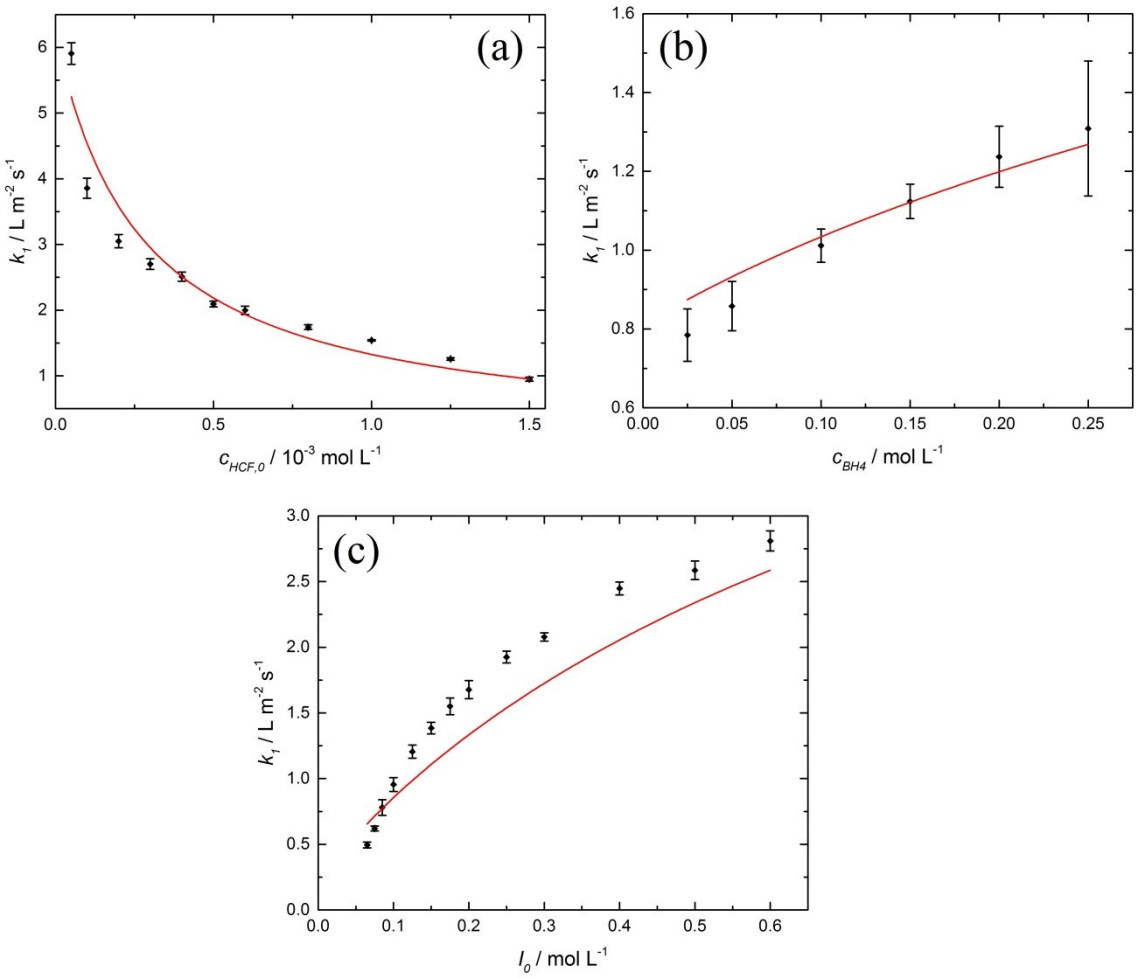

Figure 26: Surface-normalised first order rate constants k_1 (symbols) and fit (lines) of the kinetic model (all measurements were conducted at $c_{NR} = 7.23*10^{-12}$ mol L^{-1}). Reaction rate measurements at different HCF concentrations (a), measured at $c_{BH4} = 0.25$ mol L^{-1}, $I_0 = 0.296$ mol L^{-1}; at different borohydride concentration (b), measured at $c_{HCF,0} = 1*10^{-3}$ mol L^{-1}, $I_0 = 0.272$ mol L^{-1}; and at different ionic strength (c), measured at $c_{BH4} = 0.05$ mol L^{-1}, $\boldsymbol{c_{HCF,0}} = 5*10^{-4}$ mol L^{-1}.

With the fit parameter P the diffusion rate constant k_D can be calculated according to equation (3.19) as $k_D = 6.09*10^{10}$ L mol^{-1} s^{-1}. This shows that the diffusion rate is almost four orders of magnitude lower than the surface reaction rate, and the reaction is in full diffusion control as expected from the calculation of $DaII$ and shown previously.[125, 126] With equation (4.37) and $k_{off,ss}$, the number of accumulated products can be calculated. At the lowest and highest HCF concentration of $c_{HCF,0} = 5*10^{-5}$ and $1.5*10^{-3}$ mol L^{-1}, values of $p_{ss} = 69$ and 2077 are obtained, respectively. The decrease of the reaction rate constant is, therefore, a consequence of the increasing number of accumulated products which repel the reactants. The number of accumulated products corresponds to a product concentration of

~ 19% relative to the reactant concentration (if the whole shell volume is applied as reference volume to calculate a concentration). This value can be considered to be in a physically realistic regime, even if the products accumulate only in a fraction of the shell volume as expected based on the model described in chapter 4.4.1.

For the evaluation of the measurements against temperature, several temperature-dependent input parameters for the kinetic model are required. The bulk diffusion of HCF is derived with the Stokes-Einstein equation

$$D_0(T) = \frac{k_B T}{6\pi\eta(T) r_{HCF}} \tag{4.44}$$

where $r_{HCF} = 0.3$ nm is the approximate radius of the hexacyanoferrate(III) ion[125, 126] and $\eta(T)$ is the dynamic viscosity of water.[216] The experimentally determined values for the partition coefficient of NaCl determined by Kawasaki et al. (applied for $K_{part,A} = K_{part,+}$) are interpolated with a sigmoidal fit, as shown by the dashed red line in Figure 16. According to Kanduč et al., the partitioning does not significantly depend on the type of ion as their specific character is shielded by the (strongly bound) hydration shell. As no experimental values for the partition coefficient of borohydride are available, assuming a similar behaviour as for NaCl is a favourable approach compared to assuming the partition ratio to be temperature independent. Obviously, borohydride is not a small, simple ion as, e.g. chloride, but it is a monovalent ion with a symmetric charge distribution. Therefore, $K_{part,B}$ is coupled to $K_{part,A} = K_{part,+}$, based on the ratio of the partition coefficients according to

$$K_{part,B}(T) = \frac{K_{part,B}(20\,°C)}{K_{part,A}(20\,°C)} K_{part,A}(T), \tag{4.45}$$

where $K_{part,B}(20\,°C)$ is the value obtained from the fit at $T = 20$ °C.

The diffusion rate $k_{off,ss}$ at which the reaction products leave the nanoreactor is fitted with an Arrhenius dependency, anchored with the value $k_{off,ss}(20\,°C)$ obtained from the fit in the previous chapter according to

$$k_{off,ss}(T) = k_{off,ss}(20\,°C) e^{\frac{E_A}{R}\left(\frac{1}{T=293.15K} - \frac{1}{T}\right)}. \tag{4.46}$$

The results of the fits at $T = 20$ °C show that $k_{surf} \gg k_D$, therefore k_{surf} does not influence $k_{NR,ss}$ and is kept as temperature-independent parameter with the value obtained at

$T = 20$ °C. With these prerequisites, the only free (fit) parameters are the activation energy of $k_{off,ss}$ (fitted globally) and the permeability P (fitted individually at each temperature).

Figure 27 (a) shows the Arrhenius plot of the experimental rate constants (symbols) for two series of measurements obtained at different ionic strength. The data show the typical non-Arrhenius dependency which has been found repeatedly for this type of PNIPAM based nanoreactor catalysts.[119, 125, 132] The fit (lines) shows that the data can be fitted successfully at high temperatures; however, below $T = 20$ °C, the fit deviates significantly from the data measured at $I_0 = 0.1$ mol L^{-1}.

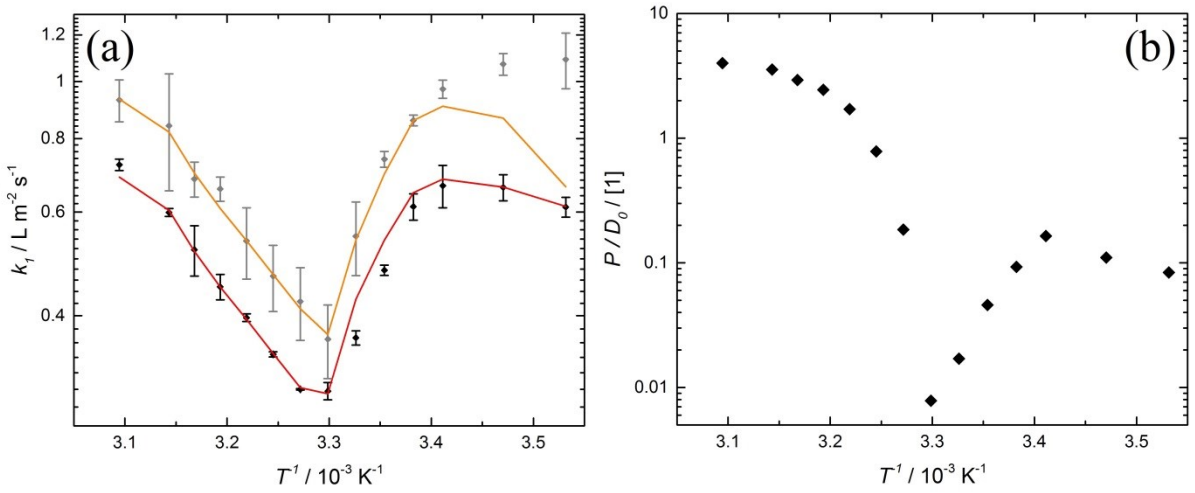

Figure 27: Arrhenius plots of the experimental reaction rate constant k_1 (symbols) and fit (lines) of the kinetic model (a) and obtained permeability of HCF (b) normalised to the temperature-dependent bulk diffusion coefficient D_0. Measurements were conducted at $c_{NR} = 1.45*10^{-11}$ mol L^{-1} $c_{BH4} = 0.05$ mol L^{-1}, $c_{HCF,0} = 5*10^{-4}$ mol L^{-1} and $I_0 = 0.064$ (black, red) and 0.1 mol L^{-1} (grey, orange).

Figure 27 (b) shows the obtained temperature dependence of the permeability of HCF normalised to its bulk diffusion. The data resemble the temperature dependency of the reaction rate with a minimum around the LCST and a general increasing trend with increasing temperature. Considering that $P = K_{part,HCF} D_g$ and $D_g \leq D_0$, it is clear that Figure 27 (b) shows the lower limit for the partition ratio of HCF ($P/D_0 = K_{part,HCF}$ if $D_g = D_0$). This means that in contrast to NaCl, the partition ratio of HCF increases with increasing temperature. As the diffusion coefficient inside the hydrogel will additionally decrease upon the collapse of the PNIPAM hydrogel, it can be expected that the increase of the partition ratio with increasing temperature will be even more pronounced than shown in Figure 27 (b).

Kanduč et al. showed that for larger molecular ions such as nitrophenolate the partition ratio increases (with increasing temperature) to values of 10 to 30 (or even 10^3 at higher ionic strength).[143, 214] It can, therefore, be assumed that for HCF, the molecular properties dominate over its ionic nature regarding the partition ratio in PNIPAM and the obtained values for the permeability are in a physically conceivable regime.

The obtained activation energy for $k_{off,ss}$ is $E_A = 3.03$ kJ mol^{-1}. As $k_{off,ss}$ describes the diffusion of the reaction product out of the nanoreactor, an activation energy in the regime of thermal energy is realistic (3.03 kJ mol^{-1} correspond to 1.24 $k_B T$ at $T = 20$ °C). Due to the low activation energy, $k_{off,ss}$ increases only by ~ 17% between $T = 10$ and 50 °C.

Overall the above analysis yields satisfactory results with only three relevant and physically meaningful fit parameters at $T = 20$ °C (k_{surf} has no influence as $k_{surf} \gg k_D$ and therefore $k_{NR} \cong k_D$), and only two fit parameters in the fit against temperature, all yielding physically reasonable values. All other parameters are either referenced or directly measured experimental values (or reasonably related to other experimental values where no direct experimental values are available). Although several effects which would complicate the model too much are not accounted for (like electrostatic reactant-reactant and reactant-product interactions or crowding effects near the catalytically active gold surface), the model shows how the complex interplay of geometric, diffusive, electrostatic and hydrogel specific effects influence the reaction kinetics in thermoresponsive nanoreactors. The newly developed rate theory[202] draws a comprehensive picture and shows that electrostatic effects play a significant role in the kinetics of diffusion-controlled reactions in hydrogels indeed.

5. Summary

This thesis comprises three parts.

The first part gives a comprehensive literature survey of mechanistic studies of the nitroarene reduction mechanism and kinetic studies of the 4-nitrophenol reduction with the focus on gold and silver catalysts. The mechanistic investigations reveal that for gold, silver, palladium and platinum the reaction follows the direct route of the Haber reaction scheme while for other metals (e.g. nickel) the reaction partly follows the condensation route. Overall the precise mechanism is highly sensitive to combinations of catalyst metal, nitroarene substituents, solvent and reaction conditions.
For the aqueous reduction of 4-nitrophenol, indications are found that the last step of the reduction from hydroxylaminophenol to aminophenol is rate-determining on gold while on silver it is the first reaction step.
The review of kinetic studies shows that isosbestic points in the UV-Vis spectra are found with a higher probability with silver- than with gold catalysts, supporting the hypothesis of a difference in the rate-determining step between gold and silver.

In the second part, the kinetics of the reduction of 4-nitrophenol on silver nanoparticles embedded in thermoresponsive core-shell nanoreactors comprising of a PS core and a PNIPAM shell is investigated. The deconvolution of the UV-Vis spectra reveals the direct conversion of the reactant to the product and the absence of intermediates in the reaction mixture, supporting the hypothesis of a rate-determining first reaction step. A modified kinetic model is derived, based on the kinetic model applied successfully for the reduction on gold catalysts. The model fits the data satisfactorily at low conversions but increasingly deviates at higher conversions. Analysis of the relative deviation between experimental data and fit indicates that the adsorption of the reaction product to the catalyst surface, not accounted for in the model, could be the reason for the deviation. The kinetic investigation of the influence of temperature discloses the typical non-Arrhenius dependency of the reaction rate, coinciding with previous results for PNIPAM based thermoresponsive catalysts. The Van't Hoff analysis of the adsorption constant of borohydride reveals that the partition ratios of the reactants are relevant parameters for the kinetic model. In conclusion, the analysis shows that the kinetic model derived for gold can be simplified in the present case as a stationary state is present from the very beginning of the reaction onwards.

In the third part, the reduction of hexacyanoferrate(III) by gold nanoparticles embedded in thermoresponsive core-shell nanoreactors comprising of a PS core and a PNIPAM shell is investigated. The kinetic measurements reveal a strong dependency on the ionic strength and an inhibition effect increasing with the reactant concentration. Based on these observations, a new kinetic model for diffusion-controlled reactions in thermoresponsive hydrogels, accounting for effects of the hydrogel, the catalyst geometry, diffusion, and electrostatic effects, is described. Due to the fast diffusion-controlled kinetics, the reaction product accumulates inside the hydrogel, repels the reactant and decreases the reaction rate.

The full kinetic analysis reveals the limitations of the model and the influence of ion partitioning inside the hydrogel. Even at constant bulk ionic strength the ionic strength inside the hydrogel is changing upon replacement of one ion species by another with a different partition coefficient.

Based on this, a refined, stationary state model, circumventing the limitations of the previous model, is derived and applied successfully. The results show that the reaction rate is increasing with increasing ionic strength because the charge of the accumulated products are screened better whereas the rate is decreasing with increasing reactant concentration due to the increasing accumulation of products. The activation energy for the diffusion of reaction products is found to be in the regime of thermal activation. The permeability of the reactant shows a minimum around the LCST of PNIPAM while it is generally increasing with increasing temperature, pointing to a strong affinity to the hydrogel at elevated temperatures.

With only three relevant and physically meaningful fit parameters, the kinetic model draws a comprehensive picture and shows that electrostatic effects play a significant role in the kinetics of diffusion-controlled reactions in hydrogels.

6. Experimental

6.1 Materials

Table 9: List of chemicals used for synthesis and kinetic measurements.

substance	**company**	**(purity)**	***MW*** **/ g mol^{-1}**
4-aminophenole	Merck	(≥ 99%)	109.13
2,2'-azobis(2-amidinopropane)-dihydrochloride (V50)	Fluka	(≥ 98%)	271.19
BHT inhibitor remover	Sigma-Aldrich		
borax buffer (pH = 10.0 @ 20 °C)	Roth		
4,4'-dihydroxyazobenzene	TCI	(≥ 98%)	214.22
gold(III)chloride trihydrate	Sigma-Aldrich	(≥ 99.9%)	393.83
hexadecyl-trimethyl-ammonium-bromide (CTAB)	Sigma-Aldrich	(≥ 99%)	364.45
N-isopropylacrylamide	Sigma-Aldrich	(≥ 97%)	113.16
N,N'-methylenebisacrylamide (Bis)	Sigma-Aldrich	(99%)	154.17
4-nitrophenol	Sigma-Aldrich	(≥ 99%)	139.11
4-nitrosophenol	TCI	(~ 40% H_2O)	123.11
potassium hexacyanoferrate (II)	Sigma Aldrich	(99%)	422.39
potassium hexacyanoferrate (III) (HCF)	Sigma Aldrich	(99%)	329.24
potassium persulfate (KPS)	Fluka	(≥ 99%)	270.32
silver nitrate	Fluka	(≥ 99.5%)	169.88
sodium borohydride	Acros	(99%)	37.83
sodium chloride	Merck	(99.5 %)	58.44
sodium dodecyl sulfate (SDS)	Sigma-Aldrich	(≥ 99%)	288.37
sodium hydroxide	Grüssing	(99%)	40.00
styrene (stab. with 250 ppm BHT)*	Sigma-Aldrich	(≥ 99%)	104.15

*Styrene was run over a column packed with inhibitor remover prior to use.

6.2 Synthesis and preparation

6.2.1 Preparation of 4-nitrosophenol

4-Nitrosophenol (water content ~ 40%) was purified according to a modified literature procedure:[217] After drying in vacuum at $T = 40$ °C overnight, the raw material was dissolved in anhydrous diethyl ether. The insoluble residue was filtered off, and the remaining water was removed over a molecular sieve (mesh size = 4 Å) overnight. After removing the ether, the crude product was redissolved in dry ether (20 g L^{-1}), and a green solution was obtained. Upon adding the 2.5-fold volume of dry hexane to the solution, orange crystal needles precipitated, were filtered off, dried in vacuum and stored at $T = 4$ °C.

6.2.2 Preparation of metal@PS-PNIPAM nanoreactors

The synthesis of the nanoreactors was carried out as described previously.[132, 156] Two types of core-shell nanoreactors have been prepared. The nanoreactors comprise of a polystyrene (PS) core surrounded by a hydrogel shell of poly-*N*-isopropylacrylamide (PNIPAM) in which silver and gold nanoparticles were immobilised, respectively. The nanoreactors with silver nanoparticles as the active catalyst metal (Ag@PS-PNIPAM) comprise negatively charged PS core particles (APS). In contrast, the nanoreactors with gold nanoparticles as the active catalyst metal (Au@PS-PNIPAM) comprise positively charged PS core particles (CPS). All syntheses of the PS cores, the CPS growth process and the PNIPAM shells were carried out in 500 ml triple-neck flasks equipped with an overhead stirrer with a moon-shaped stirrer blade, a reflux condenser and an additional opening to add the reactants. Mass concentrations c_m were calculated from the solid fraction, assuming a density of $\rho_t = 1*10^6$g m^{-3} for all particle dispersions.

6.2.2.1 Preparation of polystyrene core particles

The PS core particles were prepared by emulsion polymerisation. A mixture of the surfactant (CTAB for CPS and SDS for APS, respectively), styrene and NIPAM, dissolved in 250 ml H_2O, was stirred for 5 minutes and heated to $T = 80$ °C. After the reaction reached the desired temperature, the initiator (V50 for CPS and KPS for APS, respectively), dissolved in 20 ml H_2O, was added and the mixture was stirred at 250 rpm for 8 hours. Subsequently, the reaction was cooled down to room temperature and filtered over glass wool. Purification was

done by ultrafiltration until the permeate reached a conductivity of $\sigma \leq 30$ µS cm^{-1}. The amounts of reactants applied for the respective particles, the hydrodynamic particle radii r_H and the mass concentration c_m of the purified suspensions are given in Table 10.

Table 10: Applied amount of reactants, mass concentration of the product suspensions and hydrodynamic radii r_H of the obtained particles.

	APS	CPS
$m_{styrene}$ / g	30	30
m_{NIPAM} / g	1.63	1.63
m_{CTAB} / g	-	0.2
m_{V50} / g	-	0.3
m_{SDS} / g	0.45	-
m_{KPS} / g	0.3	-
V_{H2O} / L	0.27	0.27
r_H / nm	53	30
c_m / g L^{-1}	67.6	90.6

6.2.2.2 Polystyrene core – growth process

For the CPS core particles, it was necessary to grow the particles obtained after the synthesis described in the previous chapter. V50 (0.3 g; dissolved in 20 ml H_2O) was added to a suspension of the precursor CPS core particles (1.58 g) in 210 ml H_2O, mixed for 5 minutes and heated to $T = 80$ °C. After the desired temperature was reached, NIPAM (1.63 g; dissolved in 30 ml H_2O) and styrene (30 g) were added simultaneously over 5 hours with two syringe pumps at a rate of 6 ml h^{-1} while stirring at 250 rpm. Subsequently, the mixture was stirred for another 3 hours at $T = 80$ °C before cooling down and filtering over glass wool. Purification was done by ultrafiltration until the permeate reached a conductivity of $\sigma \leq 2$ µS cm^{-1}. The obtained particles had a hydrodynamic radius of $r_H = 71$ nm and the mass concentration of the purified particle suspension, denoted CPS2, was $c_m = 49.3$ g L^{-1}.

6.2.2.3 Preparation of the PNIPAM shell

The core-shell particles were prepared by seeded emulsion polymerisation. A mixture of the precursor core particle solution, NIPAM, Bis and additional water was stirred for 15 minutes to guarantee complete dissolution of the monomer and crosslinker. After that the mixture was heated to $T = 80$ °C, the initiator (V50 for CPS and KPS for APS, respectively), dissolved in

20 mL H_2O, was added, and the reaction was stirred at 250 rpm for 4.5 hours. Then the reaction was cooled down to room temperature and filtered over glass wool. Purification was done by ultrafiltration until the permeate reached a conductivity of $\sigma \leq 2$ µS cm^{-1}. The amount of reactants applied for the respective particles, and the mass concentration c_m of the purified suspensions are given in Table 11.

Table 11: Applied amount of reactants and mass concentration of the product suspensions.

	APS-PNIPAM	CPS-PNIPAM
m_{APS} / g	1.92	-
m_{KPS} / g	0.3	-
m_{CPS2} / g	-	4.93
m_{V50} / g	-	0.193
m_{NIPAM} / g	2.10	5.37
m_{Bis} / g	0.072	0.184
V_{H2O} / L	0.14	0.16
c_m / g L^{-1}	4.2	15.3

6.2.2.4 Preparation of metal nanoparticles inside the PNIPAM shell

The metal precursor ($AgNO_3$ and $H[AuCl_4]$ dissolved in 30 ml and 20 ml H_2O, respectively) was added dropwise to the core-shell particles, suspended in 260 (APS-PNIPAM) and 460 ml H_2O (CPS-PNIPAM), over 30 minutes, respectively. After stirring for another 2 hours, the mixture was degassed with nitrogen for 30 minutes and cooled with an ice bath. $NaBH_4$ was dissolved in 20 mL H_2O and added dropwise over 30 minutes. Subsequently, the reaction was stirred for another 30 minutes before the ice bath was removed. After warming to room temperature, the mixture was filtered over glass wool and cleaned by ultrafiltration until the permeate reached a conductivity of $\sigma \leq 1$ µS cm^{-1}. Table 12 shows the applied amounts of reactants and the mass concentration c_m of the final, purified nanoreactor suspension.

Table 12: Applied amount of reactants and mass concentration of the product suspensions.

	Ag@PS-PNIPAM	Au@PS-PNIPAM
$m_{APS-PNIPAM}$ / 10^{-3} g	300	-
$m_{CPS-PNIPAM}$ / 10^{-3} g	-	500
m_{AgNO_3} / 10^{-3} g	45	-
$m_{H[AuCl_4]}$ / 10^{-3} g	-	50
m_{BH4} / 10^{-3} g	60	100
V_{H2O} / L	0.31	0.50

	Ag@PS-PNIPAM	Au@PS-PNIPAM
c_m / g L^{-1}	0.194	0.738

6.2.2.5 Ultrafiltration

Ultrafiltration was performed to remove residual reactants and free polymer chains from the nanoparticle dispersions. Therefore, the raw product was filled in 500 mL and 100 mL cylindrical cells with a diameter of 90 and 50 mm (equipped with a magnetic stirrer to prevent sedimentation), respectively. Millipore water was fed into the cell with a pressure of approximately 1 bar from the top. After passing through the membrane at the bottom of the cell, the serum was collected to measure the conductivity. The purification was terminated after a certain threshold was undercut; for the respective threshold values see chapters 6.2.2.1 to 6.2.2.4. Filter membranes with different pore sizes were selected, depending on the individual particle size of each batch. Table 13 shows the applied cellulose nitrate membrane filters.

Table 13: Membrane filters used for ultrafiltration.

diameter / mm	**company**	**pore size / nm**
90	Millipore	50, 100 and 220
50 and 90	Whatman	200

6.3 Characterisation

6.3.1 Transmission electron microscopy

Transmission electron microscopy (TEM) was conducted on a JEM-2100 microscope (JEOL) equipped with a LaB_6 cathode. The microscope was operated at an acceleration voltage of 200 kV and images were recorded with a Tem Cam-F416 camera (TVIPS) and further processed with ImageJ v.1.49 (Wayne Rasband, National Institute of Health, USA).

Normal TEM operation mode was used to check the shape and dispersity of the synthesised particles. Samples were prepared by dropping 4 µL of the particle suspension (0.1 wt%) on CF 200 Cu grids (200 mesh; EMS) which were pre-treated by glow discharge for about one

minute to increase the wettability. After drying, the grids were loaded on an EM 2010 sample holder (JEOL) and images were obtained with the EM-Menu software v.4.0 (TVIPS).

Cryo-TEM was used to investigate the morphology of the prepared nanoreactors and the size and distribution of metal nanoparticles. Samples were prepared on lacey carbon grids (200 mesh Cu; Science Services) which were pre-treated by glow discharge for about one minute. 4 µL of the sample (0.1 wt%) was applied on a grid and vitrificated in liquid ethane with a Vitrobot™ (FEI). The blotting conditions were blot force = 0 N, blot time = 1 s, humidity = 100%, wait and drain time = 0 s and $T = 5$ °C. For cryogenic measurements, the grids were loaded on a Gatan 914 holder (Gatan), and pictures were recorded using the SerialEM software.[218]

Four hundred nanoparticles were measured with ImageJ, and their size was averaged to obtain the mean particle radius r_{NP} of the metal nanoparticles inside the nanoreactors, given in chapter 4.1.

6.3.2 Thermogravimetric analysis

Thermogravimetric analysis (TGA) was performed on an STA 409PC Luxx (Netsch) to determine the metal fraction of the nanoreactors. For a typical measurement, about 15 mg of previously freeze-dried sample was filled into a crucible and heated to 800 °C. The measurements were conducted with a heating rate of 10 K min^{-1} under argon flow (30 mL min^{-1}), and the temperature was held constant at 800 °C for 1 hour. The weight loss of the microgels with and without metal nanoparticles was measured, and the residual mass of the pure polymer was considered in the calculation of the metal fraction. From the TGA measurement of the core-shell nanoreactors before the synthesis of metal nanoparticles, the relative mass loss of the pure polymer $f_{loss,pol}$ was obtained. The TGA measurement of the nanoreactors after the synthesis of metal nanoparticles inside the shell yielded a relative mass loss $f_{loss,NR}$ which was only caused by the mass loss of the polymer. From the ratio of the latter and $f_{loss,pol}$, the polymer fraction of the nanoreactor was obtained, and the metal fraction f_m of the nanoreactor was calculated according to

$$f_m = 1 - \frac{f_{loss,NR}}{f_{loss,pol}}. \tag{6.1}$$

The relative mass losses were $f_{loss,pol} = 0.982$ and $f_{loss,NR} = 0.885$, yielding a metal share of $f_m = 0.099$ for Ag@PS-PNIPAM, and $f_{loss,pol} = 0.979$ and $f_{loss,NR} = 0.946$, yielding a metal share of $f_m = 0.034$ for Au@PS-PNIPAM.

6.3.3 Dynamic light scattering and zeta potential

DLS and zeta potential measurements were carried out on a Zetasizer Nano ZS ZEN 3500 (Malvern Instruments) equipped with a He-Ne Laser ($\lambda = 633$ nm).

DLS measurements were performed in PS cuvettes (VWR) at a mass concentration of 50 mg L^{-1}, using Millipore water for dilution and analysed with the proprietary Zetasizer Software v.7.11 (Malvern Instruments). For a typical measurement, ten runs of 30 s duration were measured at a scattering angle of 173° and averaged. For the thermoresponsive core-shell microgels, temperature-dependent measurements with a range from 10 to 50 °C and a step size of 2.5 °C were conducted.

The software transfers the Brownian motion induced light scattering intensity fluctuations into a first order autocorrelation function

$$g^1(q,\tau) = e^{-\Gamma\tau}, \tag{6.2}$$

where q is the wave vector, τ is the decay time, and Γ is the single exponential decay rate (for monodisperse particles). With the decay rate, the diffusion coefficient is obtained via

$$\Gamma = Dq^2 \tag{6.3}$$

to obtain the hydrodynamic radius r_H with the Stokes-Einstein equation (4.44).

The zeta potential of the PS core particles was measured in DTS1070 folded capillary cells (Malvern Panalytical) at a mass concentration of 100 mg L^{-1}, using Millipore water and analysed with the proprietary Zetasizer Software v.7.11 (Malvern Instruments). Measurements were performed in auto-mode at a scattering angle of 173°. To measure the zeta potential, an electric field is applied to the nanoparticle dispersion, causing the particles to move. The electrophoretic mobility U_e of the particles is determined via the Doppler shift of the laser light scattered from the moving particles, and the zeta potential ζ is calculated with the Herny equation

$$U_e = \frac{2\varepsilon_0 \varepsilon_r \zeta f_h}{3\eta} \tag{6.4}$$

where f_h is the Henry function. The results for the particle sizes and zeta potentials are given in chapter 4.1.

6.3.4 UV-Vis spectroscopy

The spectroscopic measurements were recorded on an Agilent 8453 UV-Vis spectrometer (Agilent). For a measurement, samples were either filled into or directly mixed in 110-QS cuvettes (Hellma) which can be tightly closed with a stopper. Stopped-flow measurements were conducted in the thermostatted cuvette attached to the stopped-flow apparatus. The spectrometer is connected to a K6s-NR thermostat (Huber) to adjust the temperature to $\Delta T \leq 0.1$ °C.

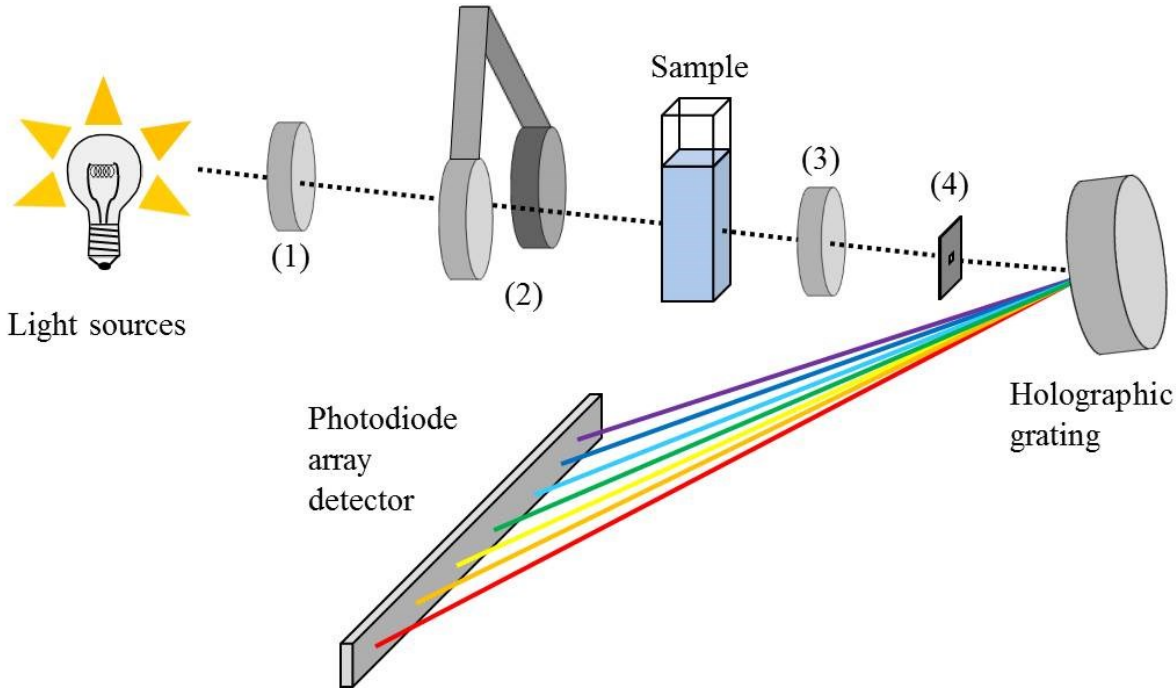

Figure 28: Schematic setup of the optical path of the Agilent 8453 spectrometer.[219]

The Agilent 8453 spectrometer has two light sources which both emit on the same optical axis. A holographic reflection grating disperses the light on a photodiode array detector and enables full spectra to be recorded at time intervals of $\Delta t = 0.5$ s with a nominal spectral slit width of 1 nm. The setup of the spectrometer is illustrated in Figure 28. To cover a wavelength range from $\lambda = 190$ to 1100 nm the spectrometer uses two lamps, a deuterium lamp that covers a wavelength range from $\lambda = 190$ to approximately 800 nm, and a low-noise

tungsten lamp, emitting from $\lambda = 370$ to 1100 nm. The light of both lamps passes the source lens (1) followed by the shutter/stray light filter (2) before it passes through the sample. Afterwards, the light passes the spectrograph lens (3) and a slit (4) before it reaches the holographic grating where the light is diffracted and dispersed onto the diode array detector where all wavelengths are recorded simultaneously. Prior to sample measurements, a reference spectrum of the pure solvent is recorded as a baseline and automatically subtracted from the measurements.

The measurement principle of UV-Vis spectroscopy is based on the excitation of valence electrons from their ground state into an excited state through photon absorption. To absorb a photon, the energy difference between the ground state and the excited state needs to correspond to the photon energy. The higher the energy difference between those two orbitals, the higher the photon energy needs to be, thus, the shorter its wavelength and vice versa. UV-Vis spectroscopy offers the possibility to distinguish between different species by the shape of their spectra as well as the quantitative determination of concentrations based on reference measurements. For that, the transmitted light intensity $I_{h\nu,T}$ relative to the initial intensity $I_{h\nu,0}$ is recorded for each wavelength and correlated with the concentration c_i via the Beer-Lambert law

$$Abs(\lambda) = \log_{10}\left(\frac{I_{h\nu,0}}{I_{h\nu,T}}\right) = \varepsilon(\lambda)\, c_i\, d, \tag{6.5}$$

where $Abs(\lambda)$ is the wavelength-dependent absorbance, $\varepsilon(\lambda)$ is the wavelength dependent molar extinction coefficient and d is the optical path length inside the sample. The Beer-Lambert law is applicable at low concentrations where a linear relationship between extinction and concentration is observed. At higher concentrations, multiple absorption and emission of photons becomes more probable and leads to a nonlinear relationship between concentration and extinction, making a simple concentration determination impossible.

6.3.5 Calculation of the metal surface area per unit volume

The ratio of the metal surface area to the mass of the metal nanoparticles $r_{A/m}$, with units of [$m^2\ L^{-1}$], is required to determine the metal surface area per unit volume S. The latter can be calculated with the radius of the metal nanoparticles r_{NP} given in chapter 4.1 and the density of the respective metal ρ_i ($19.32*10^6$ g m^{-3} for gold and $10.49*10^6$ g m^{-3} for silver, respectively[220]) according to

$$r_{A/m} = \frac{A_{NP}}{V_{NP}\,\rho_i} = \frac{4\,\pi\,r_{NP}^2}{\frac{4}{3}\,\pi\,r_{NP}^3\,\rho_i} = \frac{3}{r_{NP}\,\rho_i} \tag{6.6}$$

where A_{NP} is the surface area of one single metal nanoparticle and V_{NP} is their volume. The metal surface area to mass ratio is multiplied by the mass concentration of the final catalyst suspension c_m, given in chapter 6.2.2.4, and the metal fraction of the nanoreactors f_m, given in chapter 4.1, according to

$$S = r_{A/m}\,f_m c_m \tag{6.7}$$

to arrive at the metal surface area per unit volume for the catalyst stock solutions. The obtained values are $S = 2.0$ m^2 L^{-1} for the Ag@PS-PNIPAM catalyst and $S = 2.4$ m^2 L^{-1} for Au@PS-PNIPAM.

6.3.6 Calculation of the molar mass

In order to determine the molar mass of the core-shell nanoreactors, the mass of one core particle and the respective shell need to be calculated separately, as they were synthesised subsequently. The mass of one core particle m_{core} can be determined from its hydrodynamic radius $r_{H,core}$ determined via DLS and the bulk density of polystyrene ρ_{PS} according to

$$m_{core} = \rho_{PS}\frac{4}{3}\pi r_{H,core}^3. \tag{6.8}$$

The mass of the PNIPAM shell can be calculated by dividing the mass of reactants (which contribute to the weight of the shell) by the total number of core particles applied in the shell reaction. The number of core particles applied in the shell reaction n_{core} can be calculated according to

$$n_{core} = \frac{V_c c_{m,core}}{m_{core}}, \tag{6.9}$$

where V_c and $c_{m,core}$ are the volume and the mass concentration of the core particle suspension applied in the shell reaction. For the calculation of the shell mass of one nanoreactor m_{shell}, it needs to be taken into account, that during the shell synthesis, a fraction of the reactants forms side products like free polymer chains. The total mass of these side products $m_{s,tot}$ needs to be subtracted from the total mass of reactants $m_{r,tot}$, applied in the shell reaction. Hence, m_{shell} can be calculated according to

$$m_{shell} = \frac{m_{r,tot} - m_{s,tot}}{n_{core}} = \frac{m_{r,t} - V_t f_s \rho_t}{n_{core}}. \quad (6.10)$$

For the determination of the total mass of side products, the crude product suspension after shell synthesis was centrifuged, and the solid fraction of the supernatant f_s was determined. During centrifugation, only the particles sediment while the side products remain equally distributed. The mass of side products can then be calculated from f_s and the total reaction volume V_t, together with the density of the suspension, approximated by $\rho_t = 1*10^6$ g m^{-3} (due to overall low concentrations). By adding the volumes of the core particle suspension V_c, additional water, and the reactants (NIPAM, Bis and the reaction initiator RI), the total reaction volume V_t is obtained as

$$V_t = V_c + V_{H2O} + \frac{m_{NIPAM}}{\rho_{NIPAM}} + \frac{m_{BIS}}{\rho_{BIS}} + \frac{m_{RI}}{\rho_{RI}}. \quad (6.11)$$

The volume contribution of the reactants is calculated from their mass divided by the respective bulk densities. Equation (6.11) does not account for the volume change upon dissolution of the reactants. However, the volume contribution of the reactants to the total reaction volume is only ~3%. Therefore, the volume change upon dissolution of the reactants is negligible. The molar mass of the core-shell nanoreactors before synthesis of the metal nanoparticles can be calculated according to

$$MW_{m-} = (m_{core} + m_{shell}) N_A. \quad (6.12)$$

With the metal fraction f_m, calculated in chapter 6.3.2, the molar mass for the particles after synthesis of metal nanoparticles is derived as

$$MW_{m+} = \frac{MW_{m-}}{(1 - f_m)}. \quad (6.13)$$

The obtained molar masses are $MW_{m-} = 4.60*10^8$ g mol^{-1} and $MW_{m+} = 5.11x10^8$ g mol^{-1} for Ag@PS-PNIPAM, and $MW_{m-} = 1.63*10^9$ g mol^{-1} and $MW_{m+} = 1.69*10^9$ g mol^{-1} for Au@PS-PNIPAM.

6.4 Catalysis

6.4.1 Reduction of 4-nitrophenol

For each measurement, dry borohydride was prepared in a small vial under N_2 atmosphere to prevent the uptake of humidity (due to its hygroscopicity). Millipore water and a 4-nitrophenol (Nip) stock solution ($c_{Nip} = 0.01$ mol L^{-1}) were degassed and subsequently held under N_2 atmosphere. Shortly before the reactants were mixed, borohydride was dissolved in degassed water to yield $c_{BH4} = 0.05$ mol L^{-1} and held under N_2 atmosphere.

For a typical run, the reaction mixture was prepared directly in the cuvette. The cuvette was placed inside the thermostatted cuvette holder ($\Delta T \leq 0.1$ °C) and purged constantly with N_2 (above the liquid surface) to prevent oxygen uptake. First, water and the desired amount of Nip stock solution were added to the cuvette, followed by the corresponding amount of borohydride. After that, the catalyst was added, the N_2 purge was removed, and the cuvette was simultaneously closed. The cuvette was turned once for mixing, and the measurement was initiated immediately. Like that, the delay between adding the catalyst (i.e. start of the reaction) and start of the measurement could be kept below 5 seconds. All experiments were carried out three times and averaged to obtain more reliable results. Spectra were recorded every 5 seconds, and the time dependency of the Nip concentration was derived from the absorption at $\lambda = 400$ nm.

All measurements were performed at a catalyst concentration of $c_{NR} = 1.2*10^{-11}$ mol L, corresponding to a metal surface area per unit volume of $S = 0.0625$ m^2 L^{-1}, and with a measurement volume of 3 mL. One measurement series was conducted at constant temperature and another one against temperature. For the measurements against temperature, the reaction mixture was thermostatted for three minutes before addition of the catalyst and initiation of the measurement. All experiments are listed in Table 14.

Table 14: Applied concentration of reactants in the kinetic experiments with Ag@PS-PNIPAM nanoreactors. All experiments were carried out three times to obtain more reliable results.

Measurement series	c_{Nip} [mol L^{-1}]	c_{BH4} [mol L^{-1}]	T [°C]
constant T	$5*10^{-5}$	$5*10^{-3}$	20

Measurement series	c_{Nip} [mol L^{-1}]	c_{BH4} [mol L^{-1}]	T [°C]
constant T	7.5*10^{-5}	5*10^{-3}	20
constant T	1*10^{-4}	5*10^{-3}	20
constant T	5*10^{-5}	1*10^{-2}	20
constant T	7.5*10^{-5}	1*10^{-2}	20
constant T	1*10^{-4}	1*10^{-2}	20
constant T	5*10^{-5}	2*10^{-2}	20
constant T	7.5*10^{-5}	2*10^{-2}	20
constant T	1*10^{-4}	2*10^{-2}	20
T-dependent	1*10^{-4}	1*10^{-2}	10
T-dependent	1*10^{-4}	1*10^{-2}	15
T-dependent	1*10^{-4}	1*10^{-2}	20
T-dependent	1*10^{-4}	1*10^{-2}	25
T-dependent	1*10^{-4}	1*10^{-2}	30
T-dependent	1*10^{-4}	1*10^{-2}	35
T-dependent	1*10^{-4}	1*10^{-2}	40
T-dependent	1*10^{-4}	1*10^{-2}	45
T-dependent	1*10^{-4}	1*10^{-2}	50

6.4.2 Reduction of hexacyanoferrate(III)

For the catalytic measurements with hexacyanoferrate(III) (HCF), the spectrometer was connected to an RX2000 stopped-flow apparatus (Applied Photophysics), connected to a thermostat ($\Delta T \leq 0.1$ °C) together with the cuvette holder of the spectrometer.

For each measurement, dry borohydride was prepared in a small vial under N_2 atmosphere to prevent the uptake of humidity (due to its hygroscopicity). Millipore water, NaOH solution ($c_{NaOH} = 0.02$ mol L^{-1}), and the HCF stock solution ($c_{HCF} = 0.1$ mol L^{-1}) were degassed and subsequently held under N_2 atmosphere. For a typical run, two solutions were prepared separately and permanently held under N_2 atmosphere until being transferred to the two drive syringes of the stopped-flow apparatus (see Figure 18). For the first solution, the amount of NaCl, required to adjust the ionic strength was added first, followed by the addition of water and dissolution of the salt. After that, the desired amount of HCF and catalyst were added. For the second solution, NaOH solution was added to the previously prepared dry borohydride under N_2 atmosphere to yield $pH = 12.3$ and the desired concentration of borohydride. Like that, a pH of 12 was achieved after 1:1 mixing in the stopped-flow apparatus, suppressing the proton-catalysed decomposition of borohydride.[221]

After the dissolution of borohydride and proper mixing, the solutions were transferred to the drive syringes of the stopped-flow apparatus. Before a kinetic measurement was initiated, both solutions were thermostatted for two minutes. Before each measurement, small aliquots of the reactant mixtures (~ 0.5-1 mL) were transferred from the loading syringes into the drive syringes and flushed out through the flow lines of the apparatus three times. This ensured that no dilution of the reactants took place due to residues of water inside the loading ports and valves. All experiments were carried out three times and averaged to obtain more reliable results. A measurement was digitally triggered by the stopped-flow apparatus directly after 1:1 mixing and recorded at λ =420 nm. All measurements were performed at a ratio of $c_{BH4}/c_{HCF} \geq 25$ to ensure pseudo-unimolecular reaction conditions.[126]

Between the experiments, the drive- and stop syringes were emptied and flushed with Millipore water three times in order to clean the flow lines of the stopped-flow apparatus. After that, the whole flow circuit was filled with a 2% Hellmanex III detergent solution (Hellma) and flushed three times. Finally, the apparatus was flushed with Millipore water thoroughly to remove all impurities prior to the next measurement.

Six measurement series were conducted against catalyst-, HCF-, and borohydride concentration, ionic strength I_0, and against temperature (at two ionic strengths). The measurement volume of 0.2 mL was determined by the dimensions of the measurement cell of the stopped-flow apparatus. All experiments are listed in Table 15.

Table 15: Applied concentration of reactants in the kinetic experiments with Au@PS-PNIPAM nanoreactors. All experiments were carried out three times to obtain more reliable results. The nanoreactor concentration is stated in multiples of c_m = 1.45*10^{-12} mol L^{-1}, corresponding to a gold surface area per unit volume of S = 8.16*10^{-3} m^2 L.

Measurement	c_{NR} [c_m]	c_{HCF} [mol L^{-1}]	c_{BH4} [mol L^{-1}]	I_0 [mol L^{-1}]	T [°C]
vs. catalyst	1	5*10^{-4}	0.25	0.269	20
vs. catalyst	2.5	5*10^{-4}	0.25	0.269	20
vs. catalyst	5	5*10^{-4}	0.25	0.269	20
vs. catalyst	7.5	5*10^{-4}	0.25	0.269	20
vs. catalyst	10	5*10^{-4}	0.25	0.269	20
vs. catalyst	15	5*10^{-4}	0.25	0.269	20
vs. catalyst	20	5*10^{-4}	0.25	0.269	20
vs. HCF	5	5*10^{-5}	0.25	0.296	20
vs. HCF	5	1*10^{-4}	0.25	0.296	20
vs. HCF	5	2*10^{-4}	0.25	0.296	20

Measurement	c_{NR} [c_m]	c_{HCF} [mol L^{-1}]	c_{BH4} [mol L^{-1}]	I_0 [mol L^{-1}]	T [°C]
vs. HCF	5	3*10^{-4}	0.25	0.296	20
vs. HCF	5	4*10^{-4}	0.25	0.296	20
vs. HCF	5	5*10^{-4}	0.25	0.296	20
vs. HCF	5	6*10^{-4}	0.25	0.296	20
vs. HCF	5	8*10^{-4}	0.25	0.296	20
vs. HCF	5	1*10^{-3}	0.25	0.296	20
vs. HCF	5	1.25*10^{-3}	0.25	0.296	20
vs. HCF	5	1.5*10^{-3}	0.25	0.296	20
vs. borohydride	5	1*10^{-3}	0.025	0.272	20
vs. borohydride	5	1*10^{-3}	0.05	0.272	20
vs. borohydride	5	1*10^{-3}	0.1	0.272	20
vs. borohydride	5	1*10^{-3}	0.15	0.272	20
vs. borohydride	5	1*10^{-3}	0.2	0.272	20
vs. borohydride	5	1*10^{-3}	0.25	0.272	20
vs. ionic strength	5	5*10^{-4}	0.50	0.065	20
vs. ionic strength	5	5*10^{-4}	0.50	0.075	20
vs. ionic strength	5	5*10^{-4}	0.50	0.085	20
vs. ionic strength	5	5*10^{-4}	0.50	0.100	20
vs. ionic strength	5	5*10^{-4}	0.50	0.125	20
vs. ionic strength	5	5*10^{-4}	0.50	0.150	20
vs. ionic strength	5	5*10^{-4}	0.50	0.175	20
vs. ionic strength	5	5*10^{-4}	0.50	0.200	20
vs. ionic strength	5	5*10^{-4}	0.50	0.250	20
vs. ionic strength	5	5*10^{-4}	0.50	0.300	20
vs. ionic strength	5	5*10^{-4}	0.50	0.400	20
vs. ionic strength	5	5*10^{-4}	0.50	0.500	20
vs. ionic strength	5	5*10^{-4}	0.50	0.600	20
vs. temperature	10	5*10^{-4}	0.50	0.065	10.0
vs. temperature	10	5*10^{-4}	0.50	0.065	15.0
vs. temperature	10	5*10^{-4}	0.50	0.065	20.0
vs. temperature	10	5*10^{-4}	0.50	0.065	22.5
vs. temperature	10	5*10^{-4}	0.50	0.065	25.0
vs. temperature	10	5*10^{-4}	0.50	0.065	27.5
vs. temperature	10	5*10^{-4}	0.50	0.065	30.0
vs. temperature	10	5*10^{-4}	0.50	0.065	32.5
vs. temperature	10	5*10^{-4}	0.50	0.065	35.0
vs. temperature	10	5*10^{-4}	0.50	0.065	37.5
vs. temperature	10	5*10^{-4}	0.50	0.065	40.0
vs. temperature	10	5*10^{-4}	0.50	0.065	42.5
vs. temperature	10	5*10^{-4}	0.50	0.065	45.0

Measurement	c_{NR} [c_m]	c_{HCF} [mol L^{-1}]	c_{BH4} [mol L^{-1}]	I_0 [mol L^{-1}]	T [°C]
vs. temperature	10	5*10^{-4}	0.50	0.065	50.0
vs. temperature	10	5*10^{-4}	0.50	0.100	10.0
vs. temperature	10	5*10^{-4}	0.50	0.100	15.0
vs. temperature	10	5*10^{-4}	0.50	0.100	20.0
vs. temperature	10	5*10^{-4}	0.50	0.100	22.5
vs. temperature	10	5*10^{-4}	0.50	0.100	25.0
vs. temperature	10	5*10^{-4}	0.50	0.100	27.5
vs. temperature	10	5*10^{-4}	0.50	0.100	30.0
vs. temperature	10	5*10^{-4}	0.50	0.100	32.5
vs. temperature	10	5*10^{-4}	0.50	0.100	35.0
vs. temperature	10	5*10^{-4}	0.50	0.100	37.5
vs. temperature	10	5*10^{-4}	0.50	0.100	40.0
vs. temperature	10	5*10^{-4}	0.50	0.100	42.5
vs. temperature	10	5*10^{-4}	0.50	0.100	45.0
vs. temperature	10	5*10^{-4}	0.50	0.100	50.0

6.5 Fit algorithms

6.5.1 Time-dependent fits

The data were fitted with Mathematica (Wolfram Research) by a genetic approach with equation (4.5) for the 4-nitrophenol reduction and with equations (4.24) and (4.25) for the hexacyanoferrate(III) reduction.[196] The flow chart of the fit algorithm is shown in Figure 12.

The steps of the program code (attached in the following) are as follows:

1) Import (discrete) experimental data and transfer into continuous data with a spline fit.

2) Define experimental conversion limit to define up to which time t_l the data are fitted.

3) Define differential equations and fit parameter p_i for the fit.

4) Define range for each fit parameter p_i.

5) Derive values in N_i equidistant steps for each fit parameter p_i within the respective range and generate starting parameter sets s_j of their combinations.

6) Test the starting parameter sets s_j with the target function $\varepsilon_j(t_l, s_j)$ in equation (4.7).

7) Take the best parameter set s_j^* (for which $\varepsilon_j(t_l, s_j^*)$ is minimal) and mutate by randomly varying each parameter within the margins of $\Delta p_i \leq \pm 1\%$ to generate mutant parameter set s_j^{**}.

8) Test mutant parameter sets s_j^{**} with the target function $\varepsilon_j(t_l, s_j^{**})$.

9) If $\varepsilon_j(t_l, s_j^{**}) < \varepsilon_j(t_l, s_j^*)$, take mutant parameter set and repeat mutation cycle,
if $\varepsilon_j(t_l, s_j^{**}) \geq \varepsilon_j(t_l, s_j^*)$, keep old parameter set and repeat mutation cycle.

10) The final result is obtained if no improved parameter set $\varepsilon_j(t_l, s_j^{**}) < \varepsilon_j(t_l, s_j^*)$ is obtained for $c_n = 200$ consecutive mutation cycles.

Program code:

```
SetDirectory[NotebookDirectory[]];
data0 = Import["HCF red DATA.xlsx", "XLSX"];

KD = Take[data0[[1, 1]], {2, -1}];
Surf = Take[data0[[1, 2]], {2, -1}];
Temp = Take[data0[[1, 3]], {2, -1}];
Istr = Take[data0[[1, 4]], {2, -1}];
cBH40 = Take[data0[[1, 5]], {2, -1}];
cHCF0 = Take[data0[[1, 6]], {2, -1}];
l0Data = 0.5*(Length[Take[data0[[1, 8]], {1, -1}]] - 1);
time = Take[Transpose[Take[data0[[1]]]][[1]], {8, -1}];
l0Time = Length[time];

AllData0 =
  Table[Transpose[{Table[KD[[2 i - 1]], {l0Time}],
    Table[Surf[[2 i - 1]], {l0Time}],
    Table[Temp[[2 i - 1]], {l0Time}],
    Table[Istr[[2 i - 1]], {l0Time}],
    Table[cBH40[[2 i - 1]], {l0Time}],
    Table[cHCF0[[2 i - 1]], {l0Time}], time,
    Take[Transpose[Take[data0[[1]]]][[2 i]], {8, -1}],
    Take[Transpose[Take[data0[[1]]]][[2 i + 1]], {8, -1}]}], {i, 1, l0Data}];

df[x_] :=  Transpose[{Transpose[x][[1]],D[Interpolation[x][y], y] /. y -> Transpose[x][[1]]}]

AllDataCNR = Take[AllData, {1, 7}];
AllDataHCF1 = Take[AllData, {8, 18}];
AllDataBH4 = Take[AllData, {30, 35}];
```

```
AllDataIS = Take[AllData, {36, 48}];
AllDataTemp1 = Take[AllData, {49, 62}];
AllDataTemp2 = Take[AllData, {63, 76}];

relC1 = 1;
relC2 = 0.5;
PARSTAB = {};
GR = {};
k = 0;
filename = "cHCF2-series_Global-no-50pct-";
local = {1, 1, 1};
AllData = AllDataHCF2;
DATA = Table[
   Select[({#[[7]], #[[8]]} & /@ AllData[[k]]),
    relC1 >= #[[2]] >= relC2 &], {k, 1, Length[AllData]}];
DDATA = df[Take[#, {3, -1}]] & /@ DATA;

fitmodel0 =
  ParametricNDSolveValue[{X'[t] == -((a* X[t]*CNR)/(1 + P[t]*a*b)),
    X[0] == 1, P'[t] == (a* X[t])/(1 + P[t]*a*b) CHCF0 - P[t]*kOff,
    P[0] == 0},
   X, {t, TINTi, TINTf}, {a, b, kOff, CNR, CHCF0, TINTi, TINTf}];
dfitmodel0 =
  ParametricNDSolveValue[{X'[t] == -((a* X[t]*CNR)/(1 + P[t]*a*b)),
    X[0] == 1, P'[t] == (a* X[t])/(1 + P[t]*a*b) CHCF0 - P[t]*kOff,
    P[0] == 0},
   X', {t, TINTi, TINTf}, {a, b, kOff, CNR, CHCF0, TINTi, TINTf}];

parsTab =
  pT = Flatten[
    Table[N[{10^i, 10^j, 10^l}], {i, 9.5, 10.5, 0.25}, {j, -20, -18,
      0.25}, {l, -4, 0, 0.25}], 2];
l0 = Length[parsTab];
step = 0;
RES = {};
res0 = 10^100;

Do[
  step = step + 1;
  ress = {};
  k = 0;
  Do[
   k = k + 1;
   fitmodel[a_, b_, kOff_] :=
    Evaluate[
     fitmodel0[a, b, kOff, AllData[[k, 1, 2]], AllData[[k, 1, 6]],
      DATA[[k, 1, 1]], DATA[[k, -1, 1]]]];
   dfitmodel[a_, b_, kOff_] :=
    Evaluate[
     dfitmodel0[a, b, kOff, AllData[[k, 1, 2]], AllData[[k, 1, 6]],
      DATA[[k, 1, 1]], DATA[[k, -1, 1]]]];
```

```
    res00 =
   Mean[1/Transpose[DATA[[k]]][[2]]*
     Abs[fitmodel[pT[[step, 1]], pT[[step, 2]], pT[[step, 3]]][
       Transpose[DATA[[k]]][[1]]] - Transpose[DATA[[k]]][[2]]]];
  dres00 =
   Abs[Mean[
     1/Transpose[DDATA[[k]]][[2]]*
      Abs[dfitmodel[pT[[step, 1]], pT[[step, 2]], pT[[step, 3]]][
        Transpose[DDATA[[k]]][[1]]] - Transpose[DDATA[[k]]][[2]]]]];
  ress = Insert[ress, res00 + dres00, 1];
  , {Length[AllData]}];
   res = Mean[ress];
 If[res < res0, res0 = res;
  RES = {res0, pT[[step, 1]], pT[[step, 2]], pT[[step, 3]]};
 , {l0}];

PARS0 = Table[Take[RES, {2, -1}], {Length[AllData]}];
Err0 = RES[[1]];

m = 0;
count = 0;
Do[
 m = m + 1;
 count = count + 1;
 l0 = Length[PARS0[[1]]];
 RI = RandomInteger[{1, l0}];
 fac1 = RandomSample[
   Join[Table[RandomReal[{0.99, 1.01}], {RI}], Table[1, {l0 - RI}]],
   l0];
 PARS = (fac1*#) & /@ PARS0;
 Errs = {};
 PARSs = {};
 k = 0;
 Do[
  RI2 = RandomInteger[{1, l0}];
  fac2 =
   RandomSample[
    Join[Table[RandomReal[{0.99, 1.01}], {RI2}],
     Table[1, {l0 - RI2}]], l0];
  faclocal = If[# == 0., 1, #] & /@ (fac2*local);
  PARS = (faclocal*#) & /@ PARS;
  k = k + 1;
  fitmodel[a_, b_, kOff_] :=
   Evaluate[
    fitmodel0[a, b, kOff, AllData[[k, 1, 2]], AllData[[k, 1, 6]],
     DATA[[k, 1, 1]], DATA[[k, -1, 1]]]];
  dfitmodel[a_, b_, kOff_] :=
   Evaluate[
    dfitmodel0[a, b, kOff, AllData[[k, 1, 2]], AllData[[k, 1, 6]],
     DATA[[k, 1, 1]], DATA[[k, -1, 1]]]];
  Err00 =
```

```
  Mean[Abs[
    fitmodel[PARS[[k, 1]], PARS[[k, 2]], PARS[[k, 3]]][
      Transpose[DATA[[k]]][[1]]] - Transpose[DATA[[k]]][[2]]]/
   Transpose[DATA[[k]]][[2]]];
 dErr00 =
  Abs[Mean[
    Abs[dfitmodel[PARS[[k, 1]], PARS[[k, 2]], PARS[[k, 3]]][
       Transpose[DDATA[[k]]][[1]]] - Transpose[DDATA[[k]]][[2]]]/
    Transpose[DDATA[[k]]][[2]]]];
 Errs = Insert[Errs, Err00 + dErr00, 1];
 PARSs = Insert[PARSs, PARS[[k]], -1];
 , {Length[AllData]}];
Err = Mean[Errs];
If[Err < Err0, PARS0 = PARSs; Err0 = Err; count = 0];
If[count == 200, Break[]];
, {250000}];
```

6.5.2 Stationary state fits

The data were fitted with Anaconda Suite (Anaconda Inc.) by a genetic approach with equation (4.40).[215] The flow chart of the fit algorithm is shown in Figure 12. Other than for the time-dependent fit, no differential equations are required, no spline fit of the experimental data is necessary, and no conversion limit needs to be defined. The best 200 parameter sets s_j are subjected to the mutation cycle, and the parameters of all sets are randomly recombined prior to each mutation step.

The steps of the program code (attached in the following) are as follows:

1) Define equations and fit parameter p_i for the model.

2) Define target function $\varepsilon_k(s_j)$ in equation (4.43).

3) Import experimental data.

4) Define range for each fit parameter p_i.

5) Automated fit algorithm *differential evolution*.

6) The final result is obtained if the relative deviation between the target functions $\varepsilon_k(s_j^{**})$ is below 10^{-9}.

Program code:

```
from pylab import *
from scipy.optimize import differential_evolution
from scipy.integrate import quad
import matplotlib.pyplot as plt
def model_K1_HCF(coef, c_0_HCF, c_BH4, I_0):

    P=coef[0]
    k_off=coef[1]
    K_R=coef[2]
    K_B=coef[3]
    R_core=7.09e-8
    R_shell=14.8233e-8
    T=293.15
    e_r=80.22503
    k_1= f/s*(K_NRSS(P, K_R, R_core, R_shell)*c_NR)
    k_2=1/(1+K_NRSS(P, K_R, R_core, R_shell)**2/k_off*E_pert(P, K_B, T, e_r, c_BH4, I_0, R_core,
R_shell)*c_0_HCF)
    k1=k_1*k_2
    return k1
def model_K1_BH4(coef, c_0_HCF, c_BH4, I_0):

    P=coef[0]
    k_off=coef[1]
    K_R=coef[2]
    K_B=coef[3]
    R_core=7.09e-8
    R_shell=14.8233e-8
    T=293.15
    e_r=80.22503
    k_1= f/s*(K_NRSS(P, K_R, R_core, R_shell)*c_NR)
    k_2=1/(1+K_NRSS(P, K_R, R_core, R_shell)**2/k_off*E_pert(P, K_B, T, e_r, c_BH4, I_0, R_core,
R_shell)*c_0_HCF)
    k1=k_1*k_2
    return k1
def model_K1_I0(coef, c_0_HCF, c_BH4, I_0):

    P=coef[0]
    k_off=coef[1]
    K_R=coef[2]
    K_B=coef[3]
    R_core=7.09e-8
    R_shell=14.8233e-8
    T=293.15
    e_r=80.22503
    k_1= f/s*(K_NRSS(P, K_R, R_core, R_shell)*c_NR)
    k_2=1/(1+K_NRSS(P, K_R, R_core, R_shell)**2/k_off*E_pert(P, K_B, T, e_r,c_BH4,  I_0, R_core,
R_shell)*c_0_HCF)
    k1=k_1*k_2
    return k1

def E_pert(P, K_B,T,e_r, c_B, I_0,R_core, R_shell, K_A=0.96399,l_b=7.102e-10):
```

```
    E1=z_r*z_p*l_b/(4*pi*N_a*P)*exp(K_g(K_B,T,e_r, c_B, I_0, K_A)*R_core)/(1+(K_g(K_B,T,e_r, c_B,
I_0,K_A)*R_core))
    E2=integral(K_B,T,e_r,c_B, I_0, R_shell, R_core,K_A)
    return E1*E2
def integrand(r, kg):
    return exp(-kg*r)/r**3
def integral(K_B, T, e_r, c_B, I_0,R_shell, R_core, K_A):
    if len(shape(I_0)) >0:
        I=[]
        for i in range(0, len(I_0)):
            kg=K_g(K_B, T, e_r,c_B, I_0[i],K_A)
            I.append(quad(integrand, R_core, R_shell, args=kg)[0])
    elif len(shape(c_B)) >0:
        I=[]
        for i in range(0, len(c_B)):
            kg=K_g(K_B, T, e_r,c_B[i], I_0,K_A)
            I.append(quad(integrand, R_core, R_shell, args=kg)[0])
    else:
        kg=K_g(K_B, T, e_r,c_B, I_0,K_A)
        I=quad(integrand, R_core, R_shell, args=kg)[0]
    return array(I)
def K_g(K_B, T, e_r, c_B, I_0, K_A):
    return sqrt((2*10**3*pi*N_a*el**2*I_g(K_B, c_B, I_0,K_A))/(e_r*e_0*k_b*T))
def I_g(K_B,c_B, I_0,K_A):
    return sqrt(I_0*K_A*(I_0*K_A+(K_B-K_A)*c_B))
def K_NRSS(P, K_R, R_core, R_shell, D_0=7.15e-10):
    K_D=4*10**3*pi*N_a*D_0*R_core/(1+(D_0/P-1)*(1-R_core/R_shell))
    k=1/(1/K_D+1/K_R)
    return k
def chi(coef, data):

    data_HCF=data[0]
    data_BH4=data[1]
    data_I0=data[2]
    model1=abs(model_K1_HCF(coef, array(data_HCF[0]),0.25 ,0.2958)-
array(data_HCF[1]))/array(data_HCF[1])
    model2=abs(model_K1_BH4(coef,1e-3 ,array(data_BH4[0]) ,0.2718)-
array(data_BH4[1]))/array(data_BH4[1])
    model3=abs(model_K1_I0(coef, 5e-4,5e-2, array(data_I0[0]))-array(data_I0[1]))/array(data_I0[1])
    model=concatenate((model1/len(model1),model2/len(model2), model3/len(model1)))
    return sqrt(dot(model,model))

k_b=1.381*1e-23
N_a=6.022*1e23
e_0=8.854*1e-12
el=1.602*1e-19
R_gas=8.314462
z_r=-3
z_p=-4
f=0.576
s=8.16e-2
```

```
c_NR=1.44515E-11
x=[]
y=[]

datei=open("filename").readlines()
daten=[]
for i in range(0, len(datei)):
   x.append(float(datei[i].split()[0]))
   y.append(float(datei[i].split()[1]))
daten.append([x,y])
datei=open("filename").readlines()
x=[]
y=[]
for i in range(0, len(datei)):
   x.append(float(datei[i].split()[0]))
   y.append(float(datei[i].split()[1]))
daten.append([x,y])
datei=open("filename").readlines()
x=[]
y=[]
for i in range(0, len(datei)):
   x.append(float(datei[i].split()[0]))
   y.append(float(datei[i].split()[1]))
daten.append([x,y])
bounds=([1e-12,1e-07], [0.1, 10000000],  [1e7, 1e15], [0.961,100])
result=differential_evolution(chi, bounds, args=[daten], disp=True, popsize=50, maxiter=1500, tol=1e-
9)

def arrhenius(Ea, T):
   return exp(-Ea/R_gas*(1/(T)-1/293.15))
def model_T(P, k_off, K_R,K_B, c_0_HCF, c_BH4, I_0,T, e_r, K_A, R_shell, D_0, lb):
   R_core=7.09e-8
   k_1= f/s*(K_NRSS(P, K_R, R_core, R_shell,D_0)*c_NR)*1/(1+K_NRSS(P, K_R, R_core, R_shell,
D_0)**2/k_off*E_pert(P, K_B, T, e_r, c_BH4, I_0, R_core, R_shell, K_A, lb)*c_0_HCF)
   return k_1

bounds_T=[]
for i in range(0, 14):
   bounds_T.append([1e-12, 1e-7])
bounds_T.append([0, 1e6])

T=array([283.15,288.15,293.15,295.65,298.15,300.65,303.15,305.65,308.,310.65,313.15,315.65,318.15,323
.15])
M2=array([6.12E-01,6.61E-01,6.65E-01,6.13E-01,4.78E-01,3.67E-01,2.98E-01,3.00E-01,3.44E-01,3.97E-
01,4.48E-01,5.18E-01,5.99E-01,7.22E-01])
M1=array([1.09E+00,1.07E+00,9.71E-01,8.59E-01,7.38E-01,5.46E-01,3.65E-01,4.23E-01,4.67E-01,5.36E-
01,6.57E-01,6.83E-01,8.41E-01,9.30E-01])
k_B=array([2.822106246,2.821989232,2.82,2.813300968,2.785773504,2.67747736,2.314705754,1.54926
0884,0.828017925,0.514538325,0.424145271,0.401415367,0.395915725,0.394248281])
e_r=array([83.97254,82.0793,80.22503,79.31251,78.40973,77.51669,76.63339,75.75983,74.89601,74.041
94,73.1976,72.36301,71.53816,69.91768])
```

```
K_a=array([0.96471,0.96467,0.96399,0.9617,0.95229,0.91527,0.79126,0.5296,0.28305,0.17589,0.14499,0.13722,0.13534,0.13477])
R_shell=array([1.56350E-07,1.52967E-07,1.48233E-07,1.43617E-07,1.37467E-07,1.28550E-07,1.10583E-07,9.90667E-08,9.71833E-08,9.62500E-08,9.61833E-08,9.54167E-08,9.49000E-08,9.39333E-08])
D_0=array([5.296E-10,6.188E-10,7.150E-10,7.657E-10,8.183E-10,8.727E-10,9.289E-10,9.869E-10,1.047E-09,1.108E-09,1.172E-09,1.237E-09,1.304E-09,1.444E-09])
l_b=array([7.025E-10,7.062E-10,7.102E-10,7.123E-10,7.145E-10,7.167E-10,7.190E-10,7.213E-10,7.237E-10,7.262E-10,7.287E-10,7.312E-10,7.339E-10,7.392E-10])
prev_coef=[6.413e-11, 4.4e4,6.59e14,2.82]

def chi_T(coef_T, daten, prev_coef, k_B, e_r, K_a, R_shell, D_0, l_b):
    T=daten[0]
    M1=daten[1]
    M2=daten[2]
    P_20, k_off_20, k_R_20, k_b_20 = prev_coef
    modelT1=zeros(len(coef_T)-1)
    modelT2=zeros(len(coef_T)-1)
    for i in range(0, len(coef_T)-1):
        modelT1[i]=model_T(coef_T[i],k_off_20*arrhenius(coef_T[-1], T[i]), k_R_20, k_B[i], 5e-4, 5e-2, 0.1,T[i], e_r[i], K_a[i], R_shell[i], D_0[i], l_b[i])
        modelT2[i]=model_T(coef_T[i],k_off_20*arrhenius(coef_T[-1], T[i]), k_R_20, k_B[i], 5e-4, 5e-2, 0.06445,T[i], e_r[i], K_a[i], R_shell[i], D_0[i], l_b[i])
    res=(abs(modelT1-M1)/M1 + (abs(modelT2-M2)/M2))
    residua=sqrt(dot(res,res))/(len(T)*2)
    return residua

result_T=differential_evolution(chi_T, bounds_T, args=[[T, M1,M2], prev_coef,k_B, e_r, K_a, R_shell, D_0, l_b], disp=True, popsize=5, maxiter=1000, tol=1e-9)
```

7. Appendix

7.1 Literature tables

Table 17 to Table 19 below provide an overview of catalysts with various architectures, applied in the reduction of 4-nitrophenol on gold, silver and other metals, respectively. Listed are only catalysts where the existence of isosbestic points is depicted graphically in the particular reference. The tables state the particular reference, the support and its structure, the kinetic constant, the existence of isosbestic points, the size and shape of the active metal catalyst particles, and the temperature at which the kinetic constant was measured (if given in the reference). The existence of isosbestic points is either indicated "Yes" or "No" where a clear decision was possible; otherwise, a tendency is given in brackets. For more complex architectures of the gold- and silver-based catalysts, the location of the active metal is indicated in the "support" column. However, it is not always possible to state the location clearly in the compendious description of the support architecture. In Table 19, the used metal(s) is always stated. Potentially thermoresponsive catalysts are indicated "*". The reaction rate in the different references is given in the form of different kinetic constants explained in Table 16. All given kinetic constants were obtained from the reduction of 4-nitrophenol with borohydride in aqueous solution where not stated otherwise.

Table 16: List of kinetic rate constants given in the different references.

constant	description	units
k_{app}	pseudo first order apparent reaction rate constant	s^{-1}
k_1	pseudo first order apparent reaction rate constant normalised to metal surface area per unit volume	$L\ m^{-2}\ s^{-1}$
k_0	zero order reaction rate constant	$mol\ L^{-1}\ s^{-1}$
k_{Li}	rate constant based on own kinetic model[101]	$L^n\ mol^{-n}\ s^{-1}$ (n > 0)
k_{mass}	pseudo first order apparent reaction rate constant normalised to mass of catalyst	$s^{-1}\ g^{-1}$
k_{c-mass}	pseudo first order apparent reaction rate constant normalised to mass of catalyst per unit volume	$L\ g^{-1}s^{-1}$
k_{mol}	pseudo first order apparent reaction rate constant normalised to concentration of catalyst	$L\ mol^{-1}\ s^{-1}$

k_n	pseudo first order apparent reaction rate constant normalised to molar amount of metal atoms	$mol^{-1}\ s^{-1}$
k_{L-H}	rate constant based on Langmuir-Hinshelwood model[107]	$mol\ m^{-2}\ s^{-1}$
k_L	rate constant based on Langmuir-Hinshelwood model[222]	$mol\ m^{-2}\ s^{-1}$
TOF	turnover frequency	s^{-1}

Table 17: List of references of the nitrophenol reduction on gold catalysts. For more complex architectures, the location of the active catalyst is indicated in the "support" column.

reference	support; structure	kinetic constant	isosbest. points	size / nm; shape	*T* / °C
Fu et al., 2016[176]	Si waver macroscopic support	$k_1 = 6.0*10^{-2}$	Yes	10 polyhedral	20
	macroscopic glass tube flow experiment	-	No	-	-
He et al., 2015[97]	PMIMC@PDMAEMA hairy hollow spheres*	$k_{app} = 1.8*10^{-3}$ $k_{app} = 3.0*10^{-3}$	No	1.5 ± 0.2 spherical	25 55
Cao et al., 2015[116]	gibbsite@PDA hexagonal platelets	$k_1 = 8.0*10^{-2}$	Yes	11.7 spherical	RT
Fenger et al., 2012[117]	CTAB small ligand molecules	$k_{app} = 1.2*10^{-3}$ $k_{app} = 2.4*10^{-3}$ $k_{app} = 6.1*10^{-3}$ $k_{app} = 1.0*10^{-4}$	No	3.5 10 13 56 spherical	-
Yamamoto et al., 2012[98]	*N,N*-DMF small ligand molecules	$k_{app} = 3*10^{-3}$	No	-	-
Han et al., 2010[99]	PANI nanofibers	$k_{app} = 1.2*10^{-2}$	No	2 spherical	RT
Saha et al., 2010[223]	Ca-alginate microsphere beads	$k_0 = 2.8*10^{-8}$	Yes	5 ± 2 spherical	-
Wu et al., 2012[72]	Au@PNIPAM yolk-shell structure*	$k_1 = 2.2*10^{-1}$	Yes	15 ± 3 spherical	20
Zhao et al., 2013[100]	1,2,3-triazole-mPEG ligand molecules	$k_{app} = 5.2*10^{-3}$	No	12.6 ± 3 icosahedral	25
Rashid et al., 2008[224]	$Fe_x(NH_3)_y$ citrate small ligand molecules	$k_{app} = 1.2*10^{-2}$ $k_{app} = 3.5*10^{-3}$ $k_{app} = 1.1*10^{-2}$	Yes	100 ± 22 158 ± 49 124 ± 24 polyhedral	-
Rashid et	$Bi_x(NH_3)_y$ citrate	$k_{app} = 2.1*10^{-3}$	No	80 ± 60	15

reference	support; structure	kinetic constant	isosbest. points	size / nm; shape	*T* / °C
al., 2006[225]	small ligand molecules			spongy, spherical	
Zhang et al., 2007[60]	PS@PDMAEMA spherical polymer brush*	$k_{app} = 3.2*10^{-3}$	No	4.1 spherical	-
Panigrahi et al., 2007[118]	citrate small ligand molecules	-	Yes	20 spherical	25
	citrate+seralite SRA-400 commercial resin beads	$k_{app} = 1.6*10^{-4}$	No	20 spherical	25
Fedorczyk et al., 2015[173]	PDACz macroscopic electro-deposited polymer film	$k_0 = 9.3*10^{-8}$	No	200 nanoflowers	-
Ciganda et al., 2014[49]	1,2,3-triazole-PEG-2000 ligand molecules	$k_1 = 1.7*10^{-2}$	No	3 spherical	13
	PEG-2000-1,2,3-triazole-CH_2-O-CH_2-TTEGb ligand molecules	$k_1 = 1.4*10^{-2}$	No	3 spherical	13
	1,2,3-triazole-PEG-2000 ligand molecules	$k_1 = 4.3*10^{-2}$	No	6 spherical	20
	polymeric 1,2,3-triazole-PEG polymeric ligands	$k_1 = 1.9*10^{-2}$	Yes	3.6 spherical	20
	HS-PEG-550 ligand molecules	$k_1 = 1.0*10^{-3}$	No	3.5 spherical	20
	HS-PEG-2000 ligand molecules	$k_1 = 3.0*10^{-3}$	Yes	13.5 spherical	20
	citrate small ligand molecules	$k_1 = 4.0*10^{-4}$	Yes	13.5 spherical	20
Seo et al., 2013[53]	PEG-5000-*b*-PAA-6700 DHBC micelles	$k_{app} = 5.6*10^{-3}$	(Yes)	10 ± 4 spherical	30
Chen et al., 2008[54]	PS-*b*-P4VP micelles	$k_{app} = 9.6*10^{-4}$	(Yes)	15 spherical	20
Huang et al., 2009[226]	α-CD small ligand molecules	$k_{app} = 4.7*10^{-3}$	No	11.2 ± 1.1 spherical	25
Villalobos et al., 2014[227]	PTSC polymer membranes	$k_{app} = 1.6*10^{-4}$	Yes	2.9 spherical	RT
Fang et al., 2011[228]	PEI/PVA (electrospun) nanofiber mats	-	No	11.8 ± 3.3 spherical	-
Li et al., 2013[101]	PGMA@PAH microsphere beads	$k_{Li} = 49.9$	No	12 ± 3 spherical	22
Biondi et al., 2011[174]	imidazolium containing polyelectrolyte ligands	$k_{app} = 9.1*10^{-3}$	(No)	2.3 ± 0.5 spherical	-

reference	support; structure	kinetic constant	isosbest. points	size / nm; shape	*T* / °C
Esumi et al., 2003[110]	PAMAM-G5 dendrimers	$k_{app} = 2.4*10^{-3}$	No	6.8 ± 1.9 spherical	15
Ismail et al., 2012[106]	TiO_2 mesoporous structure	$k_{app} = 7.1*10^{-3}$	(No)	-	25
Hallet-Tapley et al., 2011[229]	hydrotalcite commercial product	$k_{app} = 1.0*10^{-2}$	No	21 spherical	23
	γ-Al_2O_3 commercial product	$k_{app} = 7.5*10^{-3}$	No	30 spherical	23
	TiO_2 P25 commercial product	$k_{app} = 2.0*10^{-3}$	(No)	33 spherical	23
Lin et al., 2013[230]	PVP stabilised Au NP loaded on commercial γ-Al_2O_3	$k_{app} = 2.0*10^{-2}$ $k_{app} = 2.6*10^{-2}$ $k_{app} = 1.8*10^{-2}$ $k_{app} = 1.5*10^{-2}$	Yes	2 ± 0.3 3.4 ± 0.6 5.7 ± 1.4 8.2 ± 3 spherical	25
Shao et al., 2016[231]	Fe_3O_4@SiO_2-Au@C yolk shell structure	$k_{app} = 1.1*10^{-2}$	Yes	3.7 ± 0.8 spherical	-
Xiong et al., 2014[171]	Fe_3O_4@carboxylated cellulose amorphous structure	$k_{app} = 9.3*10^{-3}$ $k_{app} = 4.2*10^{-3}$	No	14.3 ± 5.3 24.1 ± 6.1 spherical	25
		$k_{app} = 6.7*10^{-4}$	Yes	38.3 ± 8.8 spherical	25
Hu et al., 2013[232]	Fe_3O_4@SiO_2 microspheres	$k_{app} = 1.0*10^{-2}$	No	5 spherical	RT
Wang et al., 2013[233]	Fe_3O_4@CeO_2 microspheres	$k_{mass} = 5.7*10^{-2}$	Yes	-	RT
	Fe_3O_4@SiO_2@CeO_2 microspheres	$k_{mass} = 7.3*10^{-2}$	Yes	-	RT
Li et al., 2013[234]	MPA stabilised Au NP loaded on zeolithic imidazole framework	-	Yes	2 spherical	-
Wang et al., 2011[235]	Au@HMSM yolk shell structure	$TOF = 1.1*10^{-2}$	Yes	21 spherical	27
Wei et al., 2011[236]	SiO_2 ordered mesoporous structure	$k_{app} = 9.7*10^{-4}$	Yes	4 spherical	25
Gu et al., 2013[237]	SiO_2@Au hollow microspheres	$k_{app} = 7.5*10^{-3}$	No	4 ± 2 spherical	23
Lin et al., 2012[238]	NH_2-SiO_2@Au functionalised nanotubes	$k_{app} = 1.2*10^{-2}$	No	5 spherical	25
Zheng et	Fe_3O_4@SiO_2	$k_{app} = 1.4*10^{-2}$	Yes	5	25

reference	support; structure	kinetic constant	isosbest. points	size / nm; shape	*T* / °C
al., 2013[239]	Sn^{2+}-grafted magnetic microspheres			spherical	
Zhu et al., 2011[240]	Fe_3O_4@SiO_2 @PAH-Au-PSS magnetic microspheres	$k_{app} = 3.0*10^{-3}$	Yes	4 spherical	RT
Jin et al., 2014[241]	NiSiO nanoflowers	$k_{mass} = 4.1*10^{2}$ $k_{mass} = 4.9*10^{2}$ $k_{mass} = 5.3*10^{2}$	Yes	5 ± 1.2 4 ± 0.9 2.7 ± 0.6 spherical	-
Jin et al., 2014[242]	YSiO@Au hollow nanospheres	$k_{app} = 1.2*10^{-2}$	Yes	3.6 ± 0.9 spherical	-
Gangula et al., 2011[243]	breynia rhamnoides plant extract	$k_{app} = 9.2*10^{-3}$	No	25 spherical	-
Das et al., 2012[244]	rhizopus oryzae fungus protein extract	$k_{app} = 1.7*10^{-3}$	No	5 spherical	20
Xia et al., 2013[245]	DPS small ligand molecules	-	No	4.5 ± 0.5 spherical	25
Wang et al., 2007[52]	P4VP-*b*-PNIPAM micelles*	$k_{app} = 1.5*10^{-3}$	No	3.3 ± 0.2 spherical	25
Pich et al., 2006[65]	P(AAEM-VCL) copolymer microgel*	$k_{app} = 1.2*10^{-3}$	Yes	- spherical	20
Liu et al., 2006[246]	P(DVB-AA) copolymer microspheres	-	Yes	10 spherical	25
Jia et al., 2015[177]	α-CD-PVCL microgel	$k_1 = 2.5*10^{-2}$	(No)	- spherical	RT
Kuroda et al., 2009[12]	PMMA commercial microspheres	$k_1 = 5.1*10^{-1}$	Yes	6.9 ± 5.5 spherical	22
Shin et al., 2012[247]	Au/Au@polythiophene polymer microspheres	$k_{app} = 6.5*10^{-4}$	Yes	2 sizes spherical	-
Zhang et al., 2012[248]	SH-PDMAEMA ligand molecules	$k_{app} = 1.9*10^{-2}$	(Yes)	5 spherical	-
Chen et al., 2012[249]	Au@SiO_2@PNIPAM porous microspheres	$k_{app} = 1.0*10^{-2}$	Yes	5 spherical	30
Liu et al., 2015[66]	Fe_3O_4@P(NIPAM-DMAEMA) core-shell microgel*	$k_{app} = 2.4*10^{-3}$	Yes	10 spherical	20
Nongwe et al., 2014[250]	Au@mesoporous carbon yolk shell structure	$k_{app} = 7.0*10^{-3}$	No	15 ± 3 spherical	RT
Shi et al., 2014[75]	SH-P(NIPAM-MAA) copolymer microgel*	$k_{app} = 1.4*10^{-3}$	Yes	3.9 ± 0.6 spherical	30
Wu et al.,	Au@P(NIPAM-	$k_{app} = 2.0*10^{-3}$	No	7 ± 3	30

reference	support; structure	kinetic constant	isosbest. points	size / nm; shape	*T* / °C
2015[71]	VPBA-AAm) copolymer microgel*			spherical	
Mahamallik et al, 2015[251]	SiO_2-CTAB commercial silica gel	$k_{app} = 2.1*10^{-3}$	No	37 ± 11 spherical	RT
Wu et al., 2013[252]	graphene oxide	$k_{app} = 6.1*10^{-3}$	No	10 spherical	RT
Wu et al., 2011[178]	Au@SiO_2 yolk shell structure	$k_1 = 4.8*10^{-3}$	Yes	3.3 ± 0.6 spherical	25
Wu et al., 2011[253]	EGCG grafted collagen fibers	$k_{app} = 2.4*10^{-3}$	Yes	10.7 ± 3.8 spherical	25

Table 18: List of references on the nitrophenol reduction on silver catalysts. For more complex architectures, the location of the active catalyst is indicated in the "support" column.

reference	support; structure	kinetic constant	isosbest. points	size / nm; shape	*T* / °C
Saha et al., 2010[223]	Ca-alginate microsphere beads	$k_0 = 1.7*10^{-7}$	Yes	7 ± 2 spherical	-
Lu et al., 2006[132]	PS@PNIPAM core-shell microgel*	$k_{app} = 2.2*10^{-3}$	Yes	8.5 ± 1.5 spherical	20
Lu et al., 2006[73]	PS@PNIPAM core-shell microgel*	$k_1 = 5.2*10^{-2}$	Yes	7.3 ± 1.5 spherical	20
Lu et al., 2006[61]	PS@PEGMA spherical branched polymer brushes	$k_1 = 7.3*10^{-2}$	Yes	7.5 ± 2 spherical	20
Elias et al., 2014[222]	PVP polymeric ligands	$k_L = 1.4*10^{-3}$	Yes	8.6 ± 2.5 spherical	15
Jana et al., 2016[254]	seralite SRA-400@Ag commercial resin beads	$k_{app} = 3.2*10^{-1}$	Yes	30 ± 5 coating	30
Horecha et al., 2014[255]	SiO_2@Ag@P((I-*b*-EG)-NIPAM-Bis) yolk shell structure	$k_{app} = 1.4*10^{-1}$ in THF:H_2O (9:1)	Yes	19.3 ± 3.8 spherical	25
Pradhan et al., 2001[90]	support free Ag NP	$k_{app} = 9.5*10^{-3}$	Yes	-	-
Pradhan et al., 2002[91]	support free Ag NP	-	Yes	25 spherical	-
Ai et al., 2012[256]	Fe_3O_4@Ba-alginate microsphere beads	$k_{app} = 4.5*10^{-3}$	No	72 spherical	RT

reference	support; structure	kinetic constant	isosbest. points	size / nm; shape	*T* / °C
Pootawang et al., 2012[257]	SiO_2 mesoporous silica	$k_{app} = 3.6*10^{-2}$	No	20.3 ± 0.8 spherical	-
Geng et al., 2014[258]	PEG_{43}-*b*-P($DMAEMA_{27}$-tBA_{32}-AA_{49}) block-/copolymer micelles	$k_{app} = 4.2*10^{-2}$	(No)	2.8 ± 1 spherical	25
Liang et al., 2014[104]	ESMf eggshell membrane fibers	$k_{app} = 4.2*10^{-3}$	Yes	4 ± 2 spherical	30
Liang et al., 2014[259]	ESMf@Pro modified eggshell membrane fibers	$k_{app} = 2.9*10^{-3}$	Yes	3 ± 2 spherical	35
Liu et al., 2014[62]	PS@PAA spherical polyelectrolyte brushes	$k_{app} = 3.0*10^{-3}$	Yes	2.8 spherical	20
Begum et al., 2017[172]	P(NIPAM-HEMA-AAc) copolymer microgel	$k_{c-mass} = 6.5$	Yes	10 ± 3 spherical	22
Naik et al., 2012[260]	γ-Al_2O_3 amorphous structure	$k_{app} = 3.2*10^{-3}$ $k_{app} = 5.0*10^{-3}$	No	6 ± 1 7.5 ± 2.5 spherical	RT
Manivannan et al., 2012[261]	SSG-β-CD silicate matrix composite	-	Yes	6.1 spherical	-
Yuan et al., 2013[182]	Ag@PANI core-shell structure	$k_1 = 3.6*10^{-2}$ $k_1 = 4.5*10^{-2}$ $k_1 = 6.6*10^{-2}$	No	63.5 ± 6 64.6 ± 8 65.2 ± 8 spherical	RT
Zhang et al., 2011[262]	PAN based electrospun carbon nanofibers	$k_{app} = 4.6*10^{-3}$	Yes	28.1 spherical	25
Chang et al., 2012[263]	PANI nanofibers	$k_{app} = 2.1*10^{-2}$	Yes	60 ± 40 spherical	RT
Wu et al., 2013[252]	graphene oxide	$k_{app} = 3.5*10^{-3}$	No	7.5 spherical	RT
Wang et al., 2013[264]	SH-SiO_2 functionalised commercial microspheres	$k_{app} = 1.2*10^{-3}$	Yes	35 ± 25 spherical	22
Wang et al., 2013[265]	Fe_3O_4@SiO_2-HPW@PG magnetic microspheres	$k_{app} = 6.7*10^{-3}$	Yes	8 spherical	RT
Xiao et al., 2012[266]	PAA-PVA electrospun nanofibrous mat	-	No	5.8 ± 2.4 spherical	RT
Baruah et al., 2013[267]	PGON polyelectrolyte ligands	$k_{app} = 5.5*10^{-3}$	Yes	18 ± 1 spherical	25
Naraginti et	kiwi fruit extract	-	Yes	32.5 ± 7.5	-

reference	support; structure	kinetic constant	isosbest. points	size / nm; shape	*T* / °C
al., 2017[268]				spherical	
Karki et al., 2018[269]	Ag-Fe_3O_4-ATO nanocomposite	$k_{app} = 1.7*10^{-2}$	Yes	- spherical	-
Shah et al., 2017[74]	P(NIPAM-MAA) copolymer microgel*	$k_{app} = 3.4*10^{-3}$	(Yes)	6.5 ± 0.5 spherical	-
Zhang et al., 2017[270]	Fe_3O_4@ SiO_2@Ag nanoflowers	$k_{app} = 8.6*10^{-3}$	Yes	dendritic coating	RT
Kim et al., 2017[271]	P(TEB-DITFB)-SH macroscopic sponge	$k_{app} = 7.6*10^{-3}$	Yes	7.1 spherical	-
Das et al., 2017[175]	HAP@PDA rod like morphology	$k_{app} = 5.0*10^{-3}$	Yes	14.8 spherical	RT
Liang et al., 2018[272]	NH_2 functionalised cellulose paper	$k_{app} = 1.5*10^{-2}$	(No)	4.4 spherical	35
Kumar et al., 2018[273]	graphene oxide	-	Yes	18 spherical	RT
Eising et al., 2011[183]	Dextran T500 commercial polysaccharide	$k_1 = 1.4*10^{-1}$	No	6.1 ± 1.3 spherical	25
Tzounis et al., 2014[274]	SiO_2@PEI polymer coated microsphere beads	$k_{app} = 2.9*10^{-2}$ $k_{app} = 5.1*10^{-2}$ $k_{app} = 9.3*10^{-2}$	Yes	4.2 ± 1.1 12.8 ± 3.4 18.6 ± 3.9 spherical	20
Shabir et al., 2017[44]	NTA small ligand molecules	$k_{app} = 7.0*10^{-3}$	No	30 spherical	-
	PVP polymer ligands	$k_{app} = 2.0*10^{-3}$	No	30 spherical	-
Signori et al., 2010[184]	octane- + EtOH-functionalised branced PEI polymer ligand	$k_1 = 5.7*10^{-1}$	Yes	24.5 ± 4.1 spherical	25
Muruga-doss et al., 2008[275]	chitosan polyaminosaccharide composite	$k_{mol} = 1.1$	Yes	3.2 spherical	23
Yin et al., 2017[276]	PBMS saccharide based porous organic network	$k_{app} = 5.1*10^{-3}$	Yes	12.5 ± 7.5 spherical	RT
Patil et al., 2017[277]	3,5-G2-BED-(triazole-EG_{17})$_2$ micelles	$k_{app} = 1.2*10^{-3}$	(Yes)	7.6 spherical	-
Zeng et al., 2017[278]	(Ag@NAC)@Halloysite nanotubes	$k_{app} = 1.5*10^{-2}$	No	2.6 ± 0.7 spherical	-
Zhang et al., 2017[279]	Ag@PPy janus particle type encapsulation	$k_{mass} = 7.3*10^{1}$	Yes	- spherical	-

reference	support; structure	kinetic constant	isosbest. points	size / nm; shape	*T* / °C
Liu et al., 2017[280]	Ni-foam@C@ZnO macroscopic support	$k_{app} = 1.4*10^{-2}$	Yes	134.8 spherical	-
Lu et al., 2017[281]	PAN@PDA (electrospun) nanofiber mats	$k_{mass} = 1.6*10^{1}$	Yes	80 ± 70	RT
Jiang et al., 2015[282]	Ag@Fe_2O_3 nanoporous microcubes	$k_{mass} = 4.7$	Yes	20.9 spherical	20
Bano et al., 2016[283]	Triton X-705 commercial polymer based micropo-rous macroscopic support	$k_{app} = 1.9*10^{-3}$	(No)	200	RT
Min et al., 2015[284]	NaCl@Ag nanocubes	$k_{app} = 1.7*10^{-2}$	Yes	- cubic	25
	- hollow Ag nanocubes	$k_{app} = 3.0*10^{-2}$	Yes	500 cubic	25
Chi et al., 2012[285]	OH- + COOH-functiona-lised mesoporous carbon	$k_{app} = 5.3*10^{-3}$	Yes	4.1 ± 0.6	25
Du et al., 2012[286]	Fe_3O_4@SiO_2 core-shell particles	$k_{app} = 2.2*10^{-3}$	Yes	10 spherical	RT
Qin et al., 2012[287]	PANI microspheres	$k_{app} = 2.7*10^{-3}$	Yes	10.5 ± 9.5 spherical	-
Zhou et al., 2015[288]	Fe_3O_4@PMAA magnetic core-shell microgel particles	$k_{app} = 2.5*10^{-2}$	Yes	- spherical	-
Muthucha-my et al., 2015	SiO_2 microspheres	$k_{app} = 1.1*10^{-2}$	Yes	7 ± 1 spherical	-
Kästner et al., 2016[105]	Ag@PAA dense polymer shell	$k_{c-mass} = 4.3*10^{2}$	(Yes)	3 ± 0.6 spherical	22
Xia et al., 2013[245]	DPS small ligand molecules	-	Yes	26 ± 1.6 spherical	25

Table 19: List of references of the 4-nitrophenol reduction on other metals, mixed metal and alloy catalysts, respectively. The used metals are indicated in the "support" column.

reference	support; structure	kinetic constant	isosbest. points	size / nm; shape	*T* / °C
Wunder et al., 2010[107]	PS@PMTAC-**Pt** SPB particles	$k_{L-H} = 4.6*10^{-4}$	Yes	2.3 ± 0.4 spherical	-
Esumi et al., 2004[108]	**Pt**@PAMAM-G4 dendrimers	$k_{app} = 2.6*10^{-3}$ $k_{app} = 1.2*10^{-3}$	No	1.5 ± 0.4 1.4 ± 0.3	15

reference	support; structure	kinetic constant	isosbest. points	size / nm; shape	*T* / °C
		$k_{app} = 9.6*10^{-4}$		1.2 ± 0.2 spherical	
	Pt@PPI-G4 dendrimers	$k_{app} = 1.2*10^{-3}$	No	1.4 ± 0.3 spherical	15
Mei et al., 2005[63]	PS@PMTAC-**Pt** SPB particles	$k_1 = 5.6*10^{-1}$ $k_1 = 1.1$	No	2.1 ± 0.4 spherical	15 30
Wu et al., 2012[189]	Fe_3O_4@P(S-DVB) @PMTAC-**Pt** SPB particles	$k_1 = 3.9\ x10^{-1}$	Yes	3.5 ± 0.5 spherical	20
Yuan et al., 2010[191]	**Pt**@P-2-(P($APTS_{72}$-b-$METAI_{95}$)-IEM_{2300} organosilica hybrid nanowires	$k_1 = 3.1*10^{-1}$	No	3.0 spherical	-
Noh et al., 2014[47]	**Pd**@PAMAM-G4-OH dendrimers	$k_{L-H} = 4.6*10^{-5}$	No	2.4 ± 0.6 spherical	21
Bingwa et al., 2014[48]	**Pd**@PAMAM-G4-OH dendrimers	$k_{L-H} = 1.8*10^{-6}$	Yes	1.3 ± 0.2 spherical	25
Morales et al., 2017[102]	**Pd**@HSAG commercial product	$k_n = 1.5*10^{5}$	No	2.6 spherical	RT
Mei et al., 2007[119]	PS@PMTAC-**Pd** SPB particles	$k_1 = 1.1$	Yes	2.4 ± 0.5 spherical	15
Halder et al., 2011[192]	oleylamine capped **Pd** nanoporous structure	$k_1 = 1.3*10^{-4}$	No	-	RT
Lu et al., 2012[289]	PPy-TiO_2@**Pd** nanofibers	$k_{app} = 1.2*10^{-2}$	No	2 spherical	RT
Dutta et al., 2014[290]	unsupported **Pd**	$k_{app} = 1.2*10^{-2}$ N_2H_4 red. agent	Yes	- nanoleaves	RT
Wang et al., 2013[233]	Fe_3O_4-**Pd** microspheres	$k_{mass} = 1.1*10^{-2}$	Yes	-	RT
	Fe_3O_4@CeO_2-**Pd** microspheres	$k_{mass} = 1.2*10^{-2}$	Yes	-	RT
	Fe_3O_4@SiO_2@CeO_2-**Pd** microspheres	$k_{mass} = 1.8*10^{-2}$	Yes	-	RT
Morales et al., 2017[102]	**Cu**@HSAG commercial product	$k_n = 1.2*10^{5}$	Yes	9.8 spherical	RT
	Cu@GOE	$k_n = 6.9*10^{5}$	No	3.5 ± 1.5 spherical	RT
	Cu@N-doped GOE	$k_n = 8.1*10^{4}$	No	6.5 ± 3.5 spherical	RT
Patil et al., 2017[277]	**Cu**@3,5-G2-BED-(triazole-EG_{17})$_2$ micelles	$k_0 = 3.5*10^{-3}$	Yes	3.9 spherical	-

reference	support; structure	kinetic constant	isosbest. points	size / nm; shape	*T* / °C
Antonels et al., 2013[190]	**Ru**@PAMAM-G4-OH dendrimers	$k_{L-H} = 1.8*10^{-5}$	(No)	1.2 ± 0.1 spherical	25
Liu et al., 2015[193]	**Ni**@P(NIPAM-AMPS) copolymer macrogel*	$k_{app} = 3.8*10^{-3}$	Yes	26.2 spherical	21
Wang et al., 2013[233]	Fe_3O_4@SiO_2@CeO_2-**Au-Pd** microspheres	$k_{mass} = 4.9$	Yes	-	RT
Li et al., 2016[64]	**Au** NR@PNIPAM-**Ag** core-shell microgel*	$k_{app} = 2.2*10^{-3}$	Yes	Ag: 8 ± 2 spherical	25
Lu et al., 2010[42]	PS@PNIPAM-**Au-Pt** NR core-shell microgel*	$k_1 = 2.1*10^{-1}$	(No)	7.4 ± 0.8 (d) 39.5 ± 6.5 (L)	25
Roy et al., 2016[291]	unsupported **Ag-Rh**	$k_{mass} = 2.6*10^{2}$ N_2H_4 red. agent	Yes	-	RT
Xia et al., 2013[245]	DPS-**Au-Ag** small ligand molecules	-	No	32 ± 1.6 spherical	25
Wu et al., 2013[252]	graphene oxide-**Ag-Au**	$k_{app} = 1.3*10^{-2}$	No	5 spherical	RT

7.2 Bibliography

1. Wedler, G. *Lehrbuch der Physikalischen Chemie*; Wiley-VCH: Weinheim, 2004.

2. Tao, F. *Metal Nanoparticles for Catalysis*; The Royal Society of Chemistry: Cambridge, 2014.

3. Ozkan, U. S. *Design of Heterogeneous Catalysts*; Wiley-VCH: Weinheim, 2009.

4. Dong, X.-Y.; Gao, Z.-W.; Yang, K.-F.; Zhang, W.-Q.; Xu, L.-W. Nanosilver as a new generation of silver catalysts in organic transformations for efficient synthesis of fine chemicals. *Catal. Sci. Technol.* **2015,** *5* (5), 2554-2574.

5. Noyori, R. Synthesizing our future. *Nat. Chem.* **2009,** *1* (1), 5-6.

6. Ertl, G.; Knötzinger, H.; Schüth, F.; Weitkamp, J. *Handbook of Heterogeneous Catalysis*; Wiley-VCH: Weinheim, 2008.

7. Rothenberg, G. *Catalysis - Concepts and Green Applications*; Wiley-VCH: Weinheim, 2008.

8. Astruc, D. *Nanoparticles and Catalysis*; Wiley-VCH2008.

9. Polshettiwar, V.; Varma, R. S. Green chemistry by nano-catalysis. *Green Chem.* **2010,** *12* (5), 743-754.

10. Roa, R.; Angioletti-Uberti, S.; Lu, Y.; Dzubiella, J.; Piazza, F.; Ballauff, M. Catalysis by metallic nanoparticles in solution: Thermosensitive microgels as nanoreactors. *Z. Phys. Chem.* **2018,** *232* (5-6), 773-803.

11. Herves, P.; Perez-Lorenzo, M.; Liz-Marzan, L. M.; Dzubiella, J.; Lu, Y.; Ballauff, M. Catalysis by metallic nanoparticles in aqueous solution: Model reactions. *Chem. Soc. Rev.* **2012,** *41* (17), 5577-5587.

12. Kuroda, K.; Ishida, T.; Haruta, M. Reduction of 4-nitrophenol to 4-aminophenol over Au nanoparticles deposited on PMMA. *J. Mol. Catal. A* **2009,** *298* (1-2), 7-11.

13. Shiraishi, Y.; Toshima, N. Colloidal silver catalysts for oxidation of ethylene. *J. Mol. Catal. A* **1999,** *141* (1-3), 187192.

14. Haruta, M. When gold is not noble: Catalysis by nanoparticles. *Chem. Rec.* **2003,** *3* (2), 75-87.

15. Bond, G. C.; Sermon, P. A. Gold catalysts for olefin hydrogenation. *Gold Bull.* **1973,** *6* (4), 102-105.

16. Schwank, J. Catalytic gold: Applications of elemental gold in heterogeneous catalysis. *Gold Bull.* **1983,** *16*, 103-110.

17. Louis, C.; Pluchery, O. *Gold Nanoparticles*; Imperial College Press: London, 2012.

18. Haruta, M.; Kobayashi, T.; Sano, H.; Yamada, N. Novel gold catalysts for the oxidation of carbon monoxide at a temperature far below 0 °C. *Chem. Lett.* **1987,** *16* (2), 405-408.

19. Corma, A.; Garcia, H. Supported gold nanoparticles as catalysts for organic reactions. *Chem. Soc. Rev.* **2008,** *37* (9), 2096-2126.

20. Walters, R. D.; Weimer, J. J.; Smith, J. E. An investigation of the activity of coprecipitated gold catalysts for methane oxidation. *Catal. Lett.* **1995,** *30* (1-4), 181-188.

21. Hayashi, T.; Tanaka, K.; Haruta, M. Selective vapor-phase epoxidation of propylene over Au/TiO2 catalysts in the presence of oxygen and hydrogen. *J. Catal.* **1998,** *178* (2), 566-575.

22. Nkosi, B.; Adams, M. D.; Coville, N. J.; Hutchings, G. J. Hydrochlorination of acetylene using carbon-supported gold catalysts: A study of catalyst reactivation. *J. Catal.* **1991,** *128* (2), 378-386.

23. Daniel, M.-C.; Astruc, D. Gold nanoparticles: Assembly, supramolecular chemistry, quantum-size-related properties, and applications toward biology, catalysis, and nanotechnology. *Chem. Rev.* **2004,** *104* (1), 293-346.

24. Najeeb, J.; Ahmad, G.; Nazir, S.; Naseem, K.; Kanwal, A. Critical analysis of various supporting mediums employed for the incapacitation of silver nanomaterial for aniline and phenolic pollutants: A review. *Korean J. Chem. Eng.* **2017**, 1-16.

25. Na, K.; Zhang, Q.; Somorjai, G. A. Colloidal metal nanocatalysts: Synthesis, characterization, and catalytic applications. *J. Clust. Sci* **2013,** *25* (1), 83-114.

26. Pushkarev, V. V.; Zhu, Z.; An, K.; Hervier, A.; Somorjai, G. A. Monodisperse metal nanoparticle catalysts: Synthesis, characterizations, and molecular studies under reaction conditions. *Top. Catal.* **2012,** *55* (19-20), 1257-1275.

27. Zahmakiran, M.; Ozkar, S. Metal nanoparticles in liquid phase catalysis; from recent advances to future goals. *Nanoscale* **2011,** *3* (9), 3462-3481.

28. Sibbald, M. S.; Chumanov, G.; Cotton, T. M. Reduction of cytochrome c by halide-modified, laser-ablated silver colloids. *J. Phys. Chem.* **1996,** *100* (11), 4672-4678.

29. Mafuné, F.; Kohno, Y.; Takeda, Y.; Kondow, T. Full physical preparation of size-selected gold nanoparticles in solution: laser ablation and laser-induced size control. *J. Phys. Chem. B* **2002,** *106* (31), 7575-7577.

30. Bronstein, L.; Chernyshov, D.; Valetsky, P. Laser photolysis formation of gold colloids in block copolymer micelles. *Langmuir* **1999,** *15* (1), 83-91.

31. Campelo, J. M.; Luna, D.; Luque, R.; Marinas, J. M.; Romero, A. A. Sustainable preparation of supported metal nanoparticles and their applications in catalysis. *ChemSusChem* **2009,** *2* (1), 18-45.

32. Sau, T. K.; Pal, A.; Jana, N. R.; Wang, Z. L.; Pal, T. Size controlled synthesis of gold nanoparticles using photochemically prepared seed particles. *J. Nanopart. Res.* **2001,** *3* (4), 257-261.

33. Zhou, Y.; Wang, C. Y.; Zhu, Y. R.; Chen, Z. Y. A novel ultraviolet irradiation technique for shape-controlled synthesis of gold nanoparticles at room temperature. *Chem. Mater.* **1999,** *11* (9), 2310-2312.

34. Lee, H. J.; Je, J. H.; Hwu, Y.; Tsai, W. L. Synchrotron X-ray induced solution precipitation of nanoparticles. *Nucl. Instrum. Meth. B* **2003,** *199*, 342-347.

35. Gachard, E.; Remita, H.; Khatouri, J.; Keita, B.; Nadjo, L.; Belloni, J. Radiation-induced and chemical formation of gold clusters. *New J. Chem.* **1998,** *22* (11), 1257-1265.

36. Mills, G.; Henglein, A. Radiation chemical formation of colloidal iridium and mechanism of catalysed hydrogen formation by radicals. *Radiat. Phys. Chem.* **1985,** *26* (4), 385-390.

37. Okitsu, K.; Yue, A.; Tanabe, S.; Matsumoto, H.; Yokibo, Y. Formation of colloidal gold nanoparticles in an ultrasonic field: Control of rate of gold(III) reduction and size of formed gold particles. *Langmuir* **2001,** *17* (25), 7717-7720.

38. Chen, W.; Cai, W. P.; Liang, C. H.; Zhang, L. D. Synthesis of gold nanoparticles dispersed within pores of mesoporous silica induced by ultrasonic irradiation and its characterization. *Mater. Res. Bull.* **2001,** *36* (1-2), 335-342.

39. Nakamoto, M.; Yamamoto, M.; Fukusumi, M. Thermolysis of gold (I) thiolate complexes producing novel gold nanoparticles passivated by alkyl groups. *Chem. Commun.* **2002,** *15*, 1622-1623.

40. Begum, R.; Rehan, R.; Farooqi, Z. H.; Butt, Z.; Ashraf, S. Physical chemistry of catalytic reduction of nitroarenes using various nanocatalytic systems: Past, present, and future. *J. Nanopart. Res.* **2016,** *18* (8), 231.

41. Turkevich, J.; Stevenson, P. C.; Hillier, J. A study of the nucleation and growth processes in the synthesis of colloidal gold. *Discuss. Faraday Soc.* **1951,** *11*, 55-75.

42. Lu, Y.; Yuan, J.; Polzer, F.; Drechsler, M.; Preussner, J. In situ growth of catalytic active Au-Pt bimetallic nanorods in thermoresponsive core-shell microgels. *ACS Nano* **2010,** *4* (12), 7078-7086.

43. Kumar, A.; Mandal, S.; Selvakannan, P. R.; Pasricha, R.; Mandale, A. B.; Sastri, M. Investigation into the interaction between surface-bound alkylamines and gold nanoparticles. *Langmuir* **2003,** *19* (15), 6277-6282.

44. Shabir, J.; Rani, S.; Garkoti, C.; Mozumdar, S. Nitrolotriacetic acid assisted one step synthesis of highly stable silver nanoparticles in aqueous medium: Investigation of catalytic activity. *Mater. Lett.* **2017,** *209*, 207-211.

45. Steinigeweg, D.; Schlucker, S. Monodispersity and size control in the synthesis of 20-100 nm quasi-spherical silver nanoparticles by citrate and ascorbic acid reduction in glycerol-water mixtures. *Chem. Commun.* **2012,** *48* (69), 8682-8684.

46. Esumi, K.; Miyamoto, K.; Yoshimura, T. Comparison of PAMAM–Au and PPI–Au nanocomposites and their catalytic activity for reduction of 4-nitrophenol. *J. Colloid Interf. Sci.* **2002,** *254* (2), 402-405.

47. Noh, J.-H.; Meijboom, R. Catalytic evaluation of dendrimer-templated Pd nanoparticles in the reduction of 4-nitrophenol using Langmuir–Hinshelwood kinetics. *Appl. Surf. Sci.* **2014,** *320*, 400-413.

48. Bingwa, N.; Meijboom, R. Kinetic evaluation of dendrimer-encapsulated palladium nanoparticles in the 4-nitrophenol reduction reaction. *J. Phys. Chem. C* **2014,** *118* (34), 19849-19858.

49. Ciganda, R.; Li, N.; Deraedt, C.; Gatard, S.; Zhao, P.; Salmon, L.; Hernandez, R.; Ruiz, J.; Astruc, D. Gold nanoparticles as electron reservoir redox catalysts for 4-nitrophenol reduction: A strong stereoelectronic ligand influence. *Chem. Commun.* **2014,** *50* (70), 10126-10129.

50. Shifrina, Z. B.; Matveeva, V. G.; Bronstein, L. M. Role of polymer structures in catalysis by transition metal and metal oxide nanoparticle composites. *Chem. Rev.* **2020,** *120*, 1350-1396.

51. Tsunoyama, H.; Tsukuda, T. Magic numbers of gold clusters stabilized by PVP. *J. Am. Chem. Soc.* **2009,** *131* (51), 18216-18217.

52. Wang, Y.; Wei, G.; Zhang, W.; Jiang, X.; Zheng, P.; Shi, L.; Dong, A. Responsive catalysis of thermoresponsive micelle-supported gold nanoparticles. *J. Mol. Catal. A* **2007,** *266* (1-2), 233-238.

53. Seo, E.; Kim, J.; Hong, Y.; Kim, Y. S.; Lee, D.; Kim, B.-S. Double hydrophilic block copolymer templated Au nanoparticles with enhanced catalytic activity toward nitroarene reduction. *J. Phys. Chem. C* **2013,** *117* (22), 11686-11693.

54. Chen, X.; Zhao, D.; An, Y.; Zhang, Y.; Cheng, J.; Wang, B.; Shi, L. Formation and catalytic activity of spherical composites with surfaces coated with gold nanoparticles. *J. Colloid Interf. Sci.* **2008,** *322* (2), 414-420.

55. Kocak, G.; Bütün, V. Synthesis and stabilization of Pt nanoparticles in core cross-linked micelles prepared from an amphiphilic diblock copolymer. *Colloid. Polym. Sci.* **2015,** *293* (12), 3563-3572.

56. Ortega-Muñoz, M.; Blanco, V.; Hernandez-Mateo, F.; Lopez-Jaramillo, F. J.; Santoyo-Gonzales, F. Catalytic materials based on surface coating with poly(ethyleneimine)-stabilized gold nanoparticles. *ChemCatChem* **2017,** *9* (20), 3965-3973.

57. Zhang, Y.; Liu, P.; Li, B.-G.; Wang, W.-J. CO2-triggered recoverable metal catalyst nanoreactors using unimolecular core–shell star copolymers as carriers. *ACS Appl. Nano Mater.* **2018,** *1* (3), 1280-1290.

58. Shi, Y.; Liu, L.; Zhang, F.; Niu, M.; Zhao, Y.; Fan, Y.; Liang, Y.; Liu, M.; Zhang, Z.; Wang, J. Catalyst system for hydrogenation catalysis based on multiarm hyperbranched polymer templated metal (Au, Pt, Pd, Cu) nanoparticles. *Polymers* **2017,** *9* (9), 459.

59. Tabatabaei Rezaei, S. J.; Shamseddin, A.; Ramazani, A.; Mashhadi Malekzadeh, A.; Azimzadeh Asiabi, P. Palladium nanoparticles immobilized on amphiphilic and hyperbranched polymer-functionalized magnetic nanoparticles: An efficient semi-heterogeneous catalyst for Heck reaction. *Appl. Organomet. Chem.* **2017,** *31* (9), e3707.

60. Zhang, M.; Liu, L.; Wu, C.; Fu, G.; Zhao, H.; He, B. Synthesis, characterization and application of well-defined environmentally responsive polymer brushes on the surface of colloid particles. *Polymer* **2007,** *48* (7), 1989-1997.

61. Lu, Y.; Mei, Y.; Walker, R.; Ballauff, M.; Drechsler, M. 'Nano-tree'—type spherical polymer brush particles as templates for metallic nanoparticles. *Polymer* **2006,** *47* (14), 4985-4995.

62. Liu, J.; Wang, J.; Zhu, Z.; Li, L.; Guo, X.; Lincoln, S. F.; Prud'homme, R. K. Cooperative catalytic activity of cyclodextrin and Ag nanoparticles immobilized on spherical polyelectrolyte brushes. *AIChE J.* **2014,** *60* (6), 1977-1982.

63. Mei, Y.; Sharma, G.; Lu, Y.; Ballauff, M.; Drechsler, M.; Irrgang, T.; Kempe, R. High catalytic activity of platinum nanoparticles immobilized on spherical polyelectrolyte brushes. *Langmuir* **2005,** *21* (26), 12229-12234.

64. Li, S.; Lin, D.; Zhou, J.; Zha, L. Preparation of silver nanoparticles loaded photoresponsive composite microgels and their light-controllable catalytic activit. *J. Phys. Chem. C* **2016,** *120* (9), 4902-4908.

65. Pich, A.; Karak, A.; Lu, Y.; Ghosh, A. K.; Adler, H.-J. P. Tuneable catalytic properties of hybrid microgels containing gold nanoparticles. *J. Nanosci. Nanotechnol.* **2006,** *6* (12), 3763-3769.

66. Liu, G.; Wang, D.; Zhou, F.; Liu, W. Electrostatic self-assembly of Au nanoparticles onto thermosensitive magnetic core-shell microgels for thermally tunable and magnetically recyclable catalysis. *Small* **2015,** *11* (23), 2807-2816.

67. Brandel, T.; Sabadasch, V.; Hannappel, Y.; Hellweg, T. Improved smart microgel carriers for catalytic silver nanoparticles. *ACS Omega* **2019,** *4* (3), 4636-4649.

68. Dupin, D.; Fujii, S.; Armes, S. P. Efficient synthesis of sterically stabilized pH-responsive microgels of controllable particle diameter by emulsion polymerization. *Langmuir* **2006,** *22* (7), 3381-3387.

69. Liu, S.; Weaver, J. V. M.; Save, M.; Armes, S. P. Synthesis of pH-responsive shell cross-linked micelles and their use as nanoreactors for the preparation of gold nanoparticles. *Langmuir* **2002,** *18* (22), 8350-8357.

70. Nayak, S.; Lyon, L. A. Photoinduced phase transitions in poly (N-isopropylacrylamide) microgels. *Chem. Mater.* **2004,** *16* (13), 2623-2627.

71. Wu, Q.; Cheng, H.; Chang, A.; Xu, W.; Lu, F.; Wu, W. Glucose-mediated catalysis of Au nanoparticles in microgels. *Chem. Commun.* **2015,** *51* (89), 16068-16071.

72. Wu, S.; Dzubiella, J.; Kaiser, J.; Drechsler, M.; Guo, X.; Ballauff, M.; Lu, Y. Thermosensitive Au-PNIPA yolk-shell nanoparticles with tunable selectivity for catalysis. *Angew. Chem. Int. Ed.* **2012,** *51* (9), 2229-2233.

73. Lu, Y.; Mei, Y.; Ballauff, M. Thermosensitive core-shell particles as carrier systems for metallic nanoparticles. *J. Phys. Chem. B* **2006,** *110* (9), 3930-3937.

74. Shah, L. A.; Sayed, M.; Siddiq, M. Fabrication of Ag and Au nanoparticles in cross-linked polymer microgels for their comparative catalytic study. *Mater. Sci. Poland* **2017,** *35* (3), 651-659.

75. Shi, S.; Wang, Q.; Wang, T.; Ren, S.; Gao, Y.; Wang, N. Thermo-, pH-, and light-responsive poly(N-isopropylacrylamide-co-methacrylic acid)–Au hybrid microgels prepared by the in situ reduction method based on Au-thiol chemistry. *J. Phys. Chem. B* **2014,** *118* (25), 7177-7186.

76. Jones, C. D.; Lyon, L. A. Synthesis and characterization of multiresponsive core-shell microgels. *Macromol. Chem.* **2000,** *33* (22), 8301-8306.

77. Lanzalaco, S.; Armelin, E. Poly (N-isopropylacrylamide) and copolymers: A review on recent progresses in biomedical applications. *Gels* **2017,** *3* (4), 36.

78. M. Karg, T. H. Smart inorganic/organic hybrid microgels: Synthesis and characterisation. *J. Mater. Chem.* **2009,** *19* (46), 8714-8727.

79. de Las Heras Alarcón, C.; Pennadam, S.; Alexander, C. Stimuli responsive polymers for biomedical applications. *Chem. Soc. Rev.* **2005,** *34* (3), 276-285.

80. Nolan, C. M.; Serpe, M. J.; Lyon, L. A. Thermally modulated insulin release from microgel thin films. *Biomacromolecules* **2004,** *5* (5), 1940-1946.

81. Oh, J. K.; Drumright, R.; Siegwart, D. J.; Matyjaszewski, K. The development of microgels/nanogels for drug delivery applications. *Prog. Polym. Sci.* **2008,** *33* (4), 448-477.

82. Hendrickson, G. R.; Andrew Lyon, L. Bioresponsive hydrogels for sensing applications. *Soft Matter* **2009,** *5* (1), 29-35.

83. Lapeyre, V.; Gosse, I.; Chevreux, S.; Ravaine, V. Monodispersed glucose-responsive microgels operating at physiological salinity. *Biomacromolecules* **2006,** *7* (12), 3356-3363.

84. Ballauff, M.; Lu, Y. “Smart” nanoparticles: Preparation, characterization and applications. *Polymer* **2007,** *48* (7), 1815-1823.

85. Roy, D.; Brooks, W. L.; Sumerlin, B. S. New directions in thermoresponsive polymers. *Chem. Soc. Rev.* **2013,** *42* (17), 7214-7243.

86. Fujishige, S.; Kubota, K.; Ando, I. Phase transition of aqueous solutions of poly (N-isopropylacrylamide) and poly (N-isopropylmethacrylamide). *J. Phys. Chem.* **1989,** *93* (8), 3311-3313.

87. Xia, Y.; Xia, X.; Peng, H. C. Shape-controlled synthesis of colloidal metal nanocrystals: Thermodynamic versus kinetic products. *J. Am. Chem. Soc.* **2015,** *137* (25), 7947-7966.

88. Pal, J.; Pal, T. Faceted metal and metal oxide nanoparticles: Design, fabrication and catalysis. *Nanoscale* **2015,** *7* (34), 14159-14190.

89. Ishida, T.; Murayama, T.; Taketoshi, A.; Haruta, M. Importance of size and contact structure of gold nanoparticles for the genesis of unique catalytic processes. *Chem. Rev.* **2020,** *120*, 464-525.

90. Pradhan, N.; Pal, A.; Pal, T. Catalytic reduction of aromatic nitro compounds by coinage metal nanoparticles. *Langmuir* **2001,** *17* (5), 1800-1802.

91. Pradhan, N.; Pal, A.; Pal, T. Silver nanoparticle catalyzed reduction of aromatic nitro compounds. *Colloid Surface A* **2002,** *196* (2-3), 247-257.

92. Zhao, P.; Feng, X.; Huang, D.; Yang, G.; Astruc, D. Basic concepts and recent advances in nitrophenol reduction by gold- and other transition metal nanoparticles. *Coordin. Chem. Rev.* **2015,** *287*, 114-136.

93. Haber, F. Über stufenweise Reduktion des Nitrobenzols mit begrenztem Kathodenpotential. *Z. Electrochem.* **1898,** *4* (22), 506-514.

94. Blaser, H.-U. A golden boost to an old reaction. *Science* **2006,** *313* (5785), 312-313.

95. Baumeister, P.; Blaser, H.-U.; Studer, M. Strong reduction of hydroxylamine accumulation in the catalytic hydrogenation of nitroarenes by vanadium promoters. *Catal. Lett.* **1997,** *49* (3-4), 219-222.

96. Studer, M.; Neto, S.; Blaser, H.-U. Modulating the hydroxylamine accumulation in the hydrogenation of substituted nitroarenes using vanadium-promoted RNi catalysts. *Top. Catal.* **2000,** *13* (3), 205-212.

97. He, X.; Liu, Z.; Fan, F.; Qiang, S.; Cheng, L.; Yang, W. Poly(ionic liquids) hollow nanospheres with PDMAEMA as joint support of highly dispersed gold nanoparticles for thermally adjustable catalysis. *J. Nanopart. Res.* **2015,** *17* (2), 74.

98. Yamamoto, H.; Yano, H.; Kouchi, H.; Obora, Y.; Arakawa, R.; Kawasaki, H. N,N-Dimethylformamide-stabilized gold nanoclusters as a catalyst for the reduction of 4-nitrophenol. *Nanoscale* **2012,** *4* (14), 4148-4154.

99. Han, J.; Li, L.; Guo, R. Novel approach to controllable synthesis of gold nanoparticles supported on polyaniline nanofibers. *Macromolecules* **2010,** *43* (24), 10636-10644.

100. Zhao, P.; Li, N.; Salmon, L.; Liu, N.; Ruiz, J.; Astruc, D. How a simple "clicked" PEGylated 1,2,3-triazole ligand stabilizes gold nanoparticles for multiple usage. *Chem. Commun.* **2013,** *49* (31), 3218-3220.

101. Li, M.; Chen, G. Revisiting catalytic model reaction p-nitrophenol/NaBH4 using metallic nanoparticles coated on polymeric spheres. *Nanoscale* **2013,** *5* (23), 11919-11927.

102. Morales, M. V.; Rocha, M.; Freire, C.; Asedegbega-Nieto, E.; Gallegos-Suarez, E.; Rodríguez-Ramos, I.; Guerrero-Ruiz, A. Development of highly efficient Cu versus Pd catalysts supported on graphitic carbon materials for the reduction of 4-nitrophenol to 4-aminophenol at room temperature. *Carbon* **2017,** *111*, 150-161.

103. Cui, Q.; Shen, G.; Yan, X.; Li, L.; Mohwald, H.; Bargheer, M. Fabrication of Au@Pt multibranched nanoparticles and their application to in situ SERS monitoring. *ACS Appl. Mater. Inter.* **2014,** *6* (19), 17075-17081.

104. Liang, M.; Su, R.; Qi, W.; Yu, Y.; Wang, L.; He, Z. Synthesis of well-dispersed Ag nanoparticles on eggshell membrane for catalytic reduction of 4-nitrophenol. *J. Mater. Sci.* **2014,** *49* (4), 1639-1647.

105. Kästner, C.; Thünemann, A. F. Catalytic reduction of 4-nitrophenol using silver nanoparticles with adjustable activity. *Langmuir* **2016,** *32* (29), 7383-7391.

106. Ismail, A. A.; Hakki, A.; Bahnemann, D. W. Mesostructure Au/TiO2 nanocomposites for highly efficient catalytic reduction of p-nitrophenol. *J. Mol. Catal. A* **2012,** *358*, 145-151.

107. Wunder, S. P., Frank; Lu, Yan; Mei, Yu; Ballauff, M. Kinetic analysis of catalytic reduction of 4-nitrophenol by metallic nanoparticles immobilized in spherical polyelectrolyte brushes. *J. Phys. Chem. C* **2010,** *114* (19), 8814-8820.

108. Esumi, K.; Isono, R.; Yoshimura, T. Preparation of PAMAM- and PPI-metal (silver, platinum, and palladium) nanocomposites and their catalytic activities for reduction of 4-nitrophenol. *Langmuir* **2004,** *20* (1), 237-243.

109. Gu, S.; Wunder, S.; Lu, Y.; Ballauff, M.; Fenger, R.; Rademann, K.; Jaquet, B.; Zaccone, A. Kinetic analysis of the catalytic reduction of 4-nitrophenol by metallic nanoparticles. *J. Phys. Chem. C* **2014,** *118* (32), 18618-18625.

110. Hayakawa, K.; Yoshimura, T.; Esumi, K. Preparation of gold-dendrimer nanocomposites by laser irradiation and their catalytic reduction of 4-nitrophenol. *Langmuir* **2003,** *19* (13), 5517-5521.

111. Menumerov, E.; Hughes, R. A.; Neretina, S. Catalytic reduction of 4-nitrophenol: A quantitative assessment of the role of dissolved oxygen in determining the induction time. *Nano Lett.* **2016,** *16* (12), 7791-7797.

112. Neal, R. D.; Inoue, Y.; Hughes, R. A.; Neretina, S. Catalytic reduction of 4-nitrophenol by gold catalysts: The influence of borohydride concentration on the induction time. *J. Phys. Chem. C* **2019,** *123* (20), 12894-12901.

113. Wunder, S.; Lu, Y.; Albrecht, M.; Ballauff, M. Catalytic activity of faceted gold nanoparticles studied by a model reaction: Evidence for substrate-induced surface restructuring. *ACS Catal.* **2011,** *1* (8), 908-916.

114. Corma, A.; Concepción, P.; Serna, P. A different reaction pathway for the reduction of aromatic nitro compounds on gold catalysts. *Angew. Chem. Int. Ed.* **2007,** *46* (38), 7266-7269.

115. Gu, S.; Kaiser, J.; Marzun, G.; Ott, A.; Lu, Y.; Ballauff, M.; Zaccone, A.; Barcikowski, S.; Wagener, P. Ligand-free gold nanoparticles as a reference material for kinetic modelling of catalytic reduction of 4-nitrophenol. *Catal. Lett.* **2015,** *145* (5), 1105-1112.

116. Cao, J.; Mei, S.; Jia, H.; Ott, A.; Ballauff, M.; Lu, Y. In situ synthesis of catalytic active Au nanoparticles onto gibbsite–polydopamine core–shell nanoplates. *Langmuir* **2015,** *31* (34), 9483-9491.

117. Fenger, R.; Fertitta, E.; Kirmse, H.; Thünemann, A. F.; Rademann, K. Size dependent catalysis with CTAB-stabilized gold nanoparticles. *Phys. Chem. Chem. Phys.* **2012,** *14* (26), 9343-9349.

118. Panigrahi, S.; Basu, S.; Praharaj, S.; Pande, S.; Jana, S.; Pal, A.; Ghosh, S. K.; Pal, T. Synthesis and size-selective catalysis by supported gold nanoparticles: Study on heterogeneous and homogeneous catalytic process. *J. Phys. Chem. C* **2007,** *111* (12), 4596-4605.

119. Mei, Y.; Lu, Y.; Polzer, F.; Ballauff, M. Catalytic activity of palladium nanoparticles encapsulated in spherical polyelectrolyte brushes and core-shell microgels. *Chem. Mater.* **2007,** *19* (5), 1062-1069.

120. Freund, T. Kinetics of the reduction of inorganic ions by borohydride - I Ferricyanide. *J. Inorg. Nucl. Chem.* **1959,** *9* (3-4), 246-251.

121. Bhattacharjee, M.; Bhattacharjee, A. K.; Mahanti, M. K. Kinetics and mechanism of reduction of hexacyanoferrate(III) by sodium tetrahydroborate. *Bull. Chem. Soc. Jpn.* **1981,** *54* (11), 3566-3569.

122. Freund, P. L.; Spiro, M. Colloidal catalysis: the effect of sol size and concentration. *J. Phys. Chem.* **1985,** *89* (7), 1074-1077.

123. Narayanan, R.; El-Sayed, M. A. Shape-dependent catalytic activity of platinum nanoparticles in colloidal solution. *Nano Lett.* **2004,** *4* (7), 1343-1348.

124. Carregal-Romero, S.; Pérez-Juste, J.; Hervés, P.; Liz-Marzán, L. M.; Mulvaney, P. Colloidal gold-catalyzed reduction of ferrocyanate(III) by borohydride ions: A model system for redox catalysis. *Langmuir* **2009,** *26* (2), 1271-1277.

125. Carregal-Romero, S.; Buurma, N. J.; Pérez-Juste, J.; Liz-Marzán, L. M.; Hervés, P. Catalysis by Au@pNIPAM nanocomposites: Effect of the cross-linking density. *Chem. Mater.* **2010,** *22* (10), 3051-3059.

126. Roa, R.; Kim, W. K.; Kanduč, M.; Dzubiella, J.; Angioletti-Uberti, S. Catalyzed bimolecular reactions in responsive nanoreactors. *ACS Catal.* **2017,** *7* (9), 5604-5611.

127. Nóbrega, J. A.; Rocha, F. R. P. Ionic strength effect on the rate of reduction of Hexacyanoferrate(III) by ascorbic acid: A flow injection kinetic experiment. *J. Chem. Educ.* **1997,** *74* (5), 560-562.

128. Roy, S.; Rao, A.; Devatha, G.; Pillai, P. P. Revealing the role of electrostatics in gold-nanoparticle-catalyzed reduction of charged substrates. *ACS Catal.* **2017,** *7* (10), 7141-7145.

129. Cheng, C.; Zhang, C.; Wang, D. Using hydrogel to diversify the adaptability and applicability of functional nanoparticles: From nanotech-flavored jellies to artificial enzymes. *Langmuir* **2019,** *35* (26), 8612-8628.

130. Gawlitza, K.; Turner, S. T.; Polzer, F.; Wellert, S.; Karg, M.; Mulvaney, P.; von Klitzing, R. Interaction of gold nanoparticles with thermoresponsive microgels: Influence of the cross-linker density on optical properties. *Phys. Chem. Chem. Phys.* **2013,** *15* (37), 15623-15631.

131. Gehrke, S. H. Synthesis, equilibrium swelling, kinetics, permeability and applications of environmentally responsive gels. In *Responsive gels: Volume transitions II*; Springer: Berlin, Heidelberg, 1993, pp 81-144.

132. Lu, Y.; Mei, Y.; Drechsler, M.; Ballauff, M. Thermosensitive core-shell particles as carriers for Ag nanoparticles: Modulating the catalytic activity by a phase transition in networks. *Angew. Chem. Int. Ed.* **2006,** *45* (5), 813-816.

133. Kanduč, M.; Kim, W. K.; Roa, R.; Dzubiella, J. Modeling of stimuli-responsive nanoreactors: Rational rate control towards the design of colloidal enzymes. *Mol. Sys. Des. Eng.* **2020,** *xx*, xxxx.

134. Palasis, M.; Gehrke, S. H. Permeability of responsive poly (N-isopropylacrylamide) gel to solutes. *J. Control. Release* **1992,** *18* (1), 1-11.

135. Gehrke, S. H.; Fisher, J. P.; Palasis, M.; Lund, M. E. Factors determining hydrogel permeability. *Ann. N.-Y. Acad. Sci.* **1997,** *831* (1), 179-184.

136. Witten, J.; Ribbeck, K. The particle in the spider's web: Transport through biological hydrogels. *Nanoscale* **2017,** *9* (24), 8080-8095.

137. Amsden, B. Solute diffusion within hydrogels. Mechanisms and models. *Macromol.* **1998,** *31* (23), 8382-8395.

138. Sassi, A. P.; Shaw, A. J.; Han, S. M.; Blanch, H. W.; Prausnitz, J. M. Partitioning of proteins and small biomolecules in temperature-and pH-sensitive hydrogels. *Polymer* **1996,** *37* (11), 2151-2164.

139. Schild, H. G. Poly (N-isopropylacrylamide): experiment, theory and application. *Prog. Polym. Sci.* **1992,** *17* (2), 163-249.

140. Ahmed, Z.; Gooding, E. A.; Pimenov, K. V.; Wang, L.; Asher, S. A. UV resonance Raman determination of molecular mechanism of poly(N-isopropylacrylamide) volume phase transition. *J. Phys. Chem. B* **2009,** *113* (13), 4248-4256.

141. Upadhyay, S. K. *Chemical Kinetics and Reaction Dynamics*; Springer: New York, 2006.

142. Calef, D. F.; Deutch, J. M. Diffusion-controlled reactions. *Ann. Rev. Phys. Chem.* **1983,** *34* (34), 493-524.

143. Kanduč, M.; Kim, W. K.; Roa, R.; Dzubiella, J. Aqueous nanoclusters govern ion partitioning in dense polymer membranes. *ACS Nano* **2019,** *13* (10), 11224-11234.

144. Vannice, M. A. *Kinetics of Catalytic Reactions*; Springer: New York, 2013.

145. Freundlich, H. Über die Adsorption in Lösungen. *Z, Phys. Chem* **1907,** *57* (1), 385-470.

146. Rill, C.; Kolar, Z. I.; Kickelbick, G.; Wolterbeek, H. T.; Peters, J. A. Kinetics and thermodynamics of adsorption on hydroxyapatite of the [160Tb] terbium complexes of the bone-targeting ligands DOTP and BPPED. *Langmuir* **2009,** *25* (4), 2294-2301.

147. Jaronieck, M.; Deryło, A.; Marczewski, A. The Langmuir-Freundlich equation in adsorption from dilute solutions on solids. *Monatsh. Chem.* **1983,** *114* (4), 393-397.

148. Sips, R. On the structure of a catalyst surface. *J. Chem. Pys.* **1948,** *16* (5), 490-495.

149. Logan, S. R. *Fundamentals of Chemical Kinetics*; Longman: London, 1996.

150. Glasser, L. Rates of bimolecular heterogeneous reactions following the Langmuir-Hinshelwood mechanism. *J. Chem. Educ.* **1979,** *56* (1), 22-23.

151. Smoluchowski, M. v. Versuch einer mathematischen Theorie der Koagulationskinetik kolloider Lösnngen. *Z. Phys. Chem.* **1917,** *92*, 129-168.

152. Galanti, M.; Fanelli, D.; Angioletti-Uberti, S.; Ballauff, M.; Dzubiella, J.; Piazza, F. Reaction rate of a composite core-shell nanoreactor with multiple nanocatalysts. *Phys. Chem. Chem. Phys.* **2016,** *18* (30), 20758-20767.

153. Roa, R.; Siegl, T.; Kim, W. K.; Dzubiella, J. Product interactions and feedback in diffusion-controlled reactions. *J. Chem. Phys.* **2018,** *148* (6), 064705.

154. Evans, D. F.; Wennerström, H. *The Colloidal Domain: Where Physics, Chemistry, Biology, and Technology Meet*; Wiley-VCH: Weinheim, 1999.

155. Zhou, Y. C.; Lu, B.; Huber, G. A.; Holst, M. J.; McCammon, J. A. Continuum simulations of acetylcholine consumption by acetylcholinesterase: A Poisson-Nernst-Planck approach. *J. Phys. Chem. B* **2008,** *112* (2), 270-275.

156. Dingenouts, N.; Norhausen, C.; Ballauff, M. Observation of the volume transition in thermosensitive core-shell latex particles by small-angle X-ray scattering. *Macromolecules* **1998,** *31* (25), 8912-8917.

157. Wisniak, J.; Klein, M. Reduction of nitrobenzene to aniline. *Ind. Eng. Chem. Prod. Res. Dev.* **1984,** *23* (1), 44-50.

158. Makaryan, J. A.; Savchenko, V. I. n-Arylhydroxylamines transformation in the presense of heterogeneous catalysts. In *Studies in Surface Science and Catalysis. Vol. 75*; Elsevier, 1993, pp 2439-2442.

159. Visentin, F.; Puxty, G.; Kut, O. M.; Hungerbühler, K. Study of the hydrogenation of selected nitro compounds by simultaneous measurements of calorimetric, FT-IR, and gas-uptake signals. *Ind. Eng. Chem. Res.* **2006,** *45* (13), 4544-4553.

160. Wang, J.; Yuan, Z.; Nie, R.; Hou, Z.; Zheng, X. Hydrogenation of nitrobenzene to aniline over silica gel supported nickel catalysts. *Ind. Eng. Chem. Res.* **2010,** *49* (10), 4664-4669.

161. Gelder, E. A.; Jackson, S. D.; Lok, C. M. The hydrogenation of nitrobenzene to aniline: A new mechanism. *Chem. Commun.* **2005,** *4*, 522-524.

162. Karwa, S. L.; Rajadhyaksha, R. A. Selective catalytic hydrogenation of nitrobenzene to phenylhydroxylamine. *Ind. Eng. Chem. Res.* **1987,** *26* (9), 1746-1750.

163. Layek, K.; Kantam, M. L.; Shirai, M.; Nishio-Hamane, D.; Sasaki, T.; Maheswaran, H. Gold nanoparticles stabilized on nanocrystalline magnesium oxide as an active catalyst for reduction of nitroarenes in aqueous medium at room temperature. *Green Chem.* **2012,** *14* (11), 3164-3174.

164. Li, Z.; Xu, X.; Jiang, X.; Li, Y.; Yu, Z.; Zhang, X. Facile reduction of aromatic nitro compounds to aromatic amines catalysed by support-free nanoporous silver. *RSC Adv.* **2015,** *5* (38), 30062-30066.

165. Lou, X.-B.; He, L.; Qian, Y.; Liu, Y.-M.; Cao, Y.; Fan, K.-N. Highly chemo-and regioselective transfer reduction of aromatic nitro compounds using ammonium formate catalyzed by supported gold nanoparticles. *Adv. Synth. Catal.* **2011,** *353* (2-3), 281-286.

166. Vasilikogiannaki, E.; Gryparis, C.; Kotzabasaki, V.; Lykakis, I. N.; Stratakis, M. Facile reduction of nitroarenes into anilines and nitroalkanes into hydroxylamines via the rapid activation of ammonia-borane complex by supported gold nanoparticles. *Adv. Synth. Catal.* **2013,** *355* (5), 907-911.

167. Gkizis, P. L.; Stratakis, M.; Lykakis, I. N. Catalytic activation of hydrazine hydrate by gold nanoparticles: Chemoselective reduction of nitro compounds into amines. *Catal. Commun.* **2013,** *36*, 48-51.

168. Agrawal, A.; Tratnyek, P. G. Reduction of nitro aromatic compounds by zero-valent iron metal. *Environ. Sci. Technol.* **1996,** *30* (1), 153-160.

169. Debus, H.; Jungers, J. C. La cinétique quantitative en catalyse hétérogène l'hydrogénation du nitrobenzène sur le nickel. *Bull. Soc. Chim. Fr.* **1959,** *6*, 785-792.

170. Rylander, P. N.; Karpenko, I. M.; Pond, G. R. Selectivity in hydrogenation over platinum metal catalysts: nitroaromatics. *Ann. N. Y. Acad. Sci.* **1970,** *172* (9), 266-275.

171. Xiong, R.; Wang, Y.; Zhang, X.; Lu, C.; Lan, L. In situ growth of gold nanoparticles on magnetic γ-Fe2O3@cellulose nanocomposites: A highly active and recyclable catalyst for reduction of 4-nitrophenol. *RSC Adv.* **2014,** *4* (13), 6454-6462.

172. Begum, R.; Farooqi, Z. H.; Butt, Z.; Wu, Q.; Wu, W.; Irfan, A. Engineering of responsive polymer based nano-reactors for facile mass transport and enhanced catalytic degradation of 4-nitrophenol. *J. Environ. Sci.* **2018,** *72*, 43-52.

173. Fedorczyk, A.; Ratajczak, J.; Kuzmych, O.; Skompska, M. Kinetic studies of catalytic reduction of 4-nitrophenol with NaBH4 by means of Au nanoparticles dispersed in a conducting polymer matrix. *J. Solid State Electr.* **2015,** *19* (9), 2849-2858.

174. Biondi, I.; Laurenczy, G.; Dyson, P. J. Synthesis of gold nanoparticle catalysts based on a new water-soluble ionic polymer. *Inorg. Chem.* **2011,** *50* (17), 8038-8045.

175. Das, T. K.; Ganguly, S.; Bhawal, P.; Mondal, S.; Das, N. C. A facile green synthesis of silver nanoparticle-decorated hydroxyapatite for efficient catalytic activity towards 4-nitrophenol reduction. *Res. Chem. Intermed.* **2017,** *44* (2), 1189-1208.

176. Fu, Y.; Lu, Y.; Polzer, F.; Lux-Steiner, M. C.; Fischer, C.-H. In-situ synthesis of stabilizer-free gold nanocrystals with controllable shape on substrates as highly active catalysts for multiple use. *Adv. Synth. Catal.* **2016,** *358* (9), 1440-1448.

177. Jia, H.; Schmitz, D.; Ott, A.; Pich, A.; Lu, Y. Cyclodextrin modified microgels as "nanoreactor" for the generation of Au nanoparticles with enhanced catalytic activity. *J. Mater. Chem. A* **2015,** *3* (11), 6187-6195.

178. Wu, S.-H.; Tseng, C.-T.; Lin, Y.-S.; Lin, C.-H.; Hung, Y.; Mou, C.-Y. Catalytic nano-rattle of Au@hollow silica: Towards a poison-resistant nanocatalyst. *J. Mater. Chem.* **2011,** *21* (3), 789-794.

179. Murugadoss, A.; Chattopadhyay, A. Surface area controlled differential catalytic activities of one-dimensional chain-like arrays of gold nanoparticles. *J. Phys. Chem. C* **2008,** *112* (30), 11265-11271.

180. Schrinner, M.; Polzer, F.; Mei, Y.; Lu, Y.; Haupt, B.; Ballauff, M.; Göldel, A.; Drechsler, M.; Preussner, J.; Glatzel, U. Mechanism of the formation of amorphous gold nanoparticles within spherical polyelectrolyte brushes. *Macromol. Chem.* **2007,** *208* (14), 1542-1547.

181. Yuan, J.; Wunder, S.; Warmuth, F.; Lu, Y. Spherical polymer brushes with vinylimidazolium-type poly(ionic liquid) chains as support for metallic nanoparticles. *Polymer* **2012,** *53* (1), 43-49.

182. Yuan, C.; Xu, Y.; Zhong, L.; Zhang, L.; Yang, C.; Jiang, B.; Deng, Y.; Zeng, B.; He, N.; Luo, W.; Dai, L. Heterogeneous silver-polyaniline nanocomposites with tunable morphology and controllable catalytic properties. *Nanotechnology* **2013,** *24* (18), 185602.

183. Eising, R.; Signori, A. M.; Fort, S.; Domingos, J. B. Development of catalytically active silver colloid nanoparticles stabilized by dextran. *Langmuir* **2011,** *27* (19), 11860-11866.

184. Signori, A. M.; Santos Kde, O.; Eising, R.; Albuquerque, B. L.; Giacomelli, F. C.; Domingos, J. B. Formation of catalytic silver nanoparticles supported on branched polyethyleneimine derivatives. *Langmuir* **2010,** *26* (22), 17772-17779.

185. Lu, Y.; Mei, Y.; Schrinner, M.; Ballauff, M.; Möller, M. W.; Breu, J. In situ formation of Ag nanoparticles in spherical polyacrylic acid brushes by UV irradiation. *J. Phys. chem. C* **2007,** *111* (21), 7676-7681.

186. Lu, Y.; Spyra, P.; Mei, Y.; Ballauff, M.; Pich, A. Composite hydrogels: Robust carriers for catalytic nanoparticles. *Macromol. Chem. Phys.* **2007,** *208* (3), 254-261.

187. Zhang, H.; Li, X.; Chen, G. Ionic liquid-facilitated synthesis and catalytic activity of highly dispersed Ag nanoclusters supported on TiO2. *J. Mater. Chem.* **2009,** *19* (43), 8223-8231.

188. Zhang, J.-T.; Wei, G.; Keller, T. F.; Gallagher, H.; Stötzel, C.; Müller, F. A.; Gottschaldt, M.; Schubert, U. S.; Jandt, K. D. Responsive hybrid polymeric/metallic nanoparticles for catalytic applications. *Macromol. Mater. Eng.* **2010,** *295* (11), 1049-1057.

189. Wu, S.; Kaiser, J.; Guo, X.; Li, L.; Lu, Y.; Ballauff, M. Recoverable platinum nanocatalysts immobilized on magnetic spherical polyelectrolyte brushes. *Ind. Eng. Chem. Res.* **2012,** *51* (15), 5608-5614.

190. Antonels, N. C.; Meijboom, R. Preparation of well-defined dendrimer encapsulated ruthenium nanoparticles and their evaluation in the reduction of 4-nitrophenol according to the Langmuir-Hinshelwood approach. *Langmuir* **2013,** *29* (44), 13433-13442.

191. Yuan, J.; Schacher, F.; Drechsler, M.; Hanisch, A.; Lu, Y.; Ballauff, M.; Müller, A. H. E. Stimuli-responsive organosilica hybrid nanowires decorated with metal nanoparticles. *Chem. Mater.* **2010,** *22* (8), 2626-2634.

192. Halder, A.; Patra, S.; Viswanath, B.; Munichandraiah, N.; Ravishankar, N. Porous, catalytically active palladium nanostructures by tuning nanoparticle interactions in an organic medium. *Nanoscale* **2011,** *3* (2), 725-730.

193. Liu, J.; Wang, J.; Wang, Y.; Liu, C.; Jin, M.; Xu, Y.; Li, L.; Guo, X.; Hu, A.; Liu, T.; Lincoln, S. F.; Prud'homme, R. K. A thermosensitive hydrogel carrier for nickel nanoparticles. *Coll. Interf. Sci. Commun.* **2015,** *4*, 1-4.

194. Chen, G.; Xu, C.; Huang, X.; Ye, J.; Gu, L.; Li, G.; Tang, Z.; Wu, B.; Yang, H.; Zhao, Z.; Zhou, Z.; Fu, G.; Zheng, N. Interfacial electronic effects control the reaction selectivity of platinum catalysts. *Nat. Mater.* **2016,** *15* (5), 564-569.

195. Gu, S.; Lu, Y.; Kaiser, J.; Albrecht, M.; Ballauff, M. Kinetic analysis of the reduction of 4-nitrophenol catalyzed by Au/Pd nanoalloys immobilized in spherical polyelectrolyte brushes. *Phys. Chem. Chem. Phys.* **2015,** *17* (42), 28137-28143.

196. Mitchell, M. *An introduction to genetic algorithms*; MIT press: Cambridge, MA, 1998.

197. Kawasaki, H.; Mitou, T.; Sasaki, S.; Maeda, H. Partition of salts between N-isopropylacrylamide gels and aqueous solutions. *Langmuir* **2000,** *16* (3), 1444-1446.

198. Retnamma, R.; Novais, A. Q.; Rangel, C. M. Kinetics of hydrolysis of sodium borohydride for hydrogen production in fuel cell applications: A review. *Int. J. Hydrogen Energ.* **2011,** *36* (16), 9772-9790.

199. Prampolini, G.; Yu, P.; Pizzanelli, S.; Cacelli, I.; Yang, F.; Zhao, J.; Wang, J. Structure and dynamics of ferrocyanide and ferricyanide anions in water and heavy water: An insight by MD simulations and 2D IR spectroscopy. *J. Phys. Chem. B* **2014,** *118* (51), 14899-14912.

200. Smalley, J. F.; Geng, L.; Feldberg, S. W. Evidence for adsorption of Fe (CN)6 3−/4− on gold using the indirect laser-induced temperature-jump method. *J. Electroanal. Chem.* **1993,** *356* (1-2), 181-200.

201. Ovchinnikova, S. N. The effect of adsorption of ions of the hexacyanoferrate(II)/(III) redox pair on self-assembly of octanethiol at its adsorption from aqueous solutions on gold electrode. *Russ. J. of Electrochem.* **2018,** *53* (11), 1246-1253.

202. Besold, D.; Roa, R.; Kanduč, M.; Kim, W. K.; Risse, S.; Ronneburg, A.; Dzubiella, J.; Lu, Y.; Ballauff, M. Tuning reaction rates in responsive nanoreactors by electrostatic product inhibition and ionic partitioning. *Unpublished preprint* **2020**.

203. Debye, P. Reaction rates in ionic solutions. *Trans. Electrochem. Soc.* **1942,** *82* (1), 265-272.

204. Angioletti-Uberti, S.; Lu, Y.; Ballauff, M.; Dzubiella, J. Theory of solvation-controlled reactions in stimuli-responsive nanoreactors. *J. Phys. Chem. C* **2015,** *119* (27), 15723-15730.

205. Debye, P.; Hückel, E. Zur Theorie der Elektrolyte. I. Gefrierpunktserniedrigung und verwandte Erscheinungen. *Phys. Z.* **1923,** *24*, 185-206.

206. Bjerrum, N. K. Untersuchungen über Ionenassoziation / 1. Der Einfluss der Ionenassoziation auf die Aktivität der Ionen bei mittleren Assoziationsgraden. *Kgl. Danske Vid. Selskab, Math.-fys. medd* **1926,** *7*, 1-48.

207. Fatin-Rouge, N.; Milon, A.; Buffle, J.; Goulet, R. R.; Tessier, A. Diffusion and partitioning of solutes in agarose hydrogels: The relative influence of electrostatic and specific interactions. *J. Phys. Chem. B* **2003,** *107* (44), 12126-12137.

208. Molina, M. A.; Rivarola, C. R.; Barbero, C. A. Study on partition and release of molecules in superabsorbent thermosensitive nanocomposites. *Polymer* **2012,** *53* (2), 445-453.

209. Bortels, L.; Van den Bossche, B.; Deconinck, J.; Vandeputte, S.; Hubin, A. Analytical solution for the steady-state diffusion and migration involving multiple reaction ions. Application to the identification of Butler-Volmer kinetic parameters for the ferri-/ferrocyanide redox couple. *J. Electroanal. Chem.* **1997,** *429* (1-2), 139-155.

210. Shoup, D.; Szabo, A. Role of diffusion in ligand binding to macromolecules and cell-bound receptors. *Biophys. J.* **1982,** *40* (1), 33-39.

211. Zwanzig, R. Diffusion-controlled ligand binding to spheres partially covered by receptors: an effective medium treatment. *Proc. Natl. Acad. Sci.* **1990,** *87* (15), 5856-5857.

212. Northrup, S. H. Diffusion-controlled ligand binding to multiple competing cell-bound receptors. *J. Phys. Chem. C* **1988,** *92* (20), 5847-5850.

213. Milster, S.; Chudoba, R.; Kanduč, M.; Dzubiella, J. Cross-linker effect on solute adsorption in swollen thermoresponsive polymer networks. *Phys. Chem. Chem. Phys.* **2019,** *21* (12), 6588-6599.

214. Kanduč, M.; Chudoba, R.; Palczynski, K.; Kim, W. K.; Roa, R.; Dzubiella, J. Selective solute adsorption and partitioning around single PNIPAM chains. *Phys Chem Chem Phys* **2017,** *19* (8), 5906-5916.

215. Storn, R.; Price, K. Differential evolution – A simple and efficient heuristic for global optimization over continuous spaces. *J. Global Optim.* **1997,** *11* (4), 341-359.

216. Huber, M. L.; Perkins, R. A.; Laesecke, A.; Friend, D. G.; Sengers, J. V.; J., A. M.; Metaxa, I. N.; Vogel, E.; Mareš, R.; Miyagawa, K. New international formulation for the viscosity of H2O. *J. Phys. Chem. Ref. Data* **2009,** *38* (2), 101-125.

217. Hays, J. T.; De Butts, E. H.; Young, H. L. p-Nitrosophenol chemistry. I. Etherification of p-nitrosophenol. *J. Org. Chem.* **1967,** *32* (1), 153-158.

218. Mastronarde, D. N. Automated electron microscope tomography using robust prediction of specimen movements. *J. Struct. Biol.* **2005,** *152* (1), 36-51.

219. *Agilent 8453 UV-visible Spectroscopy System Service Manual*. Agilent Technologies, Inc., 2001.

220. Greenwood, N. N.; Earnshaw, A. *Chemie der Elemente*; 1st ed.; Wiley-VCH: Weinheim, 1988.

221. Chatenet, M.; Micoud, F.; Roche, I.; Chainet, E.; Vondrák, J. Kinetics of sodium borohydride direct oxidation and oxygen reduction in sodium hydroxide electrolyte. *Electrochim. Acta* **2006,** *51* (25), 5452-5458.

222. Elias, W. C.; Eising, R.; Silva, T. R.; Albuquerque, B. L.; Martendal, E.; Meier, L.; Domingos, J. B. Screening the formation of silver nanoparticles using a new reaction kinetics multivariate analysis and assessing their catalytic activity in the reduction of nitroaromatic compounds. *J. Phys. Chem. C* **2014,** *118* (24), 12962-12971.

223. Saha, S.; Pal, A.; Kundu, S.; Basu, S.; Pal, T. Photochemical green synthesis of calcium-alginate-stabilized Ag and Au nanoparticles and their catalytic application to 4-nitrophenol reduction. *Langmuir* **2010,** *26* (4), 2885-2893.

224. Rashid, M. H.; Mandal, T. K. Templateless synthesis of polygonal gold nanoparticles: An unsupported and reusable catalyst with superior activity. *Adv. Funct. Mater.* **2008,** *18* (15), 2261-2271.

225. Rashid, M. H.; Bhattacharjee, R. R.; Kotal, A.; Mandal, T. K. Synthesis of spongy gold nanocrystals with pronounced catalytic activities. *Langmuir* **2006,** *22* (17), 7141-7143.

226. Huang, T.; Meng, F.; Qi, L. Facile synthesis and one-dimensional assembly of cyclodextrin-capped gold nanoparticles and their applications in catalysis and surface-enhanced Raman scattering. *J. Phys. Chem. C* **2009,** *113* (31), 13636-13642.

227. Villalobos, L. F.; Neelakanda, P.; Karunakaran, M.; Cha, D.; Peinemann, K. V. Poly-thiosemicarbazide/gold nanoparticles catalytic membrane: In-situ growth of well-dispersed, uniform and stable gold nanoparticles in a polymeric membrane. *Catal. Today* **2014,** *236*, 92-97.

228. Fang, X.; Ma, H.; Xiao, S.; Shen, M.; Guo, R.; Cao, X.; Shi, X. Facile immobilization of gold nanoparticles into electrospun polyethyleneimine/polyvinyl alcohol nanofibers for catalytic applications. *J. Mater. Chem.* **2011,** *21* (12), 4493-4501.

229. Hallett-Tapley, G. L.; Crites, C.-O. L.; González-Béjar, M.; McGilvray, K. L.; Netto-Ferreira, J. C.; Scaiano, J. C. Dry photochemical synthesis of hydrotalcite, γ-Al2O3 and TiO2 supported gold nanoparticle catalysts. *J. Photoch. Photobio. A* **2011,** *224* (1), 8-15.

230. Lin, C.; Tao, K.; Hua, D.; Ma, Z.; Zhou, S. Size effect of gold nanoparticles in catalytic reduction of p-nitrophenol with NaBH4. *Molecules* **2013,** *18* (10), 12609-12620.

231. Shao, Y.; Zhou, L.; Bao, C.; Wu, Q.; Wu, W.; Liu, M. Facile preparation of tiny gold nanoparticle loaded magnetic yolk-shell carbon nanoreactors for confined catalytic reactions. *New J. Chem.* **2016,** *40* (11), 9684-9693.

232. Hu, W.; Liu, B.; Wang, Q.; Liu, Y.; Liu, Y.; Jing, P.; Yu, S.; Liu, L.; Zhang, J. A magnetic double-shell microsphere as a highly efficient reusable catalyst for catalytic applications. *Chem. Commun.* **2013,** *49* (69), 7596-7958.

233. Wang, Q.; Jia, W.; Liu, B.; Dong, A.; Gong, X.; Li, C.; Jing, P.; Li, Y.; Xu, G.; Zhang, J. Hierarchical structure based on Pd(Au) nanoparticles grafted onto magnetite cores and double layered shells: enhanced activity for catalytic applications. *J. Mater. Chem. A* **2013,** *1* (41), 12732-12741.

234. Li, Z.; Zeng, H. C. Surface and bulk integrations of single-layered Au or Ag nanoparticles onto designated crystal planes {110} or {100} of ZIF-8. *Chem. Mater.* **2013,** *25* (9), 1761-1768.

235. Wang, S.; Zhang, M.; Zhang, W. Yolk-shell catalyst of single Au nanoparticle encapsulated within hollow mesoporous silica microspheres. *ACS Catal.* **2011,** *1* (3), 207-211.

236. Wei, J.; Wang, H.; Deng, Y.; Sun, Z.; Shi, L.; Tu, B.; Luqman, M.; Zhao, D. Solvent evaporation induced aggregating assembly approach to three-dimensional ordered mesoporous silica with ultralarge accessible mesopores. *J. Am. Chem. Soc.* **2011,** *133* (50), 20369-20377.

237. Gu, H.; Wang, J.; Ji, Y.; Wang, Z.; Chen, W.; Xue, G. Facile and controllable fabrication of gold nanoparticles-immobilized hollow silica particles and their high catalytic activity. *J. Mater. Chem. A* **2013,** *1* (40), 12471-12477.

238. Lin, Y.; Qiao, Y.; Wang, Y.; Yan, Y.; Huang, J. Self-assembled laminated nanoribbon-directed synthesis of noble metallic nanoparticle-decorated silica nanotubes and their catalytic applications. *J. Mater. Chem.* **2012,** *22* (35), 18314-18320.

239. Zheng, J.; Dong, Y.; Wang, W.; Ma, Y.; Hu, J.; Chen, X.; Chen, X. In situ loading of gold nanoparticles on Fe3O4@SiO2 magnetic nanocomposites and their high catalytic activity. *Nanoscale* **2013,** *5* (11), 4894-4901.

240. Zhu, Y.; Shen, J.; Zhou, K.; Chen, C.; Yang, X.; Li, C. Multifunctional magnetic composite microspheres with in situ growth Au nanoparticles: A highly efficient catalyst system. *J. Phys. Chem. C* **2010,** *115* (5), 1614-1619.

241. Jin, R.; Sun, S.; Yang, Y.; Xing, Y.; Yu, D.; Yu, X.; Song, S. Size-dependent catalytic properties of Au nanoparticles supported on hierarchical nickel silicate nanostructures. *Dalton Trans.* **2013,** *42* (22), 7888-7893.

242. Jin, R.; Yang, Y.; Zou, Y.; Liu, X.; Xing, Y. A general route to hollow mesoporous rare-earth silicate nanospheres as a catalyst support. *Chem. Eur. J.* **2014,** *20* (8), 2344-2351.

243. Gangula, A.; Podila, R.; M, R.; Karanam, L.; Janardhana, C.; Rao, A. M. Catalytic reduction of 4-nitrophenol using biogenic gold and silver nanoparticles derived from Breynia rhamnoides. *Langmuir* **2011,** *27* (25), 15268-15274.

244. Das, S. K.; Dickinson, C.; Lafir, F.; Brougham, D. F.; Marsili, E. Synthesis, characterization and catalytic activity of gold nanoparticles biosynthesized with Rhizopus oryzae protein extract. *Green Chem.* **2012,** *14* (5), 1322-1334.

245. Xia, B.; He, F.; Li, L. Preparation of bimetallic nanoparticles using a facile green synthesis method and their application. *Langmuir* **2013,** *29* (15), 4901-4907.

246. Liu, W.; Yang, X.; Huang, W. Catalytic properties of carboxylic acid functionalized-polymer microsphere-stabilized gold metallic colloids. *J. Colloid Interf. Sci.* **2006,** *304* (1), 160-165.

247. Shin, H. S.; Huh, S. Au/Au@polythiophene core/shell nanospheres for heterogeneous catalysis of nitroarenes. *ACS Appl. Mater. Inter.* **2012,** *4* (11), 6324-6331.

248. Zhang, J.; Han, D.; Zhang, H.; Chaker, M.; Zhao, Y.; Ma, D. In situ recyclable gold nanoparticles using CO2-switchable polymers for catalytic reduction of 4-nitrophenol. *Chem. Commun.* **2012,** *48* (94), 11510-11512.

249. Chen, Z.; Cui, Z. M.; Cao, C. Y.; He, W. D.; Jiang, L.; Song, W. G. Temperature-responsive smart nanoreactors: poly(N-isopropylacrylamide)-coated Au@mesoporous-SiO2 hollow nanospheres. *Langmuir* **2012,** *28* (37), 13452-13458.

250. Nongwe, I.; Bepete, G.; Shaikjee, A.; Ravat, V.; Terfassa, B.; Meijboom, R.; Coville, N. J. Synthesis of gold encapsulated in spherical carbon capsules with a mesoporous shell structure. A robust catalyst in a nanoreactor. *Catal. Commun.* **2014,** *53*, 77-82.

251. Mahamallik, P.; Pal, A. A soft-template mediated approach for Au(0) formation on a heterosilica surface and synergism in the catalytic reduction of 4-nitrophenol. *RSC Adv.* **2015,** *5* (95), 78006-78016.

252. Wu, T.; Zhang, L.; Gao, J.; Liu, Y.; Gao, C.; Yan, J. Fabrication of graphene oxide decorated with Au–Ag alloy nanoparticles and its superior catalytic performance for the reduction of 4-nitrophenol. *J. Mater. Chem. A* **2013,** *1* (25), 7384-7390.

253. Wu, H.; Huang, X.; Gao, M.; Liao, X.; Shi, B. Polyphenol-grafted collagen fiber as reductant and stabilizer for one-step synthesis of size-controlled gold nanoparticles and their catalytic application to 4-nitrophenol reduction. *Green Chem.* **2011,** *13* (3), 651-658.

254. Jana, S.; Ghosh, S.; Nath, S.; Pande, S.; Praharaj, S.; Panigrahi, S.; Basu, S.; Endo, T.; Pal, T. Synthesis of silver nanoshell-coated cationic polystyrene beads: A solid phase catalyst for the reduction of 4-nitrophenol. *Appl. Catal. A* **2006,** *313* (1), 41-48.

255. Horecha, M.; Kaul, E.; Horechyy, A.; Stamm, M. Polymer microcapsules loaded with Ag nanocatalyst as active microreactors. *J. Mater. Chem. A* **2014,** *2* (20), 7431-7438.

256. Ai, L.; Yue, H.; Jiang, J. Environmentally friendly light-driven synthesis of Ag nanoparticles in situ grown on magnetically separable biohydrogels as highly active and recyclable catalysts for 4-nitrophenol reduction. *J. Mater. Chem.* **2012,** *22* (44), 23447-23453.

257. Pootawang, P.; Lee, S. Y. Rapid synthesis of Ag nanoparticles-embedded mesoporous silica via solution plasma and its catalysis for 4-nitrophenol reduction. *Mater. Lett.* **2012,** *80*, 1-4.

258. Geng, Q.; Du, J. Reduction of 4-nitrophenol catalyzed by silver nanoparticles supported on polymer micelles and vesicles. *RSC Adv.* **2014,** *4* (32), 16425-16428.

259. Liang, M.; Su, R.; Huang, R.; Qi, W.; Yu, Y.; Wang, L.; He, Z. Facile in situ synthesis of silver nanoparticles on procyanidin-grafted eggshell membrane and their catalytic properties. *ACS Appl. Mater. Inter.* **2014,** *6* (7), 4638-4649.

260. Naik, B.; Prasad, V. S.; Ghosh, N. N. Preparation of Ag nanoparticle loaded mesoporous γ-alumina catalyst and its catalytic activity for reduction of 4-nitrophenol. *Powder Technol.* **2012,** *232*, 1-6.

261. Manivannan, S.; Krishnakumari, B.; Ramaraj, R. Synthesis of silicate sol-gel matrix embedded silver nanostructures: Efficient nanocatalyst for the reduction of 4-nitrophenol. *Chem. Eng. J.* **2012,** *204*, 16-22.

262. Zhang, P.; Shao, C.; Zhang, Z.; Zhang, M.; Mu, J.; Guo, Z.; Liu, Y. In situ assembly of well-dispersed Ag nanoparticles (AgNPs) on electrospun carbon nanofibers (CNFs) for catalytic reduction of 4-nitrophenol. *Nanoscale* **2011,** *3* (8), 3357-3363.

263. Chang, G.; Luo, Y.; Lu, W.; Qin, X.; Asiri, A. M.; Al-Youbi, A. O.; Sun, X. Ag nanoparticles decorated polyaniline nanofibers: Synthesis, characterization, and applications toward catalytic reduction of 4-nitrophenol and electrochemical detection of H2O2 and glucose. *Catal. Sci. Technol.* **2012,** *2* (4), 800-806.

264. Wang, M.; Tian, D.; Tian, P.; Yuan, L. Synthesis of micron-SiO2@nano-Ag particles and their catalytic performance in 4-nitrophenol reduction. *Appl. Surf. Sci.* **2013,** *283*, 389-395.

265. Wang, Z.; Zhai, S.; Zhai, B.; Xiao, Z.; Zhang, F.; An, Q. In situ preparation of uniform Ag NPs onto multifunctional Fe3O4@SN/HPW@CG towards efficient reduction of 4-nitrophenol. *New J. Chem.* **2014,** *38* (8), 3999-4006.

266. Xiao, S.; Xu, W.; Ma, H.; Fang, X. Size-tunable Ag nanoparticles immobilized in electrospun nanofibers: Synthesis, characterization, and application for catalytic reduction of 4-nitrophenol. *RSC Adv.* **2012,** *2* (1), 319-327.

267. Baruah, B.; Gabriel, G. J.; Akbashev, M. J.; Booher, M. E. Facile synthesis of silver nanoparticles stabilized by cationic polynorbornenes and their catalytic activity in 4-nitrophenol reduction. *Langmuir* **2013,** *29* (13), 4225-4234.

268. Naraginti, S.; Tiwari, N.; Sivakumar, A. Green synthesis of silver and gold nanoparticles for enhanced catalytic and bactericidal activity. *IOP Conf. Ser.: Mater. Sci. Eng.* **2017,** *263* (2), 022009.

269. Karki, H. P.; Ojha, D. P.; Joshi, M. K.; Kim, H. J. Effective reduction of p-nitrophenol by silver nanoparticle loaded on magnetic Fe3O4/ATO nano-composite. *Appl. Surf. Sci.* **2018,** *435*, 599-608.

270. Zhang, K.; Wang, C.; Rong, Z.; Xiao, R.; Zhou, Z.; Wang, S. Silver coated magnetic microflowers as efficient and recyclable catalysts for catalytic reduction. *New J. Chem.* **2017,** *41* (23), 14199-14208.

271. Kim, J. G.; Cha, M. C.; Lee, J.; Choi, T.; Chang, J. Y. Preparation of a sulfur-functionalized microporous polymer sponge and in situ growth of silver nanoparticles: A compressible monolithic catalyst. *ACS Appl. Mater. Inter.* **2017,** *9* (43), 38081-38088.

272. Liang, M.; Zhang, G.; Feng, Y.; Li, R.; Hou, P.; Zhang, J.; Wang, J. Facile synthesis of silver nanoparticles on amino-modified cellulose paper and their catalytic properties. *J. Mater. Sci.* **2017,** *53* (2), 1568-1579.

273. Kumar, M.; Krishnan, U.; Devi, P.; Kumar, A. Structural analysis of graphene oxide/silver nanocomposites: Optical properties, electrochemical sensing and photocatalytic activity. *J. Mater. Sci.: Mater. Electron.* **2017,** *29* (1), 10-19.

274. Tzounis, L.; Contreras-Caceres, R.; Schellkopf, L.; Jehnichen, D.; Fischer, D.; Cai, C.; Uhlmann, P.; Stamm, M. Controlled growth of Ag nanoparticles decorated onto the surface of

SiO2 spheres: A nanohybrid system with combined SERS and catalytic properties. *RSC Adv.* **2014,** *4* (34), 17846-17855.

275. Murugadoss, A.; Chattopadhyay, A. A 'green' chitosan-silver nanoparticle composite as a heterogeneous as well as micro-heterogeneous catalyst. *Nanotechnology* **2008,** *19* (1), 015603.

276. Yin, Q.; Chen, Q.; Lu, L. C.; Han, B. H. Sugar-based micro/mesoporous hypercross-linked polymers with in situ embedded silver nanoparticles for catalytic reduction. *Beilstein J. Org. Chem.* **2017,** *13* (1), 1212-1221.

277. Patil, N. G.; Basutkar, N. B.; Ambade, A. V. Copper and silver nanoparticles stabilized by bistriazole-based dendritic amphiphile micelles for 4-nitrophenol reduction. *New J. Chem.* **2017,** *41* (11), 4546-4554.

278. Zeng, X.; Wang, Q.; Wang, H.; Yang, Y. Catalytically active silver nanoparticles loaded in the lumen of halloysite nanotubes via electrostatic interactions. *J. Mater. Sci.* **2017,** *52* (14), 8391-8400.

279. Zhang, L.; Liu, X.; Wang, Y.; Xing, S. Controllable silver embedding into polypyrrole. *J. Alloy Compd.* **2017,** *709*, 431-437.

280. Liu, Y. Y.; Guo, X. L.; Zhu, L.; Wang, X. J.; Ge, C.; Zhao, L.; Chen, J.; Zhang, Y.; Wang, Z. M.; Sun, L. T. ZnO nanosheet-assisted immobilization of Ag nanoparticles on graphene/Ni foam for highly efficient reduction of 4-nitrophenol. *RSC Adv.* **2017,** *7* (28), 16924-16930.

281. Lu, S.; Yu, J.; Cheng, Y.; Wang, Q.; Barras, A.; Xu, W.; Szunerits, S.; Cornu, D.; Boukherroub, R. Preparation of silver nanoparticles/polydopamine functionalized polyacrylonitrile fiber paper and its catalytic activity for the reduction 4-nitrophenol. *Appl. Surf. Sci.* **2017,** *411*, 163-169.

282. Jiang, Z.; Jiang, D.; Showkot Hossain, A. M.; Qian, K.; Xie, J. In situ synthesis of silver supported nanoporous iron oxide microbox hybrids from metal-organic frameworks and their catalytic application in p-nitrophenol reduction. *Phys. Chem. Chem. Phys.* **2015,** *17* (4), 2550-2559.

283. Bano, M.; Ahirwar, D.; Thomas, M.; Naikoo, G. A.; Sheikh, M. U.-D.; Khan, F. Hierarchical synthesis of silver monoliths and their efficient catalytic activity for the reduction of 4-nitrophenol to 4-aminophenol. *New J. Chem.* **2016,** *40* (8), 6787-6795.

284. Min, J.; Wang, F.; Cai, Y.; Liang, S.; Zhang, Z.; Jiang, X. Azeotropic distillation assisted fabrication of silver nanocages and their catalytic property for reduction of 4-nitrophenol. *Chem. Commun.* **2015,** *51* (4), 761-764.

285. Chi, Y.; Zhao, L.; Yuan, Q.; Yan, X.; Li, Y.; Li, N.; Li, X. In situ auto-reduction of silver nanoparticles in mesoporous carbon with multifunctionalized surfaces. *J. Mater. Chem.* **2012,** *22* (27), 13571-13577.

286. Du, X.; He, J.; Zhu, J.; Sun, L.; An, S. Ag-deposited silica-coated Fe3O4 magnetic nanoparticles catalyzed reduction of p-nitrophenol. *Appl. Surf. Sci.* **2012,** *258* (7), 2717-2723.

287. Qin, X.; Liu, S.; Lu, W.; Li, H.; Chang, G.; Zhang, Y.; Tian, J.; Luo, Y.; Asiri, A. M.; Al-Youbi, A. O.; Sun, X. Submicrometre-scale polyaniline colloidal spheres: Photopolymerization preparation using fluorescent carbon nitride dots as a photocatalyst. *Catal. Sci. Technol.* **2012,** *2* (4), 711-714.

288. Zhou, W.; Zhou, Y.; Liang, Y.; Feng, X.; Zhou, H. Silver nanoparticles on carboxyl-functionalized Fe3O4 with high catalytic activity for 4-nitrophenol reduction. *RSC Adv.* **2015,** *5* (62), 50505-50511.

289. Lu, X.; Bian, X.; Nie, G.; Zhang, C.; Wang, C.; Wei, Y. Encapsulating conducting polypyrrole into electrospun TiO2 nanofibers: A new kind of nanoreactor for in situ loading Pd nanocatalysts towards p-nitrophenol hydrogenation. *J. Mater. Chem.* **2012,** *22* (25), 12723-12730.

290. Dutta, S.; Sarkar, S.; Ray, C.; Roy, A.; Sahoo, R.; Pal, T. Mesoporous gold and palladium nanoleaves from liquid-liquid interface: enhanced catalytic activity of the palladium analogue toward hydrazine-assisted room-temperature 4-nitrophenol reduction. *ACS Appl. Mater. Inter.* **2014,** *6* (12), 9134-9143.

291. Roy, A.; Debnath, B.; Sahoo, R.; Chandrakumar, K. R. S.; Ray, C.; Jana, J.; Pal, T. Enhanced catalytic activity of Ag/Rh bimetallic nanomaterial: Evidence of an ensemble effect. *J. Phys. Chem. C* **2016,** *120* (10), 5457-5467.

7.3 List of figures

7.4 List of tables

7.5 List of abbreviations

character	meaning
Amp	4-aminophenol
APS	negatively charged PS nanoparticles
ATO	antimony doped tin oxide
(ATR-)FTIR	(attenuated total reflection) Fourier-transform infrared spectroscopy
Bis	*N,N'*-methylenebisacrylamide
BHT	2,6-di-*tert*-butyl-4-methylphenol
CD	cyclodextrin
CPS	positively charged PS nanoparticles
(cryo-)TEM	(cryogenic) transmission electron microscopy
CTAB	hexadecyl-trimethyl-ammonium bromide
DFT	density functional theory
DHAB	4,4'-dihydroxyazobenzene
DHBC	double hydrophilic block copolymer
DLS	dynamic light scattering
DMSO	dimethyl sulfoxide
DPS	degraded pueraria starch
EGCG	epigallocatechin-3-gallate
ESMf	eggshell membrane fibers
G2-BED	generation 2 benzyl ether dendron
(GC-)MS	(gas chromatography) mass spectrometry
GOE	exfoliated graphene oxide
HAP	hydroxylapatite
HCF	hexacyanoferrate(III)
HMSM	hollow mesoporous silica microspheres
HPLC	high performance liquid chromatography
HPW	phosphotungstic acid hydrate
HSAG	high surface area graphite
Hx	4-hydroxylaminophenol
KPS	potassium persulfate
LCST	lower critical solution temperature

MPA	3-mercaptopropionic acid
mPEG	polyethylene glycol monomethyl ether
NAC	*N*-acetyl-L-cysteine
Nip	4-nitrophenol
NMR	nuclear magnetic resonance spectroscopy
N,N-DMF	*N,N*-dimethyl formamide
NP(s)	nanoparticle(s)
NR	nanorod
NSP	4-nitrosophenol
NTA	nitrolotriacetic acid
(P)4VP	(poly-)4-vinylpyridine
(P)AA	(poly)acrylic acid
(P)AAEM	(poly) acetoacetoxyethyl methacrylate
(P)AAm	(poly)acrylamide
(P)AEMH	(poly-) 2-aminoethyl methacrylate hydrochloride
(P)AH	(poly)allylamine hydrochloride
(P)AMAM	(poly)amidoamine
(P)AMPS	(poly-)2-acrylamido-2-methyl-1-propane sulfonic acid
(P)AN	(poly)acrylonitrile
(P)ANI	(poly)aniline
(P)APTS	(poly-)(3-acryloylpropyl) trimethoxysilane
(P)BMS	poly(benzylated monosaccharide)
(P)DA	(poly)dopamine
(P)DACz	(poly-)1,8-diaminocarbazole
(P)DITFB	(poly-)1,4-diiodotetrafluorobenzene
(P)DMAEMA	(poly-)2-(dimethylamino)ethyl methacrylate
(P)DVB	(poly)divinyl benzene
(P)EG	(poly)ethylene glycol
(P)EGMA	(poly)(ethylene glycol) methacrylate
(P)EI	(poly)ethyleneimine
(P)EVIB	(poly-)1-ethyl-3-vinylimidazolium bromide
(P)G	(poly-)D-glucosamin
(P)GMA	(poly)glycidyl methacrylate
(P)GON	(poly)guanidinium oxanorbonene trifluoroacetate

(P)HEMA	(poly-) 2-hydroxyethyl methacrylate
(P)I	(poly)isoprene
(P)IEM	(poly-) isobutyryloxyethyl methacrylate
(P)MAA	(poly)methacrylic acid
(P)MCC	(poly) (maleated carboxymethylchitosan)
(P)METAI	(poly-)2-(methacryloyloxy)ethyl trimethylammonium iodide
(P)MIMC	(poly-)2-(1-methylimidazolium-3-yl) ethyl methacrylate chloride
(P)MMA	(poly)methyl methacrylate
(P)MTAC	(poly-)2-(methylacryloyloxy)ethyltrimethylammonium chloride
(P)NIPAM	(poly-)*N*-isopropylacrylamide
(P)PI	(poly)propyleneimine
(P)Py	(poly)pyrrole
Pro	procyanidine
(P)S	(poly)styrene
(P)SS	(poly)styrene sulfonate
(P-)*t*-BA	(poly-)*tert*-butyl acrylate
(P)TEB	(poly)triethenylbenzene
(P)TSC	polythiosemicarbazide
(P)VA	(poly)vinyl alcohol
(P)VCL	(poly-)*N*-vinylcaprolactam
(P)VP	(poly) vinylpyrrolidone
(P)VPBA	(poly-)4-vinylphenylboronic acid
RI	reaction initiator
RT	room temperature
SDS	sodium dodecyl sulfate
SPB	spherical polyelectrolyte brush
SSG	silicate sol-gel matrix
TGA	thermogravimetric analysis
TLC	thin layer chromatography
TTEGb	tris-triethylene glycol benzene
UCST	upper critical solution temperature
V50	2,2'-azobis(2-amidinopropane) dihydrochloride
X-*b*-Y	block copolymer of X and Y

7.6 List of variables and constants

variable	meaning	units
a	radius of a circular receptor	m
$Abs(t)$	time-dependent absorbance	[1]
$Abs(\lambda)$	wavelength dependent absorbance	[1]
A_{NP}	surface area of one metal nanoparticle	m^2
$c_{exp}(t)$	experimental concentration-time dependency	mol L^{-1}
$c'_{exp}(t)$	first derivative of experimental concentration-time dependency	mol L^{-1}
$c_{fit}(t)$	fitted concentration-time dependency	mol L^{-1}
$c'_{fit}(t)$	first derivative of fitted concentration-time dependency	mol L^{-1}
c_i	bulk concentration of i	mol L^{-1}
c_i^g	concentration of i inside hydrogel	mol L^{-1}
$c_{i,0}$	initial concentration of i	mol L^{-1}
c_m	mass concentration of nanoparticle suspension	g L^{-1}
c_{NR}	nanoreactor (i.e. catalyst) concentration	mol L^{-1}
c_n	limiting number of mutation cycles for fit algorithm	[1]
$c_r(t)$	reactant concentration at time t	mol L^{-1}
D_0	bulk diffusion coefficient	m^2 s^{-1}
$DaII$	second Damköhler number	[1]
D_g	diffusion coefficient inside hydrogel	m^2 s^{-1}
D_i	diffusion coefficient of i	m^2 s^{-1}
d	optical path length through sample solution	cm
ΔE_{bond}	DFT calculated binding energy	kJ mol^{-1}
ΔG	transfer free energy (between bulk and hydrogel)	J
δ	stagnant film thickness over which film diffusion occurs	m
E_A	activation energy of $k_{off,ss}$	kJ mol^{-1}
$E(P, \kappa_g)$	electrostatic perturbation (first order term)	mol s L^{-1}
$\varepsilon(\lambda)$	molar extinction coefficient	L mol^{-1} cm^{-1}
$\varepsilon_j(t_l, s_j)$	target function of the time-dependent fit algorithm	[1]
$\varepsilon_k(s_j)$	target function of the stationary state fit algorithm	[1]
$\varepsilon_r(T)$	relative permittivity of water	[1]

$\eta(T)$	dynamic viscosity of water	Pa s
$F(P, \kappa_g)$	electrostatic perturbation (second order term)	mol s L^{-1}
f_{eff}	efficiency factor	[1]
f_h	Henry function	[1]
f_{loss}	weight fraction lost during TGA measurement	[1]
f_m	metal fraction of nanoreactors	[1]
f_s	solid fraction of side products in the supernatant	[1]
$g^1(q, \tau)$	first order autocorrelation function	[1]
Γ	decay rate	s^{-1}
$I(r)$	ionic strength	mol L^{-1}
I_0	bulk ionic strength	mol L^{-1}
I_g	ionic strength inside hydrogel	mol L^{-1}
$I_{h\nu,0}$	incident light intensity	W m^{-2}
$I_{h\nu,T}$	transmitted light intensity	W m^{-2}
$k_{\#}$	nth order (apparent) reaction rate constant	mol^{1-n} L^{n-1} s^{-1}
K_{ad}	adsorption constant of i	L mol^{-1}
$K_{ad'}$	supposed adsorption constant of i	[1]
$K_{collapse}$	equilibrium constant for the transition between the swollen/collapsed state of PNIPAM	[1]
K_{part}	partition coefficient between bulk/hydrogel	[1]
k_1	surface-normalised first order reaction rate constant	L m^{-2} s^{-1}
k_a	rate constant of first step in the reduction of 4-nitrophenol	mol m^{-2} s^{-1}
k_{ad}	adsorption rate constant	s^{-1}
k_{app}	apparent first order reaction rate constant	s^{-1}
k_b	rate constant of second step in the reduction of 4-nitrophenol	mol m^{-2} s^{-1}
k_D	diffusion rate constant	L mol^{-1} s^{-1}
k_{de}	desorption rate constant	mol L^{-1} s^{-1}
k_E	diffusion rate constant for a sphere covered with N receptors	L s^{-1}
k_{L-H}	Langmuir-Hinshelwood reaction rate constant	mol m^{-2} s^{-1}
k_{NR}	intrinsic reaction rate constant	L mol^{-1} s^{-1}
$k_{NR,ss}$	intrinsic reaction rate constant (stationary state model)	L mol^{-1} s^{-1}
k_{off}	off diffusion rate of accumulated products	s^{-1}

$k_{off,ss}$	off diffusion rate of accumulated products (stationary state model)	s^{-1}
k_{on}	overall reaction rate constant	L mol^{-1} s^{-1}
$k_{on,ss}$	overall reaction rate constant (stationary state model)	L mol^{-1} s^{-1}
k_{SM}	Smoluchowski diffusion rate constant	L s^{-1}
k_{surf}	surface reaction rate constant	L mol^{-1} s^{-1}
k_{th}	theoretical reaction rate constant	s^{-1}
k_{tot}	total reaction rate constant	L mol^{-1} s^{-1}
$\kappa(r)$	inverse screening length	m^{-1}
κ_g	inverse screening length inside hydrogel	m^{-1}
λ	wavelength	nm
λ_B	Bjerrum length	m
$\lambda_D(r)$	Debye length	m
m, n	Freundlich exponents	[1]
m_{core}	mass of one PS core particle	kg
m_i	mass of reactant i used in the synthesis	g
$m_{r,tot}$	total mass of reactants in the shell synthesis	kg
$m_{s,tot}$	total mass of side products in the shell synthesis	kg
m_{shell}	mass of the PNIPAM shell of a single nanoreactor	kg
MW	molar weight	g mol^{-1}
MW_{m-}	molar weight of nanoreactors without metal nanoparticles	g mol^{-1}
MW_{m+}	molar mass of nanoreactors with including metal nanoparticles	g mol^{-1}
N	number of circular receptors on a sphere	[1]
N_{exp}	number of experiments fitted simultaneously	[1]
N_i	number of steps to derive fit parameters within defined range	[1]
N_{NP}	number of metal nanoparticles inside nanoreactor shell	[1]
$n^{\#}$	reaction order	[1]
n_{core}	number of core particles applied in the shell reaction	[1]
P	permeability of hydrogel to solute	m^2 s^{-1}
p_{ss}	number of accumulated products (stationary state model)	[1]
$p(t)$	time-dependent number of accumulated products	[1]
ϕ	Donnan potential	V
$\psi(r,t)$	electrostatic potential caused by accumulated products	V
Q_i	ion charge	C

q	scattering vector	m^{-1}
R_i	radius of nanoreactor ($i = core, shell, gap$)	m
$r(t)$	time-dependent number of accumulated reactants	[1]
$r_{A/m}$	metal surface area per mass ratio	$m^2\ g^{-1}$
r_{ad}	adsorption rate	$mol\ L^{-1}\ s^{-1}$
r_{de}	desorption rate	$mol\ L^{-1}\ s^{-1}$
r_H	hydrodynamic radius	nm
r_{HCF}	radius of hexacyanoferrate(III)	nm
r_{NP}	radius of catalyst metal nanoparticles	m
r_{SM}	Smoluchowski diffusion rate	$mol\ L^{-1}\ s^{-1}$
ρ_i	bulk density	$g\ cm^{-3}$
S	catalyst metal surface area per unit volume	$m^2\ L^{-1}$
σ	conductivity	$\mu S\ cm^{-1}$
T	temperature	K or °C
t	time	s
t_0	induction time	s
t_l	limiting time for fit algorithm	s
τ	decay time	s
θ_i	surface coverage of i	[1]
U_e	electrophoretic mobility	$m^2\ s^{-1}\ V^{-1}$
V_c	volume of core particle suspension applied in the shell synthesis	L
$V_{DH}(t)$	interaction between reactants and accumulated products	J
V_{H2O}	volume of water	m^3
V_{NP}	volume of one metal nanoparticle	m^3
V_r	partial volume of nanoreactor hydrogel shell	m^3
V_{shell}	volume of nanoreactor hydrogel shell	m^3
V_t	total reaction volume	m^3
ζ	zeta potential	V
z_i	ion valency	[1]

constant	meaning	units
$e = 1.602*10^{-19}$	elementary charge	C
$\varepsilon_0 = 8.854*10^{-12}$	vacuum permittivity	F m^{-1}
$k_B = 1.38*10^{-23}$	Boltzmann constant	J K^{-1}
$N_A = 6.022*10^{-23}$	Avogadro constant	$mol^{-1'}$
$R = 8.314$	universal gas constant	J mol^{-1} K^{-1}
$\rho_{Au} = 19.32*10^6$	bulk density of gold	g m^{-3}
$\rho_{Ag} = 10.49*10^6$	bulk density of silver	g m^{-3}
$\rho_{Bis} = 1.24*10^6$	bulk density of Bis	g m^{-3}
$\rho_{KPS} = 2.48*10^6$	bulk density of KPS	g m^{-3}
$\rho_{NIPAM} = 1.10*10^6$	bulk density of NIPAM	g m^{-3}
$\rho_{PS} = 1.05*10^6$	bulk density of PS	g m^{-3}
$\rho_t = 1.0*10^6$	density of the reaction mixture during shell synthesis	g m^{-3}
$\rho_{V50} = 0.42*10^6$	bulk density of V50	g m^{-3}

7.7 Publications

Brummel, O.; Besold, D.; Döpper, T.; Wu, Y.; Bochmann, S.; Lazzari, F.; Waidhas, F.; Bauer, U.; Bachmann, P.; Papp, C.; Steinrück, H.-P.; Görling, A.; Libuda, J.; Bachmann, J., Energy storage in strained organic molecules: (Spectro)electrochemical characterization of norbornadiene and quadricyclane. *ChemSusChem* **2016,** 9, 1424.

Besold, D.; Roa, R.; Kanduč, M.; Kim, W. Q.; Risse, S.; Ronneburg, A.; Dzubiella, J.; Lu, Y.; Ballauff, M., Tuning reaction rates in responsive nanoreactors by electrostatic product inhibition and ionic partitioning. *Unpublished preprint*.

7.8 Conferences

"Au@PNIPAM core-shell nanoreactors with tunable selectivity for catalysis", Rome, Italy, September 2016.

"Rational design of PS@PNIPAM-Ag core-shell nanoreactors with tunable activity for catalysis", Munich, Germany, October 2017.

"Stimuli responsive nanoreactors in surface catalysis", Berlin, Germany, March 2018.

Acknowledgements

At this point, I would like to express my gratitude to everyone who supported me in the process of this doctoral thesis.

First, I would like to thank my highly appreciated supervisor Professor Dr Matthias Ballauff for scientific guidance, advice and support in this interdisciplinary topic. Likewise, I would like to thank Professor Dr Joe Dzubiella for the opportunity to be part of the interdisciplinary ERC project “Multiscale modelling of stimuli-responsive nanoreactors” and for the opportunity to write this thesis. Moreover, I would like to thank my group leader Professor Dr Yan Lu, for all the advice and helpful discussions. She always had a friendly ear and suggestions to help me with my research and in writing this thesis.

Furthermore, I would like to thank Dr Sasa Gu, who introduced me to this topic at the beginning of this work. I also would like to thank Dr Zdravko Kochovski, who introduced me to TEM measurements and helped me with the cryo-TEM measurements. Special thanks to Dr Sebastian Risse for the help with Mathematica and the helpful discussions concerning the kinetic modelling. Special thanks as well to Arne Ronneburg for the help with Python.

Regarding the reduction of hexacyanoferrate(III), I would like to thank the whole team of the ERC project “Multiscale modelling of stimuli-responsive nanoreactors” under Professor Dr Joe Dzubiella. Special thanks to Dr Rafael Roa, Dr Won Kyu Kim, Dr Matej Kanduč for the cooperation on this multidisciplinary topic. Without their contribution, this work would not have been possible.

In the following, I would like to thank all the former and current colleagues at Helmholtz-Zentrum Berlin for the friendly work atmosphere and scientific discussions: Dr Andreas Ott, Dr Shilin Mei, Dr Qidi Ran, Dr Shun Yu, Dr Eneli Härk, Dr Luca Silvi, Dr Victor Ruiz López, Dr Karol Palczynski, Mila Miletic, Richard Chudoba, Sebastian Milster, Martin Kärgell, Ting Quan, Linda Schmalz, and the colleagues already mentioned above.

The work in this thesis was related and partially inspired by the ERC (European Research Council) Consolidator Grant NANOREACTOR of Professor Dr Joachim Dzubiella (grant agreement ID: 646659 in the European Union's Horizon 2020 research and innovation programme).

Statement of Authorship / Selbständigkeitserklärung

I declare that I have prepared this doctoral thesis independently and only with the help of the tools I have indicated according to § 7 Abs. 3 of the doctoral rules and regulations of the Mathematisch-Naturwissenschaftliche Fakultät of the Humboldt-Universität zu Berlin.

Furthermore, I declare that I have not otherwise attempted, with or without success, to submit a doctoral thesis or to undergo a doctoral examination.

Ich erkläre, dass ich diese Dissertation selbständig und nur unter Verwendung der von mir gemäß § 7 Abs. 3 der Promotionsordnung der Mathematisch-Naturwissenschaftlichen Fakultät, veröffentlicht im Amtlichen Mitteilungsblatt der Humboldt-Universität zu Berlin Nr. 126/2014 am 18.11.2014 angegebenen Hilfsmittel angefertigt habe.

Ferner erkläre ich, dass ich nicht anderweitig mit oder ohne Erfolg versucht habe, eine Dissertation einzureichen oder mich einer Promotionsprüfung zu unterziehen.

Berlin, den 10.5.2020

Daniel Besold